



National Library
of Canada

Acquisitions and
Bibliographic Services Branch

395 Wellington Street
Ottawa, Ontario
K1A 0N4

Bibliothèque nationale
du Canada

Direction des acquisitions et
des services bibliographiques

395, rue Wellington
Ottawa (Ontario)
K1A 0N4

Your file / Votre référence

Our file / Notre référence

NOTICE

The quality of this microform is heavily dependent upon the quality of the original thesis submitted for microfilming. Every effort has been made to ensure the highest quality of reproduction possible.

If pages are missing, contact the university which granted the degree.

Some pages may have indistinct print especially if the original pages were typed with a poor typewriter ribbon or if the university sent us an inferior photocopy.

Reproduction in full or in part of this microform is governed by the Canadian Copyright Act, R.S.C. 1970, c. C-30, and subsequent amendments.

AVIS

La qualité de cette microforme dépend grandement de la qualité de la thèse soumise au microfilmage. Nous avons tout fait pour assurer une qualité supérieure de reproduction.

S'il manque des pages, veuillez communiquer avec l'université qui a conféré le grade.

La qualité d'impression de certaines pages peut laisser à désirer, surtout si les pages originales ont été dactylographiées à l'aide d'un ruban usé ou si l'université nous a fait parvenir une photocopie de qualité inférieure.

La reproduction, même partielle, de cette microforme est soumise à la Loi canadienne sur le droit d'auteur, SRC 1970, c. C-30, et ses amendements subséquents.

FAR FIELD BOUNDARY
CONDITIONS FOR
COMPUTATION OF
COMPRESSIBLE
AERODYNAMIC FLOWS

by

SEYED ESMAIL RAZAVI

Department of Mechanical Engineering
McGill University
Montreal, Canada

February, 1995

A thesis submitted to the Faculty of Graduate Studies and Research
in partial fulfillment of the requirements for the degree of
Doctor of Philosophy.

© Seyed Esmail Razavi, 1995



National Library
of Canada

Acquisitions and
Bibliographic Services Branch

395 Wellington Street
Ottawa, Ontario
K1A 0N4

Bibliothèque nationale
du Canada

Direction des acquisitions et
des services bibliographiques

395, rue Wellington
Ottawa (Ontario)
K1A 0N4

Your file / Votre référence

Our file / Notre référence

THE AUTHOR HAS GRANTED AN IRREVOCABLE NON-EXCLUSIVE LICENCE ALLOWING THE NATIONAL LIBRARY OF CANADA TO REPRODUCE, LOAN, DISTRIBUTE OR SELL COPIES OF HIS/HER THESIS BY ANY MEANS AND IN ANY FORM OR FORMAT, MAKING THIS THESIS AVAILABLE TO INTERESTED PERSONS.

L'AUTEUR A ACCORDE UNE LICENCE IRREVOCABLE ET NON EXCLUSIVE PERMETTANT A LA BIBLIOTHEQUE NATIONALE DU CANADA DE REPRODUIRE, PRETER, DISTRIBUER OU VENDRE DES COPIES DE SA THESE DE QUELQUE MANIERE ET SOUS QUELQUE FORME QUE CE SOIT POUR METTRE DES EXEMPLAIRES DE CETTE THESE A LA DISPOSITION DES PERSONNE INTERESSEES.

THE AUTHOR RETAINS OWNERSHIP OF THE COPYRIGHT IN HIS/HER THESIS. NEITHER THE THESIS NOR SUBSTANTIAL EXTRACTS FROM IT MAY BE PRINTED OR OTHERWISE REPRODUCED WITHOUT HIS/HER PERMISSION.

L'AUTEUR CONSERVE LA PROPRIETE DU DROIT D'AUTEUR QUI PROTEGE SA THESE. NI LA THESE NI DES EXTRAITS SUBSTANTIELS DE CELLE-CI NE DOIVENT ETRE IMPRIMES OU AUTREMENT REPRODUITS SANS SON AUTORISATION.

ISBN 0-612-05781-X

Canada

Abstract

The formulation and implementation of a far field boundary condition (FFBC) model for compressible flows is reported in this thesis. This FFBC model, developed for quasi-one-dimensional and two-dimensional flows, aims to permit a substantial reduction of the computational domain, leading to a considerable improvement in the computational efficiency. The present FFBC approach uses asymptotic expansions of the Riemann variables, which are truncated up to the required degree of accuracy. Then, the far field perturbation equations are integrated in time and applied in conjunction with the solution calculated within the computational domain. The propagating information from the computational domain is determined along the outgoing characteristic fronts, based on the estimation of the wave front orientation.

The proposed FFBC model is implemented in conjunction with an implicit finite-difference flow field solver using an alternating direction implicit (ADI) scheme for solving the Euler equations. The discretized form of the governing equations are solved using a time-marching technique until the steady-state solution is reached. An accurate procedure for the solid boundary treatment was also used.

The proposed FFBC model was used for solving typical problems of confined and external compressible flows in subsonic and transonic regimes. For the transonic regime, the proposed FFBC model has been extended for the case of non-isentropic outgoing flows, which appear behind the shock waves. The solutions obtained are compared with previous theoretical and numerical results. This comparison shows that the proposed FFBC model can generate accurate solutions using a substantially reduced computational domain, which reduces by an order of magnitude the size of the block tridiagonal matrices to be inverted. This leads to a corresponding improvement in the overall computational efficiency.

Résumé

Cette thèse présente le développement d'un nouveau modèle de traitement numérique des conditions limites éloignées (CLE) pour les écoulements aérodynamiques compressibles. Ce modèle amélioré des CLE vise à permettre une réduction substantielle du domaine de calcul, dans le but d'obtenir une meilleure efficacité de calcul numérique. Cette méthode utilise un développement asymptotique des variables de Riemann, tronqué au niveau de précision désiré. Ces équations de perturbation sont intégrées dans le temps et utilisées conjointement avec la solution obtenue à l'intérieur du domaine numérique. La propagation de l'information à partir du domaine numérique est déterminée le long des lignes caractéristiques de l'écoulement.

Ce modèle pour les CLE est utilisé avec une méthode numérique de différences finies pour résoudre les équations d'Euler, basée sur un schéma implicite des directions alternantes. Les équations discrétisées sont résolues par l'intégration dans le temps, jusqu'à atteindre la solution stationnaire. Une méthode améliorée de traitement des parois solides est aussi présentée.

Le modèle présenté dans cet ouvrage a été appliqué à la solution de problèmes d'écoulements internes et externes typiques en régime subsonique et transsonique. Pour le régime transsonique, une extension du présent modèle a été développée pour les écoulements non-isentropiques, tel qu'ils se présentent en aval d'une onde de choc. Les résultats fournis par ce modèle ont été comparés aux solutions exactes et numériques disponibles. Ces comparaisons démontrent que ce modèle est capable de produire une solution précise dans un domaine numérique de dimensions réduites, réduisant de façon substantielle la taille de la matrice-bloque tridiagonale à manipuler et aussi la durée de calcul numérique.

Acknowledgement

My sincere gratitude goes to my supervisor Professor D. Mateescu for his assistance, criticism and initiation of new ideas which were used in this Thesis. He provided me an interesting and challenging field of study.

I would like to thank my parents for the faith they always had in me and their continuous encouragement. I want to thank my wife for her understanding, patience and providing a tidy environment at home during the lonely years.

Thanks are due to Dr. K. Mazaheri and Dr. S. Karni for the enlightening discussions.

The facilities, provided by the Mechanical Engineering network, McGill University, are highly appreciated.

I am greatly indebted to the Ministry of Culture and Higher Education of Iran, for providing the financial support during the course of this work.

Contents

Abstract	ii
Résumé	iii
Acknowledgements	iv
Contents	viii
List of Figures	xx
1 Introduction	1
1.1 General considerations	1
1.2 An overview of far field boundary condition procedures	6
1.3 Outline of the Thesis	10
2 Basic Features of Compressible Fluid Flow	13
2.1 Governing equations of rotational compressible flows	14
2.1.1 Conservative form of the Euler equations	14
2.1.2 Primitive variable form of the Euler equations	14
2.1.3 Characteristic form of the Euler equations	15
2.2 Behavior of the Euler equations	18
2.2.1 One space dimension	18
2.2.2 Two space dimensions	21
2.3 Compatibility relations for 2D Euler equations	23
3 Implicit Flow Field Solver and Solid Boundary Treatment	30
3.1 Implicit quasi-1D flow field solver	30
3.2 Implicit 2D flow field solver	32

3.2.1	Generalized coordinate transformations	33
3.2.2	Implicit time differencing	34
3.2.3	Flux vector linearization	35
3.2.4	Approximate factorization	36
3.2.5	Implicit and explicit dissipation	36
3.3	Grid features	38
3.4	Solid Wall Boundary Conditions	39
3.4.1	Conventional solid boundary methods	39
3.4.2	Solid boundary conditions in finite-difference methods	40
3.4.3	Characteristic solid boundary conditions	42
3.4.4	Effect of solid boundary treatment on the numerical solution	44
3.5	Remarks	45
4	Far Field Boundary Conditions for Quasi-One-Dimensional Flows	50
4.1	Introduction	50
4.1.1	Linear wave equation	51
4.1.2	First-order hyperbolic systems	52
4.2	Conventional boundary condition methods	54
4.3	Proposed FFBC formulation	56
4.3.1	Equations used for isentropic flows	56
4.3.2	Expanded Riemann variables approach	57
4.4	Boundary condition development (isentropic flow)	59
4.4.1	Upstream far-field region	60
4.4.2	Downstream far-field region	63
4.5	Outflow boundary conditions for non-isentropic flows	65
4.6	Model validation and numerical results	68
5	Far Field Boundary Conditions for Two-Dimensional Confined Flows	84
5.1	Introduction	84
5.2	Conventional FFBC treatments	85

5.2.1	Algebraic extrapolation methods	85
5.2.2	One-dimensional characteristics approach	85
5.3	Proposed FFBC formulation for 2-D confined flows	86
5.3.1	Equations used for isentropic flows	86
5.3.2	Expanded Riemann variables approach	88
5.4	Boundary condition development (isentropic flow)	92
5.4.1	Upstream far-field region	95
5.4.2	Matching the far field and near field solutions	97
5.4.3	Downstream far-field region	98
5.5	Discretization of far-field perturbation equations	100
5.6	Outflow far-field boundary conditions for non-isentropic flows	101
5.7	Numerical flow field solver	104
5.8	Model validation and numerical results	104
6	Far Field Boundary Conditions for External Flows	126
6.1	Introduction	126
6.2	Conventional far field boundary methods	127
6.3	Boundary condition development	128
6.3.1	Expanded Riemann variables approach	130
6.4	Inflow FFB formulation	132
6.5	Outflow FFB formulation	133
6.6	Discretization of the far field equations	134
6.7	Non-isentropic outflow FFBC	135
6.8	Model validation and discussion	135
7	Conclusions	152
7.1	Main Contributions of this Thesis	155
7.2	Future Extensions	155
	References	156

Appendices	167
A Compatibility Equations for the 2D Euler Equations	A-1
B Natural Coordinate Formulation of the Euler Equations	B-1
C Entropy Based formulation of the Euler Equations	C-1
D Riemann Variable Formulation of the Euler Equations	D-1
E Kinematic Conditions for the Compressible Flows	E-1
F Roe's Estimation of the Outgoing Wave Direction	F-1
G Characteristic Interpolation at Boundaries	G-1
H Determination of the Separation Factor	H-1
I Block-tridiagonal System of Equations	I-1

Nomenclature

Ordinary Symbols

a	Speed of sound
A	Conservative Jacobian matrix, x -direction
\bar{A}	Primitive Jacobian matrix, x -direction
a_∞	Free-stream speed of sound
B	Conservative Jacobian matrix, y -direction
\bar{B}	Primitive Jacobian matrix, y -direction
c	Constant
c_p, c_v	Specific heats at constant pressure and volume
C_p	Pressure coefficient
D	Dissipation function
\bar{D}	Velocity of wave front
\bar{D}	Characteristic matrix
E	Total energy
E	Flux vector in x direction
f	Function of surface front
F	Flux vector in y direction
G	Flux vector in z direction
H	Area in quasi-one-dimensional flow
i	Unit vector in Cartesian coordinates
I	Identity matrix
\hat{i}_n	Unit vector, normal to streamline direction
\hat{i}_s	Unit vector, streamline direction
j	Unit vector in Cartesian coordinates
J	Jacobian of transformation
ℓ	Far field distance
L	Length of computational domain

\bar{l}	Left eigenvector
\bar{L}	Matrix of left eigenvectors
m	Maximum number of seri elements
M	Local Mach number
M_I	Maximum number of grid points in x -direction
M_J	Maximum number of grid points in y -direction
n	Normal to streamline direction
\mathbf{n}	Normal vector
p	Pressure
p_∞	Free-stream pressure
q	Total velocity value
Q	Left-propagating Riemann variable
Q_k	Asymptotic function
Q'_k	Asymptotic function for external flow
r	Right eigenvector
R	Right-propagating Riemann variable, gas constant
\tilde{R}	Matrix of right eigenvectors
R_k	Asymptotic function
R_c	Radius of curvature
R'_k	Asymptotic function, external flow
s	Streamwise coordinate
S	Entropy
t	Time
T	Temperature
u	x -velocity component
U	Contravariant velocity along ξ
u_∞	Free-stream x -velocity component
v	y -velocity component
V	Contravariant velocity along η

V	Velocity vector
w	z -velocity component
W	Conservative vector
x, y, z	Cartesian coordinates

Greek Letters

α	Constant
β	Constant
γ	Ratio of specific heats
δ	Distance, in characteristic interpolation
Δ	Forward difference operator
ϵ	Perturbation function
ε	Dissipation coefficient
η	Generalized coordinate
θ	Flow angle
θ_g	Slope of FFB
ϑ	Constant in time discretization
λ	Eigenvalue
ξ	Generalized coordinate
π	Constant, 3.1415
ρ	Density
σ	Smoothing function
τ	Time
ϕ	Wave front velocity
∇	Backward difference operator
φ	Characterisitic wave angle
Ψ	Dummy scalar function
ω	Coefficient, internal flow
Ω	Difference, R-Q

ω Coefficient, external flow

Subscripts

b Boundary

$comp$ Computational

i x -direction index, grid index

j y -direction index, grid index

k Counter

∞ Free-stream

n Time-level, normal direction

x, y, z Cartesian coordinate directions

$\perp b$ Perpendicular to boundary

Superscripts

n Time-level, normal direction

T Transpose

ξ, η Generalized coordinate system

Note: () represents the negative values in figures.

List of Figures

2.1	Propagation of information through characteristic lines.	20
2.2	Propagation of acoustic waves in 2D flows.	23
2.3	Propagation of Riemann variables on the time-like planes for time-dependent 2D flows.	27
2.4	Space-time diagram showing the propagation of characteristic front, a particle path, and Mach cone in the (x, y, t) space.	29
3.1	Characteristic wave propagations at a solid wall boundary along the normal direction.	43
3.2	Grid configurations for the quasi-one-dimensional and two-dimensional confined (circular arc) flows, extended and reduced domains for each case.	46
3.3	Grid configurations for external flow (NACA0012 airfoil), extended and reduced computational domains.	47
3.4	Mach number distributions on the lower solid boundary, obtained with characteristic and conventional (extrapolation) solid boundary treatments, channel with circular-arc 10%. $M_\infty = 0.5$, CFL=2.	48
3.5	Convergence histories obtained by characteristic and algebraic treatments of solid boundary conditions, channel with circular arc 10%. $M_\infty = 0.5$, CFL=2.	49
4.1	Propagation of information for linear wave equation.	52
4.2	Characteristic lines for supersonic flow at inflow and outflow boundaries.	53
4.3	Characteristic lines for subsonic flow at inflow and outflow boundaries.	53

4.4	Propagation of Riemann variables at inflow and outflow boundaries.	57
4.5	Riemann variable propagations for one-dimensional flow at a boundary node.	58
4.6	Time evolution of the characteristic waves (Riemann variables) at a boundary point for two consecutive time levels.	60
4.7	Interpolation along left-propagating characteristic line at the inflow boundary.	61
4.8	Interpolation along characteristic line at the outflow boundary.	64
4.9	Entropy propagation in the steady quasi-one-dimensional flow.	66
4.10	Characteristic lines propagation for non-isentropic flow at outflow boundary.	68
4.11	Subsonic flow: Mach number distributions for extended computational domain (conventional FFBC treatment) and reduced computational domain (conventional FFBC treatment). $M_\infty = 0.6$, CFL=1.8, circular arc 10%.	72
4.12	Subsonic flow: Mach number distributions for extended computational domain (conventional FFBC treatment) and reduced computational domain (proposed FFBC model). $M_\infty = 0.6$, CFL=1.8, circular arc 10%.	73
4.13	A comparison of Mach number distributions in four cases: (enlarged view) a) Reduced computational domain (proposed FFBC model), b) Exact solution, c) Extended computational domain (conventional FFBC treatment), d) Reduced computational domain (conventional FFBC treatment). $M_\infty = 0.6$, CFL=1.8, circular arc 10%.	74
4.14	Subsonic flow: Mach number distributions within a reduced computational domain, resulted by applying the first- and second-order FFBCs in comparison with the exact solution. $M_\infty = 0.6$, CFL=1.8.	75
4.15	Transonic flow: Effect of the conventional outflow boundary conditions on Mach number distributions obtained by a fixed inflow condition and outflow methods of Eidelman	76

4.16	Transonic flow: Effect of the conventional outflow boundary conditions on pressure distributions obtained by a fixed inflow condition and outflow methods of Eidelman	77
4.17	Non-isentropic flow: Mach number distributions for extended computational domain (conventional FFBC treatment), exact solution, reduced computational domain (conventional FFBC treatment). $M_\infty = 0.7, p_s = p_\infty, CFL=0.9$	78
4.18	Non-isentropic flow: Pressure distributions for extended computational domain (conventional FFBC treatment), exact solution and reduced computational domain (conventional FFBC treatment). $M_\infty = 0.7, p_s = p_\infty, CFL=0.9$	79
4.19	Non-isentropic flow: Mach number distributions with exact solution and solution with the proposed FFBC model (reduced computational domain).	80
4.20	Non-isentropic flow: Pressure distributions with exact solution and solution with the proposed FFBC model (reduced computational domain). $M_\infty = 0.7$	81
4.21	Isentropic flow: Convergence histories for extended computational domain (conventional FFBC treatment), reduced computational domain (conventional FFBC treatment) and reduced computational domain (proposed FFBC model), $CFL=1.8$	82
4.22	Non-isentropic flow: Convergence histories for extended computational domain (conventional FFBC treatment) and reduced computational domain (proposed FFBC model), $CFL=0.9$	83
5.1	Propagation of Riemann variables at inflow and outflow portions for time-dependent two dimensional flows in a certain time level.	88
5.2	Projections of Riemann variables at FFB of two-dimensional flow at a certain time step.	89

5.3	Far field regions, extended and reduced domains for confined flow. . .	92
5.4	Propagation of the outgoing wave fronts with different orientations towards an inflow boundary in a 2D setup.	93
5.5	Oblique FFB with respect to Cartesian coordinates.	94
5.6	Propagation of left-propagating Riemann variable at inflow boundary along the calculated bicharacteristic for time-dependent two dimensional flow.	96
5.7	Propagations of the Riemann variables and entropy at a certain time-level for the two consecutive boundary points.	98
5.8	Interpolation stencil for wall values.	101
5.9	Comparison of upper and lower Mach numbers distributions for channel with circular arc 10%, obtained by conventional FFBC treatments for the extended and reduced computational domains. $M_\infty = 0.5$, CFL=3.	109
5.10	Comparison of upper and lower pressure distributions for the extended and reduced computational domains obtained by conventional FFBC treatment. $M_\infty = 0.5$, CFL=3.	110
5.11	Comparison of upper and lower Mach numbers for a) Extended computational domain, conventional FFBC treatment, b) Reduced computational domain, proposed FFBC model. $M_\infty = 0.5$, CFL=3.	111
5.12	Comparisons of upper and lower pressures between the extended computational domain (conventional FFBC treatment) and reduced computational domain (proposed FFBC model). $M_\infty = 0.5$, CFL=3.	112
5.13	Comparisons of upper and lower wall Mach number distributions for the extended computational domain solution of Ni	113
5.14	Convergence histories of extended and reduced computational domains, circular arc 10%. $M_\infty = 0.5$, CFL=3.	114
5.15	Mach number distributions for extended and reduced computational domains, channel with circular arc (10%), conventional FFBC treatments for both cases. $M_\infty = 0.675$, CFL=0.4.	115

5.16	Mach number distribution for extended computational domain and the solution obtained by Ni	116
5.17	Mach number distribution for reduced computational domain with proposed FFBC model and the solution obtained by Ni	117
5.18	Convegence histories for the extended and reduced computational domains, effect of the proposed FFBC model, circular arc 10%, $M_\infty = 0.675$, CFL=0.4.	118
5.19	Mach number contours for the subsonic flow, circular arc 10%, $M_\infty = 0.5$, CFL=3.	119
5.20	Mach number contours for the transonic flow, circular arc 10%, $M_\infty = 0.675$, CFL=0.4.	119
5.21	Mach number profiles at different longitudinal stations of the computational domain, subsonic flow, circular arc 10%, $M_\infty = 0.5$, CFL=2.2.	120
5.22	Propagation direction of the wave fronts during the time-integration process at an inflow FFB, confined flow with reduced computational domain, circular arc 10%, $M_\infty = 0.5$, CFL=2.	124
5.23	Propagation direction of the wave fronts during the time-integration process at an outflow FFB, confined flow with reduced computational domain, circular arc 10%, $M_\infty = 0.5$, CFL=2.	125
6.1	Propagations of the Riemann variables and entropy waves at the FFB of the external flow.	129
6.2	Inflow and outflow parts of the FFB at a certain time level.	130
6.3	Propagations of the outgoing waves at horizontal outflow and inflow FFBs.	133
6.4	Extended and reduced domain configurations for solving the external flow problem.	134

6.5	Mach number distributions for extended and reduced computational domains obtained by conventional FFBC method. NACA 0012 airfoil. $M_\infty = 0.6$, CFL=2.2.	139
6.6	Pressure coefficient comparisons for extended and reduced computational domains with conventional FFBC treatments. NACA 0012 airfoil. $M_\infty = 0.6$, CFL=2.2.	140
6.7	Mach numbers obtained from extended computational domain (conventional FFBC method) and reduced computational domain (proposed FFBC model), NACA 0012 airfoil. $M_\infty = 0.6$, CFL=2.2.	141
6.8	Pressure coefficient comparisons of the reduced computational domain with the solution of Jameson	142
6.9	Convergence history for NACA 0012 airfoil, extended computational domain. $M_\infty = 0.6$, CFL=2.2.	143
6.10	Convergence history for NACA 0012 airfoil, reduced computational domain. $M_\infty = 0.6$, CFL=2.2.	143
6.11	Transonic flow: Mach number comparisons of extended and reduced computational domains using conventional FFBCs. NACA 0012 airfoil. $M_\infty = 0.8$, CFL=0.4.	144
6.12	Transonic flow: Mach number comparisons of extended computational domain, NACA 0012 airfoil, CFL=0.4, Jameson <i>et al</i> solution	145
6.13	Transonic flow: Mach number comparisons of extended computational domain (with conventional FFBC treatments) and reduced computational domain with the proposed FFBC model. $M_\infty = 0.8$, CFL=0.4, zero incidence.	146
6.14	Transonic flow: Pressure coefficient comparisons of extended computational domain (conventional FFBC treatments) and reduced computational domain (conventional FFBC treatments). $M_\infty = 0.8$, CFL=0.4, zero incidence.	147

6.15	Transonic flow: Pressure coefficient comparisons of extended computational domain (conventional FFBC treatment) and reduced computational domain with the proposed FFBC model. $M_\infty = 0.8$, CFL=0.4, zero incidence.	148
6.16	Transonic flow: Pressure coefficient comparisons of reduced computational domain (proposed FFBC model) with Jameson <i>et al</i>	149
6.17	Convergence history for NACA 0012 airfoil, extended computational domain. $M_\infty = 0.8$, CFL=0.4.	150
6.18	Convergence history for NACA 0012 airfoil, reduced computational domain. $M_\infty = 0.8$, CFL=0.4.	150
6.19	Iso-Mach lines for subsonic flow over NACA 0012 airfoil, zero incidence, $M_\infty = 0.6$	151
6.20	Iso-Mach lines for transonic flow over NACA 0012 airfoil, zero incidence, $M_\infty = 0.8$	151
B.1	Cartesian and Natural coordinates.	B-2
F.1	Geometry of two-dimensional bicharacteristics.	F-3
G.1	Grid points near to the boundary in (x, t) space and their correspondent characteristic lines.	G-2
G.2	Interpolating for the left-propagating characteristic slope.	G-2
G.3	Comparison of the slopes for left-propagating Rieman variables in order to find the suitable grid points for interpolation.	G-3

Chapter 1

Introduction

1.1 General considerations

Most of the aerodynamic problems of interest are not completely naturally bounded by physical boundaries, as in the case of the flows past wings and aircraft configurations, or that of the flows through channels with open extremities, with many applications in various engineering problems.

In such cases, the flow domain has to be delimited by introducing artificial inflow and outflow boundaries which enclose the fluid-flow field of interest. These artificial boundaries may also be used to reduce the size of the computational domain and thus to increase the overall computational efficiency. Far field boundaries (FFBs) are made by introducing artificial partitions within the flow domain. Generally two kinds of boundaries are encountered in the computational fluid dynamics (CFD) calculations, namely far field (open) boundaries and solid ones. With respect to the flow direction crossing the boundary, the FFBs can be grouped into inflow and outflow boundaries. The computational treatment of FFBs is of importance because during the numerical calculations, disturbances are generated inside the computational domain and then propagate back and forth between the domain boundaries. When the steady-state solutions are sought this process is repeated until the disturbances decay and fall into the specified error band. In the conventional numerical treatment, the open

boundaries have to be situated at an appreciable distance from the source of the disturbances [101, 102, 149]. These large distances should be filled either with a very large number of grid points in the far field region where the flow variations are often unimportant, or with large grid sizes having reduced accuracy. When one attempts to locate the FFBs close to the domain of interest, an improved FFB model is required. The inflow and outflow boundary conditions (BCs) are also important for wind-tunnel simulations, because wind-tunnel flows are basically channel flows and are sensitive to far field conditions [62].

The far field boundary conditions (FFBCs) have substantial effect in the computation of internal and external aerodynamic flows. In the internal flows, these boundaries are inherently separated into inflow and outflow parts, whilst in the external flows, depending on the type of grid used and on the solid boundary position the inflow and outflow FFB ports are not distinguished as clearly as in the internal flow cases. A defective FFB treatment can destroy the stability, accuracy and convergence of a reliable numerical scheme. On the other hand, consistent FFBC modelling results in increased accuracy, reduced number of grid points (minimized computational domain) and also faster convergence.

Most of the aerodynamic flows are governed by time-dependent Euler equations, which are always hyperbolic in time. For hyperbolic systems, the method of characteristics forms the foundation of boundary condition analysis. For far-field and solid boundary modelling the equivalent characteristic equations are needed in order to figure out the number and directions of disturbances propagating to or from the boundaries. Most of the numerical simulations, based on the method of characteristics for the inflow and outflow boundary conditions, assume a certain degree of flow uniformity at these boundaries, which have thus to be situated far from the nonlinear flow region. The flow regime plays an important role in the FFBC modelling of compressible flows. Based on the theory of characteristics [99, 98], for supersonic flows crossing the FFBs, information propagates from upstream towards the boundary. Especial attention is required when solving the subsonic and transonic flows, where the

disturbances cross the boundaries in different directions. At an inflow boundary there are two waves propagating from the far field region to the computational domain, and one wave propagating from the computational domain towards this boundary. At an outflow boundary there exist two waves propagating from the computational domain and crossing this outlet port, and one wave comes from the downstream far field region. The inflow far field boundary condition (FFBC) is valid even if there is entropy production downstream of the boundary within the computational domain. For non-isentropic flows only downstream boundary conditions are required.

It is generally believed that boundary condition formulations consistent with the characteristic directions of propagation lead to stable and accurate solutions [37, 101, 102, 119, 142]. During the convergence process the numerical (residual) and acoustic waves start to travel between boundaries of the computational domain, until they decay [7, 73, 101, 102]. Inappropriate solid and far field boundary treatments cannot either absorb or transmit this kind of disturbances, thus it causes reflections from the boundaries back into the computational domain which consequently creates stability problems and may lead to inaccurate solutions.

For quasi-one-dimensional flows the characteristic paths are figured out without ambiguity, while in multi-dimensional flows finding the directions of propagations is not an easy task. However, the FFBCs are modelled based on the propagation of the characteristic fronts. In this case the normal component of the flow velocity to the boundary has been used in the past [61, 68, 134, 116]. In this thesis, it is shown that other than normal directions may be selected in applying the characteristics relations.

For internal flows the inflow and outflow FFBs are usually taken to be perpendicular to the free-stream velocity direction. On the other hand, in external flows the FFB configuration is dependent on the grid topology.

Not only the Euler equations govern the flow field, but also they describe the propagation of disturbances which travel between the boundaries of the computational domain. These disturbances carry the pressure, density or velocity differences. For flow problems governed by hyperbolic equations, boundary condition formulation

should be consistent with the directions of these propagations.

The FFBCs are exposed to two kinds of information, one from outside of the computational domain (far field region) and the other from its inside. Outgoing information is supplied by the numerical scheme used for solving the flow field. Appropriate far field modelling is needed for both types of propagations in terms of physical conditions and mathematical considerations.

Depending on the flow field the disturbances can be one or multidimensional. Analytically, 1D disturbances should maintain a constant profile as they propagate. However, they dissipate in numerical simulations or when interacting with a boundary or a shock wave. In contrast, two-dimensional (2D) disturbances decay as they move away from the center of disturbance and tend to zero strength as they approach to far distances. Any disturbance produced within the subsonic flow field would propagate and interact with the information coming from the far field regions. In mathematical expression there exist one characteristic which is always directed towards the upstream. Now if the boundary is inflow the disturbances coming from the computational domain interact with the downstream-propagating waves. As well the outflow FFB would be influenced by the upstream-propagating waves from the far field region.

At a solid boundary the characteristic waves can only propagate from the computational domain towards this boundary. Various types of solid boundary treatments have been suggested in the past [68, 113, 124, 144].

The number of flow variables that can be specified at a FFB is dependent on the propagation properties of the system and in particular on the information propagated from the boundary towards the flow region.

Since each characteristic direction can be considered as transporting a given information, expressed as a combination of conservative or primitive flow variables, the quantities transported from the inside of the computational domain towards the far field or solid boundary will influence the situation along these boundaries.

The propagation properties in a one-dimensional (1D) flow are expressed in a straightforward way by characteristic variables, or equivalently by the Riemann

variables.

However, in multidimensional flows there exist various directions for disturbance propagations. In the following chapters, it is shown that similar to one-dimensional case the Riemann variables can be extracted and used in a straightforward manner for the 2D flows. A streamline coordinate system makes an acceptable justification of the propagations of Riemann variables in 2D flows.

Any FFBC model should finally be matched to the flow field solver. This necessitates an overview of the existing Euler solvers. Generally, one can divide the existing algorithms into explicit and implicit with respect to time. The main advantage of explicit methods lies in their simplicity. The stability of these schemes can be checked by modal analysis (see [49, 78, 99]). When one has a complicated grid structure, it is almost imperative to use an explicit method [4]. The major disadvantage of explicit schemes lies in the time-step restrictions dictated by the Courant number (CFL limit), in which the numerical domain of dependence must contain the physical domain of dependence for hyperbolic equations. This limits the size of the time-step used for time-integration and results in slow convergence rates whenever small and non-uniform grids are required. For hyperbolic systems, the Courant number obtained for simple equation is used as stability criterion. When the aim is to obtain steady-state solutions then it is desirable to take large time steps in order to reach the steady-state as fast as possible. In the light of these observations, there has been increased interest in implicit schemes in recent years [11, 25, 83, 85, 115, 156, 159, 163]. The choice of boundary models can affect the stability of the implicit schemes [12, 137].

From spatial discretization point of view, the schemes can be grouped into central differencing and upwind differencing. One of the main advantages of the upwind differencing is that they do not usually need artificially added dissipation, but they have a reduced accuracy [82, 122]. The central difference schemes have been successfully developed as practical tools for aerodynamic problems by Jameson [68, 134, 69] and Pulliam [115, 116]. Recently, central differencing methods have been developed, which are implemented without adding the dissipation terms [25, 84].

The major difficulty of upwind schemes is their generalization to the multidimensional flows [82, 122]. Methods were developed to remedy this problem [120, 121, 122, 132]. However, most of the upwind methods are based on an application of a one dimensional splitting (or decomposition) along some preferential directions which purely depend on the construction of mesh.

For steady solutions the discretized equations are integrated in virtual time until relaxing to steady-state. An advantage of this procedure for the Euler equations is that they keep their hyperbolicity with respect to the time, hence they are applicable to all flow regimes. During time-integration the effect of initial conditions is damped, while any change in far field and solid boundary conditions can produce a new solution.

1.2 An overview of far field boundary condition procedures

Many workers have been active in this area in the last ten years, but their works have mainly been concerned with scalar partial differential equations (PDEs), with only a couple of recent applications to the Euler equations in specific circumstances [33, 45]. In general, the preceding attempts in far field formulation consist of two parts: analytical aspects and computational aspects. It is worthwhile to separate the analytical and computational approaches which are mostly used in practical fluid dynamics problems.

The PDE is well-posed only when appropriate initial and boundary conditions are appended to the differential equation. Numerical algorithms frequently require additional data to supplement those supplied from the outside of the domain of interest. This sometimes can be done by using one-sided schemes or spectral methods. For most methods it is necessary to check the stability of the algorithm for the combined IBVP. Different aspects of stability for hyperbolic equations are discussed in [1, 12, 49, 117, 139, 141]. An analysis of a finite-difference scheme is presented in [52]. For complicated schemes or systems of equations it is usually necessary to check the

stability conditions by numerical experiments [138]. For systems of equations the stability of the boundary conditions depends on the specific system as well as the scheme. For example, space extrapolation may be stable for the Lax-Wendroff method with a scalar equation but it need not be stable when used on a system [42].

An analytical investigation of far field conditions for less compressible flows is given in [28], based on the asymptotic behavior of pressure and velocity fields. The approximations in the boundary conditions can influence the stability of the overall scheme and have effects on the global accuracy of the numerical solutions [14, 49].

It was shown that if the numerical treatment is applied to the outgoing Riemann variables then stability for the scalar equation implies stability for the system of equations [27, 41]. A discussion of the well posedness for many of the linear cases is presented in [108]. Mostly mathematicians have tried to investigate the far field behavior by using the model equations, which includes the features such as stability, well-posedness and reflection analysis. Basis for the analytical approach has been done by Engquist and Majda [30, 31, 32]. They analysed the wave equation, which is not of practical interest. There are also some other works in hyperbolic equations done by mathematicians without direct application in CFD [52, 65, 130, 139, 141, 153].

Gustafsson and Kreiss [47] considered a hyperbolic system in (x, y, t) domain and obtained nonlocal boundary conditions involving the Fourier coefficients.

Hedstrom [53] derived the linear and nonlinear forms of BCs for the Euler equations, using an eigenvector approach. Lindman [87] introduced a new concept by considering projection operators in one dimension. This was generalized by Engquist and Majda [30] to multidimensional wave equations by using pseudo-differential operators. In general, one can construct nonreflecting boundary conditions only if one knows something about the solution near infinity [47]. An attempt to avoid the infinity conditions was to map the exterior region into a bounded one. It was found that there were reflections from the gradient of stretching [44]. In some circumstances the mapping could deteriorate the accuracy of the numerical solution.

The FFBCs have been encountered in solving the problems of various fields, such

as acoustics, geophysics, electromagnetics. Since, our concern here is the aerodynamic applications governed by the Euler equations, we limit the discussion to this field.

A survey in the literature shows that the methods, numerical experience and conclusions regarding the use of FFBCs have not been fully shared by researchers of different areas. A symptom is the variety of names based on the property of these boundaries were given such as nonreflecting, transmitting, absorbing and open boundaries. Recently a review of boundary conditions using one-dimensional methods has been given in [111].

Some authors used potential equation as the governing far field equation [35, 80, 106, 136]. For fully subsonic flows it would be no problem solving this equation at far field regions. However, it cannot be true for the non-isentropic flow cases where a shock is present in the flow field. In this case the potential equation is not capable of taking into account the entropy generation within the computational domain. From a computational view it is not possible to extend outer delimiting boundary to infinity; for example in turbomachinery flows, the FFBCs are typically less than one chord away from the blade [37].

An approach, based on the Riemann variables was given by Verhoff *et al* [148]-[151], which includes lots of analytical integrations, and many assumptions for performing them. In this case, a deficiency is the boundary condition (BC) formulation using the steady-state Euler equations, which are not hyperbolic for subsonic and transonic Mach numbers. Another one is that the grids cannot be clustered near the solid boundary by applying this method, for performing the inverse Fourier transformations. A simple method was proposed by Jameson *et al* throughout their works [68]-[70]. He used the 1D characteristic relations equations at boundaries of the 2D flows. With this type of boundary treatment the far field boundary should be at least 15 chords away from the solid one with an O-type grid.

The approach of Bayliss and Turkel was first suggested for wave-like equations [10] and then for elliptic systems [9]. It provided reduced reflections for the Navier-Stokes equations [7, 8]. For steady-state problems they were used to accelerate the

convergence [126, 127]. Bayliss and Turkel [7] expressed the linearized Euler equations in terms of pressure only, which was used as an outflow boundary condition. An interesting choice results from the analysis of Bayliss and Turkel, which has been shown by Roe [119, 120, 121] to correspond to a direction making an angle with the incident velocity directions aligned with the x axis; however, he did not report numerical results in this regard. The FFBCs based on Fourier transforms were developed by Gustafsson [45, 46, 48, 50] and by Ferm [33], in which the unsteady terms were dropped and after Fourier transforms (applied to steady equations), they were added, this is also the case in the works done by Verhoff *et al* [149]- [150]. By doing so the system loses its hyperbolicity in the subsonic and transonic flow regimes.

An approach using the group velocity for travelling disturbances was given by Trefethen [139, 141]. A few other computational attempts have been made based on some sort of algebraic extrapolation procedures [24, 35, 36, 80, 129].

At a subsonic FFB, part of the information can be specified. The rest of the information should be calculated using the numerical solution [41, 102]. When the inflow is given by free-stream conditions, it is necessary to decide which of the known quantities should be specified at the boundaries. Frequently, this can be done on physical grounds, e.g. the total enthalpy or total temperature is constant; see [21, 85, 102, 104, 154] for some disagreement on this point.

It is noted that the outgoing disturbances can reflect from all the domain boundaries, no matter they are solid or far field. The outflow boundary conditions arise in many applications like external aerodynamics, acoustics [32], and geophysics [36, 23]. The purpose for outflow treatment is to allow the FFB to be close to the region of interest. At the same time we demand that this boundary not reflects disturbance waves that destroys the solution accuracy and the convergence. When the steady-state is of importance, one wishes to choose the BCs to accelerate the convergence.

A way of absorbing the reflections of unwanted waves is to put some "sponge layers" at FFBs [67, 73, 74, 75]. However they are usually effective only for a narrow bandwidth. Outside of the sponge layer, reflections of frequencies are again created by

gradients due to the sponge layer itself. For many problems the boundary conditions at the body surfaces are the most crucial. According to theory [49], one can use an approximation that is one order less accurate at the boundary than in the interior domain. However, in many problems the solutions in the neighborhood of the boundary is the most important part of the solution, e.g. we wish to calculate the loading forces on the boundary. Hence, the precise implementation of the solid boundary conditions is important. In [129] a selection of boundary treatments is analyzed for stability requirements. An alternative FFBC method is to use the 1D characteristic equations, in which the FFB is locally assumed to be one-dimensional [109]. The disadvantage of this treatment is discussed in [101].

The extrapolation methods for solid boundary treatments are widely used [19, 68, 115, 124, 144]. They all are considered one dimensional treatments. One should be aware that this can lead to incorrect solutions. Most of the proposed models for treating the FFBCs have been used in conjunction with the explicit schemes [73, 119, 148]. Throughout the present work, the applicability of the proposed far field and solid boundary models have been investigated using an implicit scheme. Usually, for solving the fluid dynamic problems the implicit schemes are encountered with the drastic sizes of matrix manipulations. It will be shown in the next chapters that when an appropriate model for the FFBs is employed, the reduction in the grid size and consequently memory requirements can be kept at minimum level, while maintaining the accuracy of computations.

1.3 Outline of the Thesis

The main goal in this thesis is to investigate, formulate and implement a FFBC model for solving the inviscid compressible flow problems within the subsonic and transonic ranges. It is mainly based on the Riemann variables expansions and outgoing information related to the first-order hyperbolic PDE systems.

The remainder of this thesis describes the development and application of the

proposed FFBC model for the quasi-one and two-dimensional internal and external flows.

Chapter 2 presents some key features and mathematical specifications of the Euler equations, which recovers foundations for FFBC formulation. The Euler equations from the characteristics point of view are taken into account. Also a formulation for the characteristic compatibility equations of 2D time-dependent Euler equations is addressed. Based on these compatibility equations the direction of the outgoing waves were approximated and used in the next chapters.

The formulations of finite-difference flow field solver are presented in Chapter 3, for both quasi-one- and two-dimensional compressible flows. A factored ADI scheme is used for 2D flows, in which the block pentadiagonal coefficient matrix is decomposed into two tridiagonal ones along the coordinate axes. The discretized equations are integrated in the transient time until relaxing to the steady-state. A modified artificial dissipation is also discussed. The numerical solid boundary treatment is discussed, and a modified method is presented, which is based on the combination of normal-momentum equation and characteristic compatibility relations. It is shown that the solid boundary treatment can affect the solution accuracy and convergence towards steady-state.

The developed FFBC model for quasi-one-dimensional flows is discussed in chapter 4, which is based on the Riemann variables expansions and interpolations along the outgoing characteristic waves. Numerical solutions obtained by using the proposed FFBC model are compared and validated against the available exact analytic solutions. The results of the conventional FFBC treatments are also shown and compared with the exact solutions.

The proposed FFBC model is extended for 2D confined compressible flows in Chapter 5. The inflow and outflow FFBCs are determined from Riemann variables expansions and corresponding perturbation equations, in conjunction with the outgoing information from the computational domain, calculated along the outgoing waves. For computation of confined flow, the FFBC model is applied to a channel with a

circular-arc-bump. The model is validated by comparing the present solutions with previous results obtained by different authors for the same geometry.

In Chapter 6 the proposed FFBC model is extended for external aerodynamic flows. The corresponding perturbation equations are solved outside of the computational domain for achieving the far field values on the outer boundary. These equations are used to reduce the size of the computational domain, while maintaining the accuracy. The solutions generated by the proposed model are compared and validated with available existing solutions for certain applications (NACA 0012 airfoil).

The conclusions and main contributions are presented in Chapter 7, which also contains some suggestions for further extensions of this work.

Chapter 2

Basic Features of Compressible Fluid Flow

This chapter presents the basic equations of compressible flows and elements of the characteristics theory for the hyperbolic systems of equations. The behavior of the time-dependent Euler equations in one and two space dimensions are overviewed. Then characteristic compatibility relations were developed based on the orientations of the propagating wave fronts. It was shown that similar to the 1D flow, the compatibility relations can be obtained for the 2D Euler equations. However in this case the equations depend on the orientations (angle) of the propagating fronts. The dominant propagation direction was approximately determined based on the compatibility relations. The 2D characteristic compatibility relations and wave front orientation will be used in the next chapters to calculate the information from the computational domain.

2.1 Governing equations of rotational compressible flows

2.1.1 Conservative form of the Euler equations

The three-dimensional Euler equations can be written in conservation form as

$$\frac{\partial \mathbf{W}}{\partial t} + \frac{\partial \mathbf{E}}{\partial x} + \frac{\partial \mathbf{F}}{\partial y} + \frac{\partial \mathbf{G}}{\partial z} = \mathbf{0}, \quad (2.1)$$

where the state vector $\mathbf{W} = [\rho, \rho u, \rho v, \rho w, \rho E]^T$, contains the density ρ , the three velocity components u, v, w and the energy per unit mass E . The flux vectors \mathbf{E} , \mathbf{F} and \mathbf{G} are given by

$$\mathbf{E} = \begin{bmatrix} \rho u \\ \rho u^2 + p \\ \rho uv \\ \rho uw \\ (\rho E + p)u \end{bmatrix}, \quad \mathbf{F} = \begin{bmatrix} \rho v \\ \rho v^2 + p \\ \rho vw \\ (\rho E + p)v \end{bmatrix}, \quad \mathbf{G} = \begin{bmatrix} \rho w \\ \rho w^2 + p \\ (\rho E + p)w \end{bmatrix}, \quad (2.2)$$

and the pressure is related to the state variables as

$$p = (\gamma - 1)\rho E - \frac{\gamma - 1}{2}\rho(u^2 + v^2 + w^2), \quad \gamma = \frac{c_p}{c_v}. \quad (2.3)$$

Usually the conservative form is used as the flow field solver in shock capturing methods, while the primitive variable form is used in the boundary condition formulation.

2.1.2 Primitive variable form of the Euler equations

The primitive variable approach forms the basis for the shock fitting schemes [27, 103] and is also widely used in the boundary condition formulation [102, 104, 105, 137]. In this case the Euler equations are expressed as

$$\frac{\partial \mathbf{U}}{\partial t} + \bar{\mathbf{A}} \frac{\partial \mathbf{U}}{\partial x} + \bar{\mathbf{B}} \frac{\partial \mathbf{U}}{\partial y} + \bar{\mathbf{C}} \frac{\partial \mathbf{U}}{\partial z} = \mathbf{0}, \quad (2.4)$$

where $\mathbf{U} = [\rho, u, v, w, p]^T$ is the primitive variables vector and the Jacobians of the primitive variables are given by

$$\begin{aligned} \bar{\mathbf{A}} &= \begin{bmatrix} u & \rho & 0 & 0 & 0 \\ 0 & u & 0 & 0 & 1/\rho \\ 0 & 0 & u & 0 & 0 \\ 0 & 0 & 0 & u & 0 \\ 0 & \rho a^2 & 0 & 0 & u \end{bmatrix}, & \bar{\mathbf{B}} &= \begin{bmatrix} v & 0 & \rho & 0 & 0 \\ 0 & v & 0 & 0 & 0 \\ 0 & 0 & v & 0 & 1/\rho \\ 0 & 0 & 0 & v & 0 \\ 0 & 0 & \rho a^2 & 0 & v \end{bmatrix}, \\ \bar{\mathbf{C}} &= \begin{bmatrix} w & 0 & 0 & \rho & 0 \\ 0 & w & 0 & 0 & 0 \\ 0 & 0 & w & 0 & 0 \\ 0 & 0 & 0 & w & 1/\rho \\ 0 & 0 & 0 & \rho a^2 & w \end{bmatrix}. \end{aligned} \quad (2.5)$$

where a is the speed of sound. Since the primitive Jacobians (equation (2.5)) are related to the conservative Jacobians ($\frac{\partial \mathbf{E}}{\partial \mathbf{W}}, \frac{\partial \mathbf{F}}{\partial \mathbf{W}}, \frac{\partial \mathbf{G}}{\partial \mathbf{W}}$) by similarity transformations, the two sets of Jacobians have identical eigenvalues. These eigenvalues are in fact the speeds of information propagations. In the next chapters the system (2.4) will be expressed in terms of the Riemann variables for the FFB formulation.

2.1.3 Characteristic form of the Euler equations

This is the most important feature of the Euler equations and hyperbolic PDEs that considers the propagation of signals through the flow domain. Basically the Euler equations describe the motion of such surfaces [135, 164]. Finding the characteristic form of the Euler equations is to seek for wave-like solutions of the form [37, 157]

$$\mathbf{U} = \mathbf{U}(\zeta), \quad (2.6)$$

for the equation (2.4), where $\zeta = xk_x + yk_y + zk_z - \lambda t$.

The solution \mathbf{U} is constant on some hypersurfaces in the (x, y, z, t) space. The characteristic fronts are moving with speed λ along their normal vector, $\tilde{\mathbf{n}} = (n_x, n_y, n_z)^T$, which is a generic unit vector, $|\tilde{\mathbf{n}}| = 1$, related to the vector $(k_x, k_y, k_z)^T$. Substituting solution (2.6) into equation (2.4) yields

$$\det |\tilde{\mathbf{D}}_{\mathbf{n}} - \lambda \mathbf{I}| = 0, \quad (2.7)$$

where \mathbf{I} is the identity matrix. Hence,

$$\tilde{\mathbf{D}}_{\mathbf{n}} = \tilde{\mathbf{A}}n_x + \tilde{\mathbf{B}}n_y + \tilde{\mathbf{C}}n_z = \begin{bmatrix} V_n & \rho n_x & \rho n_y & \rho n_z & 0 \\ 0 & V_n & 0 & 0 & n_x/\rho \\ 0 & 0 & V_n & 0 & n_y/\rho \\ 0 & 0 & 0 & V_n & n_z/\rho \\ 0 & \rho a^2 n_x & \rho a^2 n_y & \rho a^2 n_z & V_n \end{bmatrix}. \quad (2.8)$$

where V_n is the projection of the velocity \mathbf{V} in direction \mathbf{n} , which is

$$V_n = \mathbf{V} \cdot \tilde{\mathbf{n}} = un_x + vn_y + wn_z. \quad (2.9)$$

System (2.4) is said to be hyperbolic if the matrix $\tilde{\mathbf{D}}_{\mathbf{n}}$ has real eigenvalues and a complete set of linearly independent eigenvectors for all $\tilde{\mathbf{n}}$. One can diagonalize matrix $\tilde{\mathbf{D}}_{\mathbf{n}}$, but it is not possible to diagonalize simultaneously the three Jacobians $\tilde{\mathbf{A}}, \tilde{\mathbf{B}}, \tilde{\mathbf{C}}$. The eigenvalues of matrix $\tilde{\mathbf{D}}_{\mathbf{n}}$ are found by solving the algebraic equation (2.7), which gives

$$\begin{aligned} \lambda_1 = \mathbf{V} \cdot \mathbf{n}, \quad \lambda_2 = \mathbf{V} \cdot \mathbf{n}, \quad \lambda_3 = \mathbf{V} \cdot \mathbf{n}, \\ \lambda_4 = \mathbf{V} \cdot \mathbf{n} + a, \quad \lambda_5 = \mathbf{V} \cdot \mathbf{n} - a. \end{aligned} \quad (2.10)$$

It is well known that the eigenvalue λ_n has a multiplicity order equal to the number of space dimensions. This means that, while for 1D case a unique definition of the left and right eigenvectors exists, in two and in three space dimensions different choices are possible.

The left eigenvectors of matrix $\tilde{\mathbf{D}}_{\mathbf{n}}$ considered as line vectors $\tilde{\mathbf{l}}$ (or $\tilde{\mathbf{L}}$ if grouped in a matrix), can be found solving

$$\tilde{\mathbf{l}}\tilde{\mathbf{D}}_{\mathbf{n}} = \lambda\tilde{\mathbf{l}}, \quad (2.11)$$

or equivalently in matrix form

$$\tilde{\mathbf{L}}\tilde{\mathbf{D}}_{\mathbf{n}} = \Lambda\tilde{\mathbf{L}}, \quad (2.12)$$

where matrix Λ is a diagonal matrix with the eigenvalues λ_j and $j \in \{1, 5\}$.

$$\tilde{\mathbf{L}} = \begin{bmatrix} 1 & 0 & 0 & 0 & -1/a^2 \\ 0 & 0 & -n_z/(n_y^2 + n_z^2) & n_y/(n_y^2 + n_z^2) & 0 \\ 0 & 1 & -n_x n_y/(n_y^2 + n_z^2) & -n_x n_z/(n_y^2 + n_z^2) & 0 \\ 0 & n_x & n_y & n_z & 1/(\rho a) \\ 0 & -n_x & -n_y & -n_z & 1/(\rho a) \end{bmatrix}. \quad (2.13)$$

The inverse $\tilde{\mathbf{R}} = \tilde{\mathbf{L}}^{-1}$, which consists of the right eigenvectors of $\tilde{\mathbf{D}}_n$, is found solving

$$\tilde{\mathbf{L}}\tilde{\mathbf{D}}_n\tilde{\mathbf{R}} = \Lambda, \quad (2.14)$$

which yields

$$\tilde{\mathbf{R}} = \begin{bmatrix} 1 & 0 & 0 & \rho/(2a) & \rho/(2a) \\ 0 & 0 & n_y^2 + n_z^2 & n_x/2 & -n_x/2 \\ 0 & -n_z & -n_x n_y & n_y/2 & -n_y/2 \\ 0 & n_y & -n_x n_z & n_z/2 & -n_z/2 \\ 0 & 0 & 0 & \rho a/2 & \rho a/2 \end{bmatrix}. \quad (2.15)$$

Having determined the left and right eigenvectors matrices, the characteristic variables can be defined as

$$d\mathbf{Z} = \tilde{\mathbf{L}}d\mathbf{U}, \quad (2.16)$$

where $d\mathbf{U} = [d\rho, du, dv, dw, dp]^T$. Hence, one gets the following characteristic variables vector

$$d\mathbf{Z} = \begin{bmatrix} d\rho - \frac{d\rho}{\rho} \bar{s} \\ d\mathbf{V} \cdot \bar{\mathbf{s}} \\ d\mathbf{V} \cdot \bar{\mathbf{t}} \\ d\mathbf{V} \cdot \bar{\mathbf{n}} + \frac{dp}{\rho a} \\ d\mathbf{V} \cdot \bar{\mathbf{n}} - \frac{dp}{\rho a} \end{bmatrix}, \quad (2.17)$$

where the normalized vectors $\bar{\mathbf{s}}$ and $\bar{\mathbf{t}}$, whose components are

$$\bar{\mathbf{s}} = \left[0, \frac{-n_z}{n_y^2 + n_z^2}, \frac{n_y}{n_y^2 + n_z^2} \right]^T, \quad \bar{\mathbf{t}} = \left[1, \frac{-n_x n_y}{n_y^2 + n_z^2}, \frac{-n_x n_z}{n_y^2 + n_z^2} \right]^T, \quad (2.18)$$

form an orthonormal base vector with $\bar{\mathbf{n}}$, i.e. $\bar{\mathbf{n}} \times \bar{\mathbf{s}} = \bar{\mathbf{t}}$. The first element in the equation (2.17) corresponds to the entropy wave. The second and third ones are the shear waves and the fourth and fifth are acoustic waves. Note that these solutions are linearized and may not reflect whole the behavior of the 3D flow field when applied to the FFB. In the conventional approaches to the FFBs, these simple waves have been used [3, 119, 120, 144]. In conventional FFBC methods, equation (2.17) is also used to figure out the number of necessary boundary conditions. Also it is locally discretized and used for far field calculations [68, 144]. In the next sections an alternative approach based on the directions of the propagating fronts will be given.

2.2 Behavior of the Euler equations

Since the quasi-one- and two-dimensional flows have been considered in the FFBC formulation, we proceed with them in some detail.

2.2.1 One space dimension

Consider the Euler equations for ideal 1D flow of a perfect gas in a constant area duct

$$\frac{\partial \mathbf{U}}{\partial t} + \bar{\mathbf{A}} \frac{\partial \mathbf{U}}{\partial x} = \mathbf{0}, \quad (2.19)$$

where

$$\mathbf{U} = \begin{bmatrix} \rho \\ u \\ p \end{bmatrix}, \quad \bar{\mathbf{A}} = \begin{bmatrix} u & \rho & 0 \\ 0 & u & 1/\rho \\ 0 & \rho a^2 & u \end{bmatrix}.$$

The matrix $\bar{\mathbf{A}}$ has real eigenvalues and a complete set of eigenvectors, therefore it can be decomposed as

$$\bar{\mathbf{A}} = \bar{\mathbf{R}} \Lambda \bar{\mathbf{L}}, \quad (2.20)$$

where $\bar{\mathbf{R}}$ is the matrix of right eigenvectors (columns) and $\bar{\mathbf{L}}$ is the matrix of left eigenvectors (rows). The following relation holds

$$\bar{\mathbf{R}}^T \bar{\mathbf{L}}^T = \bar{\mathbf{L}} \bar{\mathbf{R}} = \mathbf{I}, \quad (2.21)$$

where \mathbf{I} is the identity matrix. Now, the equation (2.19) could be decomposed to three scalar equations and, then any of the scalar equations could be integrated on the corresponding characteristic lines. Initially the matrix $\bar{\mathbf{A}}$ is assumed to be constant. Considering the relations (2.20) and (2.21), equation (2.19) when premultiplied by $\bar{\mathbf{L}}$ becomes

$$\frac{\partial(\bar{\mathbf{L}}\mathbf{U})}{\partial t} + \bar{\mathbf{L}}\Lambda\bar{\mathbf{L}}^{-1} \frac{\partial(\bar{\mathbf{L}}\mathbf{U})}{\partial x} = \mathbf{0}, \quad (2.22)$$

which can also be written as

$$\frac{\partial \mathbf{P}}{\partial t} + \Lambda \frac{\partial \mathbf{P}}{\partial x} = \mathbf{0}, \quad (2.23)$$

where $\mathbf{P} = \tilde{\mathbf{L}}\mathbf{U}$. Equation (2.23) indicates three disturbances which are moving with the velocities equal to the eigenvalues of the matrix $\tilde{\mathbf{A}}$. At each point of the flow field, there will be three characteristic curves, along any of them an ordinary differential equation (ODE) holds. To find these ODE's, one just needs the left eigenvectors of the Jacobian matrix $\tilde{\mathbf{A}}$, which are

$$\begin{aligned} \mathbf{l}_1 &= [0, \rho a, 1], \\ \mathbf{l}_2 &= [-a^2, 0, 1], \\ \mathbf{l}_3 &= [0, -\rho a, 1]. \end{aligned} \quad (2.24)$$

The equation (2.19), when multiplied by these eigenvectors, after algebraic manipulations gives the characteristic relations

$$\begin{aligned} dw_1 &= dp + \rho a du = 0, \quad \text{along } dx/dt = \lambda_1 = u + a, \\ dw_2 &= dp - a^2 d\rho = 0, \quad \text{along } dx/dt = \lambda_2 = u, \\ dw_3 &= dp - \rho a du = 0, \quad \text{along } dx/dt = \lambda_3 = u - a. \end{aligned} \quad (2.25)$$

Equations (2.25) are describing the acoustic and entropy waves with the corresponding propagation speeds λ_j (eigenvalues of the matrix $\tilde{\mathbf{A}}$). Based on these equations, the information propagates through the flow field, including the boundaries. For different flow regimes the equations (2.25) will have different directions of propagations. Equations (2.25) can also be written as

$$\begin{aligned} \frac{dp}{dt} + \rho a \frac{du}{dt} &= 0, \\ \frac{dp}{dt} - a^2 \frac{d\rho}{dt} &= 0, \\ \frac{dp}{dt} - \rho a \frac{du}{dt} &= 0, \end{aligned} \quad (2.26)$$

where

$$\frac{d}{dt} = \frac{\partial}{\partial t} + \lambda_j \frac{\partial}{\partial x}. \quad (2.27)$$

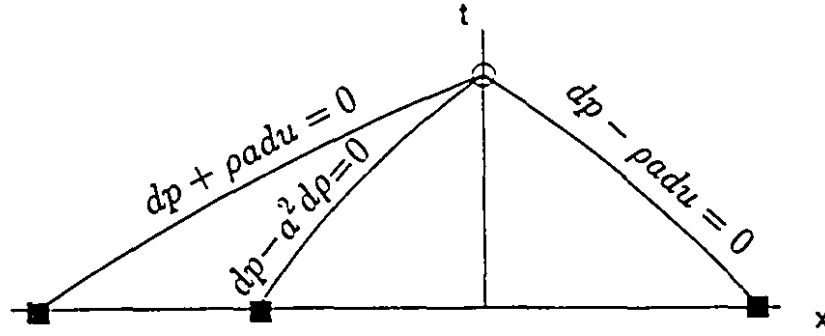


Figure 2.1: Propagation of information through characteristic lines.

Expanding the equations (2.26) along the corresponding characteristic lines in (x, t) space yields [99]

$$\begin{aligned}
 \left[\frac{\partial p}{\partial t} + \rho a \frac{\partial u}{\partial t} \right] + (u + a) \left[\frac{\partial p}{\partial x} + \rho a \frac{\partial u}{\partial x} \right] &= 0, \\
 \left[\frac{\partial p}{\partial t} - a^2 \frac{\partial \rho}{\partial t} \right] + u \left[\frac{\partial p}{\partial x} - a^2 \frac{\partial \rho}{\partial x} \right] &= 0, \\
 \left[\frac{\partial p}{\partial t} - \rho a \frac{\partial u}{\partial t} \right] + (u - a) \left[\frac{\partial p}{\partial x} - \rho a \frac{\partial u}{\partial x} \right] &= 0.
 \end{aligned} \tag{2.28}$$

In the extreme far field regions some authors [53, 68, 126] have neglected the spatial derivatives in equations (2.28), which reduce to

$$\begin{aligned}
 \frac{\partial p}{\partial t} + \rho a \frac{\partial u}{\partial t} &= 0, \\
 \frac{\partial p}{\partial t} - a^2 \frac{\partial \rho}{\partial t} &= 0, \\
 \frac{\partial p}{\partial t} - \rho a \frac{\partial u}{\partial t} &= 0.
 \end{aligned} \tag{2.29}$$

The boundary conditions (2.29), derived for 1D flows, are commonly used in multidimensional applications for the far field regions [68, 126, 127, 144]. In genuinely multidimensional flows, 1D analysis is only valid for disturbances normal to the boundary and asymptotic expansions are required for waves in other directions. Figure 2.1 depicts how the information propagates along the characteristic lines.

2.2.2 Two space dimensions

In two space dimensions, the time-dependent Euler equations can be written as

$$\frac{\partial \mathbf{U}}{\partial t} + \bar{\mathbf{A}} \frac{\partial \mathbf{U}}{\partial x} + \tilde{\mathbf{B}} \frac{\partial \mathbf{U}}{\partial y} = 0. \quad (2.30)$$

where

$$\mathbf{U} = \begin{bmatrix} \rho \\ u \\ v \\ p \end{bmatrix}, \quad \bar{\mathbf{A}} = \begin{bmatrix} u & \rho & 0 & 0 \\ 0 & u & 0 & 1/\rho \\ 0 & 0 & u & 0 \\ 0 & \gamma p & 0 & u \end{bmatrix}, \quad \tilde{\mathbf{B}} = \begin{bmatrix} v & 0 & \rho & 0 \\ 0 & v & 0 & 0 \\ 0 & 0 & v & 1/\rho \\ 0 & 0 & \gamma p & v \end{bmatrix}.$$

The Jacobian matrices $\bar{\mathbf{A}}$ and $\tilde{\mathbf{B}}$ cannot be diagonalized simultaneously. Simple wave solutions, in which \mathbf{U} is constant on some planes in the (x, y, t) space, could be written in the form

$$\mathbf{U} = \mathbf{U}(\zeta), \quad (2.31)$$

where

$$\zeta = x \cos \varphi + y \sin \varphi - \lambda t. \quad (2.32)$$

Equation (2.31) indicates solutions which are constant on straight lines in (x, y) plane (i.e. constant in (x, y, t) planes), moving with speed λ in the direction of the unit normal $\mathbf{n} = (\cos \varphi, \sin \varphi)$. Introducing these solutions and requiring non-trivial solutions for \mathbf{U} , results in the relation

$$\det [\bar{\mathbf{A}} \cos \varphi + \tilde{\mathbf{B}} \sin \varphi - \lambda \mathbf{I}] = 0. \quad (2.33)$$

Substitution of $\bar{\mathbf{A}}$ and $\tilde{\mathbf{B}}$ gives

$$(u \cos \varphi + v \sin \varphi - \lambda)^2 [(u \cos \varphi + v \sin \varphi - \lambda)^2 - a^2] = 0, \quad (2.34)$$

which has four real roots. This shows the characteristic surfaces (or simple wave fronts) are moving with the speeds

$$\begin{aligned} \lambda_1 &= u \cos \varphi + v \sin \varphi + a, \\ \lambda_2 &= u \cos \varphi + v \sin \varphi, \\ \lambda_3 &= u \cos \varphi + v \sin \varphi, \\ \lambda_4 &= u \cos \varphi + v \sin \varphi - a. \end{aligned} \quad (2.35)$$

and they carry disturbances proportional to the right eigenvectors of $\tilde{\mathbf{A}} \cos \varphi + \tilde{\mathbf{B}} \sin \varphi$:

$$\mathbf{r}_1 = \begin{bmatrix} \rho \\ a \cos \varphi \\ a \sin \varphi \\ \rho a^2 \end{bmatrix}, \quad \mathbf{r}_2 = \begin{bmatrix} \rho \\ 0 \\ 0 \\ 0 \end{bmatrix}, \quad \mathbf{r}_3 = \begin{bmatrix} 0 \\ \sin \varphi \\ -\cos \varphi \\ 0 \end{bmatrix}, \quad \mathbf{r}_4 = \begin{bmatrix} \rho \\ -a \cos \varphi \\ -a \sin \varphi \\ \rho a^2 \end{bmatrix}. \quad (2.36)$$

One can trace movements of a wave front in (x, y) space [119, 120]. Each wave front is specified by its speed λ_i , direction φ , and the type of disturbance, \mathbf{r}_i . An entropy or shear wavefront has the speed of flow particles, $u \cos \varphi + v \sin \varphi$. Note that the particle paths may differ from the front normal. An entropy wave carries the disturbance \mathbf{r}_2 (only a change in density). A shear wave, includes a change in velocity in a direction parallel to its front (i.e. no changes in the normal component of the velocity, pressure and density, as described by \mathbf{r}_3). Finally, acoustic wavefronts move with the velocities λ_1 and λ_4 . Consider a wavefront passing through the origin at time 0. It will move forward as much as $(u \cos \varphi + v \sin \varphi \pm a)\Delta t$, which is a combination of two movements. First the wavefront is moved $(u \cos \varphi + v \sin \varphi)\Delta t$ forward, after which it passes through point O in Figure 2.2 (for all values of φ), and then there is another (forward or backward) movement by an amount $a\Delta t$. Hence, regardless of the value of φ , the wavefront will be finally tangent to the circle in Figure 2.2. Changes caused by acoustic waves are proportional to \mathbf{r}_1 and \mathbf{r}_4 . It was shown that they influence the convergence process [101]. A rough estimation of the dominant wave direction gives

$$\frac{\partial \lambda_i}{\partial \varphi} = 0, \quad (2.37)$$

in which a value is found for the direction of the outgoing waves as

$$\tan \varphi \approx \frac{v}{u} = \tan \theta. \quad (2.38)$$

This value can locally be used for approximating the direction of the wave fronts [75].

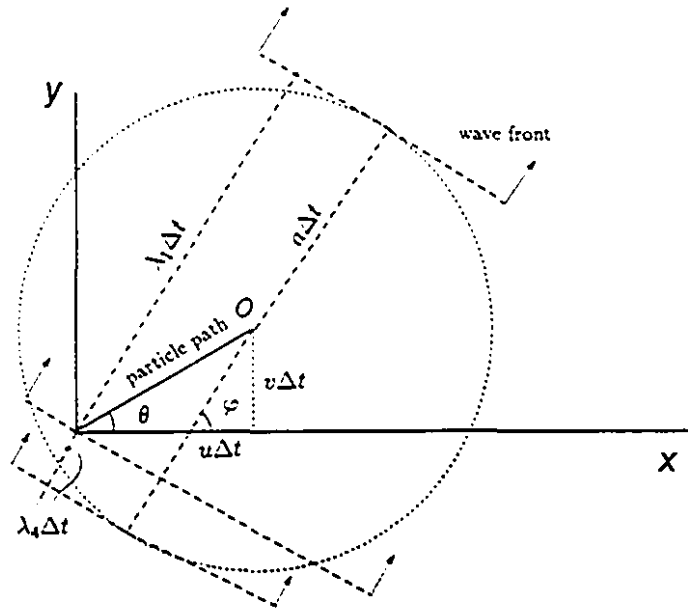


Figure 2.2: Propagation of acoustic waves in 2D flows.

2.3 Compatibility relations for 2D Euler equations

The simple wave approach shown in section 2.2.2 is limited to linearized equations and is not capable of showing the nonlinear effects of wave propagation. However, at the regions far from the highly nonlinear part of the flow the simple wave approach could be valid with good degree of accuracy. If one is interested to come closer to the nonlinear parts, they might not be valid. A new approach is followed to derive the equivalent characteristic set for the 2D Euler equations.

The solution of equations (2.30) for known initial conditions (origin of disturbance) is assumed to be a moving surface

$$f(x, y, t) = 0, \quad (2.39)$$

which is the surface of the disturbance front. Since the acoustic wave fronts carry small disturbances of the fluid, the flow variables (ρ, u, v, p, a) change only by infinitesimal

amounts, but their derivatives with respect to the coordinates (for constant time) or with respect to time (for constant coordinates) may change by finite amounts during a short time interval. Consequently these derivatives can experience a discontinuity when a wavefront passes at a certain location of the flow field. Such discontinuities are weak in contrast to the shock waves, in which the flow variables themselves experience discontinuities.

In the theory of PDEs, fronts of this type are denoted by characteristic surfaces [26, 34, 63, 123]. Considering the surface equation (2.39), the flow variables such as ρ, u, v, p can be specified along the surface. Using the derivatives $\frac{dx}{df}, \frac{dy}{df}, \frac{dt}{df}$ and $\frac{dz}{df}$ in the governing equations (2.30) results in the following characteristic condition

$$\Delta = \begin{vmatrix} 0 & 0 & \frac{1}{\rho} \frac{\partial f}{\partial x} & 0 \\ 0 & 0 & \frac{1}{\rho} \frac{\partial f}{\partial y} & 0 \\ \rho \frac{\partial f}{\partial x} & \rho \frac{\partial f}{\partial y} & 0 & 0 \\ 0 & 0 & 0 & -a^2 \phi \end{vmatrix} = 0, \quad (2.40)$$

where

$$\phi = \frac{df}{dt} = \frac{\partial f}{\partial t} + u \frac{\partial f}{\partial x} + v \frac{\partial f}{\partial y}. \quad (2.41)$$

The equation $\Delta = 0$ defines the characteristic surfaces. For the derivation of Δ see Appendix A. After some algebraic manipulation one can get from equation (2.40) as

$$\phi^2 \left\{ \phi^2 - a^2 \left[\left(\frac{\partial f}{\partial x} \right)^2 + \left(\frac{\partial f}{\partial y} \right)^2 \right] \right\} = 0. \quad (2.42)$$

The solution $\phi = 0$ corresponds to the equations of streamlines. Another solution of equation (2.42) is

$$\phi^2 = a^2 \left[\left(\frac{\partial f}{\partial x} \right)^2 + \left(\frac{\partial f}{\partial y} \right)^2 \right]. \quad (2.43)$$

The equation of wave front motion is obtained by combining the equations (2.41) and (2.43) as

$$\frac{\partial f}{\partial t} + u \frac{\partial f}{\partial x} + v \frac{\partial f}{\partial y} = \pm a \sqrt{\left(\frac{\partial f}{\partial x} \right)^2 + \left(\frac{\partial f}{\partial y} \right)^2}. \quad (2.44)$$

By the aid of chain rule derivatives, one gets

$$\phi = \frac{df}{dt}, \quad \frac{du}{dt} = \frac{du}{df} \frac{df}{dt} = \frac{du}{df} \phi. \quad (2.45)$$

and the following isentropic relation from gas dynamics

$$\frac{\partial p}{\partial x} = \frac{dp}{d\rho} \frac{\partial \rho}{\partial x}. \quad (2.46)$$

We now return to the momentum equations in system (2.30) and rewrite them as

$$\frac{du}{df} \phi + \frac{1}{\rho} \frac{dp}{d\rho} \frac{\partial \rho}{\partial x} = 0. \quad (2.47)$$

$$\frac{dv}{df} \phi + \frac{1}{\rho} \frac{dp}{d\rho} \frac{\partial \rho}{\partial y} = 0. \quad (2.48)$$

Partial derivatives of flow variables in (x, y, t) space, on both sides of the characteristic surface $f(x, y, t) = 0$, are evaluated. All these derivatives are proportional to the corresponding derivatives of the $f(x, y, t)$. This relationship for ρ is

$$\frac{\frac{\partial \rho}{\partial t}}{\frac{\partial f}{\partial t}} = \frac{\frac{\partial \rho}{\partial x}}{\frac{\partial f}{\partial x}} = \frac{\frac{\partial \rho}{\partial y}}{\frac{\partial f}{\partial y}} = \frac{d\rho}{df}. \quad (2.49)$$

For more details of condition (2.49) see Appendix E and [77, 135]. Considering the relation (2.49), one could write

$$\frac{\partial \rho}{\partial x} = \frac{d\rho}{df} \frac{\partial f}{\partial x}. \quad (2.50)$$

By introducing the value of $\frac{\partial \rho}{\partial x}$ from relation (2.50) into equation (2.47), one gets

$$\frac{du}{df} \phi + \frac{1}{\rho} \frac{dp}{d\rho} \frac{d\rho}{df} \frac{\partial f}{\partial x} = 0, \quad (2.51)$$

or after simplification

$$\phi du + \frac{dp}{\rho} \frac{\partial f}{\partial x} = 0. \quad (2.52)$$

Introducing the value of ϕ from relation (2.43) into (2.52) results in

$$\left[\pm a \sqrt{\left(\frac{\partial f}{\partial x} \right)^2 + \left(\frac{\partial f}{\partial y} \right)^2} \right] du + \frac{dp}{\rho} \frac{\partial f}{\partial x} = 0, \quad (2.53)$$

in which, one can define

$$\cos \varphi = \frac{\frac{\partial t}{\partial x}}{\sqrt{(\frac{\partial t}{\partial x})^2 + (\frac{\partial t}{\partial y})^2}}, \quad \sin \varphi = \frac{\frac{\partial t}{\partial y}}{\sqrt{(\frac{\partial t}{\partial x})^2 + (\frac{\partial t}{\partial y})^2}}. \quad (2.54)$$

For the propagating disturbances along the x -direction, equation (2.53) can be written as

$$\pm du + \cos \varphi \frac{dp}{\rho a} = 0. \quad (2.55)$$

In a similar manner the propagating disturbances along the y -direction becomes

$$\pm dv + \sin \varphi \frac{dp}{\rho a} = 0. \quad (2.56)$$

The relations (2.55) and (2.56) are the 2D compatibility equations presenting a general case of 1D characteristic relations.

Taking the squares of the equations (2.55) and (2.56) and adding yields

$$(du)^2 + (dv)^2 = \left(\frac{dp}{\rho a}\right)^2. \quad (2.57)$$

and defining the differential of resultant velocity, dq , as

$$(dq)^2 = (du)^2 + (dv)^2. \quad (2.58)$$

If the velocity changes in magnitude and not in direction, one obtains

$$(dq)^2 = \left(\frac{dp}{\rho a}\right)^2. \quad (2.59)$$

By integrating equation (2.59), one gets the Riemann variables in terms of the velocity q and sound speed a

$$q \pm \frac{2}{\gamma - 1} a = \text{const}. \quad (2.60)$$

This expression has been used by Verhoff *et al* either for boundary treatment [148, 149, 151] or in the flow field solver [152]. Relation (2.60) will be used in next chapters for the FFBC formulation and analysis of time-dependent 2D flows in natural coordinate system. Integrating the equations (2.55) and (2.56) results in the

$$\begin{aligned} \int du + \cos \varphi \int \frac{dp}{\rho a} &= R_u, & \int du - \cos \varphi \int \frac{dp}{\rho a} &= Q_u, \\ \int dv + \sin \varphi \int \frac{dp}{\rho a} &= R_v, & \int dv - \sin \varphi \int \frac{dp}{\rho a} &= Q_v. \end{aligned} \quad (2.61)$$

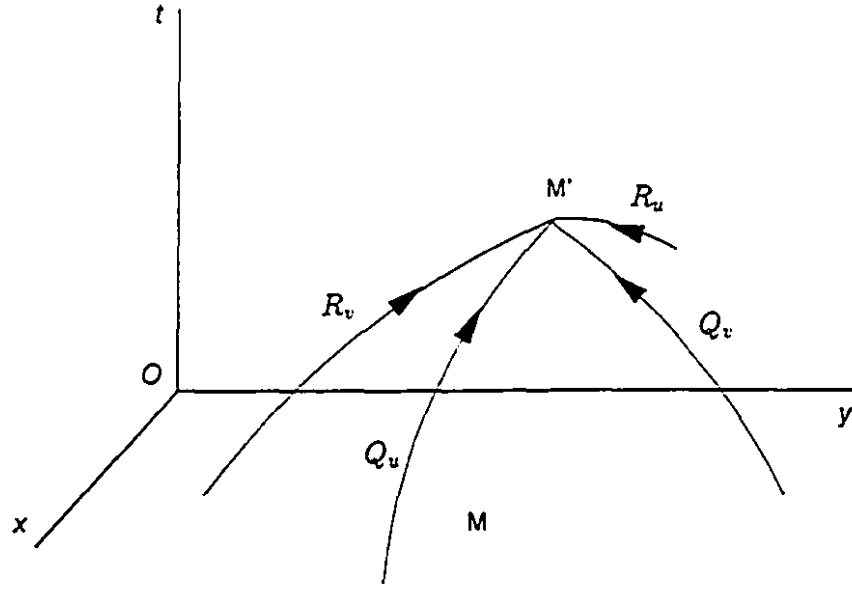


Figure 2.3: Propagation of Riemann variables on the time-like planes for time-dependent 2D flows.

which can be expressed for x and y directions in the following forms

$$\begin{aligned} R_u &= u + \cos \varphi \frac{2}{\gamma - 1} a, & Q_u &= u - \cos \varphi \frac{2}{\gamma - 1} a, \\ R_v &= v + \sin \varphi \frac{2}{\gamma - 1} a, & Q_v &= v - \sin \varphi \frac{2}{\gamma - 1} a. \end{aligned} \quad (2.62)$$

The projected Riemann variables show the paths of information propagation of multi-dimensional inviscid compressible flows. Considering the domain of dependence and how the Mach cone is cut by the boundary (see Figure 2.4), the number of BCs are known. Each bicharacteristic which brings information from outside of the domain should be replaced by a BC. The relation between the projected Riemann variables and direction of propagation is given by

$$\tan \varphi = \frac{R_v - Q_v}{R_u - Q_u}. \quad (2.63)$$

The equations (2.55) and (2.56) can also be expressed as

$$\begin{aligned} \cos \varphi \frac{dp}{dt} \pm \rho a \frac{du}{dt} &= 0, \\ \sin \varphi \frac{dp}{dt} \pm \rho a \frac{dv}{dt} &= 0. \end{aligned} \quad (2.64)$$

Along the particle path one has

$$\frac{d}{dt} = \frac{\partial}{\partial t} + u \frac{\partial}{\partial x} + v \frac{\partial}{\partial y}, \quad (2.65)$$

and for the bicharacteristics the following operator holds

$$\frac{d}{dt} = \frac{\partial}{\partial t} + (\hat{D} \cdot \nabla), \quad (2.66)$$

where $\nabla = \frac{\partial}{\partial x} \mathbf{i} + \frac{\partial}{\partial y} \mathbf{j}$ and \hat{D} is the velocity of acoustic wave fronts [135], given by

$$\hat{D} = (u \pm a \cos \varphi) \mathbf{i} + (v \pm a \sin \varphi) \mathbf{j}, \quad (2.67)$$

where \mathbf{i} and \mathbf{j} are the unit vectors in Cartesian coordinates.

Considering the operator (2.66), equations (2.64) are expressed as

$$\begin{aligned} & \cos \varphi \left[\frac{\partial p}{\partial t} + (u \pm a \cos \varphi) \frac{\partial p}{\partial x} + (v \pm a \sin \varphi) \frac{\partial p}{\partial y} \right] \\ & \pm \rho a \left[\frac{\partial u}{\partial t} + (u \pm a \cos \varphi) \frac{\partial u}{\partial x} + (v \pm a \sin \varphi) \frac{\partial u}{\partial y} \right] = 0, \\ & \sin \varphi \left[\frac{\partial p}{\partial t} + (u \pm a \cos \varphi) \frac{\partial p}{\partial x} + (v \pm a \sin \varphi) \frac{\partial p}{\partial y} \right] \\ & \pm \rho a \left[\frac{\partial v}{\partial t} + (u \pm a \cos \varphi) \frac{\partial v}{\partial x} + (v \pm a \sin \varphi) \frac{\partial v}{\partial y} \right] = 0. \end{aligned} \quad (2.68)$$

It can be assumed that at far field regions the variations of flow variables with respect to space are negligible, therefore in the limit of vanishing spatial variations, the equations (2.68) reduce to

$$\begin{aligned} \cos \varphi \frac{\partial p}{\partial t} \pm \rho a \frac{\partial u}{\partial t} &= 0, \\ \sin \varphi \frac{\partial p}{\partial t} \pm \rho a \frac{\partial v}{\partial t} &= 0, \end{aligned} \quad (2.69)$$

and hence

$$\left(\frac{\partial p}{\partial t} \right)^2 = (\rho a)^2 \left[\left(\frac{\partial u}{\partial t} \right)^2 + \left(\frac{\partial v}{\partial t} \right)^2 \right]. \quad (2.70)$$

To determine the wave angles, one combines the equations (2.69) and gets

$$\tan \varphi = \frac{\partial v / \partial t}{\partial u / \partial t}. \quad (2.71)$$

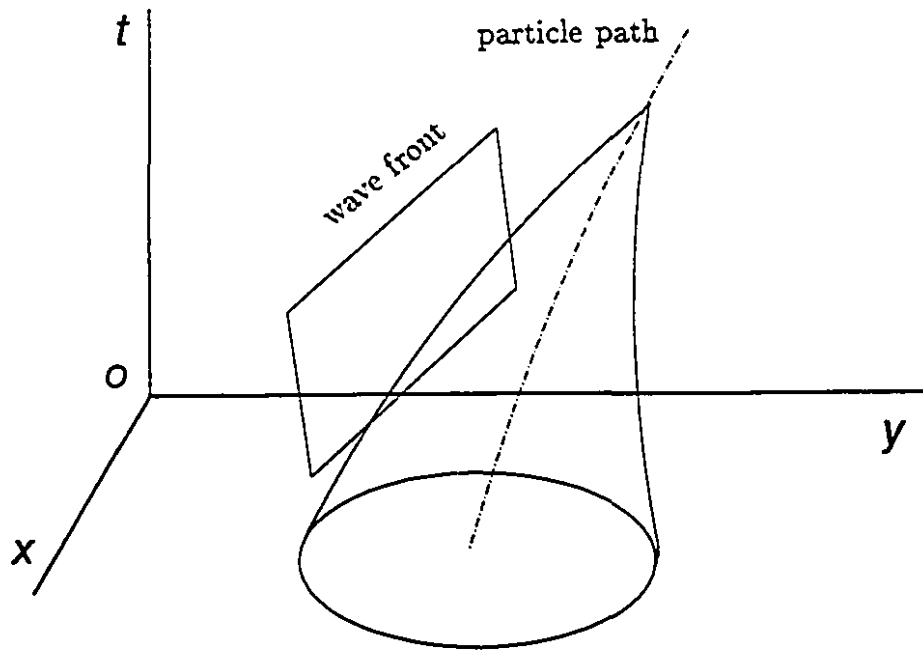


Figure 2.4: Space-time diagram showing the propagation of characteristic front, a particle path, and Mach cone in the (x, y, t) space.

Equation (2.71) will be used in the next chapters to find the direction of outgoing waves. This is an alternative to the Roe's approach [119], who approximated this wave angle using the linearized Euler equations; for more details see Appendix F.

It is often assumed that the disturbances strike the FFB with the wave fronts parallel to the boundary (i.e. the partial derivative with respect to the tangential direction is negligible). This assumption results in the 1D characteristic boundary treatments for multi-dimensional flows. If the wave fronts are not parallel to the boundary, the wave will partially be reflected back into the computational domain which slows the convergence process and may generate inaccurate solutions.

Chapter 3

Implicit Flow Field Solver and Solid Boundary Treatment

In this chapter the implicit time-marching methods for solving the quasi-one- and two-dimensional flow fields are discussed. For solving the 2D flow a factored scheme was used, similar to that developed by Beam and Warming [11]. A modified solid boundary method is also discussed.

3.1 Implicit quasi-1D flow field solver

The Euler equations for a quasi-one-dimensional flow may be expressed as

$$H \frac{\partial \mathbf{W}}{\partial t} + \frac{\partial \mathbf{F}}{\partial x} - \mathbf{G} = 0, \quad (3.1)$$

where $\mathbf{W} = [\rho, \rho u, \rho E]^T$, and $H = H(x)$ is the variable cross-sectional height. The flux and source vectors are

$$\mathbf{F} = \begin{bmatrix} \rho u \\ \rho u^2 + p \\ (\rho E + p)u \end{bmatrix} H, \quad \mathbf{G} = \begin{bmatrix} 0 \\ p \\ 0 \end{bmatrix} \frac{dH}{dx}. \quad (3.2)$$

By an implicit time discretization (Euler implicit scheme), the equation (3.1) takes the form

$$H \frac{\Delta \mathbf{W}}{\Delta t} + \left(\frac{\partial \mathbf{F}}{\partial x} \right)^{n+1} - \mathbf{G}^{n+1} = 0. \quad (3.3)$$

where

$$\Delta W = W^{n+1} - W^n. \quad (3.4)$$

The finite-difference equation (3.3) is recast in terms of ΔW (or delta form). By approaching to the steady-state, ΔW would tend to zero. A linearization procedure for equation (3.3) yields

$$F^{n+1} = F^n + \frac{\partial F}{\partial t} \Delta t + O(\Delta t^2). \quad (3.5)$$

Since $F = f(W, H)$, the chain rule of differentiation gives

$$\frac{\partial F}{\partial t} = A \frac{\partial W}{\partial t} + \frac{\partial F}{\partial H} \frac{\partial H}{\partial t}. \quad (3.6)$$

where the flux Jacobian matrix is

$$A = \frac{\partial F}{\partial W} = \begin{bmatrix} 0 & 1 & 0 \\ \frac{\gamma-3}{2}u^2 & -(\gamma-3)u & \gamma-1 \\ -\gamma u E + (\gamma-1)u^3 & \gamma E - \frac{3(\gamma-1)}{2}u^2 & \gamma u \end{bmatrix}. \quad (3.7)$$

For non-moving solid boundaries, $\frac{\partial H}{\partial t} = 0$ and hence

$$\frac{\partial F}{\partial t} = A \frac{\partial W}{\partial t} \approx A \frac{\Delta W}{\Delta t}. \quad (3.8)$$

Substituting relation (3.8) into (3.5) gives

$$F^{n+1} = F^n + A \Delta W + O(\Delta t^2). \quad (3.9)$$

In a similar fashion one can linearize the source vector

$$G^{n+1} = G^n + B \Delta W + O(\Delta t^2). \quad (3.10)$$

where

$$B = \frac{\partial G}{\partial W} = (\gamma-1) \frac{dH}{dx} \begin{bmatrix} 0 & 0 & 0 \\ \frac{1}{2}u^2 & -u & 1 \\ 0 & 0 & 0 \end{bmatrix}, \quad (3.11)$$

and $\gamma = \frac{c_p}{c_v} = 1.4$. The first order hyperbolic equation (3.1) has the property that the flux vector F is a homogeneous function of first degree in W ; i.e. $F(kW) =$

$k\mathbf{F}(\mathbf{W})$, where k is an arbitrary constant. In general, Euler equations possess this property [131, 132].

The eigenvalues of \mathbf{A} represent the characteristic directions for information propagation. For stability considerations one is referred to [132].

The linearized form of equation (3.3) in terms of Jacobian matrices then is

$$H \frac{\Delta \mathbf{W}}{\Delta t} + \frac{\partial}{\partial x} (\mathbf{A} \Delta \mathbf{W}) - \mathbf{B} \Delta \mathbf{W} = -\frac{\partial \mathbf{F}^n}{\partial x} + \mathbf{G}^n, \quad (3.12)$$

which can be recast as

$$[H\mathbf{I} + \Delta t \frac{\partial}{\partial x} \mathbf{A} - \Delta t \mathbf{B}] \Delta \mathbf{W} = -\Delta t \left(\frac{\partial \mathbf{F}^n}{\partial x} - \mathbf{G}^n \right), \quad (3.13)$$

where \mathbf{I} is the identity matrix and $\frac{\partial}{\partial x} (\mathbf{A} \Delta \mathbf{W})$ is discretized by central differencing as

$$\left[\frac{\partial}{\partial x} (\mathbf{A} \Delta \mathbf{W}) \right]_i = \frac{1}{2\Delta x} (\mathbf{A}_{i+1} \Delta \mathbf{W}_{i+1} - \mathbf{A}_{i-1} \Delta \mathbf{W}_{i-1}). \quad (3.14)$$

Equation (3.13) generates a block-tridiagonal system of equations, when discretized by (3.14).

3.2 Implicit 2D flow field solver

Implicit schemes have widely been used for stability considerations. In practice for nonlinear systems the stability bounds encountered for implicit schemes are less restrictive than for explicit schemes. However, they produce large linear systems of algebraic equations which are computationally expensive to solve. Hence, factored methods [4, 11, 16] are used to split the problem along the coordinates.

For 2D compressible flows, the Euler equations in the conservation form can be written as

$$\frac{\partial \mathbf{W}}{\partial t} + \frac{\partial \mathbf{F}}{\partial x} + \frac{\partial \mathbf{G}}{\partial y} = 0, \quad (3.15)$$

where $\mathbf{W} = [\rho, \rho u, \rho v, \rho E]^T$ and flux vectors are

$$\mathbf{F} = \begin{bmatrix} \rho u \\ \rho u^2 + p \\ \rho uv \\ (\rho E + p)u \end{bmatrix}, \quad \mathbf{G} = \begin{bmatrix} \rho v \\ \rho uv \\ \rho v^2 + p \\ (\rho E + p)v \end{bmatrix}. \quad (3.16)$$

The pressure is related to the conservative flow variables, \mathbf{W} , by the equation of state

$$p = (\gamma - 1)\rho E - \frac{\gamma - 1}{2}\rho(u^2 + v^2). \quad (3.17)$$

The choice of nondimensional parameters depends on the flow nature. Here the stagnation values are used

$$\rho^* = \frac{\rho}{\rho_0}, \quad u^* = \frac{u}{a_0}, \quad v^* = \frac{v}{a_0}, \quad E^* = \frac{E}{a_0^2}, \quad p^* = \frac{p}{\rho_0 a_0^2}, \quad t^* = \frac{a_0 t}{L_{ref}}. \quad (3.18)$$

where L_{ref} represents the chord length. For simplicity, the superscript $*$ will be dropped in the following equations, in which all quantities are nondimensional.

3.2.1 Generalized coordinate transformations

The 2D Euler equations are transformed from cartesian coordinates to general curvilinear coordinates where for a time-independent grid

$$\tau = t, \quad \xi = \xi(x, y), \quad \eta = \eta(x, y). \quad (3.19)$$

The coordinate transformation introduced here follows the development of Vinokur [155]. The transformations are chosen so that the grid spacing in the curvilinear space is uniform and of unit length. This produces a rectangular computational domain in (ξ, η) space with uniform grid ($\Delta\xi = 1$, $\Delta\eta = 1$), hence unweighted differencing schemes are used.

The following relation is used to represent the Cartesian derivatives in terms of the curvilinear derivatives

$$\begin{bmatrix} \partial/\partial t \\ \partial/\partial x \\ \partial/\partial y \end{bmatrix} = \begin{bmatrix} 1 & \xi_x & \eta_x \\ 0 & \xi_x & \eta_x \\ 0 & \xi_y & \eta_y \end{bmatrix} \begin{bmatrix} \partial/\partial \tau \\ \partial/\partial \xi \\ \partial/\partial \eta \end{bmatrix}, \quad (3.20)$$

where

$$\begin{aligned} \xi_x &= Jy_\eta, & \xi_y &= -Jx_\eta, \\ \eta_x &= -Jy_\xi, & \eta_y &= Jx_\xi, \end{aligned} \quad (3.21)$$

in which J represents the Jacobian of the transformation

$$J = \xi_x \eta_y - \xi_y \eta_x. \quad (3.22)$$

Equations (3.21) are discretized by a second-order central differencing scheme. Near the boundaries they are switched to one-sided second-order ones.

After transformation the Euler equations take the form

$$\frac{\partial \hat{\mathbf{W}}}{\partial t} + \frac{\partial \hat{\mathbf{F}}}{\partial \xi} + \frac{\partial \hat{\mathbf{G}}}{\partial \eta} = \mathbf{0}. \quad (3.23)$$

$$\hat{\mathbf{W}} = \frac{1}{J} \begin{bmatrix} \rho \\ \rho u \\ \rho v \\ \rho E \end{bmatrix}, \quad \hat{\mathbf{F}} = \frac{1}{J} \begin{bmatrix} \rho U \\ \rho u U + \xi_x p \\ \rho v U + \xi_y p \\ (\rho E + p)U \end{bmatrix}, \quad \hat{\mathbf{G}} = \frac{1}{J} \begin{bmatrix} \rho V \\ \rho u V + \eta_x p \\ \rho v V + \eta_y p \\ (\rho E + p)V \end{bmatrix}, \quad (3.24)$$

where

$$U = \xi_x u + \xi_y v, \quad V = \eta_x u + \eta_y v. \quad (3.25)$$

are the contravariant velocity components.

The transformed equations (3.23) are somewhat more complicated than the original Cartesian form but offer several significant advantages. One advantage is that boundaries in the physical plane are mapped onto rectangular configuration in the computational plane.

3.2.2 Implicit time differencing

Consider an implicit three-point time differencing scheme [156]

$$\frac{\partial \hat{\mathbf{W}}}{\partial t} = \frac{1}{\Delta t} \frac{(1 + \vartheta_1)\Delta^n - \vartheta_1 \nabla^n}{1 + \vartheta_2 \Delta^n} \hat{\mathbf{W}} + (\vartheta_2 - \vartheta_1 - \frac{1}{2})O(\Delta t) + O(\Delta t^2), \quad (3.26)$$

where Δ^n and ∇^n represent the forward and backward time difference operators respectively, for example: $\Delta^n \hat{\mathbf{W}} = \hat{\mathbf{W}}^{n+1} - \hat{\mathbf{W}}^n$. The parameters ϑ_1 and ϑ_2 can be chosen to produce different schemes of either first- or second-order accuracy in time. For $\vartheta_1 = 0$ and $\vartheta_2 = 1$, we have the first-order Euler implicit scheme, which is

$$\hat{\mathbf{W}}^{n+1} = \hat{\mathbf{W}}^n + \Delta t \left(\frac{\partial \hat{\mathbf{W}}}{\partial t} \right)^{n+1} + O(\Delta t^2). \quad (3.27)$$

For $\theta_1 = \frac{1}{2}$ and $\theta_2 = 1$, one obtains the three-point implicit scheme of second-order accuracy.

Using the first-order Euler scheme, equation (3.23) is discretized as

$$\hat{\mathbf{W}}^{n+1} - \hat{\mathbf{W}}^n + \Delta t(\hat{\mathbf{F}}_\xi^{n+1} + \hat{\mathbf{G}}_\eta^{n+1}) = 0. \quad (3.28)$$

3.2.3 Flux vector linearization

The flux vectors $\hat{\mathbf{F}}$ and $\hat{\mathbf{G}}$ are nonlinear functions of $\hat{\mathbf{W}}$ and therefore equation (3.28) is nonlinear in $\hat{\mathbf{W}}^{n+1}$. The nonlinear terms are linearized in time about $\hat{\mathbf{W}}^n$ by Taylor series such that

$$\begin{aligned} \hat{\mathbf{F}}^{n+1} &= \hat{\mathbf{F}}^n + \hat{\mathbf{A}}^n \Delta^n \hat{\mathbf{W}} + O(\Delta t^2), \\ \hat{\mathbf{G}}^{n+1} &= \hat{\mathbf{G}}^n + \hat{\mathbf{B}}^n \Delta^n \hat{\mathbf{W}} + O(\Delta t^2), \end{aligned} \quad (3.29)$$

where $\hat{\mathbf{A}} = \partial \hat{\mathbf{F}} / \partial \hat{\mathbf{W}}$ and $\hat{\mathbf{B}} = \partial \hat{\mathbf{G}} / \partial \hat{\mathbf{W}}$ are the transformed flux Jacobians and $\Delta^n \hat{\mathbf{W}}$ is $O(\Delta t)$. The linearizations are second order accurate and so if a second-order time scheme had been chosen, the linearizations would not degrade the time accuracy.

Applying relations (3.29) to equation (3.28) and combining the $\Delta^n \hat{\mathbf{W}}$ terms produces the unfactored "delta form" of the algorithm

$$\left[\mathbf{I} + \Delta t \left(\frac{\partial}{\partial \xi} \hat{\mathbf{A}}^n + \frac{\partial}{\partial \eta} \hat{\mathbf{B}}^n \right) \right] \Delta^n \hat{\mathbf{W}} = -\Delta t \left(\frac{\partial \hat{\mathbf{F}}^n}{\partial \xi} + \frac{\partial \hat{\mathbf{G}}^n}{\partial \eta} \right). \quad (3.30)$$

The Jacobian matrices are [115]

$$\hat{\mathbf{A}} \text{ or } \hat{\mathbf{B}} = \begin{bmatrix} 0 & \kappa_x & \kappa_y & 0 \\ -u\epsilon + \kappa_x \psi & \epsilon - (\gamma - 2)\kappa_x u & \kappa_y u - (\gamma - 1)\kappa_x v & (\gamma - 1)\kappa_x \\ -v\epsilon + \kappa_y \psi & \kappa_x v - (\gamma - 1)\kappa_y u & \epsilon - (\gamma - 2)\kappa_y v & (\gamma - 1)\kappa_y \\ \epsilon(\psi - c_1) & \kappa_x c_1 - (\gamma - 1)u\epsilon & \kappa_y c_1 - (\gamma - 1)v\epsilon & \gamma\epsilon \end{bmatrix}, \quad (3.31)$$

where $c_1 = \gamma E - \psi$, $\epsilon = \kappa_x u + \kappa_y v$, $\psi = \frac{1}{2}(\gamma - 1)(u^2 + v^2)$, and $\kappa = \xi$ or η for $\hat{\mathbf{A}}$ or $\hat{\mathbf{B}}$, respectively.

The convective derivatives in equation (3.30) are approximated by three point central differences.

3.2.4 Approximate factorization

An approximate factorization is used for the left hand side of equation (3.30), which can be written as

$$\left[\mathbf{I} + \Delta t \frac{\partial}{\partial \xi} \hat{\mathbf{A}}^n + \Delta t \frac{\partial}{\partial \eta} \hat{\mathbf{B}}^n \right] \Delta \hat{\mathbf{W}} = \left[\mathbf{I} + \Delta t \frac{\partial}{\partial \xi} \hat{\mathbf{A}}^n \right] \left[\mathbf{I} + \Delta t \frac{\partial}{\partial \eta} \hat{\mathbf{B}}^n \right] \Delta \hat{\mathbf{W}} - \Delta t^2 \frac{\partial}{\partial \xi} \hat{\mathbf{A}}^n \frac{\partial}{\partial \eta} \hat{\mathbf{B}}^n \Delta \hat{\mathbf{W}}. \quad (3.32)$$

The cross term is of a second order and can therefore be neglected: the factored form of equation (3.30) is

$$\left[\mathbf{I} + \Delta t \frac{\partial}{\partial \xi} \hat{\mathbf{A}}^n \right] \left[\mathbf{I} + \Delta t \frac{\partial}{\partial \eta} \hat{\mathbf{B}}^n \right] \Delta^n \hat{\mathbf{W}} = -\Delta t \left(\frac{\partial \hat{\mathbf{F}}^n}{\partial \xi} + \frac{\partial \hat{\mathbf{G}}^n}{\partial \eta} \right). \quad (3.33)$$

They lead to block tridiagonal systems after the spatial discretization. This equation can be solved in two different sweeps along ξ and η directions, by introducing the intermediate variable $\Delta^n \hat{\mathbf{W}}^*$, in the form

$$\begin{aligned} \left[\mathbf{I} + \Delta t \frac{\partial}{\partial \xi} \hat{\mathbf{A}}^n \right] \Delta^n \hat{\mathbf{W}}^* &= -\Delta t \left(\frac{\partial \hat{\mathbf{F}}^n}{\partial \xi} + \frac{\partial \hat{\mathbf{G}}^n}{\partial \eta} \right), \\ \left[\mathbf{I} + \Delta t \frac{\partial}{\partial \eta} \hat{\mathbf{B}}^n \right] \Delta^n \hat{\mathbf{W}} &= \Delta^n \hat{\mathbf{W}}^*. \end{aligned} \quad (3.34)$$

The spatial derivatives $\frac{\partial}{\partial \xi} \hat{\mathbf{A}}^n$ and $\frac{\partial}{\partial \eta} \hat{\mathbf{B}}^n$ are discretized by central differencing, similar to equation (3.14); this leads to a block tridiagonal system of equations for each sweep. The block matrix size is $4M_I \times 4M_J$. At each time step the system is solved by block *LU* decomposition (see Appendix I).

3.2.5 Implicit and explicit dissipation

Although linear stability analysis shows unconditional stability for this implicit algorithm, in practice stability bounds are encountered. This is because of shock waves and boundary condition problems. The wave interactions lead to high and low frequency waves. The lower frequencies postpone the convergence, but higher frequencies violates the numerical stability, when they exceed the mesh size. For coping with this

problem, a numerical dissipation is added with an error level that does not interfere with the solution accuracy.

An implicit second-order dissipation is inserted into the respective implicit block operators

$$\begin{aligned} D_{2\xi} &= -\varepsilon_i \Delta t J^{-1} \nabla_\xi \Delta_\xi J, \\ D_{2\eta} &= -\varepsilon_i \Delta t J^{-1} \nabla_\eta \Delta_\eta J, \end{aligned} \quad (3.35)$$

where ∇ and Δ represent the backward and forward spatial difference operators respectively. The parameter ε_i is of $O(1)$. Also, a nonlinear explicit dissipation is added to the right hand side of equation (3.33) and will be shown later. After applying the dissipation terms, equation (3.34) becomes

$$\left[\mathbf{I} + \Delta t \left(\frac{\partial}{\partial \xi} \hat{\mathbf{A}}'^n + \frac{\partial}{\partial \eta} \hat{\mathbf{B}}'^n \right) \right] \Delta^n \hat{\mathbf{W}} = -\Delta t \left(\frac{\partial \hat{\mathbf{F}}^n}{\partial \xi} + \frac{\partial \hat{\mathbf{G}}^n}{\partial \eta} \right) + D, \quad (3.36)$$

where $\hat{\mathbf{A}}'^n$ and $\hat{\mathbf{B}}'^n$ are the matrices after introducing the implicit dissipation. The implicit dissipation is used to extend the stability range. The explicit dissipation [68, 114] is

$$D = \nabla_\xi \sigma_\xi \left[\varepsilon_\xi^{(2)} \Delta_\xi - \varepsilon_\xi^{(4)} \Delta_\xi \nabla_\xi \Delta_\xi \right] \mathbf{W} + \nabla_\eta \sigma_\eta \left[\varepsilon_\eta^{(2)} \Delta_\eta - \varepsilon_\eta^{(4)} \Delta_\eta \nabla_\eta \Delta_\eta \right] \mathbf{W} \quad (3.37)$$

where

$$\begin{aligned} \sigma_\xi &= \lambda_{i+1j}^{(\xi)} J_{i+1j}^{-1} + \lambda_{ij}^{(\xi)} J_{ij}^{-1}, \\ \sigma_\eta &= \lambda_{ij+1}^{(\eta)} J_{ij+1}^{-1} + \lambda_{ij}^{(\eta)} J_{ij}^{-1}. \end{aligned} \quad (3.38)$$

The $\lambda^{(\xi)}$ and $\lambda^{(\eta)}$ are the spectral radii of the transformed Jacobian matrices $\hat{\mathbf{A}}$ and $\hat{\mathbf{B}}$ respectively,

$$\begin{aligned} \lambda^{(\xi)} &= |\mathcal{U}| + a \sqrt{\xi_x^2 + \xi_y^2}, \\ \lambda^{(\eta)} &= |V| + a \sqrt{\eta_x^2 + \eta_y^2}. \end{aligned} \quad (3.39)$$

They show the largest propagation speeds in the computational space. The coefficients $\varepsilon_\xi^{(2)}$, $\varepsilon_\eta^{(2)}$, $\varepsilon_\xi^{(4)}$, and $\varepsilon_\eta^{(4)}$ are

$$\varepsilon_\xi^{(2)} = k_2 \Delta t \max(\nu_{i+1j}, \nu_{ij}, \nu_{i-1j}),$$

$$\begin{aligned}
\varepsilon^{(2)} &= k_2 \Delta t \max(\nu_{i,j+1}, \nu_{i,j}, \nu_{i,j-1}), \\
\varepsilon_\xi^{(4)} &= \max(0, k_4 \Delta t - \varepsilon_\xi^{(2)}), \\
\varepsilon_\eta^{(4)} &= \max(0, k_4 \Delta t - \varepsilon_\eta^{(2)}),
\end{aligned} \tag{3.40}$$

where $k_2 = 0.25$ and $k_4 = 0.01$ and ν is a sensor to feel the steep gradients

$$\nu_\xi = \left| \frac{p_{i+1,j} - 2p_{i,j} + p_{i-1,j}}{p_{i+1,j} + 2p_{i,j} + p_{i-1,j}} \right|, \quad \nu_\eta = \left| \frac{p_{i,j+1} - 2p_{i,j} + p_{i,j-1}}{p_{i,j+1} + 2p_{i,j} + p_{i,j-1}} \right|. \tag{3.41}$$

The scaling factors of equations (3.38) consider both spatial directions, by using the eigenvalues. Near the steep pressure gradients, $\varepsilon^{(2)}$ takes larger values due to larger values of ν related to the steep pressure gradients there, so that from equations (3.40), $\varepsilon^{(4)}$ drops to zero, hence only the second-order dissipation is added. In the smooth flow regions, $\varepsilon^{(2)}$ is vanishingly small and only the fourth-order dissipation is applied.

Based on propagation speeds the switch functions are modified as

$$\nu'_\xi = \left(\frac{M}{M_\infty} \right)^d \nu_\xi, \quad \nu'_\eta = \left(\frac{M}{M_\infty} \right)^d \nu_\eta, \tag{3.42}$$

where constant values are $d = 1, 2$. The inclusion of local Mach number increases the dissipation value near the steep gradients and reduces it near the stagnation point. This procedure allows to use rather coarser grids to perform the calculations. The computations are performed from $i = 2$ to $i = M_I - 1$ and from $j = 2$ to $j = M_J - 1$. At the boundaries the dissipation is switched off.

3.3 Grid features

A grid with variable spacing was generated by an algebraic method. The numerical grid is aligned with the solid walls for confined flow and with airfoil contour for the external flow problems. A rectangular outer boundary was used in order to facilitate the application of the far field perturbation equations for both cases. On the arc-shaped wall and airfoil, 26 and 28 grid points were used, respectively. Our main concern here being a comparative study of the far field behavior in both the extended and reduced computational domains having the same specifications. The grid points

were equally-spaced along the x -direction, while in the y -direction they were stretched hyperbolically, starting from the nozzle wall or the airfoil surface. The computational grids used for the flow in a duct with a circular-arc-bump on the lower wall (nozzle flow) and for the external flow past a NACA0012 airfoil are illustrated in Figures 3.2 and 3.3.

3.4 Solid Wall Boundary Conditions

The computational treatment of solid boundaries is an essential aspect of a numerical scheme. The effect of solid boundary conditions on the solution accuracy and convergence is discussed and a method based on the characteristics relations in conjunction with normal-momentum equation is presented.

3.4.1 Conventional solid boundary methods

For the computation of aerodynamic flows, it is important to implement numerically the solid boundary conditions. Since, on the solid boundary not all of the flow variables are specified by the boundary conditions, and there are more unknowns than available equations. In the finite-difference methods, the transformation to a generalized coordinate system makes the application of the solid boundary affordable. Good solid boundary conditions must ensure the disturbance dissipation in the computational domain without reflection. The propagation of perturbations is consistent with the characteristic properties of the Euler equations [101], expressed by compatibility relations [88]. Violating the characteristic directions leads to inaccurate solutions and delayed convergence. Inconsistent solid boundary treatment destroys the global conservation [113].

A conventional procedure is to discretize the governing equations from the boundary into the flow field by one-sided difference scheme (in general different from that applied to the other interior points). Usually free-stream stagnation enthalpy is held constant along the solid surface. After the velocity components and pressure

were computed a value of density is obtained at the solid boundary [131]. Rizzi [124] states that for a solid body more than one characteristic equation is necessary. He also introduced the use of normal momentum equation avoiding the need for extrapolation.

A first-order boundary method is consistent with a second-order interior scheme and the convergence to the true solution is still of second order [123]. The soft wall boundary was developed and applied to aerodynamic flows to accelerate the convergence process [101].

3.4.2 Solid boundary conditions in finite-difference methods

In the solid boundary treatment, the normal component of the flux vector reduces thus only to the contribution of pressure. In the computational space, on the solid boundaries the relations (3.25) for contravariant velocity components become

$$\begin{bmatrix} \xi_x & \xi_y \\ \eta_x & \eta_y \end{bmatrix} \begin{bmatrix} u \\ v \end{bmatrix} = \begin{bmatrix} U \\ 0 \end{bmatrix}, \quad (3.43)$$

because on the solid boundary $V = 0$. From relations (3.43) one could find the physical velocity components as

$$u = \frac{1}{J} \eta_y U, \quad v = -\frac{1}{J} \eta_x U. \quad (3.44)$$

In the conventional solid boundary methods, U is extrapolated from the computational domain. The pressure is either calculated from the normal-momentum equation or extrapolated from the neighboring grid points. Having calculated the velocity components (u, v) and pressure (p) , the density (ρ) can be determined from the assumption that on the solid boundary the total enthalpy is equal to the total enthalpy of the free-stream flow.

The normal-momentum equation is used to determine the pressure on the solid boundary. Starting from the momentum equation, one has

$$\rho \frac{dV}{dt} + \nabla p = 0. \quad (3.45)$$

At a solid wall, the impenetrability condition is expressed as

$$q_{\perp} = \mathbf{V} \cdot \mathbf{i}_n = 0, \quad (3.46)$$

where \mathbf{i}_n is the unit vector normal to the solid boundary. Note that on the solid boundary, the streamline follows the body shape, therefore equation (3.46) leads to $\tan \theta_i = \frac{v}{u}$, where θ_i is the solid boundary inclination. By differentiating equation (3.46) with respect to time, one gets

$$\frac{d}{dt}(\mathbf{V} \cdot \mathbf{i}_n) = 0 \quad (3.47)$$

Projecting the momentum equation (3.45) along normal to the solid boundary gives

$$\rho \mathbf{i}_n \cdot \frac{d\mathbf{V}}{dt} + \mathbf{i}_n \cdot \nabla p = 0. \quad (3.48)$$

Combining the equations (3.47) and (3.48) leads to

$$\rho \mathbf{V} \cdot \frac{d\mathbf{i}_n}{dt} = \mathbf{i}_n \cdot \nabla p. \quad (3.49)$$

For non-moving solid boundary ($\frac{\partial \mathbf{i}_n}{\partial t} = 0$), equation (3.49) is simplified to

$$\rho \mathbf{V} \cdot (\mathbf{V} \cdot \nabla) \mathbf{i}_n = \mathbf{i}_n \cdot \nabla p \quad (3.50)$$

Using the relations (3.20) and (B.4), equation (3.50) can be expressed in generalized coordinate system as

$$-\rho U \left(\eta_x \frac{\partial u}{\partial \xi} + \eta_y \frac{\partial v}{\partial \xi} \right) = (\xi_x \eta_x + \xi_y \eta_y) \frac{\partial p}{\partial \xi} + (\eta_x^2 + \eta_y^2) \frac{\partial p}{\partial \eta}. \quad (3.51)$$

In equation (3.51) the derivatives with respect to ξ are approximated with second-order central differences, while the derivatives with respect to η are replaced by second-order one-sided differences. For example one has

$$\begin{aligned} \frac{\partial p}{\partial \xi} &= \frac{p_{i+1,1} - p_{i-1,1}}{2\Delta\xi}, \\ \frac{\partial p}{\partial \eta} &= \frac{-3p_{i,1} + 4p_{i,2} - p_{i,3}}{2\Delta\eta}. \end{aligned} \quad (3.52)$$

Equation (3.51) becomes thus in discretized form.

$$a'p_{i-1,1} + b'p_{i,1} + c'p_{i+1,1} = d', \quad (3.53)$$

where the coefficients a' , b' , c' and d' have the expressions

$$\begin{aligned} a' &= -\frac{1}{2\Delta\xi}(\xi_x\eta_x + \xi_y\eta_y), \\ b' &= -\frac{3}{2\Delta\eta}(\eta_x^2 + \eta_y^2), \\ c' &= \frac{1}{2\Delta\xi}(\xi_x\eta_x + \xi_y\eta_y), \\ d' &= -\rho u\left(\eta_x\frac{\partial u}{\partial\xi} + \eta_y\frac{\partial v}{\partial\xi}\right) - \frac{1}{2\Delta\eta}(\eta_x^2 + \eta_y^2)(4p_{i,2} - p_{i,3}). \end{aligned} \quad (3.54)$$

The tridiagonal system (3.53) is solved at each iteration step and a value of pressure on the solid boundary, p_b , is then found. Values of the flow variables such as ρ , u , and v , which appear in the equation (3.53), are taken from the previous time step.

3.4.3 Characteristic solid boundary conditions

At the solid boundary, one characteristic does not come from the flow domain, hence one physical boundary condition is needed. This condition is expressed by vanishing normal velocity to the wall (because no mass, or other convective flux, can penetrate the solid body, in which only one eigenvalue is positive). Hence, the condition $\mathbf{V} \cdot \mathbf{i}_n = 0$ is imposed. The pressure on the solid wall is calculated from the equation (3.53), then velocity components and density is determined along the characteristic lines. In Figure 3.1 the characteristic waves at the solid boundary are shown.

An effective way of solid boundary treatment is to use the method of characteristics. Considering equation (2.17), the vector of characteristic variables for 2D flow becomes

$$d\mathbf{Z} = \begin{bmatrix} d\rho - \frac{dp}{a^2} \\ d\mathbf{V} \cdot \mathbf{t} \\ d\mathbf{V} \cdot \mathbf{\bar{n}} + \frac{dp}{\rho a} \\ d\mathbf{V} \cdot \mathbf{\bar{n}} - \frac{dp}{\rho a} \end{bmatrix} = \begin{bmatrix} d\rho - \frac{dp}{a^2} \\ dq_{\parallel} \\ dq_{\perp} + \frac{dp}{\rho a} \\ dq_{\perp} - \frac{dp}{\rho a} \end{bmatrix}, \quad (3.55)$$

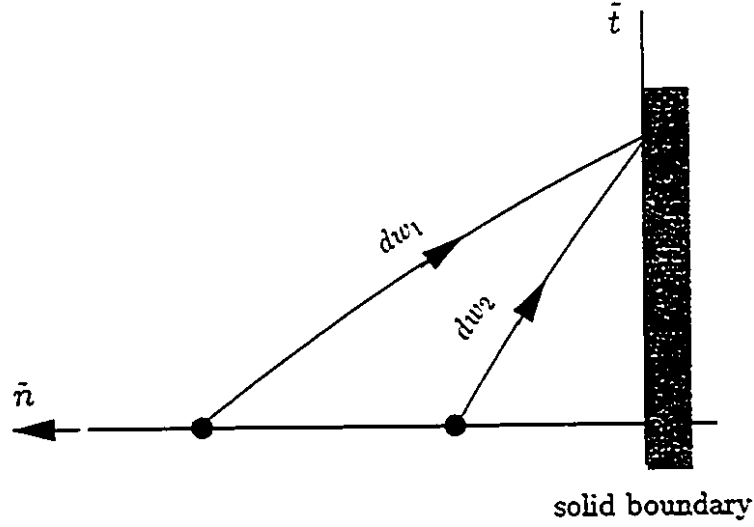


Figure 3.1: Characteristic wave propagations at a solid wall boundary along the normal direction.

where the normal and parallel velocity components to the solid boundary are

$$\begin{aligned} dq_{\perp} &= -du \sin \theta_b + dv \cos \theta_b, \\ dq_{\parallel} &= du \cos \theta_b + dv \sin \theta_b. \end{aligned} \quad (3.56)$$

Similar to equations (2.25), the compatibility relations are modified along the normal to solid boundary. Note that in this case $d\mathbf{V} \cdot \vec{n} = -dq_{\perp}$, regarding the positive normal vector which is directed outward of the solid boundary. Hence,

$$\begin{aligned} dw_{1\perp} &= dp - \rho adq_{\perp} = 0, \\ dw_{2\perp} &= dp - a^2 d\rho = 0, \\ dw_{3\perp} &= dp + \rho adq_{\perp} = 0, \end{aligned} \quad (3.57)$$

At a solid boundary the waves $dw_{1\perp}$ and $dw_{2\perp}$ are propagating towards this boundary (Figure 3.1). Using two of the compatibility relations (3.57) in discrete form at solid boundary and neighboring grid points yields

$$\begin{aligned} p_{i,j} - p_b - \rho_{i,j}^{\vec{n}} a_{i,j}^{\vec{n}} (q_{i,j\perp} - q_{\perp b}) &= 0, \\ p_{i,j} - p_b - (a_{i,j}^{\vec{n}})^2 (\rho_{i,j}^{\vec{n}} - \rho_b) &= 0, \end{aligned} \quad (3.58)$$

where $q_{\perp b} = 0$ on the solid surface. Combining equations (3.58) with each other, the density at the boundary is determined as

$$\rho_b = \rho_{i,2}^* + \frac{q_{i,2}^*}{a_{i,2}^*} \rho_{i,3}^* \quad (3.59)$$

Near the solid boundaries the grid points are clustered, therefore the velocity components on the solid boundary can be approximated using the neighboring points and a weighted extrapolation

$$\begin{aligned} u_b &= (1 + \mu)u_{i,2} - \mu u_{i,3}, \\ v_b &= (1 + \mu)v_{i,2} - \mu v_{i,3}, \end{aligned} \quad (3.60)$$

where

$$\mu = \frac{y_{i,2} - y_{i,1}}{y_{i,3} - y_{i,2}} \quad (3.61)$$

Some authors use $\mu = 0.5$ for computations [83, 85, 101, 144]. The lower order extrapolation increases the amount of dissipation near the solid boundaries. Finally the energy at the solid boundary is calculated as

$$E_b = \frac{1}{\gamma - 1} \frac{p_b}{\rho_b} + \frac{1}{2}(u_b^2 + v_b^2). \quad (3.62)$$

3.4.4 Effect of solid boundary treatment on the numerical solution

During the convergence process, disturbances originate near the solid boundary and propagate into the computational domain. Numerical experiments show that solid boundary is more reflective at the first convergence steps, depending on the type of solid boundary treatment. Disturbance reflection at the solid and far-field boundaries delays the convergence. Using characteristic compatibility relations in the numerical solid boundary treatment prevents inaccuracies and instabilities.

Effect of solid boundary treatment on the solution accuracy is shown for the channel flow. Figure 3.4 shows the symmetry loss due to using the conventional

method and improved approach. Since, in inviscid flows the pressure solution is important, therefore it necessitates using accurate solid boundary conditions.

Figure 3.5 shows how the solid boundary treatment can improve the convergence towards the steady-state by reducing the reflections. Accurate solid boundary treatment is necessary on the circular-arc-bump and is of less interest on the upper flat wall for the channel problem. For the external flow problem, the same characteristic solid boundary method was used.

3.5 Remarks

Implicit factored scheme was presented in this chapter with a modified solid boundary method and displayed very good computational efficiency and accuracy for all cases tested. The codes namely EU1D and EUTD were developed for the flow field calculations. The schematic grid geometries are shown in Figures 3.2 and 3.3 for quasi-1D and 2D flows. All the computations were performed on a 486/33 PC using a Lahey F77L-EM/32 FORTRAN compiler.

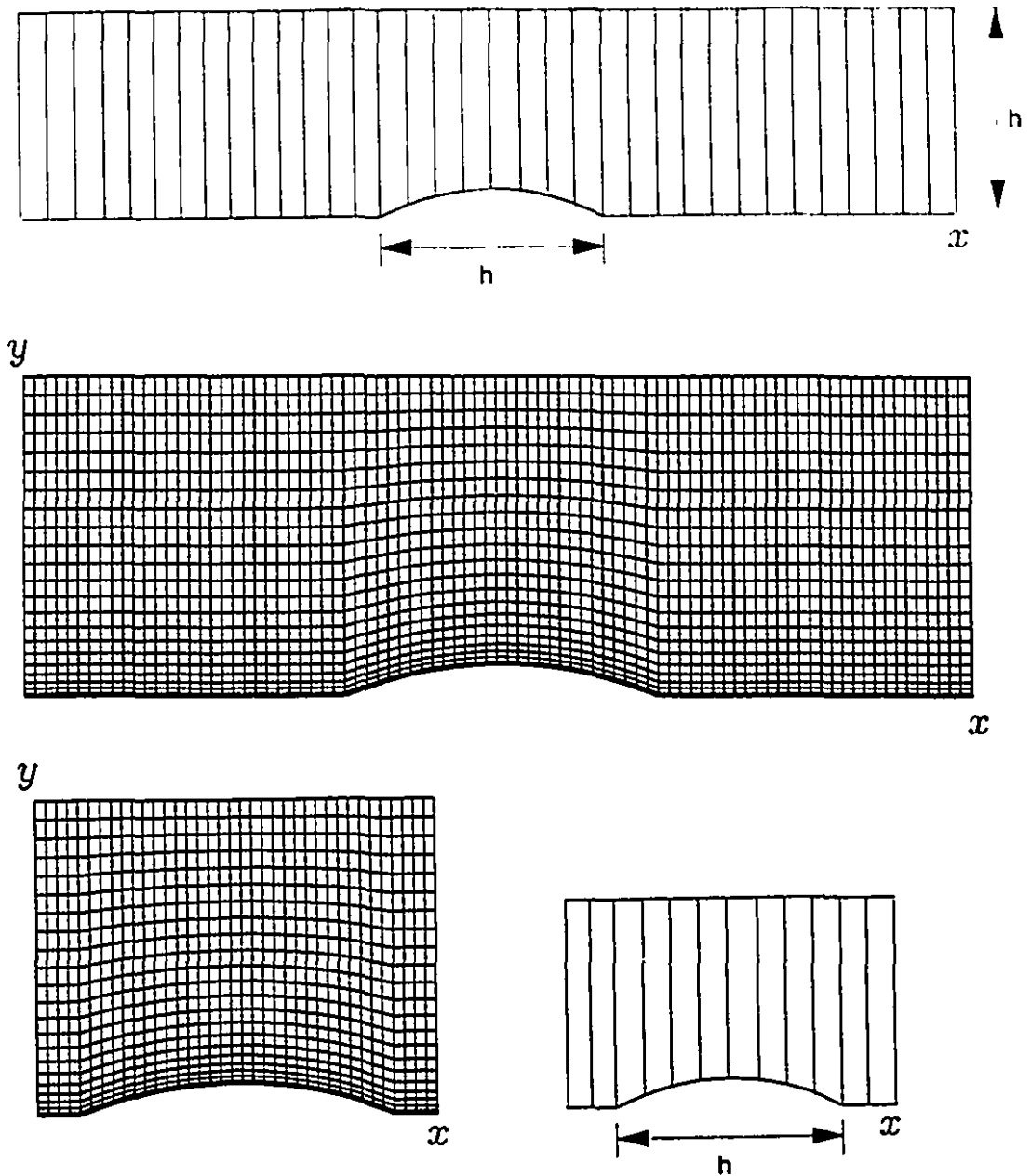


Figure 3.2: Grid configurations for the quasi-one-dimensional and two-dimensional confined (circular arc) flows, extended and reduced domains for each case.

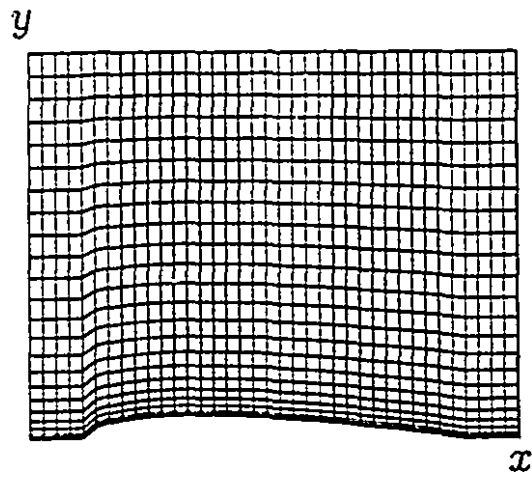
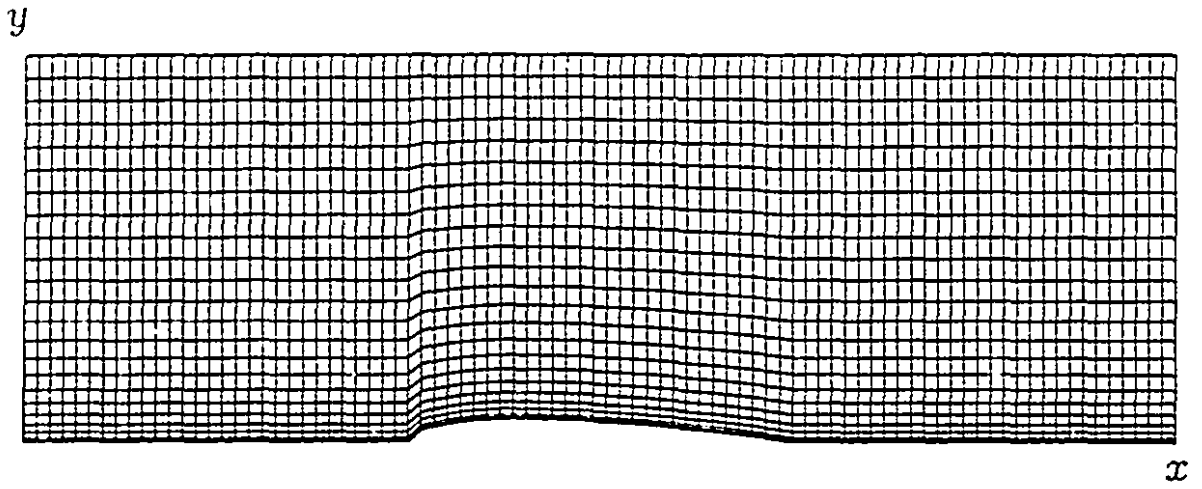


Figure 3.3: Grid configurations for external flow (NACA0012 airfoil), extended and reduced computational domains.

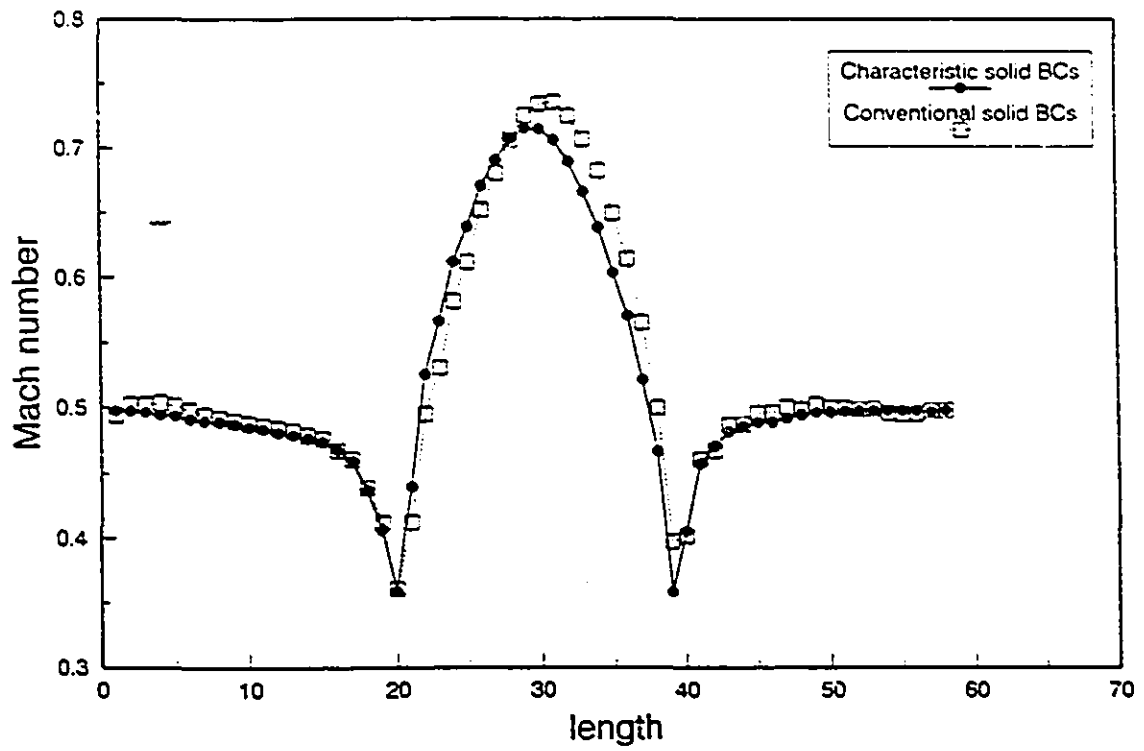


Figure 3.4: Mach number distributions on the lower solid boundary, obtained with characteristic and conventional (extrapolation) solid boundary treatments, channel with circular-arc 10%. $M_\infty = 0.5$, CFL=2.

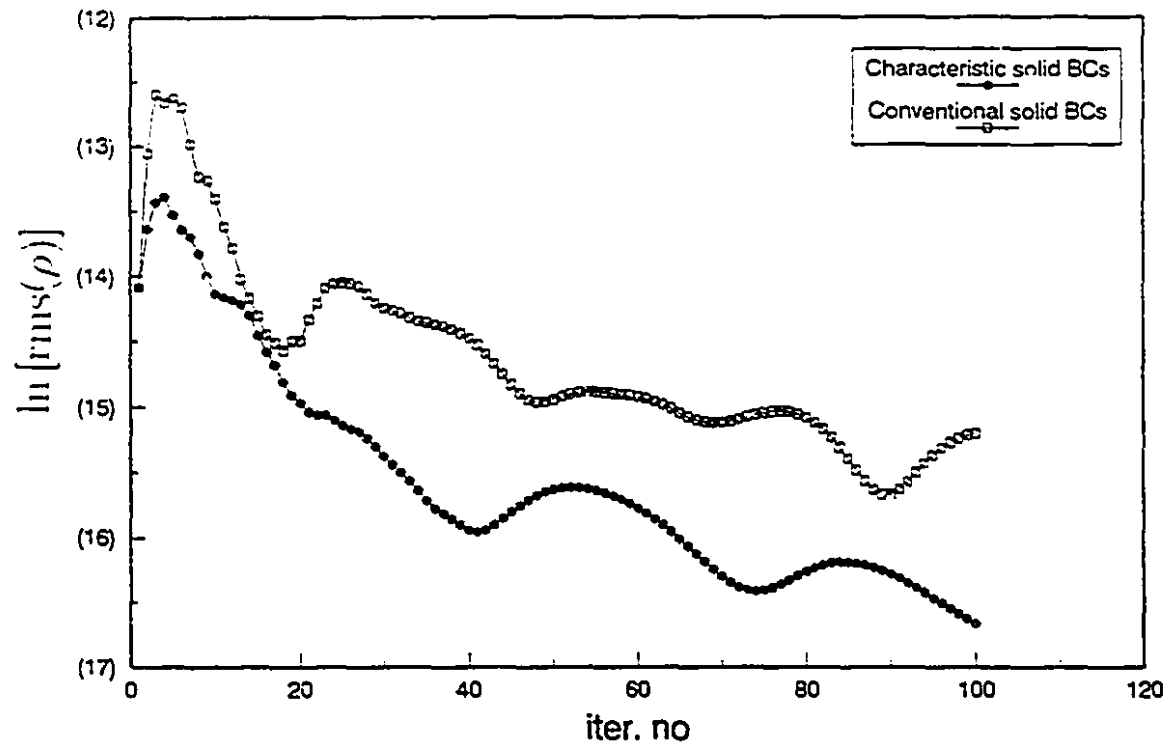


Figure 3.5: Convergence histories obtained by characteristic and algebraic treatments of solid boundary conditions, channel with circular arc 10%. $M_\infty = 0.5$, CFL=2.

Chapter 4

Far Field Boundary Conditions for Quasi-One-Dimensional Flows

4.1 Introduction

Boundary condition modelling in the context of quasi-one-dimensional flows is presented throughout this chapter for isentropic and non-isentropic flows. A model for inflow and outflow boundary conditions was developed. The formulation is based on the Riemann variables expansions simulating the far field solutions and characteristic interpolations along the outgoing simple waves. This FFBC model takes into account the physical and mathematical behavior of the flow at far field regions from information propagation aspect. The FFBC formulation was first developed for the isentropic flows, then modified for non-isentropic flows by considering the effect of entropy generation within the computational domain. The inflow and outflow FFBCs receive information from the far field regions and also from the computational domain. After solving the far field perturbation equations the corresponding Riemann variables are updated and matched with the solution within the computational domain. The FFBC model was validated for different test cases by comparing the numerical and available exact solutions. The results are presented at the end of this chapter.

4.1.1 Linear wave equation

The following first-order linear hyperbolic equation can be used for studying the boundary condition concepts

$$\frac{\partial u}{\partial t} + c \frac{\partial u}{\partial x} = 0, \quad (4.1)$$

with the initial condition

$$u(x, 0) = f(x), \quad (4.2)$$

at an open domain. The boundaries at $x = 0$ and $x = L$ are introduced to delimit the domain. There are many interesting features of the hyperbolic equations that this simple form can represent. If $c > 0$, the solution $u(x, t) = f(x - ct)$ represents a right-moving wave. Hence, the characteristics lines, ($x - ct = \text{const.}$), have positive slopes, and the boundary condition can be imposed at $x = 0$ from the information outside of the domain (Figure 4.1a). The solution at the boundary $x = L$ is obtained by following the characteristics back to the domain, so $u(L, t) = f(L - ct)$; hence, at $x = L$ the boundary condition cannot be obtained from the information outside. If $c = 0$, the equation (4.1) becomes $\frac{\partial u}{\partial t} = 0$ (see Figure 4.1b); the characteristics are vertical lines (see Figure 4.1b). If $c < 0$, the characteristics ($x - ct = \text{const}$) are propagating towards the boundary at $x = 0$. Hence, $u(0, t) = f(-ct)$ in this case, since the boundary conditions cannot be set from the information outside at $x = 0$. Note that $du = 0$ on lines with slope $dx/dt = c$, hence u is constant on these lines. The simple wave is a disturbance propagating on one family of characteristics. In general, for systems of hyperbolic PDEs, these curves are not straight lines, and the solution is not constant along them. For the case of the Euler equations within the subsonic and transonic ranges, both of the above mentioned waves exist, which are used in the FFBC formulation.

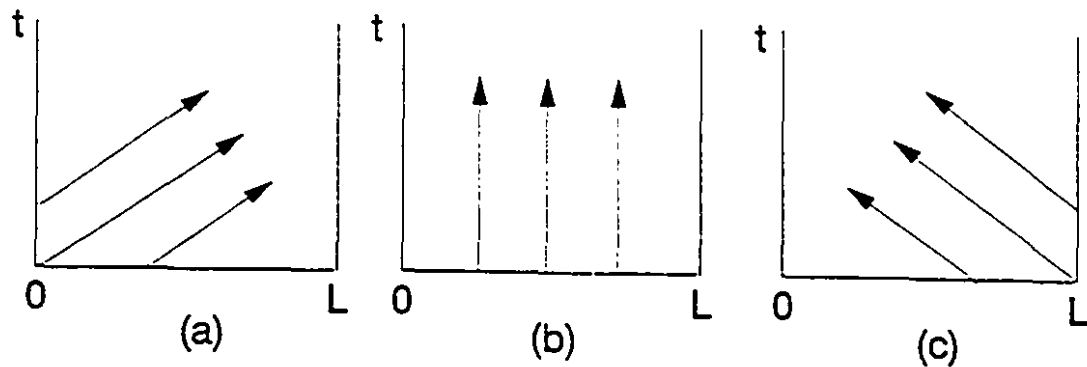


Figure 4.1: Propagation of information for linear wave equation.

4.1.2 First-order hyperbolic systems

Recall the equation (2.23) from Chapter 2

$$\frac{\partial \mathbf{P}}{\partial t} + \Lambda \frac{\partial \mathbf{P}}{\partial x} = 0.$$

Equation (2.23) was decomposed to three characteristic equations (see section 2.2.1). The analogy of linear wave equation can be used. Depending on the flow regime it will produce different propagation patterns shown in Figures 4.2 and 4.3.

Figure 4.2 shows for supersonic flow crossing the inflow boundary all the information propagates from outside to the computational domain, while at supersonic outflow boundary all the information propagates from computational domain to the outside. For subsonic flow crossing the inflow boundary one of the eigenvalues is negative, so one information propagates from the computational domain towards this boundary (Figure 4.3). Outflow boundary is being crossed by the subsonic flow thereby two information propagate from the computational domain and one comes out of it. This is equivalent with imposing one flow variable, such as the static pressure, at the subsonic outflow boundary. For achieving a unique solution, boundary conditions should properly close the hyperbolic system.

In the computational FFBC treatment two kinds of information should be taken into account: one is propagating from far field region outside of the computational

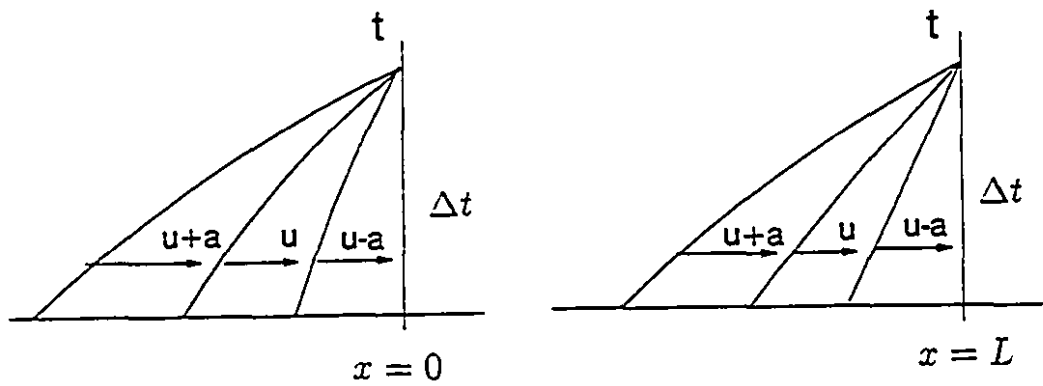


Figure 4.2: Characteristic lines for supersonic flow at inflow and outflow boundaries.

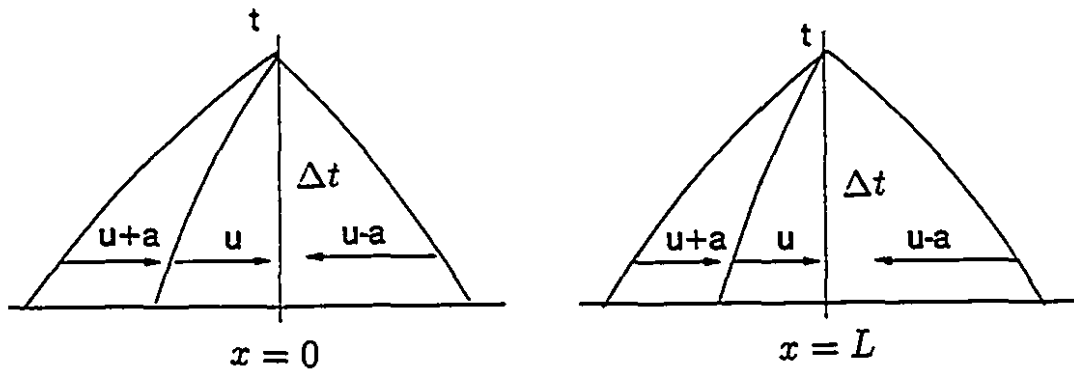


Figure 4.3: Characteristic lines for subsonic flow at inflow and outflow boundaries.

domain, and another is coming from the computational domain itself. Now, at the FFB these two types of information should be matched for calculating the flow variables. The subsonic and transonic regimes are of major importance because of the different directions of propagation occurring in the flow field. The characteristic paths in the flow field should be used to figure out the number of incoming and outgoing disturbances.

4.2 Conventional boundary condition methods

The previous works in this field can be grouped into mathematical aspects of the boundary conditions on the stability and wellposedness [78, 162, 163] and practical aspects [19, 43, 160, 163]. (**Definition:** An initial boundary value problem is *well-posed* if it possesses a unique solution, continuously dependent on the initial and boundary conditions.)

Various boundary condition treatments are available for the quasi-one-dimensional flows as was referred in Chapter 1; in this regard see also [12, 92, 160, 162, 163]. The classical boundary treatments mainly include the algebraic extrapolation and discrete form of the characteristic compatibility relations. The important point in all kinds of boundary treatments is that the directions of propagations should be taken into account. For example at a subsonic inflow the compatibility equations (2.25) along the characteristic lines are discretized between the free-stream and a boundary grid point

$$\begin{aligned}p_b - p_\infty + \rho a(u_b - u_\infty) &= 0, \\p_b - p_\infty - a^2(\rho_b - \rho_\infty) &= 0, \\p_b - p_{comp} - \rho a(u_b - u_{comp}) &= 0,\end{aligned}\tag{4.3}$$

where ρ_b, u_b, p_b are the boundary values, while u_{comp}, p_{comp} are calculated from the computational domain. The values ρ and a are locally linearized and determined by lagging procedure.

For linear equations, the BCs can be one order lower than the interior scheme without reducing the global order of accuracy of the complete scheme [49]. Hence, the zero-order space-accurate BCs will reduce the overall accuracy of second-order schemes, while this will not be the case for the first-order ones. During numerical experiments, the second-order extrapolation did not demonstrate extra advantage than the first-order ones. The extrapolation techniques are discussed in [42, 43], for applications to the MacCormack and two-step Lax-Wendroff type schemes see [85, 162, 163].

A type of inflow BC [29, 107] is chosen to be analysed in the following. At a subsonic inflow boundary the total enthalpy and entropy are specified, in which

$$\frac{\gamma}{\gamma - 1} \frac{p}{\rho} + \frac{1}{2} u^2 = h_0. \quad (4.4)$$

$$S \propto \frac{p}{\rho^\gamma} = \frac{p_\infty}{\rho_\infty^\gamma}. \quad (4.5)$$

The density ρ is calculated from equation (4.5) and introduced into the equation (4.4), which provides

$$\frac{\gamma}{\gamma - 1} \frac{p_\infty^{\frac{\gamma}{\gamma-1}}}{\rho_\infty^{\frac{\gamma}{\gamma-1}}} p^{\frac{\gamma-1}{\gamma}} + \frac{1}{2} u^2 = h_0. \quad (4.6)$$

Differentiating the equation (4.6) and simplifying leads to the following momentum equation

$$dp + \rho u du = 0. \quad (4.7)$$

In fact equation (4.7) is equivalent to the conditions (4.4) and (4.5). Note that equation (4.7) is not equivalent to the right-propagating characteristic equation $dp + \rho u du = 0$, which should be used at an inflow boundary.

As another test case the outflow BC developed by Rudy and Strikwerda [126, 127] is analyzed. They modified the following left-propagating characteristic relation

$$\frac{\partial p}{\partial t} - \rho a \frac{\partial u}{\partial t} = 0, \quad (4.8)$$

into

$$\frac{\partial p}{\partial t} - \rho a \frac{\partial u}{\partial t} + \alpha_p (p - p_\infty) = 0. \quad (4.9)$$

The parameter α_p is an empirical coefficient and is adjusted in order to yield rapid decay of transient disturbances. It needs adjustment in 2D setup. A drawback to equation (4.9) is that at the steady-state, one has the boundary condition $p = p_\infty$, which is reflective according to the discrete characteristic waves. Figures 4.15 and 4.16 illustrate the solutions obtained by using this method. Note the effect of outflow BC on the shock position.

4.3 Proposed FFBC formulation

4.3.1 Equations used for isentropic flows

For modelling the inflow and outflow FFBCs, the Euler equations in primitive variable form are used. This is because the primitive variables can be related to the characteristic compatibility relations in a straightforward manner. The Euler equations for isentropic quasi-one-dimensional flows can be expressed as

$$\begin{aligned}\frac{\partial \rho}{\partial t} + \frac{1}{H} \frac{\partial(\rho u H)}{\partial x} &= 0, \\ \frac{\partial u}{\partial t} + u \frac{\partial u}{\partial x} + \frac{1}{\rho} \frac{\partial p}{\partial x} &= 0,\end{aligned}\quad (4.10)$$

where $H = H(x)$ is the cross-sectional area. It is noted that for FFBC modelling of isentropic flows, the energy equation is excluded, and the isentropic relation, $\frac{p}{\rho^\gamma} = \text{const.}$ is used instead. Converting the equations (4.10) in terms of the sound speed is an effective way in the boundary condition approach in terms of wave propagation. For this purpose the continuity and momentum equations in (4.10) are reformulated based on the velocity and speed of sound, in the form

$$\begin{aligned}\frac{\partial a}{\partial t} + u \frac{\partial a}{\partial x} + \frac{\gamma-1}{2} a \frac{\partial u}{\partial x} &= -\frac{\gamma-1}{2} a u \frac{1}{H} \frac{dH}{dx}, \\ \frac{\partial u}{\partial t} + u \frac{\partial u}{\partial x} + \frac{2}{\gamma-1} a \frac{\partial a}{\partial x} &= 0.\end{aligned}\quad (4.11)$$

Replacing the dependent variables with Riemann variables results in

$$\begin{aligned}\frac{\partial R}{\partial t} + (\alpha R + \beta Q) \frac{\partial R}{\partial x} &= -\frac{\gamma-1}{S} (R^2 - Q^2) \frac{1}{H} \frac{dH}{dx}, \\ \frac{\partial Q}{\partial t} + (\beta R + \alpha Q) \frac{\partial Q}{\partial x} &= +\frac{\gamma-1}{S} (R^2 - Q^2) \frac{1}{H} \frac{dH}{dx},\end{aligned}\quad (4.12)$$

$$\frac{\partial S}{\partial t} + \frac{R+Q}{2} \frac{\partial S}{\partial x} = 0, \quad (4.13)$$

where R and Q are the right- and left-propagating Riemann variables, S represents the entropy, and a the speed of sound,

$$R = u + \frac{2}{\gamma-1} a, \quad Q = u - \frac{2}{\gamma-1} a, \quad a = \sqrt{\gamma \frac{p}{\rho}}, \quad (4.14)$$

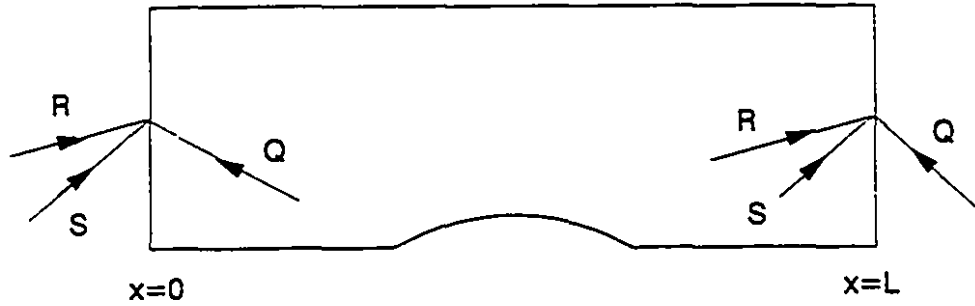


Figure 4.4: Propagation of Riemann variables at inflow and outflow boundaries.

and where $\alpha = (1 + \gamma)/4$ and $\beta = (3 - \gamma)/4$ are constant values, and $\gamma = 1.4$ for air. Equations (4.12) and (4.13) express the propagation of pressure and velocity waves by Riemann variables and propagation of entropy along the streamlines. For isentropic flow with $H = \text{const}$ at the upstream and downstream far field regions, the system of equations (4.12) would be simplified. This yields the following nonlinear sets of equations expressed in terms of the Riemann variables

$$\begin{aligned} \frac{\partial R}{\partial t} + (\alpha R + \beta Q) \frac{\partial R}{\partial x} &= 0, \\ \frac{\partial Q}{\partial t} + (\beta R + \alpha Q) \frac{\partial Q}{\partial x} &= 0. \end{aligned} \quad (4.15)$$

Equations (4.15) state the variations of the Riemann variables as functions of time and space: it is noted that for isentropic flows the equation (4.13) is not used. In Figure 4.4 the Riemann variables are shown when propagating through the domain boundaries. The propagations of Riemann variables are shown in Figure 4.5 for a grid point located on the boundary. In this case the disturbances can only travel along or opposite to the flow direction.

4.3.2 Expanded Riemann variables approach

In the far field regions, the physical and numerical perturbations generated within the computational domain will decay [7, 57, 92, 101, 145]. In regions of the flow field where nonlinear effects are weak, the flow can be treated as a perturbation to a

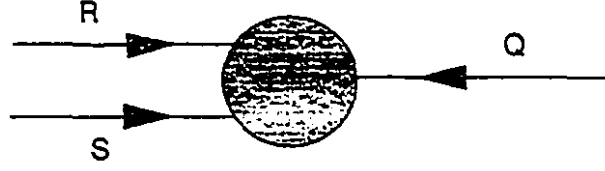


Figure 4.5: Riemann variable propagations for one-dimensional flow at a boundary node.

constant free-stream, rectilinear flow. Such regions occur near and beyond the FFBs.

Numerical experiments also confirm the validity of the behavior that as one gets far from the highly non-linear region, the Riemann variables tend to their free stream values. Therefore, the intensity of the perturbations are in inverse relation with the distance to far field. Both the right- and left-propagating Riemann variables are expanded into series as

$$\begin{aligned} R &= R_\infty + \sum_{k=1}^m R_k(t)\epsilon_k(x), \\ Q &= Q_\infty + \sum_{k=1}^m Q_k(t)\epsilon_k(x), \end{aligned} \quad (4.16)$$

where R_∞ and Q_∞ refer to the free-stream Riemann variables defined as

$$R_\infty = u_\infty + \frac{2}{\gamma - 1}a_\infty, \quad Q_\infty = u_\infty - \frac{2}{\gamma - 1}a_\infty, \quad (4.17)$$

and where the perturbation functions are $\epsilon_k(x) = e^{k\omega x}$, where ω is a tunable factor and can be estimated, by taking a lead from the work of Verhoff *et al* [148], as

$$\omega = \frac{\pi s_c}{\sqrt{1 - M_\infty^2}}, \quad (4.18)$$

where s_c is a safety factor less than one, which can be calibrated by numerical tests. This factor can be optimized thereby leading to fast convergence. The Riemann variables are expanded up to the desired degree of accuracy

$$\begin{aligned} R &= R_\infty + \epsilon R_1 + \epsilon^2 R_2 + \dots, \\ Q &= Q_\infty + \epsilon Q_1 + \epsilon^2 Q_2 + \dots, \end{aligned} \quad (4.19)$$

where the notation $\epsilon = e^{-x}$ has been introduced. These expansions reflect the far field behavior of the inviscid compressible and viscous compressible flows. Introducing the expansions (4.19) into the equations (4.15) and doing some algebraic manipulation results in the linearized equations in terms of the first- and second-order perturbation equations. These equations are uncoupled. First order perturbation equations are

$$\frac{\partial R_1}{\partial t} + \omega(\alpha R_\infty + \beta Q_\infty)R_1 = 0. \quad (4.20)$$

$$\frac{\partial Q_1}{\partial t} + \omega(\beta R_\infty + \alpha Q_\infty)Q_1 = 0. \quad (4.21)$$

and second order perturbation equations take the form

$$\begin{aligned} \frac{\partial R_2}{\partial t} + 2\omega(\alpha R_\infty + \beta Q_\infty)R_2 + \omega(\alpha R_1 + \beta Q_1)R_1 &= 0, \\ \frac{\partial Q_2}{\partial t} + 2\omega(\beta R_\infty + \alpha Q_\infty)Q_2 + \omega(\beta R_1 + \alpha Q_1)Q_1 &= 0. \end{aligned} \quad (4.22)$$

In the far field regions downstream of the computational domain, the solutions cannot accept exponentially growing terms. Therefore, the functions $\epsilon_k(-x)$ should be used in the expansions (4.19). This is equivalent to a sign change for ω in the equations (4.20)-(4.22). Considering the second-order equations (4.22) in addition to the first-order ones may lead to more accurate results, however, they demand more computational effort than the first-order equations. Figure 4.6 shows the propagations of the Riemann variables and entropy waves at two consecutive time steps. The slopes of the characteristic lines will be varying during the time-integration process.

4.4 Boundary condition development (isentropic flow)

The FFBCs are formulated in the next sections based on the assumptions made for the flow behavior at the far field regions. Linear characteristic theory determines the directions of wave motion in and out of the computational domain. For FFBC development it was assumed that:

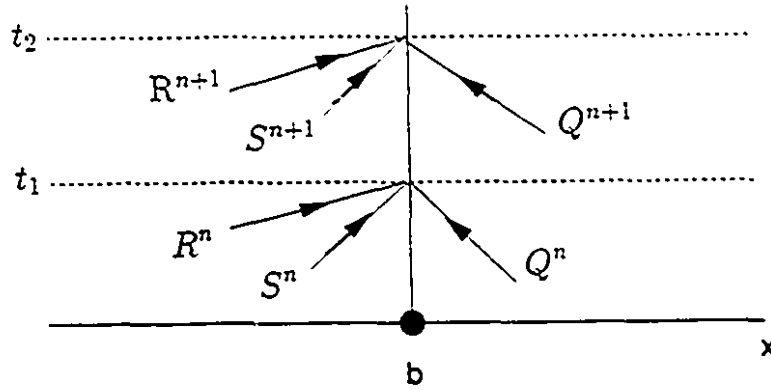


Figure 4.6: Time evolution of the characteristic waves (Riemann variables) at a boundary point for two consecutive time levels.

1. Disturbances decay as they approach to the undisturbed free-stream.
2. The free-stream region flow variables do not vary with time.
3. Disturbances consist of residual, acoustic and entropy waves.

4.4.1 Upstream far-field region

For the region upstream of the computational FFB (i.e. $x \leq 0$) the exponential terms in expansions (4.19) will be suppressed, then R and Q would tend to far field free-stream values. If the origin is located at the inflow boundary ($x = 0$) the spatial functions $\epsilon_k(x)$ would become unity, hence

$$\begin{aligned}
 R &= R_\infty + R_1 + R_2 + \dots, \\
 Q &= Q_\infty + Q_1 + Q_2 + \dots
 \end{aligned}
 \tag{4.23}$$

For locally-subsonic flows, there are two downstream-propagating waves carrying information from outside of the computational domain to the inflow boundary and one upstream-propagating wave carrying information from the computational domain (numerical solution) along the characteristic lines. For updating the far field solution at

the inflow boundary one has to solve the first-order perturbation equation

$$\frac{\partial R_1}{\partial t} + \omega(aR_x - \beta Q_x)R_1^* = 0. \quad (4.24)$$

It can be integrated in time either by an explicit or implicit method; the explicit approach is chosen here.

$$\frac{R_1^{n+1} - R_1^n}{\Delta t} + \omega(aR_x + \beta Q_x)R_1^n = 0. \quad (4.25)$$

The time step for integrating the perturbation equation (4.24) is taken smaller than the time step used for solving the flow field. This smaller time-step delays the perturbation waves in reaching the FFBs of the computational domain [73, 92]. Then the quantity R is updated from the expansion (4.23) up to the first order degree at each time-step

$$R^{n+1}(i) = R_\infty + R_1^{n+1}(i). \quad (4.26)$$

The information which is carried out by the left-propagating Riemann variable Q , is obtained from the computational domain following the corresponding characteristic line. This kind of interpolation is more stable than extrapolation methods and is consistent with the direction of outgoing wave from the computational domain in which the relations $u_M = f_1(u_i, u_{i+1})$ and $a_M = f_2(u_i, u_{i+1})$ hold. This interpolation is expressed as

$$Q_{comp}^{n+1} = Q_{M_i} = Q_M = (1 - \frac{\delta}{\Delta x})Q_i^n + \frac{\delta}{\Delta x}Q_{i+1}^n, \quad (4.27)$$

where δ is calculated from Appendix G. Once the value of $Q_{comp}^{n+1}(i)$ is known, the perturbation function Q_1^{n+1} is computed from the equation (4.23) as

$$Q_1^{n+1}(i) = Q_{comp}^{n+1}(i) - Q_\infty, \quad (4.28)$$

which is needed for the second-order formulation of the boundary conditions. Then, the values of the left- and right-propagating Riemann variables are known, therefore the far field and inner domain solutions are matched to determine the flow variables

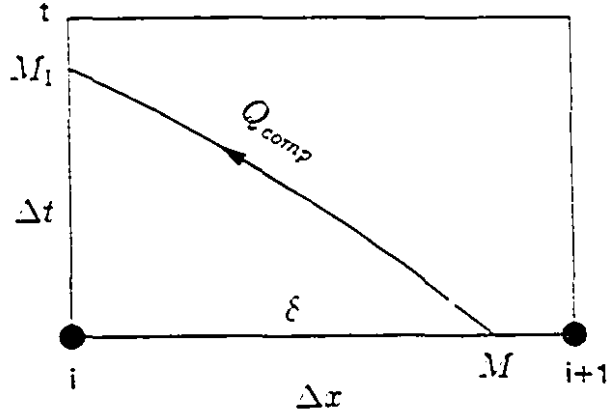


Figure 4.7: Interpolation along left-propagating characteristic line at the inflow boundary.

at the boundary. For inflow boundary the following relations are used to calculate the boundary values at each time step

$$\begin{aligned}
 u_{in}^{n+1} &= \frac{1}{2}(R^{n+1} + Q_{comp}^{n+1}), & a_{in}^{n+1} &= \frac{\gamma-1}{4}(R^{n+1} - Q_{comp}^{n+1}), \\
 \rho_{in}^{n+1} &= \left[\frac{\rho_{\infty}}{\gamma p_{\infty}} (a_{in}^{n+1})^2 \right]^{\frac{1}{\gamma-1}}, & p_{in}^{n+1} &= \frac{1}{\gamma} \rho_{in}^{n+1} (a_{in}^{n+1})^2, \\
 E_{in}^{n+1} &= \frac{1}{\gamma-1} \frac{p_{in}^{n+1}}{\rho_{in}^{n+1}} + \frac{1}{2} (u_{in}^{n+1})^2. & & (4.29)
 \end{aligned}$$

The flow crossing the inflow boundary is assumed to be isentropic (this is the case for most of the applications), therefore isentropic relation holds between the far field region and the inflow boundary. The conservative flow vector $[\rho_{in}^{n+1}, (\rho u)_{in}^{n+1}, (\rho E)_{in}^{n+1}]^T$ is then calculated and coupled to the numerical scheme in order to close the system of hyperbolic equations.

The second-order perturbation equation could be used for inflow boundary if one solves the following equation

$$\frac{\partial R_2}{\partial t} + 2\omega(\alpha R_{\infty} + \beta Q_{\infty})R_2 + \omega(\alpha R_1^{n+1} + \beta Q_1^{n+1})R_1^{n+1} = 0, \quad (4.30)$$

where the values of R_1 and Q_1 have already been calculated by solving the first-order perturbation equation (4.24). Then R is updated using three terms taken from the expansions (4.19). The time-step which was used for solving the far field perturbation

equations was less than the global time-step for the computational domain. This delays the disturbances in reaching the boundaries [73, 74, 92].

4.4.2 Downstream far-field region

In order to suppress the growing modes at the downstream region of the computational boundary (i.e. $x \geq L$), the functions $\epsilon_k(-x)$ have to be used in the expansions (4.16), e.g.

$$\begin{aligned} R &= R_\infty + \epsilon R_1 + \epsilon^2 R_2 + \dots, \\ Q &= Q_\infty + \epsilon Q_1 + \epsilon^2 Q_2 + \dots, \end{aligned} \quad (4.31)$$

where in this case $\epsilon = e^{-\omega x}$. For locally-subsonic isentropic flows, there are two downstream-running waves carrying information to the downstream boundary from the numerical solution and one upstream-running wave carrying information from outside of the computational domain. The updating process for the outflow FFB is done by solving the following first-order perturbation equation

$$\frac{\partial Q_1}{\partial t} - \omega(\beta R_\infty + \alpha Q_\infty)Q_1 = 0. \quad (4.32)$$

With an explicit time-integration scheme, it becomes

$$\frac{Q_1^{n+1} - Q_1^n}{\Delta t} - \omega(\beta R_\infty + \alpha Q_\infty)Q_1^n = 0. \quad (4.33)$$

Similar to the upstream boundary case, the quantity Q is updated from the expansion relation (4.31) at each time step

$$Q^{n+1} = Q_\infty + \epsilon Q_1^{n+1}. \quad (4.34)$$

The right-propagating Riemann variable R is computed from the computational domain along the corresponding characteristic line

$$R_{comp}^{n+1} = R_N = R_N = \left(1 - \frac{\delta}{\Delta x}\right)R_{i-1}^n + \frac{\delta}{\Delta x}R_i^n, \quad (4.35)$$

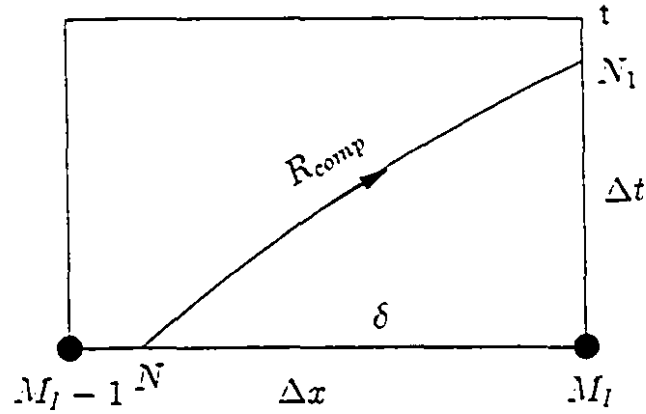


Figure 4.8: Interpolation along characteristic line at the outflow boundary.

where $u_N = g_1(u_{i-1}, u_i)$ and $a_N = g_2(a_{i-1}, a_i)$. In the interpolation relation (4.35), the direction of outgoing wave has been taken into account. Upon computation of R_{comp}^{n+1} , the R_1^{n+1} is determined from the following relation

$$R_1^{n+1}(i) = \epsilon^{-1}(R_{comp}^{n+1} - R_\infty), \quad (4.36)$$

which is needed for the second-order formulation of the boundary condition. Then the velocity and speed of sound at the outflow boundary are determined by matching the far field and near field solutions at each time step, as

$$u_{out}^{n+1} = \frac{1}{2}(R_{comp}^{n+1} + Q^{n+1}), \quad a_{out}^{n+1} = \frac{\gamma - 1}{4}(R_{comp}^{n+1} - Q^{n+1}). \quad (4.37)$$

Then, the rest of flow parameters are calculated as

$$\rho_{out}^{n+1} = \left[\frac{\rho_\infty^\gamma (a_{out}^{n+1})^2}{\gamma p_\infty} \right]^{\frac{1}{\gamma-1}}, \quad p_{out}^{n+1} = \frac{1}{\gamma} \rho_{out}^{n+1} (a_{out}^{n+1})^2, \\ E_{out}^{n+1} = \frac{1}{\gamma - 1} \frac{p_{out}^{n+1}}{\rho_{out}^{n+1}} + \frac{1}{2} (u_{out}^{n+1})^2. \quad (4.38)$$

The conservative flow vector $[\rho_{out}^{n+1}, (\rho u)_{out}^{n+1}, (\rho E)_{out}^{n+1}]^T$ is then completely calculated. This vector is coupled to the numerical scheme for properly closing the system of hyperbolic equations. For outflow boundary treatment, the outgoing information carried by R is calculated from the computational domain. The second-order perturbation equation for the outflow boundary can also be used for more accuracy in the

form

$$\frac{\partial Q_2}{\partial t} + 2\omega(\beta R_{\infty} + \alpha Q_{\infty})Q_2^2 + \omega(\beta R_1^{\gamma+1} + \alpha Q_1^{\gamma+1})Q_1^{\gamma-1} = 0. \quad (4.39)$$

The value of Q is then updated using three terms from the expansions (4.31).

Many numerical solution algorithms for Euler equations use the FFBCs in which R_{∞} and Q_{∞} are specified at inflow and outflow boundaries respectively; however, this requires an extremely large computational domain, with very negative effects on the computational efficiency. The proposed model allows flexible variations of the Riemann variables during the time-integration process.

Although the entropy should be theoretically constant for the isentropic flows, it can vary due to discretization and boundary treatment errors. To avoid this situation the value of total enthalpy should be checked during the numerical computation.

4.5 Outflow boundary conditions for non-isentropic flows

For quasi-1D flows the non-isentropic conditions occur when entropy is generated within by the formation of a normal shock in the diverging part of the nozzle. Entropy variation after the normal shock is convected to the downstream of the flow within the computational domain. For this case the Riemann variable formulations of Euler equations are modified by considering the entropy change inside the computational domain in the form

$$\frac{\partial R}{\partial t} + (\alpha R + \beta Q) \frac{\partial R}{\partial x} = \mathcal{F}_1(R, Q, S), \quad (4.40)$$

$$\frac{\partial Q}{\partial t} + (\beta R + \alpha Q) \frac{\partial R}{\partial x} = \mathcal{F}_2(R, Q, S), \quad (4.41)$$

$$\frac{\partial S}{\partial t} + \frac{R+Q}{2} \frac{\partial S}{\partial x} = 0, \quad (4.42)$$

where the functions $\mathcal{F}_1(R, Q, S)$ and $\mathcal{F}_2(R, Q, S)$ are

$$\mathcal{F}_1(R, Q, S) = -\frac{\gamma-1}{S} \frac{1}{S} (R-Q) \left(S - \frac{2}{\gamma-1} \right) \left[\frac{\partial(R+Q)}{\partial x} - \frac{2}{\gamma-1} \frac{1}{S} \frac{\partial(R-Q)}{\partial x} \right],$$

$$\mathcal{F}_2(R, Q, S) = \frac{\gamma-1}{S} \frac{1}{S} (R-Q) \left(S - \frac{2}{\gamma-1} \right) \left[\frac{\partial(R+Q)}{\partial x} + \frac{2}{\gamma-1} \frac{1}{S} \frac{\partial(R-Q)}{\partial x} \right], \quad (4.43)$$

and where $\alpha = \frac{\gamma-1}{2S}$, $\beta = \frac{\gamma-1}{2S}$ and the entropy S are not constants as in the isentropic flow case. For details about the equations (4.40) and (4.41) see Appendix D. In these equations, the entropy is connected to the state variables as following [110, 151]

$$S = \frac{2}{\gamma-1} - \frac{1}{\gamma(\gamma-1)} \ln \frac{p}{\rho^\gamma}, \quad (4.44)$$

and the Riemann variables have been modified for the non-isentropic case as [148, 149] (see also Appendix C)

$$R = u + Sa, \quad Q = u - Sa. \quad (4.45)$$

From the relations (4.44) and (4.45), the pressure is related to the Riemann variables and entropy as

$$p = \gamma^{-\frac{\gamma}{\gamma-1}} \left(\frac{R-Q}{2S} \right)^{\frac{\gamma}{\gamma-1}} e^{\gamma(S-\frac{2}{\gamma-1})}. \quad (4.46)$$

The modified equations (4.40) and (4.41) take into account the effect of entropy change across the shock wave. At each time step the entropy S is convected towards the outflow boundary and eventually propagates out of the computational domain by another non-isentropic (mixing) process. The entropy generation downstream in the flow domain does not affect the upstream and isentropic inflow BCs are still valid. Therefore, for non-isentropic flow only the outflow boundary condition is formulated by using the expansions of the Riemann variables and considering the characteristic propagation directions. As in the isentropic case, the modified Riemann variables are expanded into asymptotic series (equation (4.19))

$$R = R_\infty + \epsilon R_1,$$

$$Q = Q_\infty + \epsilon Q_1.$$

Here the first-order outflow boundary condition is developed for the non-isentropic flows. After introducing the above expansions into the equation (4.41) and considering

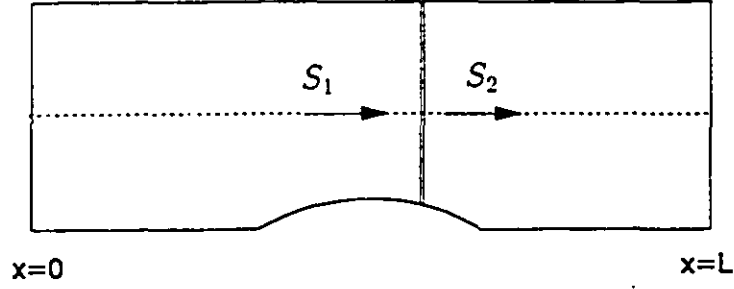


Figure 4.9: Entropy propagation in the steady quasi-one-dimensional flow.

the fact that, the entropy wave is convected towards downstream. One gets for the left-propagating Riemann variable

$$\frac{\partial Q_1}{\partial t} - \omega(\beta R_\infty + \alpha Q_\infty)Q_1 = \mathcal{G}(R_1, Q_1, S), \quad (4.47)$$

where

$$\mathcal{G}(R_1, Q_1, S) = \frac{(\gamma - 1)\omega}{8S} \left(S - \frac{2}{\gamma - 1} \right) (R_\infty - Q_\infty) \left[R_1 + Q_1 + \frac{2(R_1 - Q_1)}{(\gamma - 1)S} \right]. \quad (4.48)$$

In the above equation S is calculated from the computational domain based on the relation (4.44). After solving equation (4.47) as shown in section 4.4.2, the deviation of Q_1^{n+1} from the far field value is also calculated. The R_{comp}^{n+1} is calculated by the interpolation (indicated in section 4.4.2); hence,

$$R_1^{n+1}(i) = \epsilon^{-1}(R_{comp}^{n+1}(i) - R_\infty).$$

Then the velocity and speed of sound are found in the form

$$u_{out}^{n+1} = \frac{1}{2}(R_{comp}^{n+1} + Q^{n+1}), \quad a_{out}^{n+1} = \frac{R_{comp}^{n+1} - Q^{n+1}}{2S_{comp}^{n+1}}. \quad (4.49)$$

Note that $R_b^{n+1} = R_{comp}^{n+1}$ and $S_b^{n+1} = S_{comp}^{n+1}$ (Figure 4.10) are calculated from the numerical solution in the computational domain considering the characteristic directions. At each iteration step the discretized form of the equation (4.47) is solved explicitly for Q^{n+1} and the updated value for Q_1^{n+1} is then determined. Finally, as in the isentropic case, the rest of the flow variables are computed from the values for

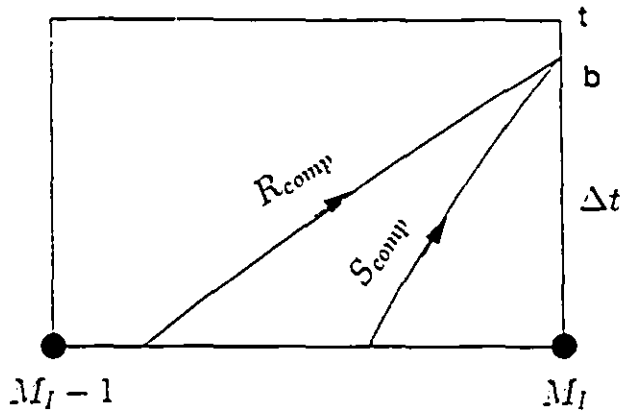


Figure 4.10: Characteristic lines propagation for non-isentropic flow at outflow boundary.

R_{comp}^{n+1} , S_{comp}^{n+1} and Q^{n+1} . The information propagation for the non-isentropic is shown in Figure 4.10 for an outflow boundary.

Remark: The reflection concept applies to physical and numerical phenomena. The nonreflecting boundary conditions were proposed by several authors [30, 37, 53, 74]. Equations (2.25) in discrete form can be written based on their intensities as

$$\begin{aligned}
 \Delta w_1 &= \Delta p + \rho a \Delta u, \\
 \Delta w_2 &= \Delta p - a^2 \Delta \rho, \\
 \Delta w_3 &= \Delta p - \rho a \Delta u.
 \end{aligned} \tag{4.50}$$

In discretized form, the intensities Δw_1 , Δw_2 and Δw_3 are not exactly zero unlike their analytic counterparts. In numerical calculations this causes errors (or disturbances) at the boundaries. Different waves propagate at different velocities. Hence, a time step appropriate for the fastest waves may be inefficient for other waves. In 1D flow, waves travel perpendicularly to the FFBs. For multidimensional flows finding the propagation direction is not so trivial and it can be found approximately [101, 119, 75].

4.6 Model validation and numerical results

Using the proposed FFBC model enabled us to reduce significantly the size of the computational domain and, as a result, also the size of the block tridiagonal matrix to be inverted.

Numerical computations were conducted for two types of computational domains, namely extended and reduced. Basically, the domain consisted of a channel having a circular-arc-bump, which is located at the middle of the lower-wall and the upper-wall is straight. The thickness of the circular-arc was 10% of its chord length. Also the channel height was taken to be equal to the chord length. The extended computational domain has a total length of five chords. It is extended two chords from both upstream and downstream sides with respect to the circular-arc-bump. In this case the computational domain contained 60 equally-spaced grid points.

The reduced computational domain consists of the circular-arc and an extension of just two grid intervals (or $\frac{2}{N}$ of chord length) at both the upstream and downstream, where N is the number of grids along the circular-arc portion. In this case, it contained 24 equally-spaced grid points. In fact, both the extended and reduced computational domains have the same geometry, the only difference is between their lengths and hence the number of grid points.

Two different flow regimes (subsonic and transonic) were calculated by implementing different types of boundary conditions at the inflow and outflow boundaries. The exact solutions (which can be obtained for the quasi-one-dimensional case) were used for comparison purposes.

Table 4.1 shows the results obtained for different longitudinal extensions of the computational domain (first column) with different formulations for the far-field boundary conditions; in this table, the indicated Mach numbers are calculated at the mid-point of the circular-arc-bump (or minimum cross-sectional area) calculated for several cases. By contrast, the solution obtained by using the conventional boundary conditions for a reduced domain shows a deviation of around 5.7% in comparison to

Table 4.1: Comparisons between the reduced and extended computational domains with different types of FFBC treatments. CFL=4.

	Mach number at mid-chord	Grid points	Error%	Iterations
Conventional FFBC treatment, extended domain	0.7110	60	0.140	194
Conventional FFBC treatment, reduced domain	0.6714	24	5.70	176
Present FFBC model, reduced domain	0.7102	24	0.252	141
Exact solution	0.7120	24	0.000	-

the exact solution. It was also found that the present FFBC model on the reduced grid displays a much better computational efficiency, requiring about 2.5 times less computing time than the conventional FFBC treatment for the same geometry in an extended domain.

It was found that the solution obtained with the proposed FFBC model is in very good agreement with the exact solution. Memory requirements are substantially reduced with decreasing the number of grid points by applying the proposed FFBC model.

The subsonic flow solutions, obtained with isentropic FFBCs, are shown in Figures 4.11- 4.14, and the transonic flow solutions, obtained using a non-isentropic outflow boundary condition, are illustrated in Figures 4.15-4.20.

Figure 4.12 compares the solutions for the extended and reduced computational domains with the conventional and proposed FFBC methods, respectively. Good agreement was found between the solutions obtained with the proposed FFBC model for the reduced domain and the conventional FFBC treatment for the extended domain. The extended computational domain can be used as a criterion for comparison purposes, as it can be seen from the comparison with the exact solution in Figure 4.13 (enlarged view).

In Figure 4.14 the effect of the first- and second-order perturbation equations is

examined and compared versus exact solution. Applying the second-order equation improves only slightly the accuracy, whilst it increases substantially the amount of calculations required.

For the non-isentropic flow, the numerical experiments were conducted for transonic flows in the same circular-arc (10%) channel and the results are shown at the end of this Chapter. A small amount of over- and undershooting takes place through the shock in the case of transonic flow by using the proposed FFBC model. Memory requirement is reduced with decreasing the number of grid points by applying the proposed FFBC model.

Figures 4.15 and 4.16 show how much the solutions can be affected by implementing the different outflow boundary conditions for a transonic flow, while keeping the conventional inflow boundary condition the same.

Figure 4.17 illustrates the effect of the conventional FFBC treatments for the transonic flow case. The shock position is dependent on the type of outflow FFBC method that used. Pressure distributions for the same case are shown in Figure 4.18.

Figures 4.19 and 4.20 illustrate the Mach number and pressure distributions obtained with the proposed FFBC model compared with exact solutions for the quasi-one-dimensional flow. A good agreement was found between these solutions.

The convergence histories are plotted for both subsonic and transonic flows in Figures 4.21 and 4.22. Using the proposed FFBC model led to reduced iteration steps in subsonic case, however no considerable difference is observed in transonic case. It could be because of the strong reflections from the domain boundaries, when a shock is present inside the domain. As it is shown in Figures 4.15 and 4.16, the outflow BC has the dominant effect on the numerical solutions.

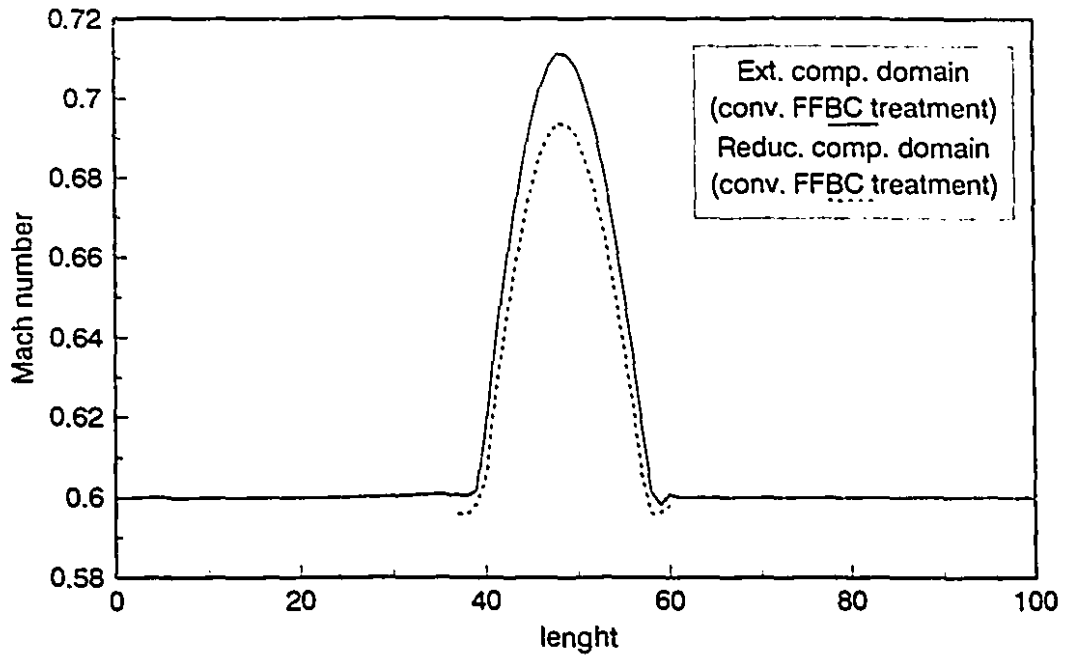


Figure 4.11: Subsonic flow: Mach number distributions for extended computational domain (conventional FFBC treatment) and reduced computational domain (conventional FFBC treatment). $M_\infty = 0.6$, CFL=1.8, circular arc 10%.

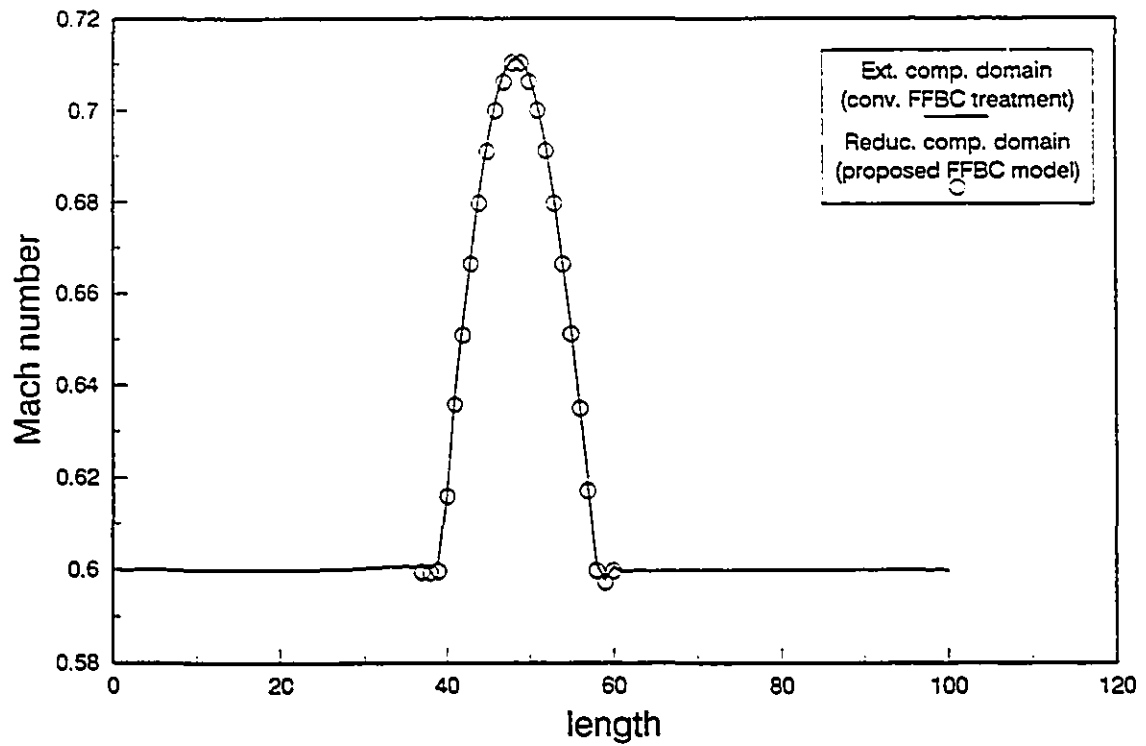


Figure 4.12: Subsonic flow: Mach number distributions for extended computational domain (conventional FFBC treatment) and reduced computational domain (proposed FFBC model). $M_\infty = 0.6$, CFL=1.8, circular arc 10%.

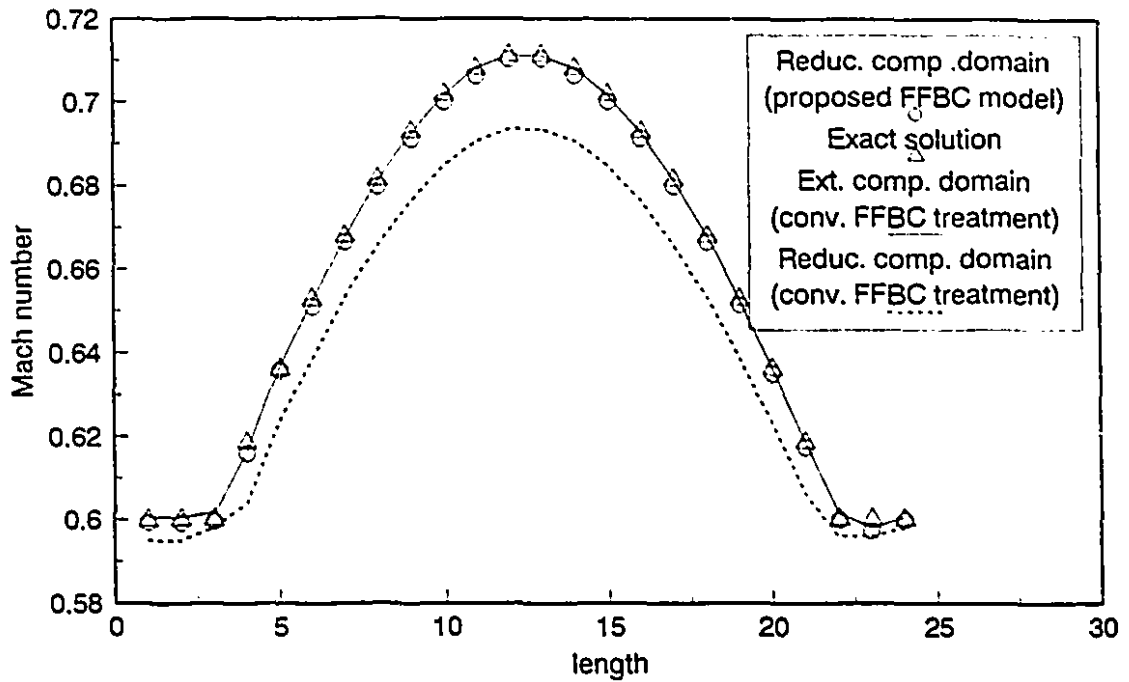


Figure 4.13: A comparison of Mach number distributions in four cases: (enlarged view) *a*) Reduced computational domain (proposed FFBC model), *b*) Exact solution, *c*) Extended computational domain (conventional FFBC treatment), *d*) Reduced computational domain (conventional FFBC treatment). $M_\infty = 0.6$, CFL=1.8, circular arc 10%.

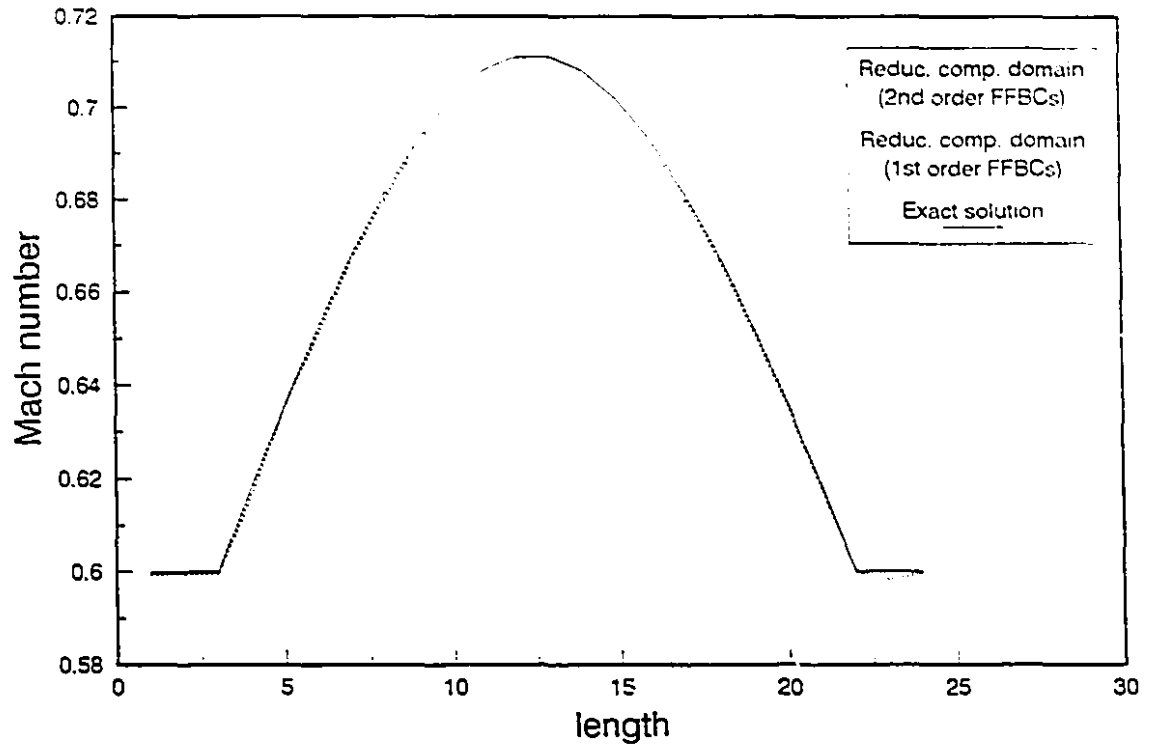


Figure 4.14: Subsonic flow: Mach number distributions within a reduced computational domain, resulted by applying the first- and second-order FFBCs in comparison with the exact solution. $M_\infty = 0.6$, CFL=1.8.

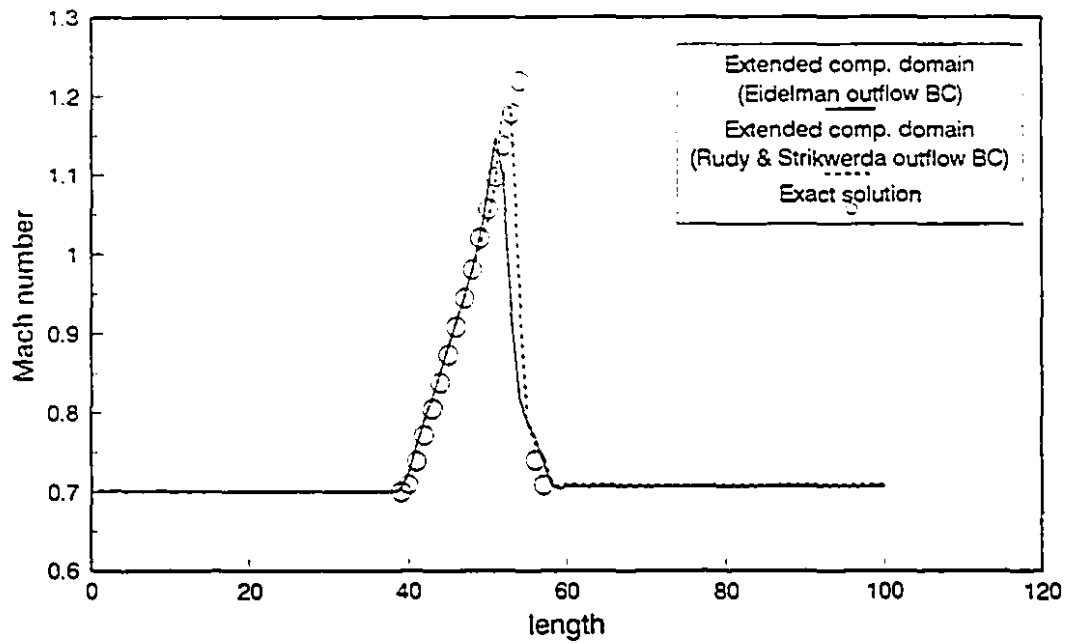


Figure 4.15: Transonic flow: Effect of the conventional outflow boundary conditions on Mach number distributions obtained by a fixed inflow condition and outflow methods of Eidelman [29], Rudy and Strikwerda [126]. $M_\infty = 0.71, p_b = p_\infty, CFL=1.2$, compared with exact solution.

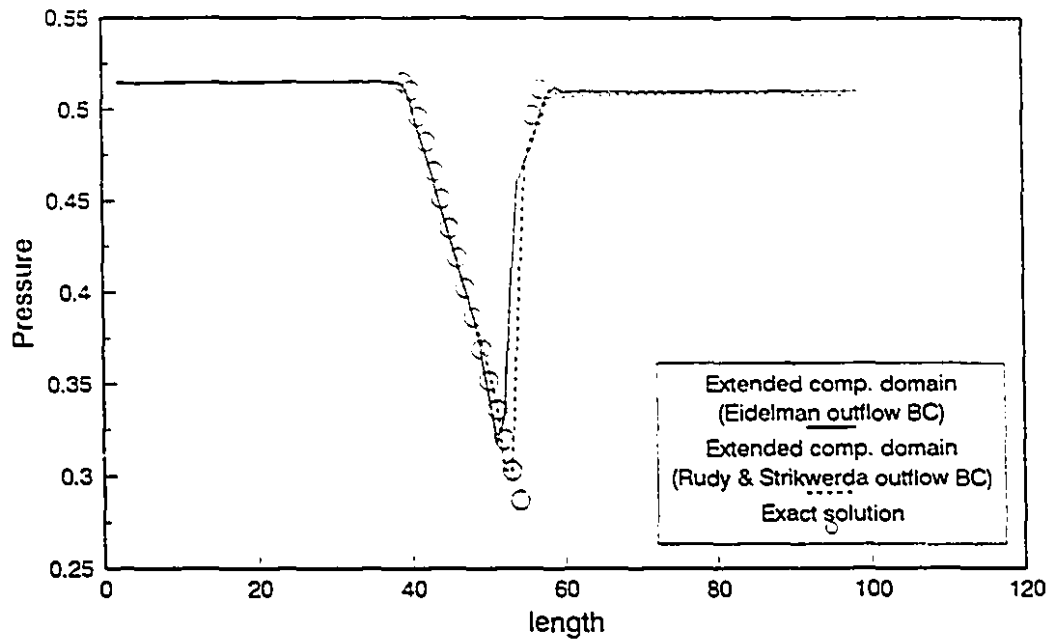


Figure 4.16: Transonic flow: Effect of the conventional outflow boundary conditions on pressure distributions obtained by a fixed inflow condition and outflow methods of Eidelman [29], Rudy and Strikwerda [126]. $M_\infty = 0.71$, $p_b = p_\infty$, CFL=1.2, compared with exact solution.

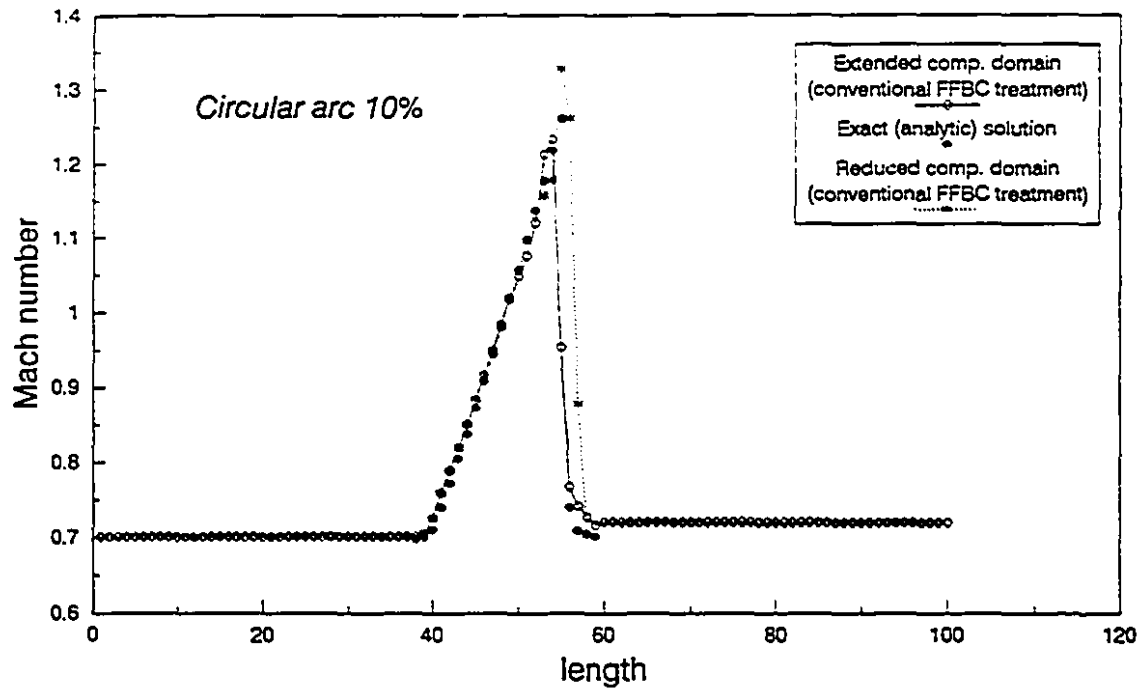


Figure 4.17: Non-isentropic flow: Mach number distributions for extended computational domain (conventional FFBC treatment), exact solution, reduced computational domain (conventional FFBC treatment). $M_\infty = 0.7$, $p_b = p_\infty$, CFL=0.9.

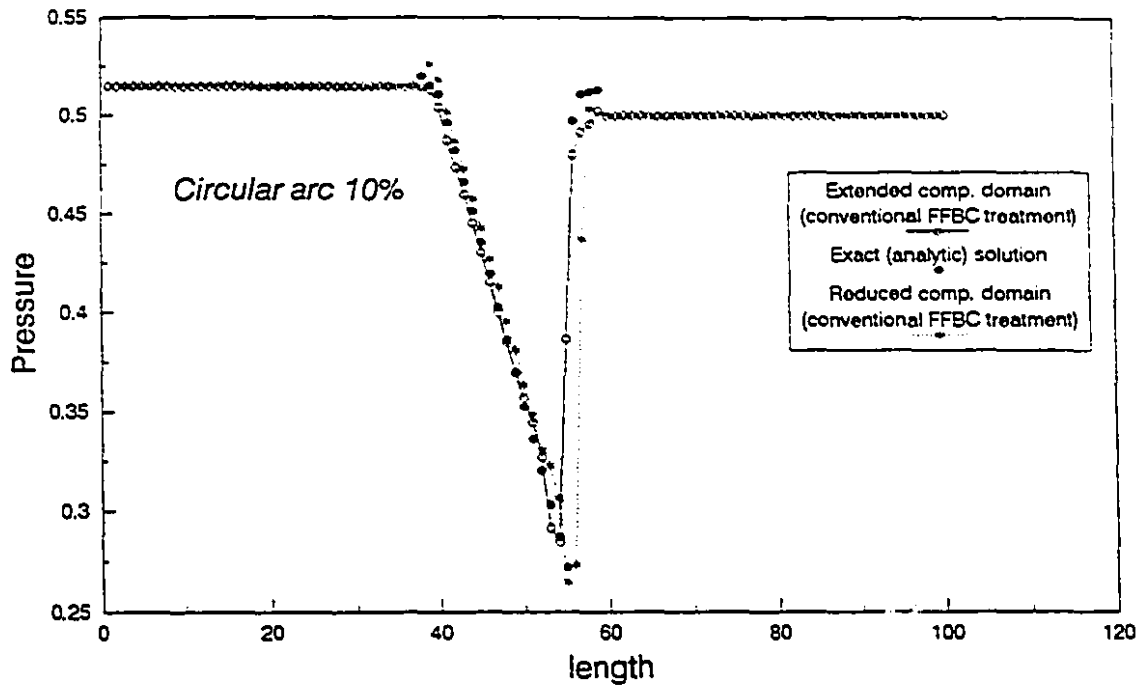


Figure 4.18: Non-isentropic flow: Pressure distributions for extended computational domain (conventional FFBC treatment), exact solution and reduced computational domain (conventional FFBC treatment). $M_\infty = 0.7$, $p_b = p_\infty$, $CFI=0.9$.

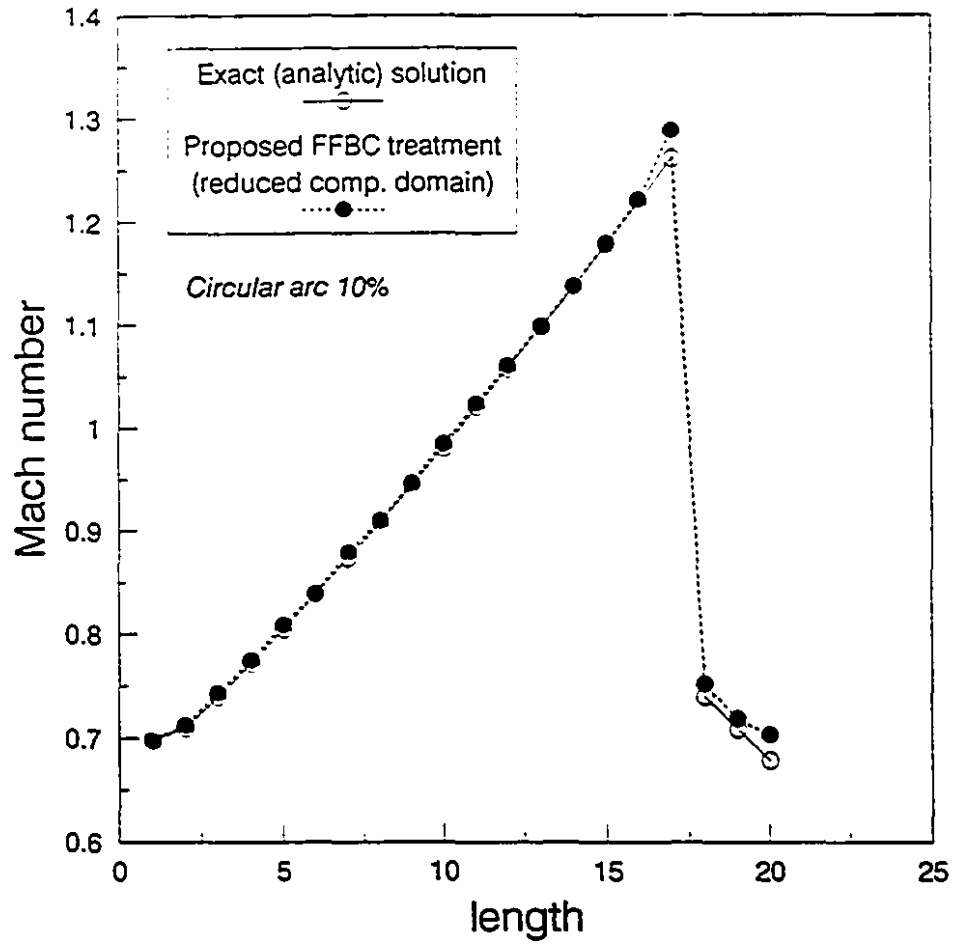


Figure 4.19: Non-isentropic flow: Mach number distributions with exact solution and solution with the proposed FFBC model (reduced computational domain). $M_\infty = 0.7$, $p_b = p_\infty$, CFL=3.9.

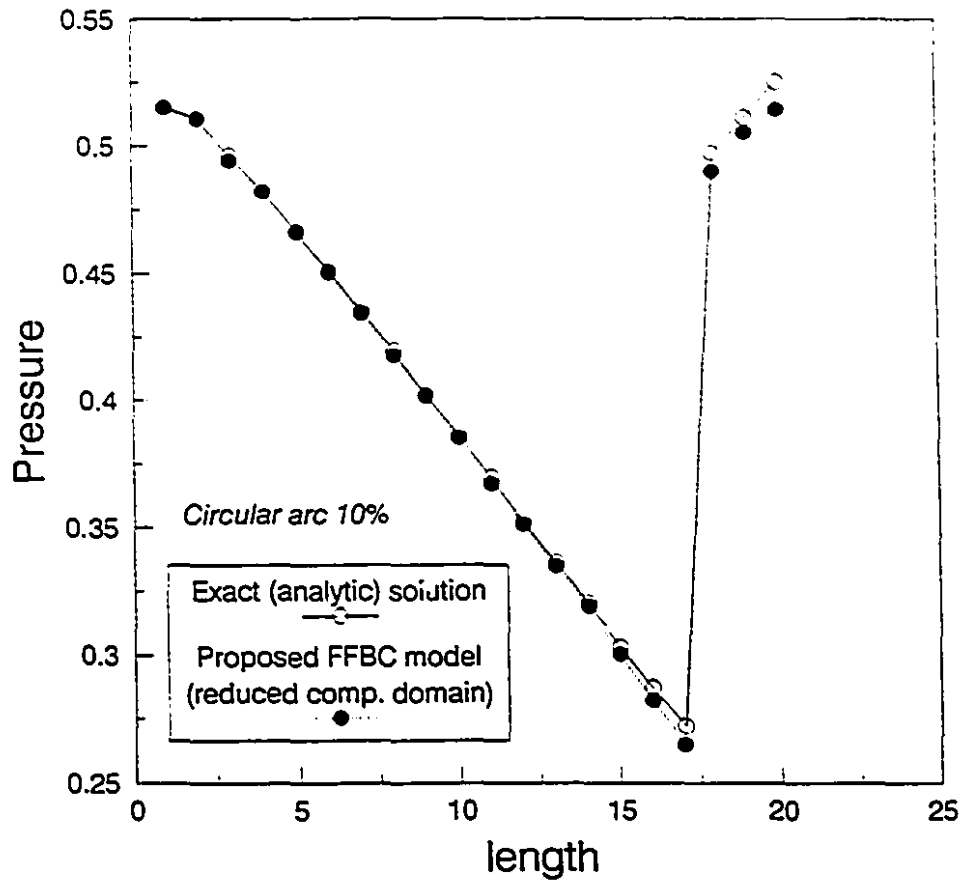


Figure 4.20: Non-isentropic flow: Pressure distributions with exact solution and solution with the proposed FFBC model (reduced computational domain). $M_\infty = 0.7$, $p_b = p_\infty$, CFL=0.9.

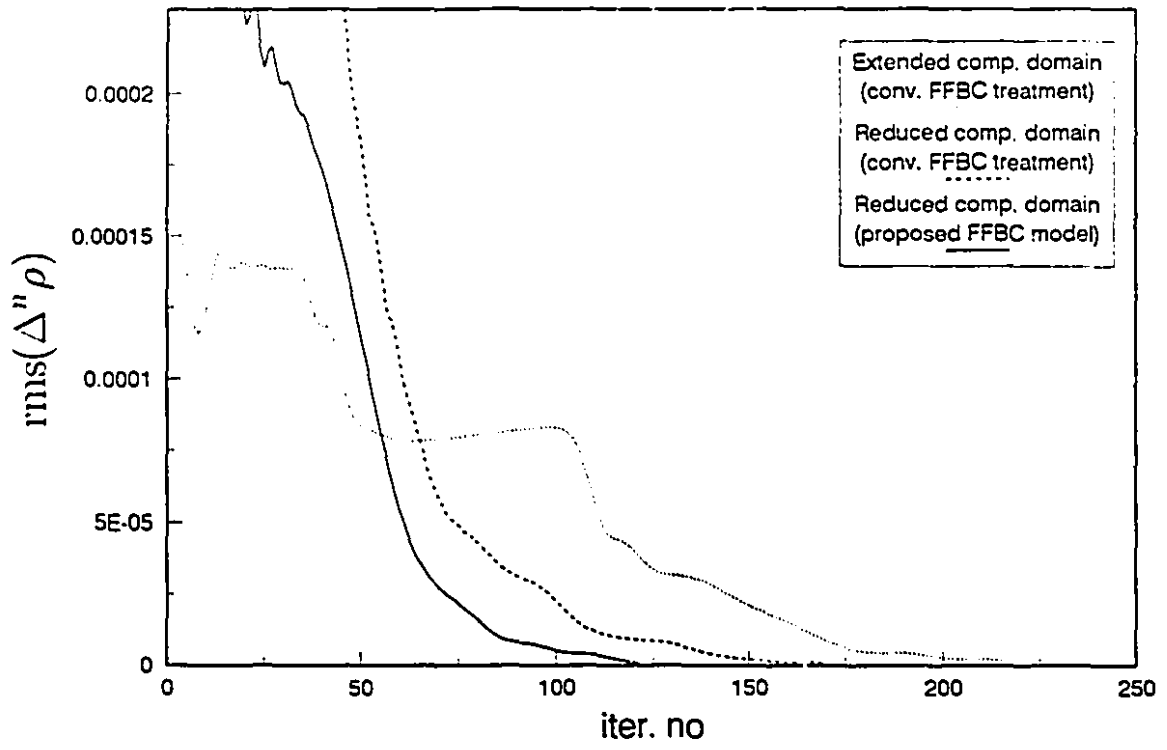


Figure 4.21: Isentropic flow: Convergence histories for extended computational domain (conventional FFBC treatment), reduced computational domain (conventional FFBC treatment) and reduced computational domain (proposed FFBC model), CFL=1.8.

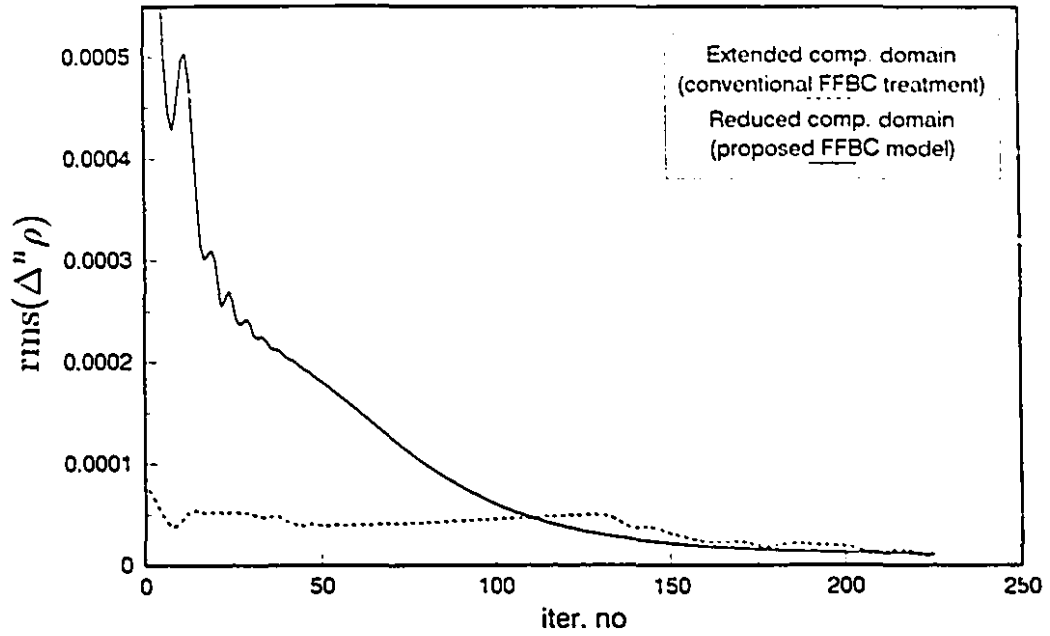


Figure 4.22: Non-isentropic flow: Convergence histories for extended computational domain (conventional FFBC treatment) and reduced computational domain (proposed FFBC model), CFL=0.9.

Chapter 5

Far Field Boundary Conditions for Two-Dimensional Confined Flows

5.1 Introduction

Throughout this chapter the strategy developed for 1D flows in the previous chapter is followed in order to formulate the inflow and outflow FFBCs for the time-dependent 2D internal flows. This model considers the asymptotic decay of the flow perturbations and allows FFBCs to be located much closer to the nonlinear region of the computational domain.

The natural coordinate system for Euler equations were used in order to define the Riemann variables in two spatial dimensions. The FFBC model was formulated and applied to the isentropic and non-isentropic flows. Proposed model alleviates the difficulty related to the directions of information propagation. Expansions of the Riemann variables were used to describe the perturbation decay in the far field regions along the main flow direction. Present model incorporates the information from the far field regions and also computational domain. The numerical solutions obtained with the conventional FFBC methods and the proposed FFBC model are shown and compared at the end of this chapter.

5.2 Conventional FFB treatments

5.2.1 Algebraic extrapolation methods

Algebraic extrapolation consists of zero-, first- and second-order degrees. They can be in time, space or their combination. During the numerical experiments, it was found that usually first-order extrapolation is a good approximation for the most of schemes, in an extended computational domain. At subsonic inflow boundary, the flow angle, the total entalpy, and entropy are specified and held constant. At subsonic outflow boundary, the static pressure is specified and other flow variables are defined by using an algebraic extrapolation of zero or one degree. This procedure has been used by different authors [29, 96, 69].

5.2.2 One-dimensional characteristics approach

This way of boundary treatment which is widely used by the authors for multidimensional flow problems. It depends on the grid topology used for generating the physical domain and FFB. In this approach, the normal component of the velocity to the FFB is taken into account and the tangential component is assumed to have no effect on the boundary treatment [68, 116, 125, 136]. In this case equations (4.3) can be rewritten by replacing the velocity by its component normal to the FFB, in the form

$$\begin{aligned} p_b - p_\infty + \rho a(u_{\perp b} - u_{\perp \infty}) &= 0, \\ p_b - p_\infty - a^2(\rho_b - \rho_\infty) &= 0, \\ p_b - p_{comp} - \rho a(u_{\perp b} - u_{\perp comp}) &= 0. \end{aligned} \tag{5.1}$$

It was proved that this assumption is not true regarding the outgoing waves directions [101]. Other directions than the normal to the boundary surface may be selected in applying the characteristic relations. One choice results from an analysis of Bayliss and Turkel [7] which has been shown by Roe [119] to correspond to a direction making

an angle with the incident velocity direction (see Appendix F). An alternative to this was given in Chapter 2, where the wave direction was approximately found for the far field regions.

5.3 Proposed FFBC formulation for 2-D confined flows

5.3.1 Equations used for isentropic flows

In practice, internal aerodynamic flows are represented by compressible flows between solid walls. For this kind of flows having subsonic free-stream Mach numbers, the perturbations in the presence of solid obstacles are propagated to appreciable distances upstream and downstream of the solid obstacle, which is a highly nonlinear process. For 2D formulation of FFBCs we proceed with Euler equations

$$\begin{aligned}
 \frac{\partial \rho}{\partial t} + u \frac{\partial \rho}{\partial x} + v \frac{\partial \rho}{\partial y} + \rho \left(\frac{\partial u}{\partial x} + \frac{\partial v}{\partial y} \right) &= 0, \\
 \frac{\partial u}{\partial t} + u \frac{\partial u}{\partial x} + v \frac{\partial u}{\partial y} + \frac{1}{\rho} \frac{\partial p}{\partial x} &= 0, \\
 \frac{\partial v}{\partial t} + u \frac{\partial v}{\partial x} + v \frac{\partial v}{\partial y} + \frac{1}{\rho} \frac{\partial p}{\partial y} &= 0, \\
 \frac{\partial}{\partial t} \left(\frac{p}{\rho^\gamma} \right) + u \frac{\partial}{\partial x} \left(\frac{p}{\rho^\gamma} \right) + v \frac{\partial}{\partial y} \left(\frac{p}{\rho^\gamma} \right) &= 0,
 \end{aligned} \tag{5.2}$$

where the energy equation is replaced by the isentropic relation. For wave propagation problems the density and pressure in the equations (5.2) are expressed in terms of sound speed, therefore, one gets

$$\begin{aligned}
 \frac{\partial a}{\partial t} + u \frac{\partial a}{\partial x} + v \frac{\partial a}{\partial y} + \frac{\gamma - 1}{2} a \left(\frac{\partial u}{\partial x} + \frac{\partial v}{\partial y} \right) &= 0, \\
 \frac{\partial u}{\partial t} + u \frac{\partial u}{\partial x} + v \frac{\partial u}{\partial y} + \frac{2}{\gamma - 1} a \frac{\partial a}{\partial x} &= 0, \\
 \frac{\partial v}{\partial t} + u \frac{\partial v}{\partial x} + v \frac{\partial v}{\partial y} + \frac{2}{\gamma - 1} a \frac{\partial a}{\partial y} &= 0, \\
 \frac{\partial}{\partial t} \left(\frac{p}{\rho^\gamma} \right) + u \frac{\partial}{\partial x} \left(\frac{p}{\rho^\gamma} \right) + v \frac{\partial}{\partial y} \left(\frac{p}{\rho^\gamma} \right) &= 0.
 \end{aligned} \tag{5.3}$$

When the equations (5.3) are expressed in natural coordinate system, they can be formulated as following

$$\begin{aligned}
\frac{\partial R}{\partial t} + (\alpha R + \beta Q) \frac{\partial R}{\partial s} &= -\frac{\gamma-1}{8} (R^2 - Q^2) \frac{\partial \theta}{\partial n}, \\
\frac{\partial Q}{\partial t} + (\beta R + \alpha Q) \frac{\partial Q}{\partial s} &= +\frac{\gamma-1}{8} (R^2 - Q^2) \frac{\partial \theta}{\partial n}, \\
\frac{\partial \theta}{\partial t} + \frac{R+Q}{2} \frac{\partial \theta}{\partial s} &= -\frac{\gamma-1}{4} \frac{R-Q}{R+Q} \frac{\partial (R-Q)}{\partial n}, \\
\frac{\partial S}{\partial t} + \frac{R+Q}{2} \frac{\partial S}{\partial s} &= 0.
\end{aligned} \tag{5.4}$$

in which the left- and right-propagating Riemann variables are defined by

$$\begin{aligned}
R &= q + \frac{2}{\gamma-1} a, & Q &= q - \frac{2}{\gamma-1} a, \\
\theta &= \tan^{-1} \frac{v}{u}, & q &= \sqrt{u^2 + v^2}.
\end{aligned} \tag{5.5}$$

where the $\alpha = \frac{1+\gamma}{4}$ and $\beta = \frac{3-\gamma}{4}$ are constants. For derivation of equations (5.4) see Appendixes B and D. Equations (5.4) express the propagation of pressure waves by Riemann variables, the propagation of entropy along the streamlines, and the variation in time of the inclination angle, θ , of the streamlines. The system of equations (5.4) was also used by Verhoff *et al* [152] as flow field solver.

The spatial derivatives in the Cartesian and natural coordinates are related by the following equations, as discussed in section 3.2.1,

$$\begin{aligned}
\frac{\partial}{\partial s} &= \cos \theta \frac{\partial}{\partial x} + \sin \theta \frac{\partial}{\partial y}, & \frac{\partial}{\partial n} &= -\sin \theta \frac{\partial}{\partial x} + \cos \theta \frac{\partial}{\partial y}, \\
\frac{\partial}{\partial x} &= \cos \theta \frac{\partial}{\partial s} - \sin \theta \frac{\partial}{\partial n}, & \frac{\partial}{\partial y} &= \sin \theta \frac{\partial}{\partial s} + \cos \theta \frac{\partial}{\partial n}.
\end{aligned} \tag{5.6}$$

To discretize the equations (5.4) with finite-difference methods along the FFB, it is advantageous to transfer them into the Cartesian coordinates; thus for isentropic flows ($S = \text{const}$), equations (5.4) become

$$\begin{aligned}
\frac{\partial R}{\partial t} + (\alpha R + \beta Q) \left(\cos \theta \frac{\partial R}{\partial x} + \sin \theta \frac{\partial R}{\partial y} \right) &= \\
-\frac{\gamma-1}{8} (R^2 - Q^2) \left[-\sin \theta \frac{\partial \theta}{\partial x} + \cos \theta \frac{\partial \theta}{\partial y} \right], &
\end{aligned}$$

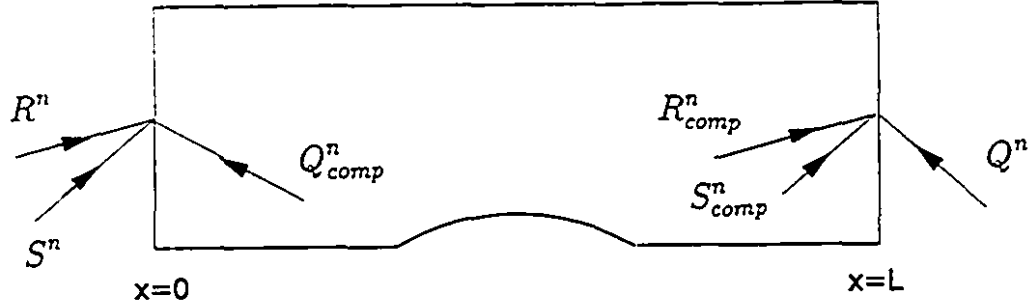


Figure 5.1: Propagation of Riemann variables at inflow and outflow portions for time-dependent two dimensional flows in a certain time level.

$$\begin{aligned}
 \frac{\partial Q}{\partial t} + (\beta R + \alpha Q)(\cos \theta \frac{\partial Q}{\partial x} + \sin \theta \frac{\partial Q}{\partial y}) = \\
 \frac{\gamma - 1}{8} (R^2 - Q^2) \left[-\sin \theta \frac{\partial \theta}{\partial x} + \cos \theta \frac{\partial \theta}{\partial y} \right], \\
 \frac{\partial \theta}{\partial t} + \frac{R + Q}{2} (\cos \theta \frac{\partial \theta}{\partial x} + \sin \theta \frac{\partial \theta}{\partial y}) = \\
 -\frac{\gamma - 1}{4} \frac{R - Q}{R + Q} \left[-\sin \theta \frac{\partial (R - Q)}{\partial x} + \cos \theta \frac{\partial (R - Q)}{\partial y} \right]. \quad (5.7)
 \end{aligned}$$

Equations (5.7) are the governing equations for the isentropic compressible flows expressed in terms of Riemann variables and flow inclination angle. The system of equations (5.7) includes nonlinear terms which are linearized using the expansions of the Riemann variables as far field solutions. This system also express the propagation of left- and right-propagating Riemann variables and the flow direction. The trigonometric functions are linearized by lagging procedure. Figure 5.2 shows that only the projections along x -direction contribute to the boundary formulation, if the flow crosses the boundary at a right angle. The directions of the outgoing waves are found from the equations (2.69) of Chapter 2.

5.3.2 Expanded Riemann variables approach

The Riemann variables possess an important role in the information propagation. In 1D flows they are defined along the characteristic lines, while in two and three space

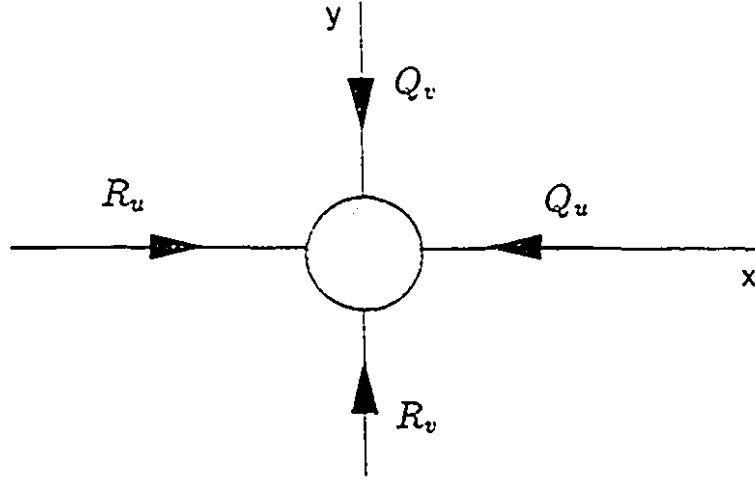


Figure 5.2: Projections of Riemann variables at FFB of two-dimensional flow at a certain time step.

dimensions they consist of surfaces or hypersurfaces. Usually the far field values can be reached by asymptotic expansions of the Riemann variables (such as Fourier expansions in [148]). Note that the Fourier expansions obey the exponentially decaying property [59]. In light of these observations the Riemann variables are expanded asymptotically along the main flow direction. Since in this direction the flow variation is steeper than the other directions. The physical understanding comes from the fact that at distances far from the nonlinear region of the computational domain, the perturbations would be attenuated to have very small intensities. Therefore,

$$\begin{aligned}
 R(x, y, t) &= R_\infty + \sum_{k=1}^m R_k(y, t) \epsilon_k(x), \\
 Q(x, y, t) &= Q_\infty + \sum_{k=1}^m Q_k(y, t) \epsilon_k(x), \\
 \theta(x, y, t) &= \theta_\infty + \sum_{k=1}^m \theta_k(y, t) \epsilon_k(x),
 \end{aligned} \tag{5.8}$$

where $\epsilon_k(x) = e^{k\omega x}$, and ω is the separation factor which is estimated from the work of Verhoff *et al* [148] as $\omega = \frac{\pi s_f}{\sqrt{1-M_\infty^2}}$, s_f is a safety coefficient. For derivation of the separation factor see Appendix H. The R_∞ and Q_∞ refer to the far field Riemann

variables

$$R_\infty = q_\infty + \frac{2}{\gamma - 1} a_\infty, \quad Q_\infty = q_\infty - \frac{2}{\gamma - 1} a_\infty.$$

For our channel flow the free-stream velocity is parallel to the solid walls, i.e. $q_\infty = u_\infty$. Also, the unknown functions R_k and Q_k are determined numerically. Predefined trigonometric functions have been used for simulating the perturbations along the y -direction [45, 46]. Since the propagation directions are not known along y -axis, therefore, the consistent way is the space discretization of the Riemann variables. Expanded Riemann variables as far field solutions are sought for the regions beyond the FFBs. The underlying principle is that the streamline variations of both upstream and downstream propagating perturbation waves should decay to zero at infinity. A physical model of the flow outside of the FFBs provides the boundary conditions which interacts with the interior flow. Hence, the equations (5.8) are expanded up to the desired degree of accuracy

$$\begin{aligned} R(x, y, t) &= R_\infty + \epsilon R_1(y, t) + \epsilon^2 R_2(y, t) + \dots, \\ Q(x, y, t) &= Q_\infty + \epsilon Q_1(y, t) + \epsilon^2 Q_2(y, t) + \dots, \\ \theta(x, y, t) &= \theta_\infty + \epsilon \theta_1(y, t) + \epsilon^2 \theta_2(y, t) + \dots, \end{aligned} \quad (5.9)$$

where $\epsilon = e^{-\omega x}$ and $\theta_\infty = 0$ for the confined flow applications. Introducing the expanded Riemann variables (5.9) into equations (5.7) and performing some algebraic manipulation yields the following partly uncoupled equations. The first-order perturbation equations become

$$\begin{aligned} \frac{\partial R_1}{\partial t} + (\alpha R_\infty + \beta Q_\infty) \left[\omega R_1 \cos \theta + \frac{\partial R_1}{\partial y} \sin \theta \right] = \\ -\frac{\gamma - 1}{8} (R_\infty^2 - Q_\infty^2) \left[-\omega \theta_1 \sin \theta + \frac{\partial \theta_1}{\partial y} \cos \theta \right], \end{aligned} \quad (5.10)$$

$$\begin{aligned} \frac{\partial Q_1}{\partial t} + (\beta R_\infty + \alpha Q_\infty) \left[\omega Q_1 \cos \theta + \frac{\partial Q_1}{\partial y} \sin \theta \right] = \\ \frac{\gamma - 1}{8} (R_\infty^2 - Q_\infty^2) \left[-\omega \theta_1 \sin \theta + \frac{\partial \theta_1}{\partial y} \cos \theta \right], \end{aligned} \quad (5.11)$$

$$\begin{aligned} & \frac{\partial \theta_1}{\partial t} + \frac{1}{2}(R_\infty + Q_\infty) \left[\omega \theta_1 \cos \theta + \frac{\partial \theta_1}{\partial y} \sin \theta \right] = \\ & -\frac{\gamma-1}{4} \frac{R_\infty - Q_\infty}{R_\infty + Q_\infty} \left[-\omega(R_1 - Q_1) \sin \theta + \frac{\partial(R_1 - Q_1)}{\partial y} \cos \theta \right], \end{aligned} \quad (5.12)$$

in which the non-linear terms like $\sin \theta$ and $\cos \theta$ are calculated by lagging procedure.

To achieve higher accuracy, the second-order perturbation equations can be used.

The second-order perturbation equations are expressed as

$$\begin{aligned} & \frac{\partial R_2}{\partial t} + (\alpha R_\infty + \beta Q_\infty) \left[2\omega R_2 \cos \theta + \frac{\partial R_2}{\partial y} \sin \theta \right] + \\ & (\alpha R_1 + \beta Q_1) \left[\omega R_1 \cos \theta + \frac{\partial R_1}{\partial y} \sin \theta \right] = \\ & -\frac{\gamma-1}{8} [(R_\infty^2 - Q_\infty^2)(-2\omega \theta_2 \sin \theta + \frac{\partial \theta_2}{\partial y} \cos \theta) + \\ & 2(R_\infty R_1 - Q_\infty Q_1)(-\omega \theta_1 \sin \theta + \frac{\partial \theta_1}{\partial y} \cos \theta)], \end{aligned} \quad (5.13)$$

$$\begin{aligned} & \frac{\partial Q_2}{\partial t} + (\beta R_\infty + \alpha Q_\infty) \left[2\omega Q_2 \cos \theta + \frac{\partial Q_2}{\partial y} \sin \theta \right] + \\ & (\beta R_1 + \alpha Q_1) \left[\omega Q_1 \cos \theta + \frac{\partial Q_1}{\partial y} \sin \theta \right] = \\ & \frac{\gamma-1}{8} [(R_\infty^2 - Q_\infty^2)(-2\omega \theta_2 \sin \theta + \frac{\partial \theta_2}{\partial y} \cos \theta) + \\ & 2(R_\infty R_1 - Q_\infty Q_1)(-\omega \theta_1 \sin \theta + \frac{\partial \theta_1}{\partial y} \cos \theta)], \end{aligned} \quad (5.14)$$

$$\begin{aligned} & \frac{\partial \theta_2}{\partial t} + \frac{R_1 + Q_1}{R_\infty + Q_\infty} \frac{\partial \theta_1}{\partial t} + \frac{1}{2}(R_\infty + Q_\infty) \left[2\omega \theta_2 \cos \theta + \frac{\partial \theta_2}{\partial y} \sin \theta \right] + \\ & (R_\infty + Q_\infty)(R_1 + Q_1) \left[\omega \theta_1 \cos \theta + \frac{\partial \theta_1}{\partial y} \sin \theta \right] = \\ & -\frac{\gamma-1}{4} \frac{R_\infty - Q_\infty}{R_\infty + Q_\infty} \left[-2\omega(R_2 - Q_2) \sin \theta + \frac{\partial(R_2 - Q_2)}{\partial y} \cos \theta \right] - \\ & \frac{\gamma-1}{4} \frac{R_1 - Q_1}{R_\infty + Q_\infty} \left[-\omega(R_1 - Q_1) \sin \theta + \frac{\partial(R_1 - Q_1)}{\partial y} \cos \theta \right]. \end{aligned} \quad (5.15)$$

The solution of second-order perturbation equations (5.13), (5.14) and (5.15) is possible after solving the first-order ones and finding the R_1 , Q_1 and θ_1 . However, as shown in quasi-1D case, the first-order FFBC equations provide an acceptable overall accuracy of the numerical solutions.

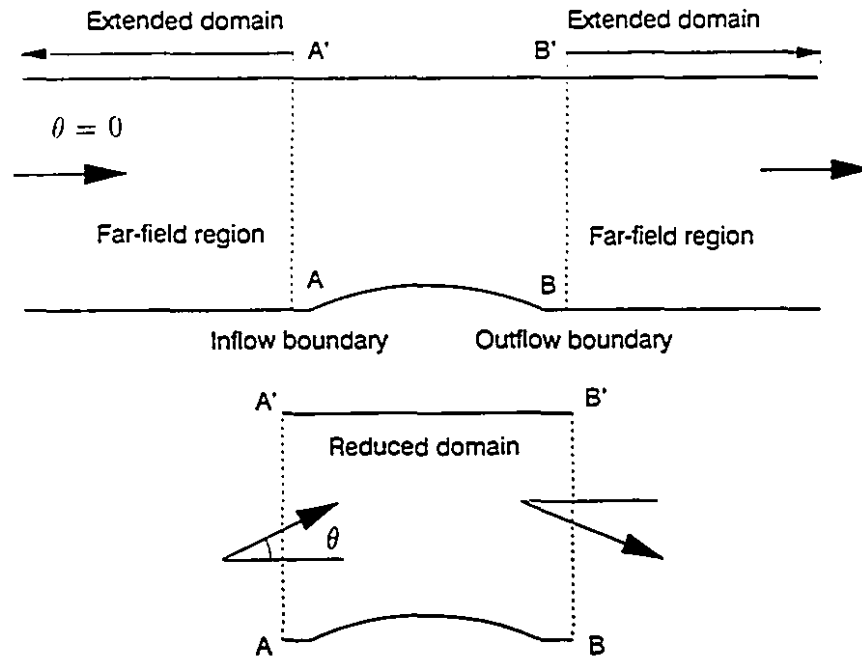


Figure 5.3: Far field regions, extended and reduced domains for confined flow.

5.4 Boundary condition development (isentropic flow)

In time-dependent 2D flows the FFBC modelling should be consistent with the hyperbolic nature of the problem; it should take into account the signals that separately reach to the FFBs. In time-dependent 2D flows, a point is reached by a multitude of signals whose paths are the bicharacteristics converging to it. Therefore, a dominant wave direction is required. For FFBC modelling, note that a part of information is supplied by far field solution, while the other part is provided by the numerical scheme within the computational domain.

This FFBC model takes into account the information interchange between the computational domain and the outer absent world at the FFBs. In Figure 5.3 the extended and reduced computational domains, also the far field regions are shown for the confined flow case. Approximate outgoing wave direction (equation (2.71))

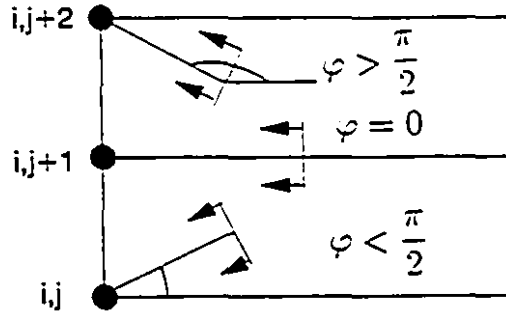


Figure 5.4: Propagation of the outgoing wave fronts with different orientations towards an inflow boundary in a 2D setup.

is restricted to the neighborhood of FFB and is not valid globally. Before applying the equations (2.55) to outgoing waves a value of φ_{ij} is found and compared to $\pi/2$. When $\varphi_{ij} = 0$, then equations (2.56) yield $dv = 0$ or $v = \text{const}$. This means that for a FFB aligned with y -direction, equations (2.56) do not contribute to the information exchange between the far field and computational domain. However, in confined flow applications, propagations along y -direction affects the values on the solid walls. Figure 5.4 illustrates the possible directions of the propagations of the outgoing waves at each grid point. In fact each grid point, located at a FFB, can experience these three possible cases during the time-integration process. To determine the value of φ , equation (2.71) in discretized form is used. Note that this equation is locally valid. A multitude of waves move inside the computational domain during the iteration process. However, we are interested in locating the ones which strike the FFBs. Since each wave carries information from the numerical solution. For the oblique FFB with respect to the x and y directions, both the equations (2.55) and (2.56) are used. From Figure 5.5, along the direction normal to FFB, one has for left- and right-propagating Riemann variables the following

$$\begin{aligned}
 R_{\perp b} &= R_u \sin \theta_g - Q_v \cos \theta_g, \\
 Q_{\perp b} &= -Q_u \sin \theta_g + R_v \cos \theta_g,
 \end{aligned}
 \tag{5.16}$$

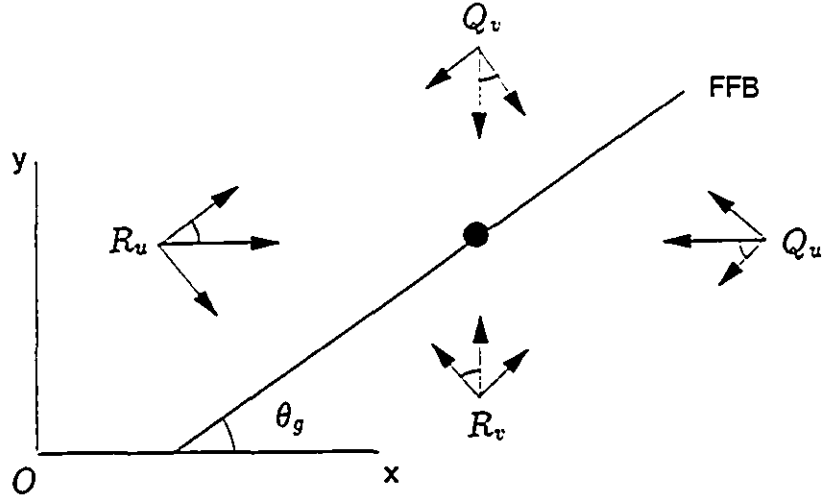


Figure 5.5: Oblique FFB with respect to Cartesian coordinates.

where θ_g denotes the FFB inclination, which is also shown in Figure 5.5. Plugging the values of R_u , R_v and Q_u , Q_v from equations (2.62) into the equations (5.16) and doing some algebraic manipulation, it follows that

$$\begin{aligned} R_{\perp b} &= q_{\perp b} + \sin(\theta_g + \varphi) \frac{2}{\gamma - 1} a, \\ Q_{\perp b} &= -q_{\perp b} + \sin(\theta_g + \varphi) \frac{2}{\gamma - 1} a, \end{aligned} \quad (5.17)$$

where $q_{\perp b}$ is the velocity component normal to FFB defined by

$$q_{\perp b} = u \sin \theta_g - v \cos \theta_g. \quad (5.18)$$

At each grid point on the FFB, one has

$$\begin{aligned} q_{\perp b} &= \frac{1}{2}(R_{\perp b} - Q_{\perp b}) \\ a &= \frac{\gamma - 1}{4 \sin(\theta_g + \varphi)}(R_{\perp b} + Q_{\perp b}) \end{aligned} \quad (5.19)$$

Having calculated the values of $q_{\perp b}$ and θ , the velocity components are found using the equation (5.18)

$$u = \frac{\cos \theta}{\sin(\theta_g - \theta)} q_{\perp b}, \quad v = \frac{\sin \theta}{\sin(\theta_g - \theta)} q_{\perp b}. \quad (5.20)$$

Note that the flow direction θ is calculated from the first-order equation (5.12), since $\theta = \theta_\infty + \theta_1$. The above relations are used for information calculation from the computational domain.

5.4.1 Upstream far-field region

For upstream region far from the computational boundary (i.e., $x \ll 0$), the exponential terms in the expansions (5.9) become very small, and hence R and Q would tend to far-field free stream values. If the origin is located at the inflow boundary ($x = 0$) the functions $e^{k\omega x}$ become unity, and hence

$$\begin{aligned} R &= R_\infty + R_1 + R_2, \\ Q &= Q_\infty + Q_1 + Q_2. \end{aligned} \quad (5.21)$$

For isentropic flows, there are two downstream-propagating waves carrying information from far-field regions towards the upstream FFB and one upstream-propagating wave carrying information from the numerical solution. At an inflow FFB the perturbation equations (5.10) and (5.12) hold as

$$\begin{aligned} \frac{\partial R_1}{\partial t} + (\alpha R_\infty + \beta Q_\infty) \left[\omega R_1 \cos \theta + \frac{\partial R_1}{\partial y} \sin \theta \right] = \\ -\frac{\gamma-1}{8} (R_\infty^2 - Q_\infty^2) \left[-\omega \theta_1 \sin \theta + \frac{\partial \theta_1}{\partial y} \cos \theta \right], \\ \frac{\partial \theta_1}{\partial t} + \frac{1}{2} (R_\infty + Q_\infty) \left[\omega \theta_1 \cos \theta + \frac{\partial \theta_1}{\partial y} \sin \theta \right] = \\ -\frac{\gamma-1}{4} \frac{R_\infty - Q_\infty}{R_\infty + Q_\infty} \left[-\sin \theta (R_1 - Q_1) \omega + \cos \theta \frac{\partial (R_1 - Q_1)}{\partial y} \right]. \end{aligned}$$

After discretization of the above equations in time and y -direction, which is discussed in section 5.5, the perturbation values (namely R_1^{n+1} and θ_1^{n+1}) are obtained by proceeding in time. Then the value of Q_1 is determined from

$$Q_1^{n+1}(1, j) = Q_{comp}^{n+1}(1, j) - Q_\infty, \quad (5.22)$$

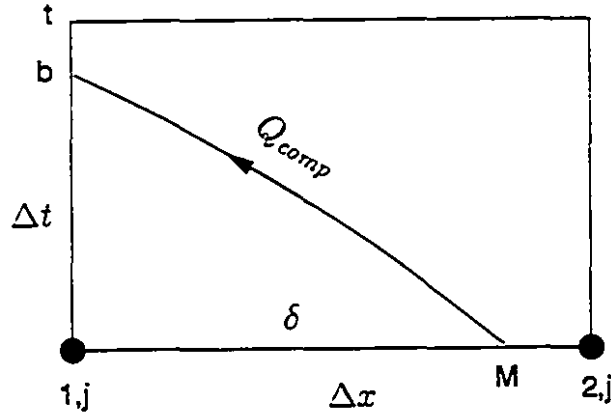


Figure 5.6: Propagation of left-propagating Riemann variable at inflow boundary along the calculated bicharacteristic for time-dependent two dimensional flow.

where Q_{comp} is the Riemann variable obtained from the numerical solution along the dominant wave direction. Numerical experiments showed that interpolation along the dominant wave is advantageous than extrapolation in terms of accuracy, convergence, and stability. Calculating the outgoing wave direction is an important issue, and differs from one grid point to the next. Furthermore, this direction does not need to remain fixed during the computation. Interpolation along bicharacteristics does not rely on a fixed direction of the outgoing wave. The only assumption made is that at each grid point there is one such direction, φ_{ij} , which is calculated locally. This direction may also be found by geometrical considerations [119]. A rough choice might be the local flow angle (e.g. $\varphi \approx \theta$). The outgoing waves can be damped near the FFB that was proposed by various authors [67, 74]. The damping proposed by Kosloff and Kosloff [81] acts on both incoming and outgoing waves. For confined flows the inflow and outflow FFBs are often taken perpendicular to the free-stream velocity direction. Therefore, when $\theta_g = \pi/2$, one has $q_{\perp b} = u$. Hence the Riemann variables from equations (5.17) become

$$\begin{aligned}
 R_{\perp b} &= u + \cos \varphi \frac{2}{\gamma - 1} a = R_u, \\
 Q_{\perp b} &= -u + \cos \varphi \frac{2}{\gamma - 1} a = Q_u.
 \end{aligned}
 \tag{5.23}$$

By assuming $\varphi \approx \theta$, one comes up with

$$\frac{Q_u}{\cos \varphi} = \frac{u}{\cos \varphi} - \frac{2}{\gamma - 1} a = Q, \quad (5.24)$$

where $\frac{u}{\cos \varphi} = q$. Figure 5.6 shows how the values of u and a are interpolated between the grid points $(1, j)$ and $(2, j)$ as in section 4.4.1, then the value of Q^{n+1} is known. Also, the R^{n+1} and θ^{n+1} are computed from the equations (5.10) and (5.12). An alternative is to use the equation (2.71), which was derived in Chapter 2. Equation (2.71) is approximated by forward time discretization as

$$\tan \varphi_{ij} = \frac{v_{ij}^{n+1} - v_{ij}^n}{u_{ij}^{n+1} - u_{ij}^n}. \quad (5.25)$$

The calculated flow variables at the previous time-step are then updated

$$u^{n+1} = \frac{1}{2}(R_u^{n+1} + Q_u^{n+1}), \quad a^{n+1} = \frac{\gamma - 1}{4 \cos \varphi}(R_u^{n+1} - Q_u^{n+1}), \quad (5.26)$$

so the velocity q is known from

$$q^{n+1} = \frac{u^{n+1}}{\cos \theta^{n+1}}, \quad (5.27)$$

and finally

$$Q_{comp}^{n+1} = Q_b = Q_M = q^{n+1} - \frac{2}{\gamma - 1} a^{n+1}. \quad (5.28)$$

Having the value of Q_{comp}^{n+1} from the above equation, the R^{n+1} and θ^{n+1} are known by solving the equations (5.10) and (5.12). Equation (5.25) showed better performance regarding the convergence than the assumption ($\varphi \approx \theta$). In Figure 5.7, the propagations of the Riemann variables at two neighboring boundary points are shown at a certain time. For each boundary grid point, these variables are calculated based on their directions of propagations.

5.4.2 Matching the far field and near field solutions

Having calculated the values of Riemann variables and the flow angle at the inflow FFB, one can determine in a straightforward manner the remaining flow parameters

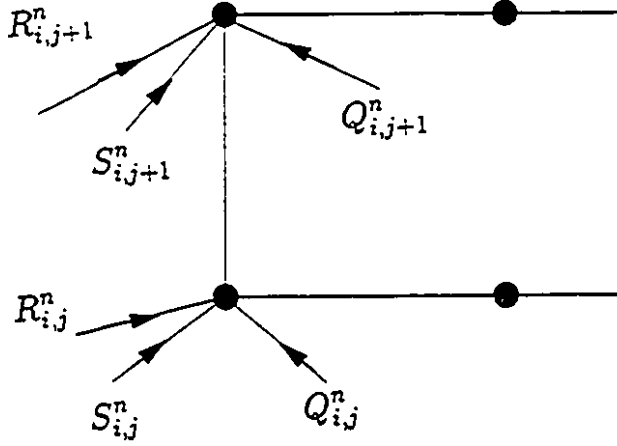


Figure 5.7: Propagations of the Riemann variables and entropy at a certain time-level for the two consecutive boundary points.

as following

$$\begin{aligned}
 q_{in}^{n+1} &= \frac{1}{2}(R^{n+1} + Q_{comp}^{n+1}), & a_{in}^{n+1} &= \frac{\gamma-1}{4}(R^{n+1} - Q_{comp}^{n+1}), \\
 u_{in}^{n+1} &= q_{in}^{n+1} \cos \theta^{n+1}, & v_{in}^{n+1} &= q_{in}^{n+1} \sin \theta^{n+1}, \\
 \rho_{in}^{n+1} &= \left[\frac{\rho_{\infty}^{\gamma}}{\gamma p_{\infty}} (a_{in}^{n+1})^2 \right]^{\frac{1}{\gamma-1}}, & p_{in}^{n+1} &= \frac{1}{\gamma} \rho_{in}^{n+1} (a_{in}^{n+1})^2, \\
 E_{in}^{n+1} &= \frac{1}{\gamma-1} \frac{p_{in}^{n+1}}{\rho_{in}^{n+1}} + \frac{1}{2} \left((u_{in}^{n+1})^2 + (v_{in}^{n+1})^2 \right). & & (5.29)
 \end{aligned}$$

The far-field and computational-domain solutions are genuinely coupled by the Riemann variables along the propagation directions. Then at each iteration step the conservative flow vector $[\rho_{in}^{n+1}, (\rho u)_{in}^{n+1}, (\rho v)_{in}^{n+1}, (\rho E)_{in}^{n+1}]^T$ is known and joined to the numerical scheme.

5.4.3 Downstream far-field region

For the outflow FFB being crossed by an isentropic flow, the left-propagating Riemann variable is needed, which carries the information from downstream far-field region. The value of Q is determined from the equation (5.11). For the region downstream of the computational boundary (i.e. $x > 0$), the exponential functions should take the

form $\epsilon_k(x) = e^{-k\omega x}$, hence

$$\begin{aligned} R &= R_\infty + \epsilon R_1 + \dots, \\ Q &= Q_\infty + \epsilon Q_1 + \dots \end{aligned} \quad (5.30)$$

where $\epsilon = e^{-\omega x}$ in this case. In the streamline coordinates for isentropic flows, there are two downstream-propagating waves carrying information to the downstream boundary from the numerical solution and one upstream-propagating wave carrying information from far-field region.

At an outflow FFB the right-propagating Riemann variable and the entropy are calculated from the computational domain, and the Q from the following perturbation equation

$$\begin{aligned} \frac{\partial Q_1}{\partial t} + (\beta R_\infty + \alpha Q_\infty) \left[\omega Q_1 \cos \theta + \frac{\partial Q_1}{\partial y} \sin \theta \right] = \\ \frac{\gamma - 1}{S} (R_\infty^2 - Q_\infty^2) \left[-\omega \theta_1 \sin \theta + \frac{\partial \theta_1}{\partial y} \cos \theta \right]. \end{aligned}$$

An explicit discretization of equation (5.11) results in

$$\begin{aligned} \frac{Q_1^{n+1} - Q_1^n}{\Delta t} + (\beta R_\infty + \alpha Q_\infty) \left[\omega Q_1 \cos \theta + \frac{\Delta Q_1}{\Delta y} \sin \theta \right] = \\ \frac{\gamma - 1}{S} (R_\infty^2 - Q_\infty^2) \left[-\sin \theta \omega \theta_1 + \cos \theta \frac{\Delta \theta_1}{\Delta y} \right]. \end{aligned} \quad (5.31)$$

The flow variables at the outflow FFB are determined in a similar manner to that used for inflow boundary. Then the conservative state vector is completed and joined to the flow field solver.

Remark: Many numerical solution algorithms for Euler equations use characteristic FFBCs in which R_∞ and Q_∞ are specified at inflow and outflow FFBs. The new approach uses expansion of these quantities in a consistent manner with the physical far field, while maintaining the hyperbolic character of the governing equations.

5.5 Discretization of far-field perturbation equations

The time and space derivatives which were appeared in the far field equations for the inflow and outflow FFBs are discretized as

$$\begin{aligned}\frac{\partial R_1}{\partial t} &\approx \frac{R_1^{n+1}(j) - R_1^n(j)}{\Delta t}, \\ \frac{\partial \theta_1}{\partial t} &\approx \frac{\theta_1^{n+1}(j) - \theta_1^n(j)}{\Delta t}, \\ \frac{\partial R_1}{\partial y} &\approx \frac{R_1^n(1, j+1) - R_1^n(1, j-1)}{y(1, j+1) - y(1, j-1)}.\end{aligned}\quad (5.32)$$

and similar relations for Q_1 . At an inflow boundary, typically the perturbation equations (5.10) and (5.12) should be discretized and updated during the time-integration process. An explicit discretization with respect to time is used. Spatial derivatives in the equation (5.10) are approximated by central differencing, since the directions of disturbance propagation along the y -axis are not known. Along y -direction, these disturbances move from both sides towards a grid point situated at the inflow or outflow boundaries. One needs the perturbation values on the lower and upper solid walls. For this purpose an interpolation is performed between the free-stream far field value (R_∞) and the inner grid points on the walls, namely $R(2, 1)$ and $R(2, M_J)$, as shown in Figure 5.8. This procedure is described in the following. For the right-propagating Riemann variables on the solid walls, one gets

$$\begin{aligned}R|_{y=0} &= R_\infty + R_1(0, t) = R(1, 1), \\ R|_{y=1} &= R_\infty + R_1(1, t) = R(1, M_J).\end{aligned}\quad (5.33)$$

Note that the nondimensional height of channel is taken here as unity. Linear interpolation yields

$$\begin{aligned}R_{\text{solid-wall}} &= R(1, 1) = \frac{\Delta x}{\ell + \Delta x} R_\infty + \frac{\ell}{\ell + \Delta x} R(2, 1) \\ R_{\text{solid-wall}} &= R(1, M_J) = \frac{\Delta x}{\ell + \Delta x} R_\infty + \frac{\ell}{\ell + \Delta x} R(2, M_J).\end{aligned}\quad (5.34)$$

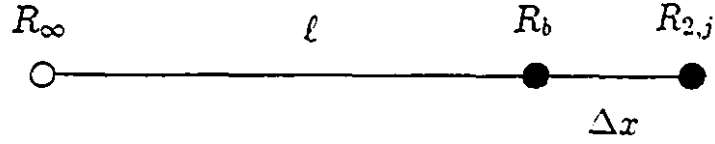


Figure 5.8: Interpolation stencil for wall values.

Now, if $\ell \rightarrow \infty$, in the limit, one gets from the equations (5.33) and (5.34) the following

$$\begin{aligned} R(1,1) &= R(2,1), \\ R(1, M_J) &= R(2, M_J). \end{aligned} \quad (5.35)$$

The value of ℓ can be taken two or three chords away from the inflow and or outflow FFBs. These distances are equivalent with the theoretical infinite ones. For the perturbation equation (5.12) the boundary values are quite simple. One just need to put $\theta = 0$ or $v = 0$ on the solid walls. In fact on the solid walls, equations (5.4) reduce to (4.15).

The time-step in the perturbation equation discretization was taken smaller than the one used for solving the flow domain. This delays the travelling of the perturbations in reaching to the FFBs [73, 74, 92].

5.6 Outflow far-field boundary conditions for non-isentropic flows

For non-isentropic flow crossing the outflow boundary, the equation for the extended left-propagating Riemann variable is expressed as (see equation (D.12) in Appendix D)

$$\frac{\partial Q}{\partial t} + (\beta R + \alpha Q) \frac{\partial Q}{\partial s} = \mathcal{F}_Q(R, Q, S, \theta), \quad (5.36)$$

where $\alpha = \frac{\gamma-1}{2S}$ and $\beta = \frac{\gamma-1}{2S}$. The right hand side is

$$\mathcal{F}_Q(R, Q, S, \theta) = \frac{\gamma-1}{8} \frac{R-Q}{S} \left(S - \frac{2}{\gamma-1} \right) \left[\frac{\partial(R+Q)}{\partial s} + \frac{2}{\gamma-1} \frac{\partial}{\partial s} \left(\frac{R-Q}{S} \right) \right] + \frac{\gamma-1}{8} (R^2 - Q^2) \frac{\partial \theta}{\partial n}. \quad (5.37)$$

To apply the equation (5.36) at the outflow FFB, it is transformed to the Cartesian coordinates

$$\frac{\partial Q}{\partial t} + (\beta R + \alpha Q) \left[\cos \theta \frac{\partial Q}{\partial x} + \sin \theta \frac{\partial Q}{\partial y} \right] = \mathcal{G}_Q(R, Q, S, \theta), \quad (5.38)$$

where

$$\begin{aligned} \mathcal{G}_Q(R, Q, S, \theta) = & \frac{\gamma-1}{8} \frac{R-Q}{S} \left(S - \frac{2}{\gamma-1} \right) \left[\cos \theta \frac{\partial(R+Q)}{\partial x} + \sin \theta \frac{\partial(R+Q)}{\partial y} + \right. \\ & \frac{2}{\gamma-1} \cos \theta \frac{1}{S^2} \left(S \frac{\partial(R-Q)}{\partial x} - (R-Q) \frac{\partial S}{\partial x} \right) + \\ & \left. \frac{2}{\gamma-1} \sin \theta \frac{1}{S^2} \left(S \frac{\partial(R-Q)}{\partial y} - (R-Q) \frac{\partial S}{\partial y} \right) \right] + \\ & \frac{\gamma-1}{8} (R^2 - Q^2) \left(-\sin \theta \frac{\partial \theta}{\partial x} + \cos \theta \frac{\partial \theta}{\partial y} \right). \end{aligned} \quad (5.39)$$

Entropy varies from one streamline to the other in non-isentropic flows. That is, one has entropy change normal to the streamline direction. For steady transonic flows, entropy is convected towards the downstream region along each streamline; however, it may vary from one streamline to the other. Therefore, along y -direction the entropy variation is steeper than the x -direction, beyond the outflow FFB. Entropy variations in y -direction depend on the flow regime and the shock wave configuration. In this approach, a space discretization is performed along the y -direction as shown in section 5.3. For the non-isentropic flows, in addition to the Riemann variables, the entropy is also expanded as

$$S = S_\infty + \epsilon S_1 + \epsilon^2 S_2, \quad (5.40)$$

where S_∞ is the upstream entropy. As was discussed in Chapter 4, only the outflow FFBCs are needed for the non-isentropic flow of a compressible fluid through a channel. The isentropic inflow FFBC model maintains its validity for transonic flows (see

section 4.4). After introducing the expansions of R , Q and S into the equation (5.38), it is expressed as

$$\frac{\partial Q_1}{\partial t} + (\beta R_\infty + \alpha Q_\infty) \left[\omega Q_1 \cos \theta + \frac{\partial Q_1}{\partial y} \sin \theta \right] = \frac{\gamma - 1}{8} (\kappa_\infty T_1 + T_2), \quad (5.41)$$

where

$$\kappa_\infty = (R_\infty - Q_\infty) \left(S_\infty - \frac{2}{\gamma - 1} \right),$$

$$\begin{aligned} T_1 = & \omega(R_1 + Q_1) \cos \theta + \frac{\partial(R_1 + Q_1)}{\partial y} \sin \theta + \\ & \frac{2}{\gamma - 1} \frac{1}{S_\infty^3} \cos \theta [S_\infty \omega(R_1 - Q_1) - (R_\infty - Q_\infty) \omega S_1] + \\ & \frac{2}{\gamma - 1} \frac{1}{S_\infty^3} \sin \theta \left[S_\infty \frac{\partial(R_1 - Q_1)}{\partial y} - (R_\infty - Q_\infty) \frac{\partial S_1}{\partial y} \right]. \end{aligned}$$

$$T_2 = (R_\infty^2 - Q_\infty^2) \left[-\omega \theta_1 \sin \theta + \frac{\partial \theta_1}{\partial y} \cos \theta \right].$$

One gets the second-order perturbation equation for the left-propagating Riemann variable as

$$\begin{aligned} \frac{\partial Q_2}{\partial t} + (\beta R_\infty + \alpha Q_\infty) \left[2\omega Q_2 \cos \theta + \frac{\partial Q_2}{\partial y} \sin \theta \right] + \\ (\beta R_1 + \alpha Q_1) \left[\omega Q_1 \cos \theta + \frac{\partial Q_1}{\partial y} \sin \theta \right] + \\ 3 \frac{S_1}{S_\infty} \left[\frac{\partial Q_1}{\partial t} + (\beta R_\infty + \alpha Q_\infty) (\omega Q_1 \cos \theta + \frac{\partial Q_1}{\partial y} \sin \theta) \right] = \\ \frac{\gamma - 1}{8} (\kappa_\infty T_3 + T_1 T_4 + T_5), \quad (5.42) \end{aligned}$$

where

$$\begin{aligned} T_3 = & 2\omega(R_2 + Q_2) \cos \theta + 3 \frac{S_1}{S_\infty} \omega(R_1 + Q_1) \cos \theta + \\ & \frac{\partial(R_2 + Q_2)}{\partial y} \sin \theta + 3 \frac{S_1}{S_\infty} \frac{\partial(R_1 + Q_1)}{\partial y} \sin \theta + \\ & \frac{2}{\gamma - 1} \frac{1}{S_\infty^3} \cos \theta [2S_\infty \omega(R_2 - Q_2) + \omega S_1(R_1 - Q_1) \\ & - 2\omega(R_\infty - Q_\infty)S_2 - \omega(R_1 - Q_1)S_1] + \\ & \frac{2}{\gamma - 1} \frac{1}{S_\infty^3} \sin \theta \left[S_\infty \frac{\partial(R_2 - Q_2)}{\partial y} + S_1 \frac{\partial(R_1 - Q_1)}{\partial y} \right. \\ & \left. - (R_\infty - Q_\infty) \frac{\partial S_2}{\partial y} - (R_1 - Q_1) \frac{\partial S_1}{\partial y} \right], \end{aligned}$$

$$\mathcal{T}_4 = (R_\infty - Q_\infty)S_1 + (R_1 - Q_1)\left(S_\infty - \frac{2}{\gamma - 1}\right).$$

$$\mathcal{T}_5 = (R_\infty^2 - Q_\infty^2) \left[-2\omega\theta_2 \sin\theta + \frac{\partial\theta_2}{\partial y} \cos\theta \right] + \left[2(R_\infty R_1 - Q_\infty Q_1) + 3\frac{S_1}{S_\infty}(R_\infty^2 - Q_\infty^2) \right] \left[-\omega\theta_1 \sin\theta + \frac{\partial\theta_1}{\partial y} \cos\theta \right].$$

The non-isentropic flow crosses the downstream FFB and go to the far field region. Equation (5.41) is discretized and integrated, then a value for Q is found. The right-going Riemann variable R and the entropy S are computed from the computational domain. Finally the far field solutions are matched to the solution of the computational domain through relations (5.29). To achieve higher accuracy the second-order equations can be solved.

5.7 Numerical flow field solver

To validate the proposed FFBC model and its ability on the accuracy improvement, the time-dependent Euler equations in conservation law form are employed, which have the shock capturing feature. The factored scheme was used, as shown in Chapter 3. This scheme was developed by Beam and Warming [11] and later extended by Pulliam [114]. Applying the proposed FFBC model led to a considerable reduction in the size of the block tridiagonal matrix (along ξ -direction) needed to be inverted at each iteration step.

5.8 Model validation and numerical results

The FFBC model in Chapter 4 is extended for 2D flows, which is based on the Riemann variable approach. For flow simulation and testing the effect of BC treatments on the solution accuracy, geometry of Chapter 4 is used. ✓

Two kinds of domains were used in the numerical computations, namely extended and reduced. In each domain, subsonic and transonic flows were computed

by different FFBC methods. The first-order FFBC models were used, which are sufficiently general and can be combined with other numerical Euler solvers.

In both domains a circular-arc-bump is located at the middle of the lower wall, while the upper wall is straight. In the extended domain, the FFB stations were located one chord in both upstream and downstream sides of the circular-arc. In the reduced computational domain the FFBs were positioned much closer to the circular-arc (two longitudinal spacing steps in each side). The 2D grid setup has already been shown in Figure 3.2 of Chapter 3. Basically, the geometry is similar to the quasi-one-dimensional case, which is treated two-dimensionally here. The total channel length was three chord lengths for the case of extended domain, whilst for the reduced domain, it was increased only by a small fraction of the chord length, $\frac{2}{N}$, at both sides of its extremities, where N represents the number of intervals along the circular-arc. In the present calculations the grid points are clustered near the circular-arc-bump along the y -direction hyperbolically, while equally-spaced grids are used along the x -direction (in order to avoid the further effect of highly stretched grids near the far field region). The grids used for extended and reduced computational domains had the dimensions 60×20 and 24×20 , respectively.

To illustrate the influence of computational domain size and of the implementation of various FFBC models on the accuracy of the numerical solutions and convergence rate, the computations were conducted with different FFBC methods and different sizes of computational domain.

The numerical solutions were obtained and compared for 2D channel flow (for subsonic and transonic regimes) in the following cases:

1. Extended computational domain (60×20) with conventional FFBC treatment.
2. Reduced computational domain (24×20) with conventional FFBC treatment.
3. Reduced computational domain (24×20) with the proposed FFBC model.
4. Previous numerical solutions obtained by Ni [107].

Different aspects of the proposed FFBC model were considered such as solutions accuracy and computational time. The numerical solutions obtained with the proposed FFBC model are compared with the results obtained by Ni [107]. The convergence histories for the proposed FFBC model are compared with those obtained by Eidelman [29] BCs. It was found that a reduced convergence is reached by applying the proposed FFBC model for a subsonic flow. The first-order FFBC model is sufficiently general and can be combined with other Euler solvers. The extended domain can also be used as a reference for comparing the 2D solutions, in which the exact solutions are not available.

Figure 5.9 shows how the numerical solutions are affected by reducing the domain size without implementing an appropriate FFBC model. It proves that solution accuracy depends on the domain size and FFBC models. Note that by reducing the domain size, the accuracy and symmetry of solutions are substantially deteriorated. This is due to the fact that in the conventional FFBC methods the flow directions are imposed to be zero at the inflow and outflow ports instead of being determined accurately. For example at an inflow boundary, when one approaches to the arc-bump the streamlines deviate from the far field streamlines and they are not parallel to x -axis anymore. Another factor is a consequence of the reflection phenomena occurs at FFBCs thereby affecting the solution accuracy and convergence.

In Figure 5.10 the pressure distributions on the upper and lower walls for extended and reduced domains with the conventional FFBC treatment are shown. The difference between two pressure solutions is somewhat smaller in comparison to the Mach number solutions of Figure 5.9, although they are still important.

It was found that the proposed FFBC model led to a significant improvement in the computational efficiency due to a substantial reduction of the computational domain (by a factor of 2.5 times) and in the number of iterations (about 30% reduction).

The improved solutions obtained by using the proposed FFBC model are illustrated in Figures 5.11 and 5.12.

The present solutions are also compared in Figure 5.13, for validation with the solutions obtained by Ni [107], which were found in good agreement with the present results obtained with the proposed FFBC model for the reduced computational domain.

Comparisons were made in Figure 5.14 between the convergence histories of the reduced computational domain with the conventional and proposed FFBC models. The present FFBC model displayed a better rate of convergence.

The transonic flow solutions are illustrated in Figure 5.15 for $M_\infty = 0.675$. This inlet Mach number was used by the authors for comparison purposes. When the reduced computational domain is calculated with the conventional FFBC treatment, it is observed that how the shock is not well positioned.

For transonic flow, the comparison of Mach number distributions for the extended computational domain and the solution of Ni [107] is shown in Figure 5.16. Ni used an explicit second-order accurate finite-volume method, incorporating multigrid solution techniques, on a 65×17 grid. Figure 5.17 shows the results of applying the proposed FFBC model in comparison with the solution of Ni. Good agreement for the upper wall exists, however, near the shock a small difference is observed; this could be due to grid resolution and type of numerical flow solver.

The convergence history for reduced computational domains with conventional FFBC treatment and the proposed FFBC model is shown in Figure 5.18. The dashed line is related to the FFBC model. There is no considerable reduction in the iteration numbers for this case. This could be due to the strong reflections from the shock in the computational domain.

In Figures 5.19 and 5.20 the iso-Mach lines are illustrated for subsonic and transonic flows. The evolution of Mach number profiles for the subsonic flow is illustrated in Figures 5.21. These profiles show how the presence of a solid obstacle could affect the flow status at upstream and downstream far-field regions. Near the leading edge of the circular-arc the compressibility is high and Mach number is reduced, but on the upper flat wall the deviation from the far field state is negligible. Note that

by getting far away from the circular-arc, deflections are reduced.

Figures 5.22 and 5.23 show typical propagations of the outgoing wave fronts at the inflow and outflow boundaries of a reduced computational domain. In this Figures the values of the outgoing wave angles have been calculated during the convergence process at different grid points located on the inflow and outflow parts. At the first stages they have chaotic pattern but after a few time steps they become regulated. This is an important feature of measuring such variations near the FFBs. As it is seen the wave fronts hit the boundaries not at the right angles (unlike to the usual assumptions made in the past and was refered in section 5.2.2).

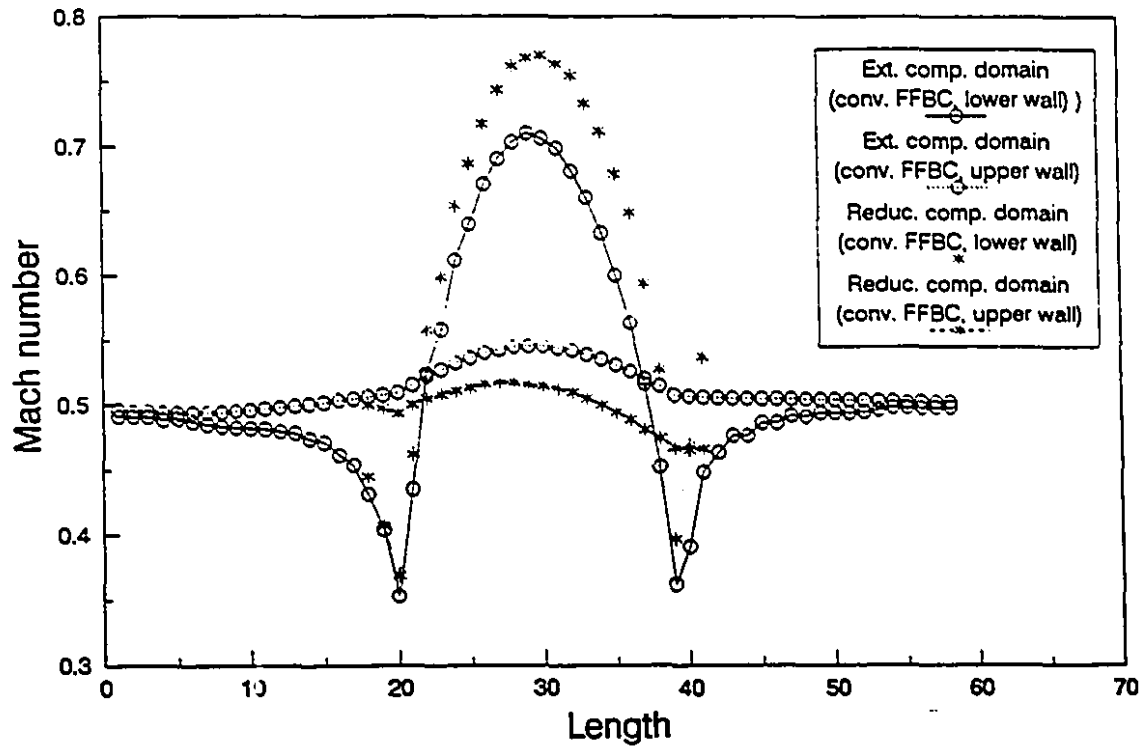


Figure 5.9: Comparison of upper and lower Mach numbers distributions for channel with circular arc 10%, obtained by conventional FFBC treatments for the extended and reduced computational domains. $M_\infty = 0.5$, CFL=3.

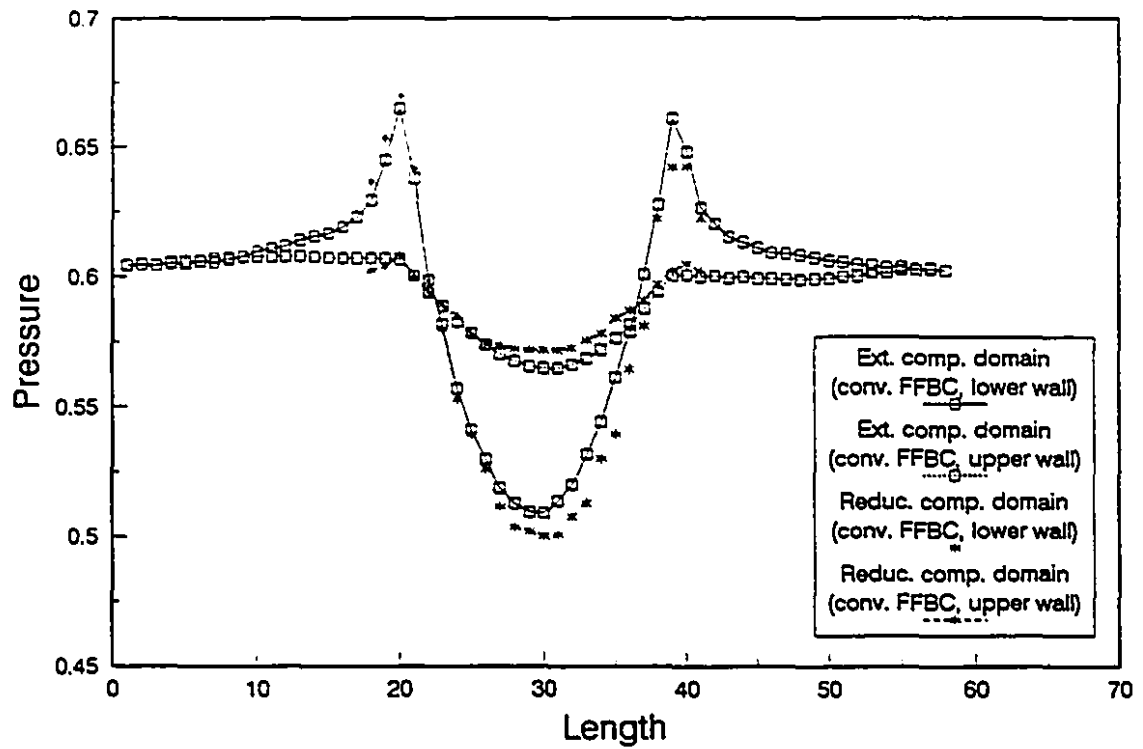


Figure 5.10: Comparison of upper and lower pressure distributions for the extended and reduced computational domains obtained by conventional FFBC treatment. $M_\infty = 0.5$, CFL=3.

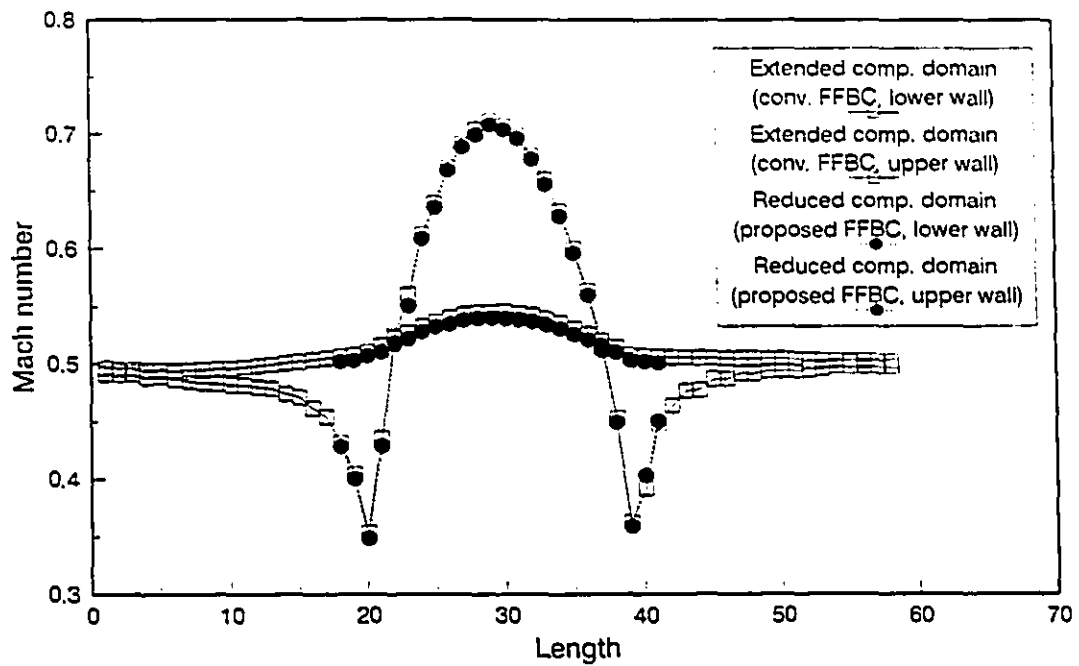


Figure 5.11: Comparison of upper and lower Mach numbers for a) Extended computational domain, conventional FFBC treatment, b) Reduced computational domain, proposed FFBC model. $M_\infty = 0.5$, CFL=3.

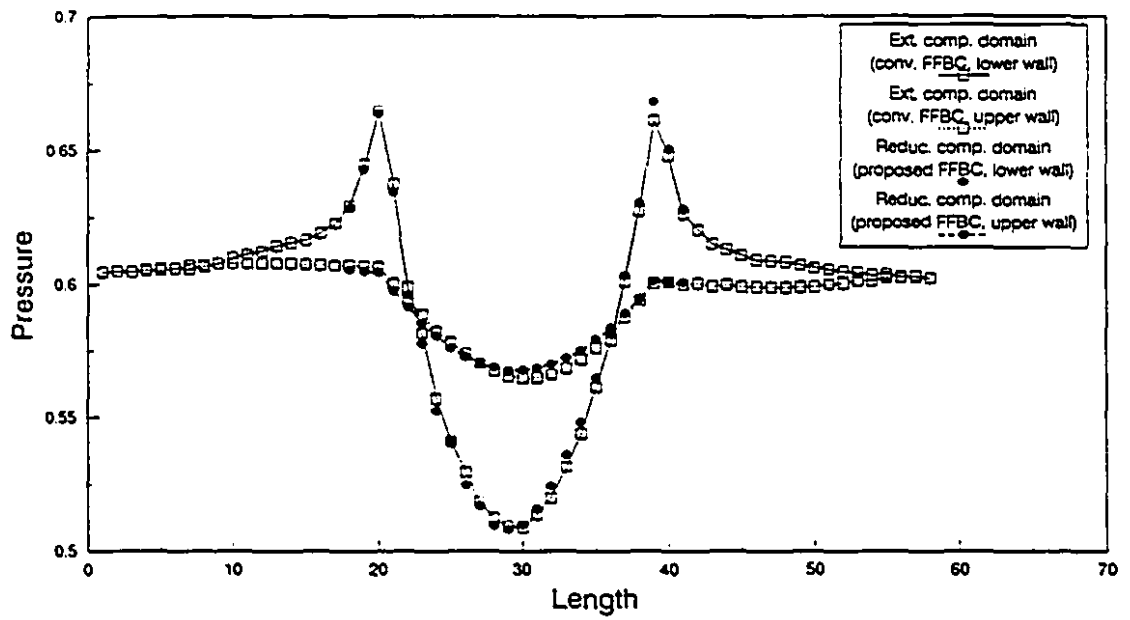


Figure 5.12: Comparisons of upper and lower pressures between the extended computational domain (conventional FFBC treatment) and reduced computational domain (proposed FFBC model). $M_\infty = 0.5$, $CFL=3$.

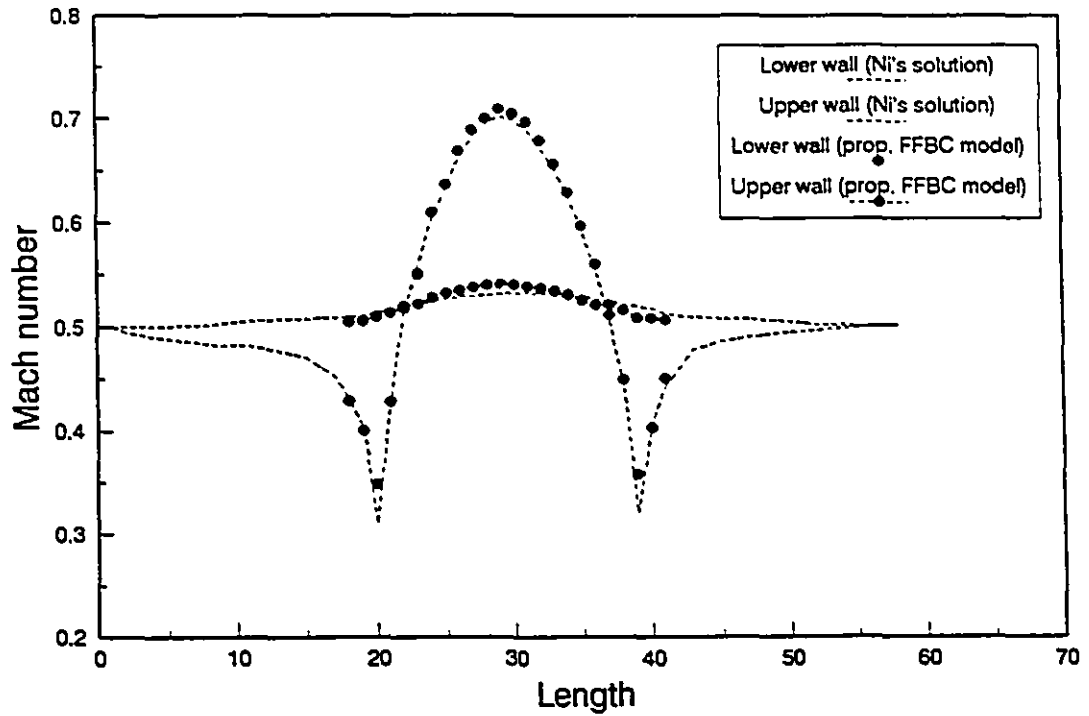


Figure 5.13: Comparisons of upper and lower wall Mach number distributions for the extended computational domain solution of Ni [107] and reduced computational domain (proposed FFBC model).

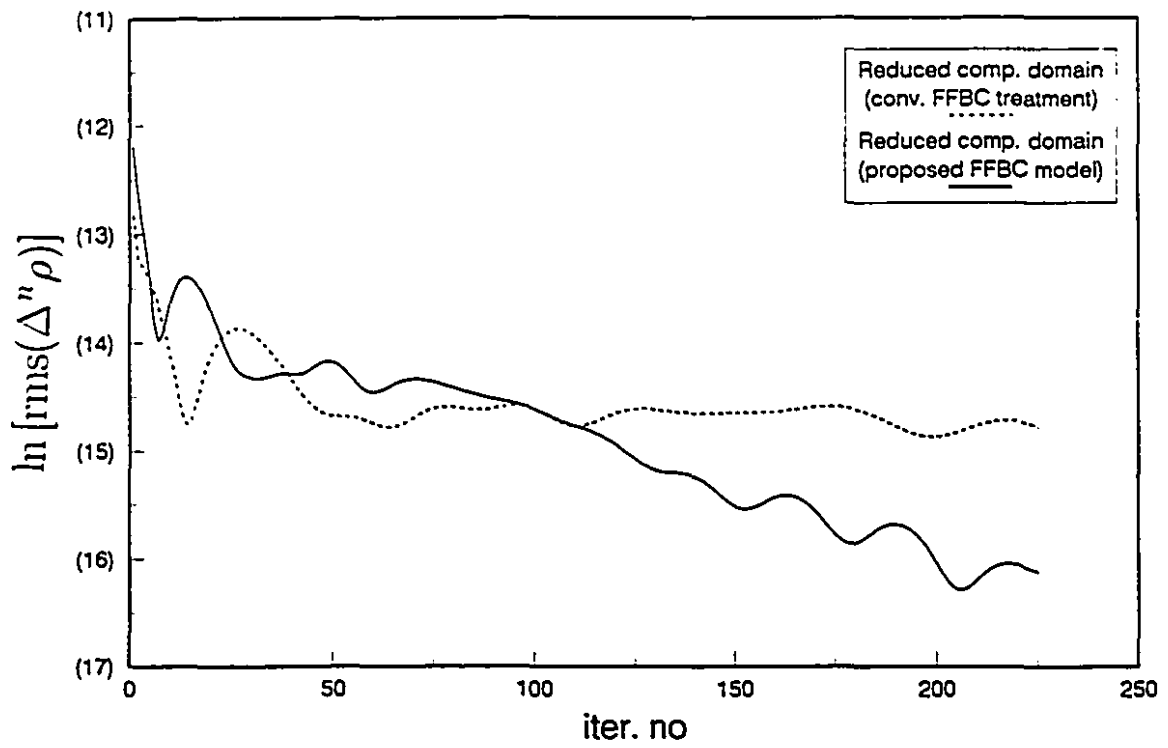


Figure 5.14: Convergence histories of extended and reduced computational domains, circular arc 10%. $M_\infty = 0.5$, CFL=3.

Note: () represents the negative values in figures.

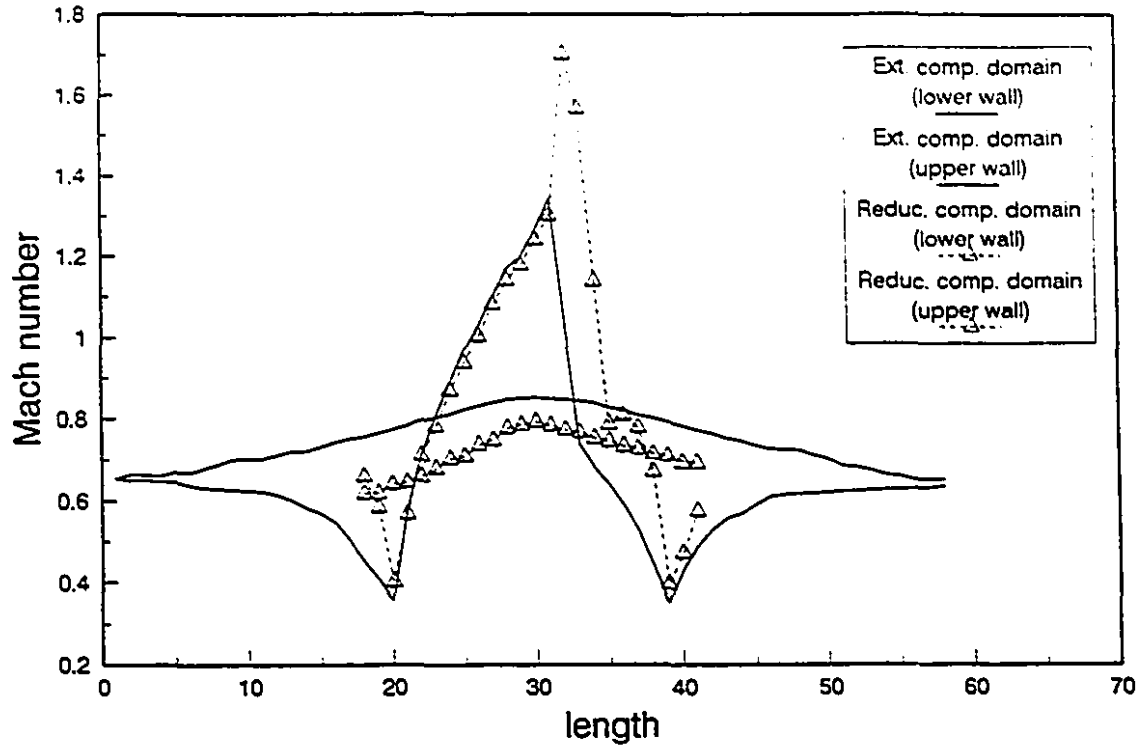


Figure 5.15: Mach number distributions for extended and reduced computational domains, channel with circular arc (10%), conventional FFBC treatments for both cases. $M_\infty = 0.675$, CFL=0.4.

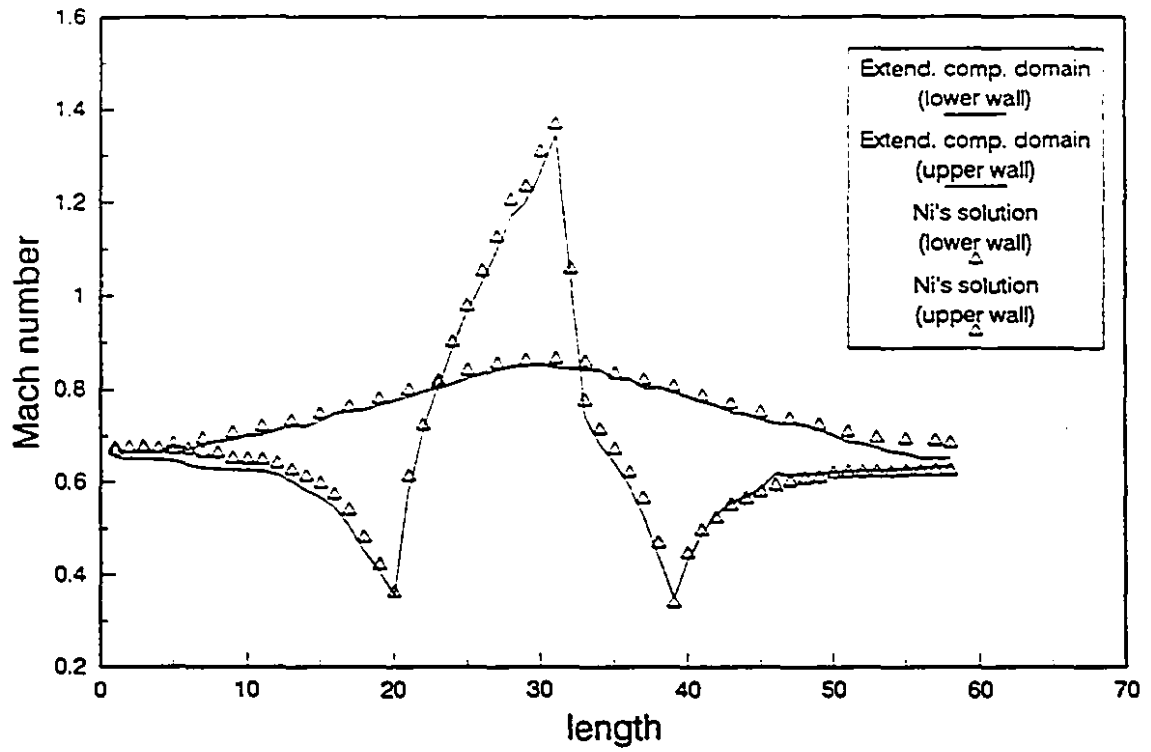


Figure 5.16: Mach number distribution for extended computational domain and the solution obtained by Ni [107], conventional FFBC treatment for extended computational domain. $M_\infty = 0.675$, CFL=0.4.

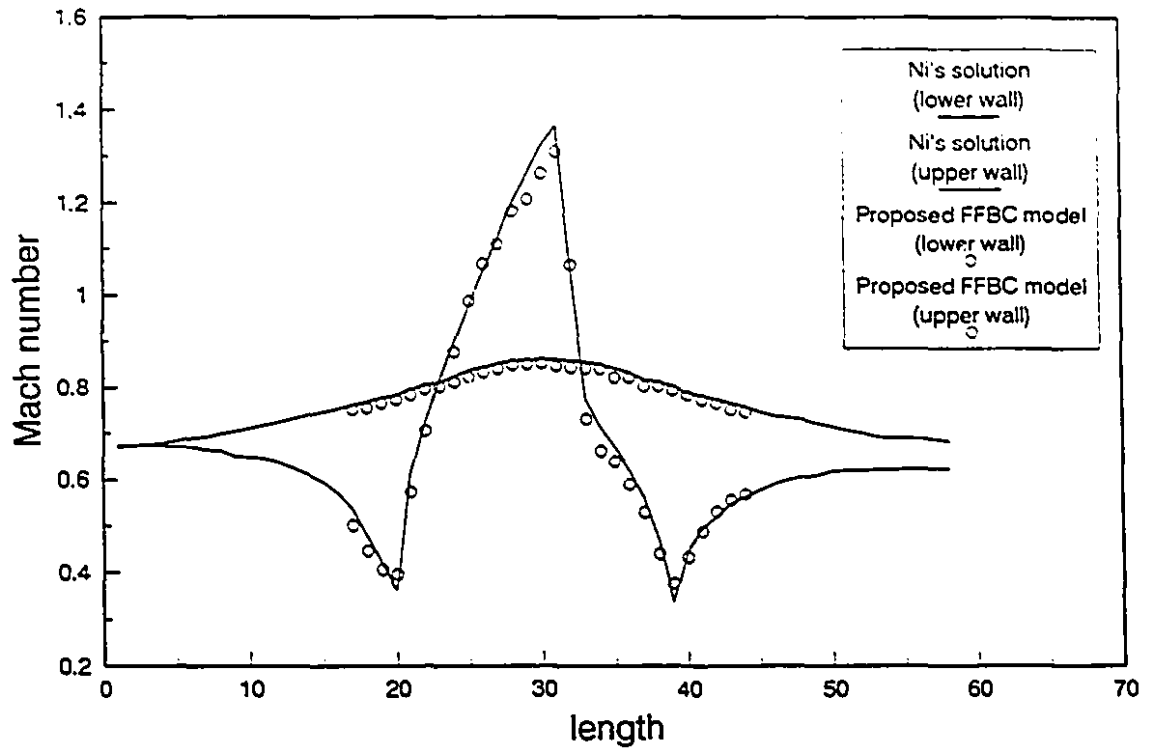


Figure 5.17: Mach number distribution for reduced computational domain with proposed FFBC model and the solution obtained by Ni [107]. $M_\infty = 0.675$, CFL=0.4.

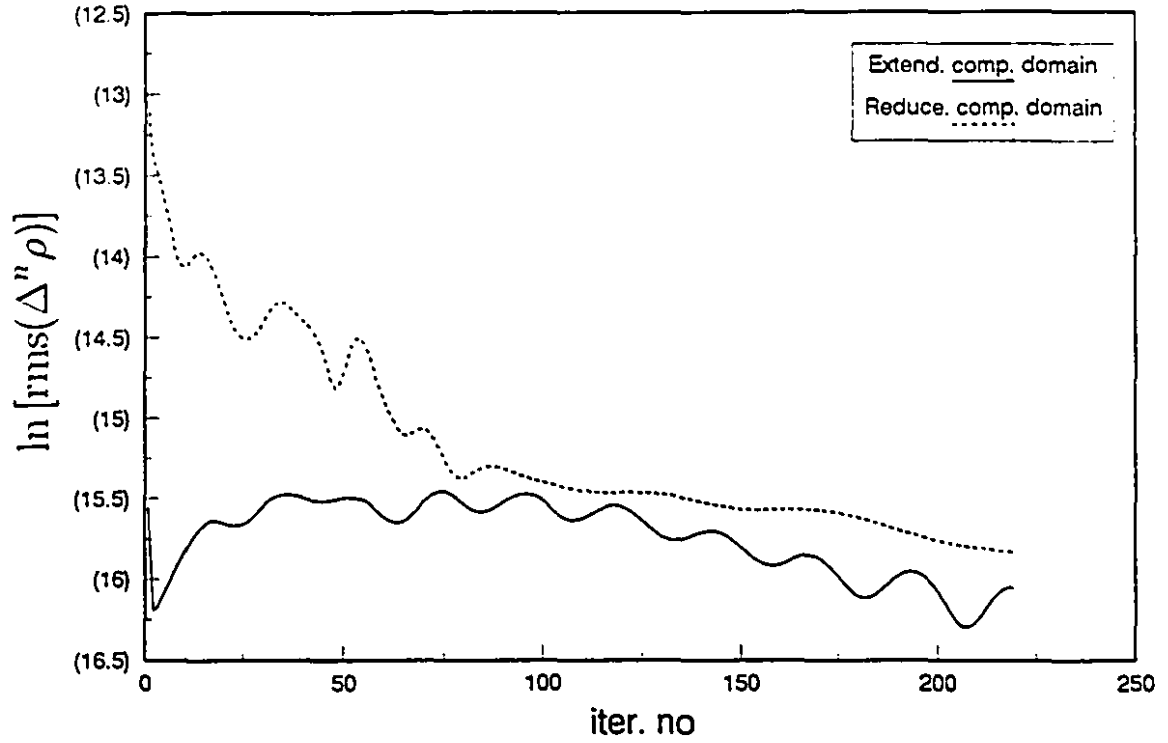


Figure 5.18: Convergence histories for the extended and reduced computational domains, effect of the proposed FFBC model, circular arc 10%. $M_\infty = 0.675$. CFL=0.4.

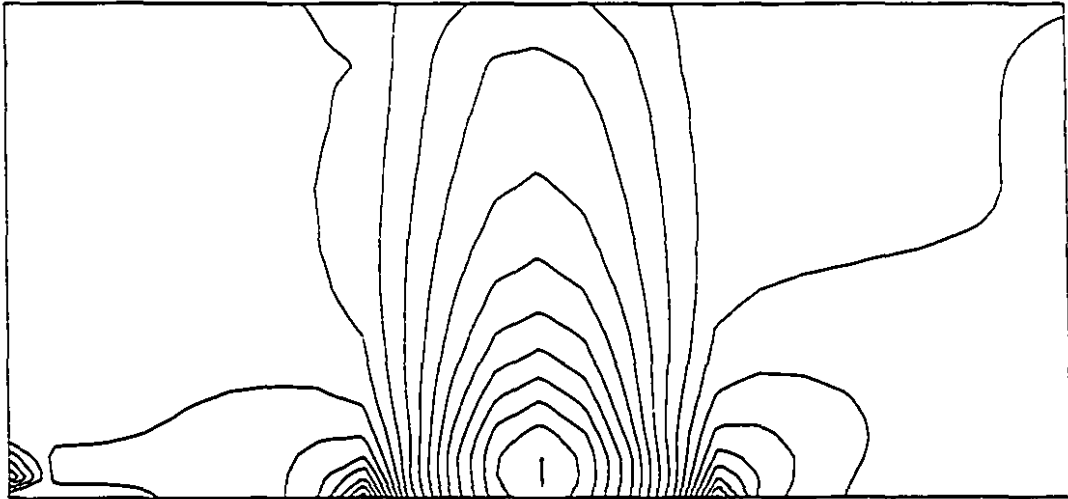


Figure 5.19: Mach number contours for the subsonic flow, circular arc 10%. $M_\infty = 0.5$, CFL=3.

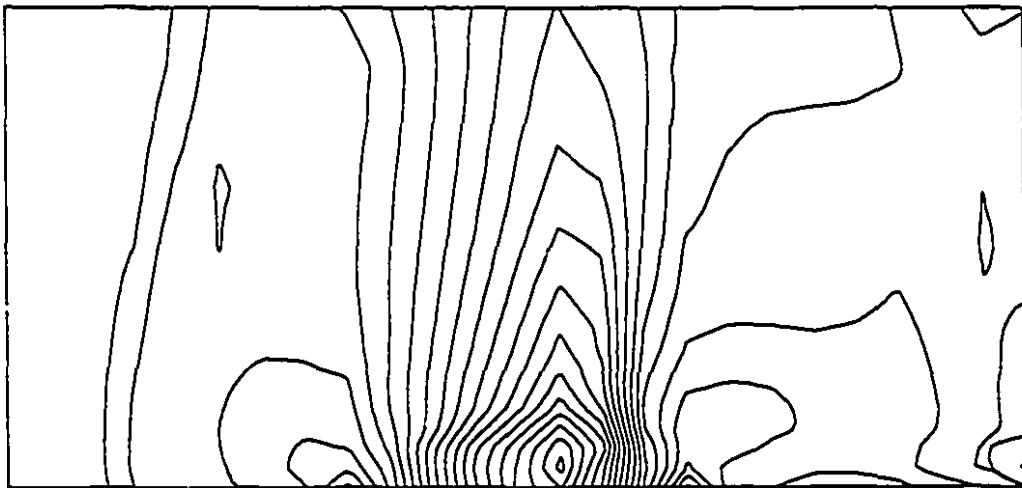


Figure 5.20: Mach number contours for the transonic flow, circular arc 10%. $M_\infty = 0.675$, CFL=0.4.

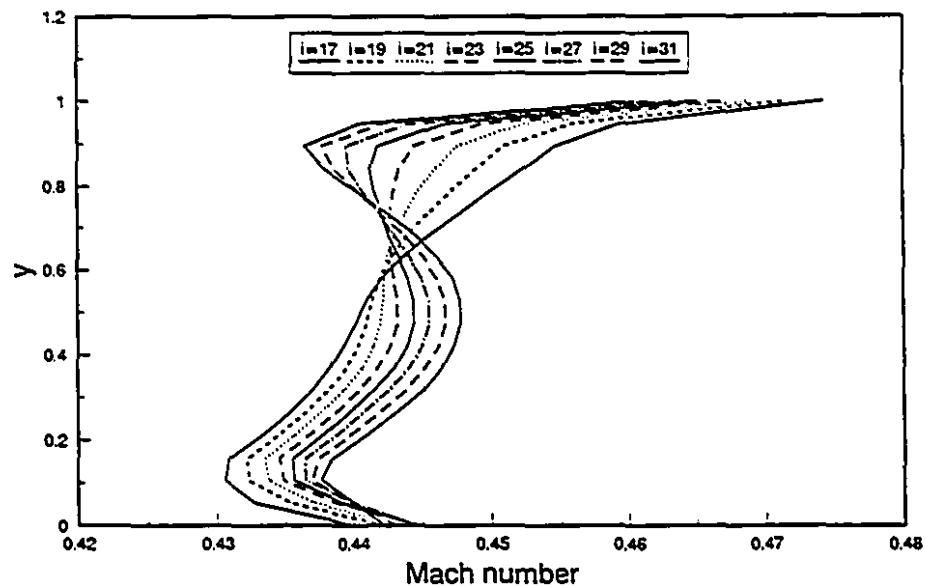
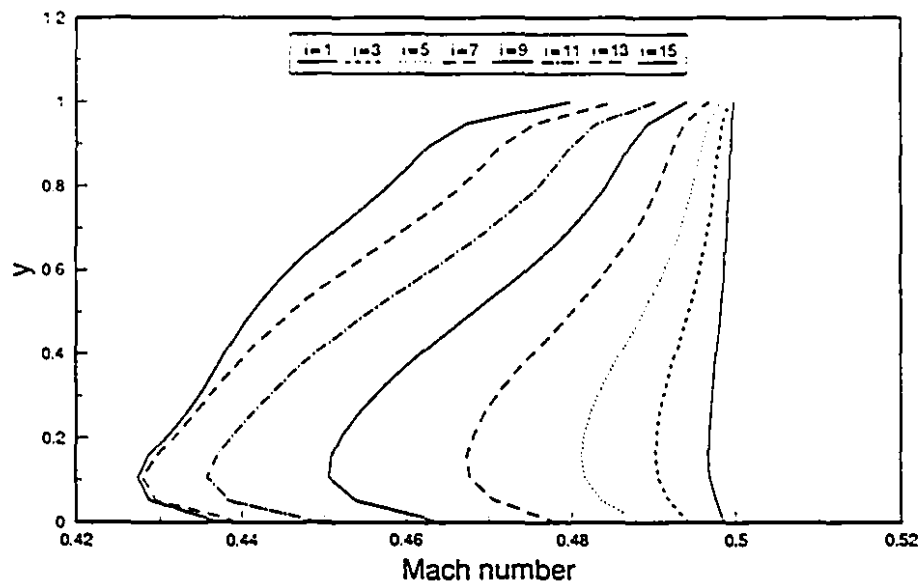


Figure 5.21: Mach number profiles at different longitudinal stations ($i = 1$ to 31) of the computational domain, subsonic flow, circular arc 10%. $M_\infty = 0.5$, CFL=2.2.

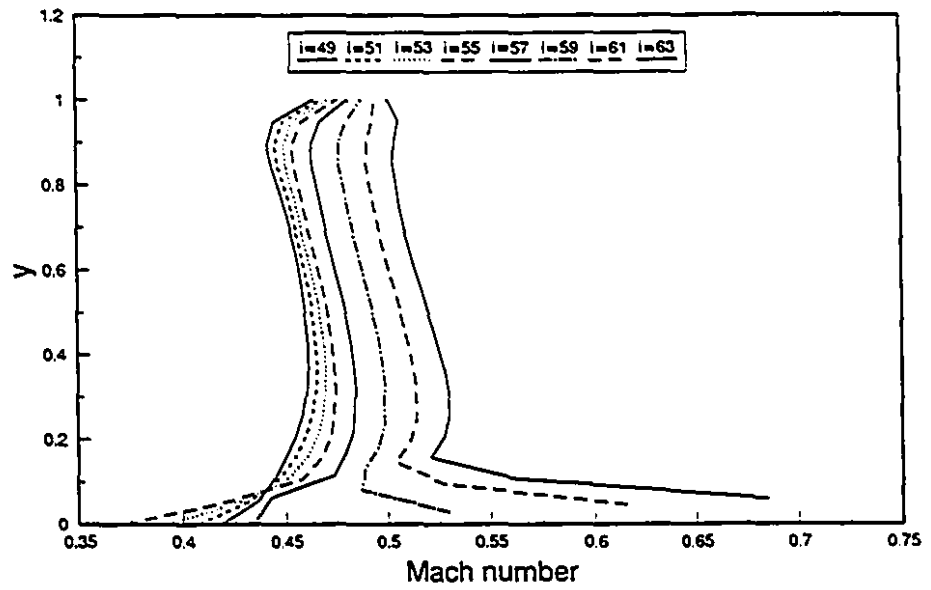
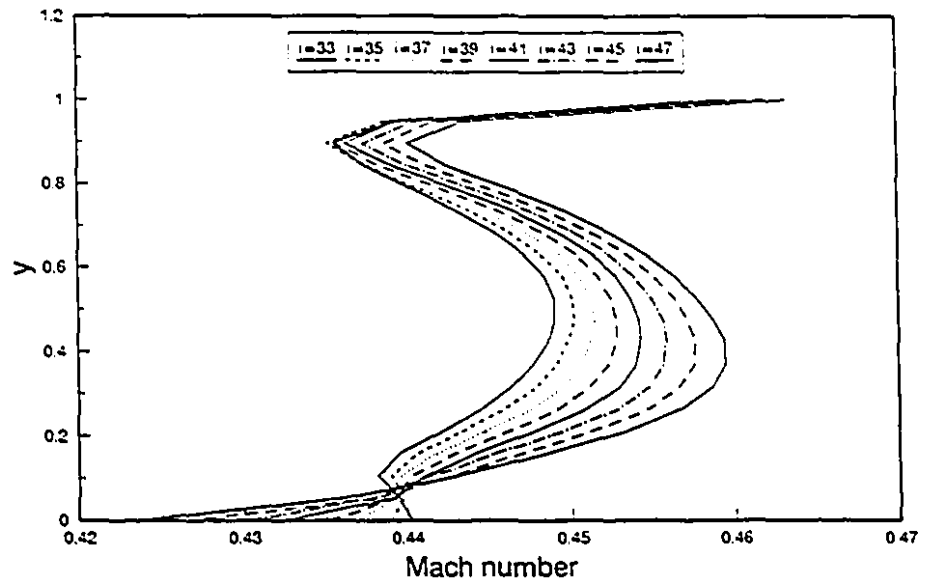


Figure 5.21: (Continued) Mach number profiles at different longitudinal stations ($i = 33$ to 63) of the computational domain, subsonic flow, circular arc 10%. $M_\infty = 0.5$, CFL=2.2.

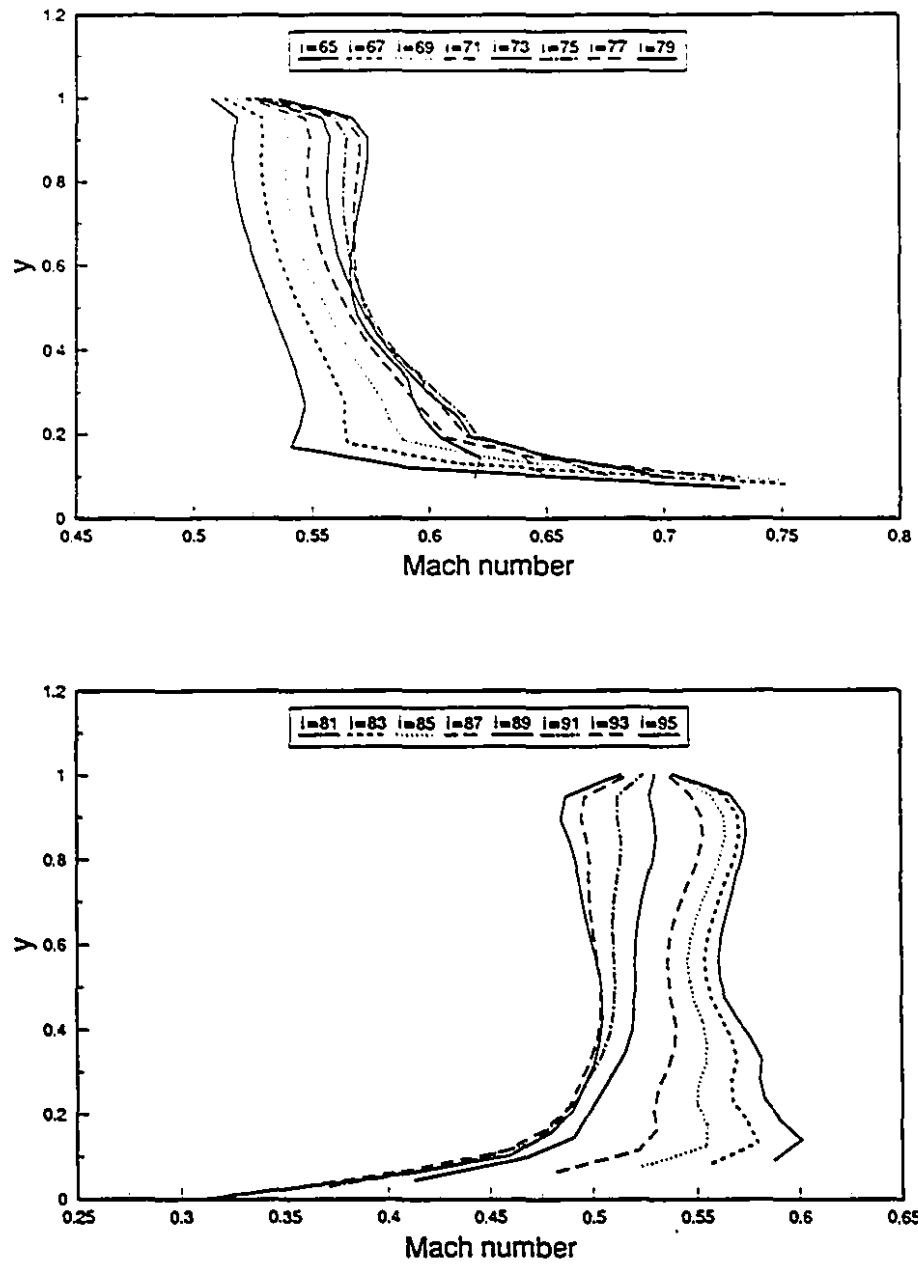


Figure 5.21: (Continued) Mach number profiles at different longitudinal stations ($i = 65$ to 95) of the computational domain, subsonic flow, circular arc 10%. $M_\infty = 0.5$, CFL=2.2.

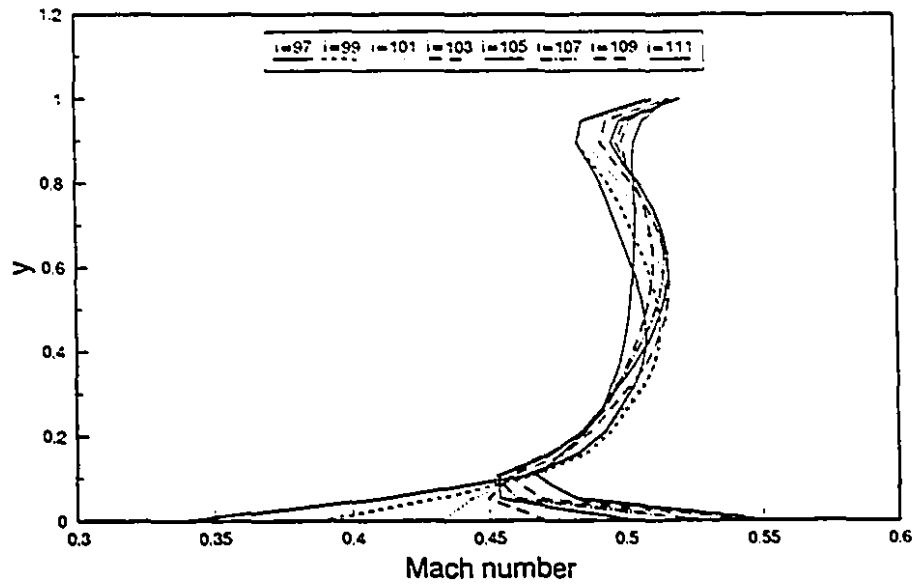


Figure 5.21: (Continued) Mach number profiles at different longitudinal stations ($i = 97$ to 111) of the computational domain, subsonic flow, circular arc 10%. $M_\infty = 0.5$, CFL=2.2.

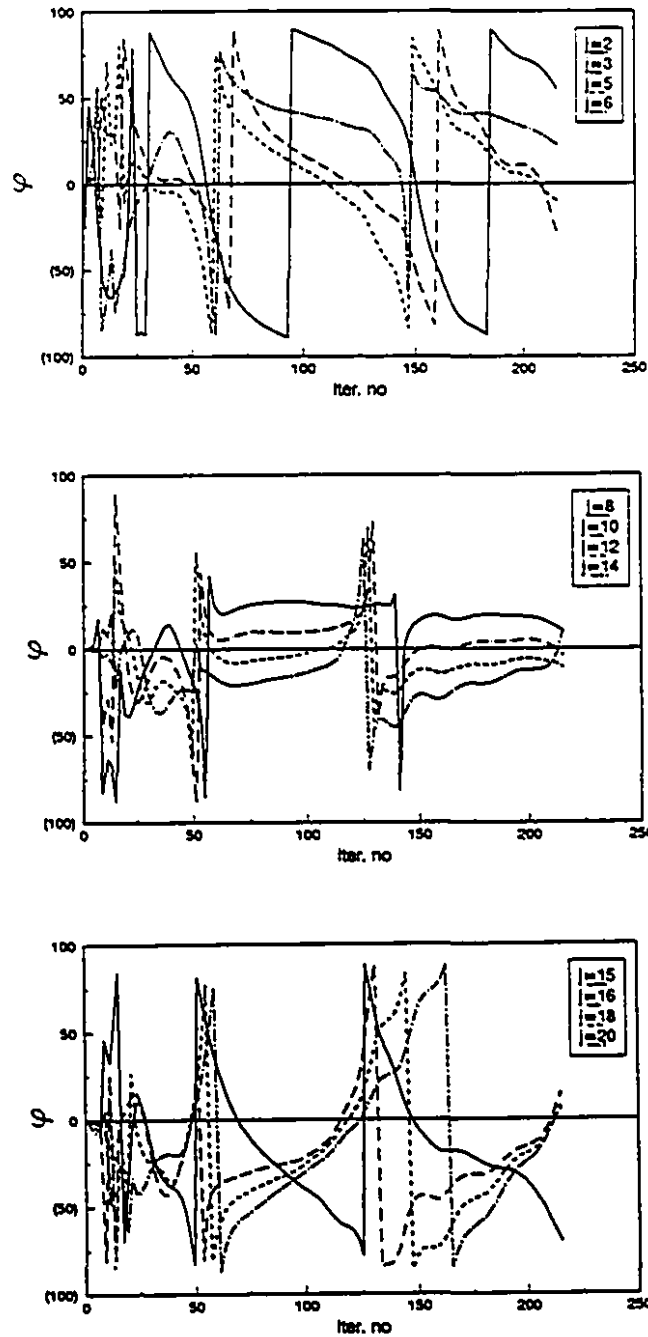


Figure 5.22: Propagation direction of the wave fronts during the time-integration process at an inflow FFB. confined flow with reduced computational domain, circular arc 10%. $M_\infty = 0.5$. CFL=2.

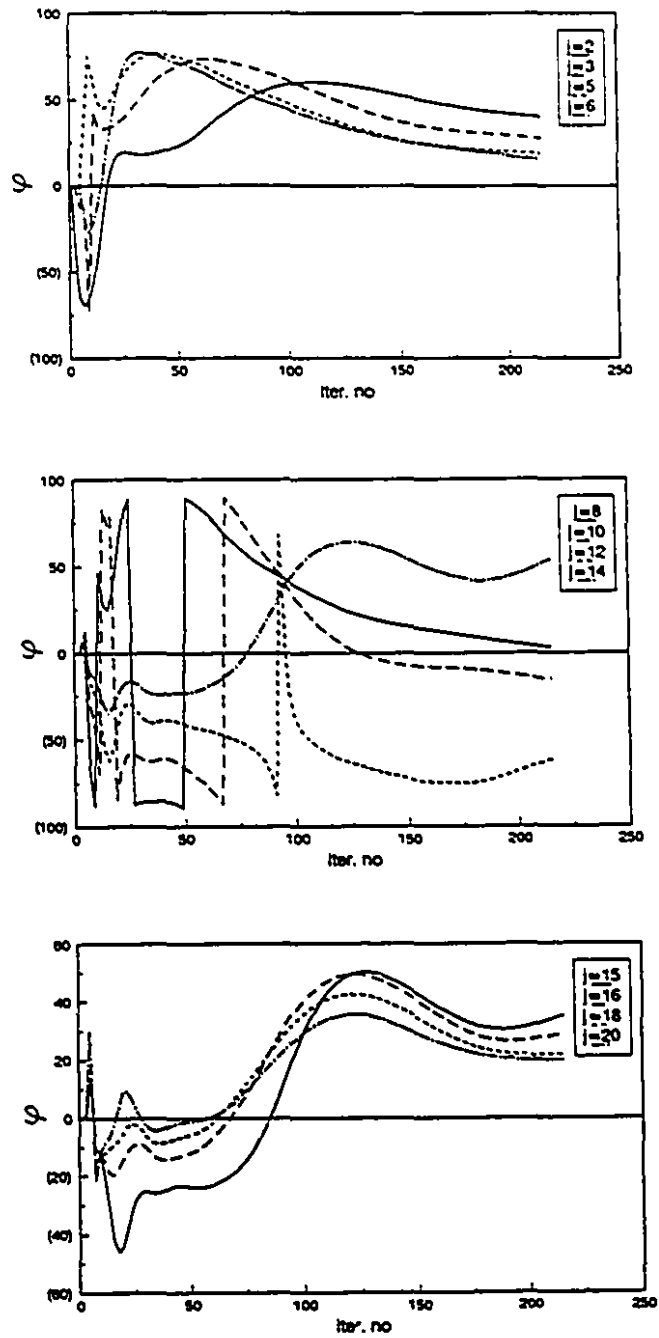


Figure 5.23: Propagation direction of the wave fronts during the time-integration process at an outflow FFB, confined flow with reduced computational domain, circular arc 10%. $M_\infty = 0.5$, CFL=2.

Chapter 6

Far Field Boundary Conditions for External Flows

6.1 Introduction

In this chapter the FFBC model developed for solving the confined flows is extended and used for the external flow problem. As in Chapter 5 the expanded Riemann variables are used in conjunction with the interpolation along the outgoing characteristics. The FFB was divided into horizontal and vertical parts, in which each part was treated by the methods developed in Chapter 5. The present FFBC model permitted the computational domain reduction while maintaining the solution accuracy. A comparative study was performed to verify the capability of the proposed FFBC model with respect to the conventional methods for subsonic and transonic flows. It was found that, further grid extension from the center of disturbance (airfoil) does not improve the solution accuracy, when the proposed FFBC model is used. In external aerodynamics, the FFB configuration depends on the grid type, which is mostly problem dependent. Here, a Cartesian type grid was used with the FFBC model.

6.2 Conventional far field boundary methods

In conventional methods of solving the external flows, the FFB is constructed with a body-fitted grid and extends sufficiently far from the airfoil surface (depending also on the grid topology). Such length scales are disproportioned with the small grid dimensions required near the airfoil to resolve the solution. This can be overcome either by using a large number of grid points, which leads to long execution times (also memory requirements), or extreme grid stretching, which leads to meshes of high aspect ratio and consequently lower accuracy.

The conventional methods discussed in Chapter 5 have also been applied to external flows with the difference that in the external flows the inflow and outflow ports should be distinguished prior to exploiting the FFBC methods. The small perturbation potential equation has been used in the past as the governing far field behavior [35, 80, 106, 136]. Due to the limited capability of linearized potential equation, it would not be appropriate for predicting the flows having large perturbations and also non-isentropic flows. The problem was analysed by using Fourier transforms without reporting computational results [47].

Many flow solvers use extended computational domains with simple FFBC treatments [68, 142, 143]. An O-type FFB is stretched about thirty chords thereby using the free-stream flow values or 1D characteristic equations (5.1) [69, 144]. The 1D treatment of FFB is not efficient and correct for multidimensional flows. Therefore, such 1D boundary conditions cannot be used in regions with even moderate distances from the airfoil, because of violating the flow behavior. It was shown that for lifting airfoils such approximations can generate inaccurate lift [136]. Recently, a method have been developed by Verhoff *et al* [149, 150] which uses a C-grid for solving the flow over an airfoil and is not flexible to be applied in arbitrary FFB topologies (see also Chapter 1).

In the following sections the FFBC model of Chapter 5 is modified for the external flow problem: This model alleviates the one dimensionality assumption which

is present in the previous works in this area.

6.3 Boundary condition development

The flow field disturbances generated by an airfoil at subsonic and transonic free-stream Mach numbers extend outward to large distances from the airfoil surface (around 20 chords for steady flow and more than that in the unsteady case). For supersonic free-stream, the domain of dependence is considerably reduced and, consequently, the size of the computational domain is reduced relative to that of subsonic flow. Therefore supersonic FFBs do not demand a special type of treatment.

In 1D problems, the task of distinguishing the incoming and outgoing disturbances is straightforward. However, in multidimensional external flows, it is complicated as the perturbation waves may propagate in a multitude of directions (discussed in Chapter 2). In either case the characteristic field decomposition is necessary for a consistent FFBC modelling. First, the FFBCs of isentropic flows are worked out, then the formulation is modified for the non-isentropic flows.

In order to model the FFBCs for the external flow problem (airfoil with zero angle of attack), the Riemann variable formulations of the Euler equations from Chapter 5 (equations (5.7)) are used

$$\begin{aligned}\frac{\partial R}{\partial t} + (\alpha R + \beta Q) \left(\cos \theta \frac{\partial R}{\partial x} + \sin \theta \frac{\partial R}{\partial y} \right) &= \mathcal{F}(R, Q, \theta), \\ \frac{\partial Q}{\partial t} + (\beta R + \alpha Q) \left(\cos \theta \frac{\partial Q}{\partial x} + \sin \theta \frac{\partial Q}{\partial y} \right) &= -\mathcal{F}(R, Q, \theta), \\ \frac{\partial \theta}{\partial t} + \frac{R + Q}{2} \left(\cos \theta \frac{\partial \theta}{\partial x} + \sin \theta \frac{\partial \theta}{\partial y} \right) &= \mathcal{G}(R, Q, \theta).\end{aligned}\quad (6.1)$$

where

$$\begin{aligned}\mathcal{F}(R, Q, \theta) &= -\frac{\gamma-1}{8} (R^2 - Q^2) \left(-\sin \theta \frac{\partial \theta}{\partial x} + \cos \theta \frac{\partial \theta}{\partial y} \right), \\ \mathcal{G}(R, Q, \theta) &= -\frac{\gamma-1}{4} \frac{R-Q}{R+Q} \left(-\sin \theta \frac{\partial (R-Q)}{\partial x} + \cos \theta \frac{\partial (R-Q)}{\partial y} \right).\end{aligned}$$

Equations (6.1) in the transformed form express the propagation of the information in Cartesian coordinate system as was used in Chapter 5.

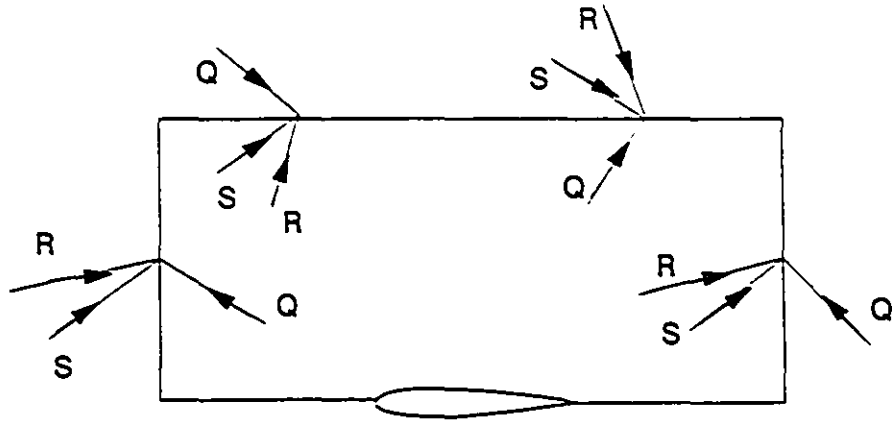


Figure 6.1: Propagations of the Riemann variables and entropy waves at the FFB of the external flow.

In Figure 6.1 the propagations of the Riemann variables and entropy waves at different positions of the FFB are shown. The directions of propagations may vary on the horizontal FFB. Unlike the confined flow case the horizontal part of the FFB needs modelling, especially, along the horizontal FFB (Figure 6.1), when the Riemann variables change direction. The flow perturbations and numerical disturbances travel in an unconstrained manner until they hit the FFB. Dissimilar to internal flows, there are no physical restraints except the artificially made FFB. For external flow problems the inflow and outflow parts of the FFB are not completely distinct in contrast to the confined flows. The grids located on the FFB can intermittently be changed into inflow and outflow during the transient time integration (Figure 6.2). For low frequency disturbances, where the disturbance wavelength is of order of a few chords, a large grid spacing may reflect the outgoing waves [7, 161].

In the following sections the FFBC models for treating the vertical and horizontal parts of the FFB will be introduced. For more details, one is referred to Chapter 5.

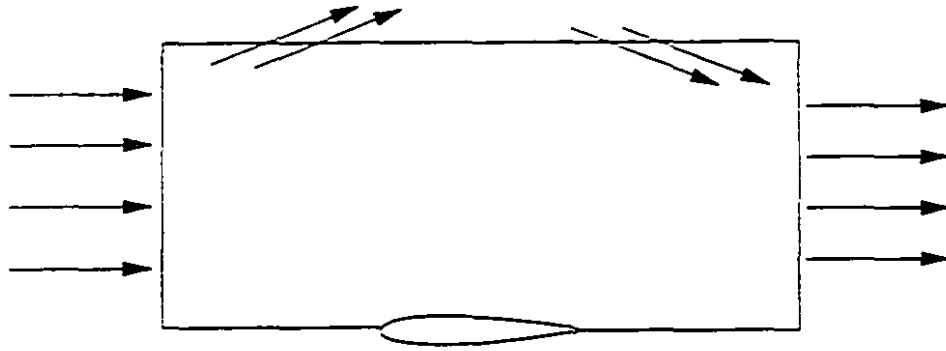


Figure 6.2: Inflow and outflow parts of the FFB at a certain time level.

6.3.1 Expanded Riemann variables approach

In the present study the FFB is divided into vertical and horizontal parts. For symmetric flow the computational domain would contain a symmetry line, two vertical and one horizontal FFB parts. For inviscid flow cases the symmetry line is treated as a solid boundary. The expanded Riemann variables are used, based on the main flow direction and along the normal to that direction for different parts of the FFB. Similar to confined flows, it is assumed that at distances far from the solid boundary, the perturbations would decay to zero. For the vertical parts of the FFB (clearly inflow or outflow) they expressed as

$$\begin{aligned}
 R(x, y, t) &= R_\infty + \sum_{k=1}^m R_k(y, t) \epsilon_k(x), \\
 Q(x, y, t) &= Q_\infty + \sum_{k=1}^m Q_k(y, t) \epsilon_k(x), \\
 \theta(x, y, t) &= \theta_\infty + \sum_{k=1}^m \theta_k(y, t) \epsilon_k(x),
 \end{aligned} \tag{6.2}$$

where $\epsilon_k(x) = e^{-kx}$ and ω are indicated in Chapter 5, and $\theta_\infty = 0$ for nonlifting airfoils. The free-stream Riemann variables are

$$R_\infty = u_\infty + \frac{2}{\gamma - 1} a_\infty, \quad Q_\infty = u_\infty - \frac{2}{\gamma - 1} a_\infty.$$

Introducing the expansions (6.2) into the equations (6.1) would result in the following first-order perturbation equations

$$\frac{\partial R_1}{\partial t} + (\alpha R_\infty + \beta Q_\infty) \left(\omega R_1 \cos \theta + \frac{\partial R_1}{\partial y} \sin \theta \right) = \tilde{\mathcal{F}}(\theta, \theta_1), \quad (6.3)$$

$$\frac{\partial Q_1}{\partial t} + (\beta R_\infty + \alpha Q_\infty) \left(-\omega Q_1 \cos \theta - \frac{\partial Q_1}{\partial y} \sin \theta \right) = -\tilde{\mathcal{F}}(\theta, \theta_1), \quad (6.4)$$

$$\frac{\partial \theta_1}{\partial t} + \frac{1}{2} (R_\infty + Q_\infty) \left(-\omega \theta_1 \cos \theta + \frac{\partial \theta_1}{\partial y} \sin \theta \right) = \tilde{\mathcal{G}}(R_1, Q_1, \theta, \theta_1), \quad (6.5)$$

where

$$\begin{aligned} \tilde{\mathcal{F}}(\theta, \theta_1) &= -\frac{\gamma-1}{S} (R_\infty^2 - Q_\infty^2) \left[-\omega \theta_1 \sin \theta + \frac{\partial \theta_1}{\partial y} \cos \theta \right], \\ \tilde{\mathcal{G}}(R_1, Q_1, \theta, \theta_1) &= -\frac{\gamma-1}{4} \frac{R_\infty - Q_\infty}{R_\infty + Q_\infty} \left[-\omega (R_1 - Q_1) \sin \theta - \frac{\partial (R_1 - Q_1)}{\partial y} \cos \theta \right]. \end{aligned}$$

For horizontal part of the FFB, Riemann variables are expanded in a similar manner to the vertical parts

$$\begin{aligned} R(x, y, t) &= R_\infty + \sum_{k=1}^m \tilde{R}_k(x, t) \tilde{\epsilon}_k(y), \\ Q(x, y, t) &= Q_\infty + \sum_{k=1}^m \tilde{Q}_k(x, t) \tilde{\epsilon}_k(y), \\ \theta(x, y, t) &= \theta_\infty + \sum_{k=1}^m \tilde{\theta}_k(x, t) \tilde{\epsilon}_k(y), \end{aligned} \quad (6.6)$$

where $\tilde{\epsilon}_k(y) = e^{-k\omega y}$ and $\theta_\infty = 0$. In a similar manner, when the expansions (6.6) are introduced into the equations (6.1), results in the first-order far-field perturbation equations

$$\frac{\partial \tilde{R}_1}{\partial t} + (\alpha R_\infty + \beta Q_\infty) \left(\tilde{\omega} \tilde{R}_1 \sin \theta + \frac{\partial \tilde{R}_1}{\partial x} \cos \theta \right) = \tilde{\mathcal{F}}(\theta, \tilde{\theta}_1), \quad (6.7)$$

$$\frac{\partial \tilde{Q}_1}{\partial t} + (\beta R_\infty + \alpha Q_\infty) \left(\tilde{\omega} \tilde{Q}_1 \cos \theta + \frac{\partial \tilde{Q}_1}{\partial x} \cos \theta \right) = -\tilde{\mathcal{F}}(\theta, \tilde{\theta}_1), \quad (6.8)$$

$$\frac{\partial \tilde{\theta}_1}{\partial t} + \frac{1}{2} (R_\infty + Q_\infty) \left(\tilde{\omega} \tilde{\theta}_1 \sin \theta + \frac{\partial \tilde{\theta}_1}{\partial x} \cos \theta \right) = \tilde{\mathcal{G}}(\tilde{R}_1, \tilde{Q}_1, \theta, \tilde{\theta}_1), \quad (6.9)$$

where

$$\begin{aligned}\tilde{\mathcal{F}}(\theta, \tilde{\theta}_1) &= -\frac{\gamma-1}{8}(R_\infty^2 - Q_\infty^2) \left(\tilde{\omega} \tilde{\theta}_1 \sin \theta + \frac{\partial \tilde{\theta}_1}{\partial x} \cos \theta \right), \\ \tilde{\mathcal{G}}(\tilde{R}_1, \tilde{Q}_1, \theta, \tilde{\theta}_1) &= \frac{R_\infty - Q_\infty}{R_\infty + Q_\infty} \left(\tilde{\omega}(\tilde{R}_1 - \tilde{Q}_1) \cos \theta - \frac{\partial(\tilde{R}_1 - \tilde{Q}_1)}{\partial x} \sin \theta \right).\end{aligned}$$

To treat the horizontal FFB, first it is checked at each grid point if it is either an inflow or outflow boundary (corresponding to $v < 0$ or $v > 0$). When $v = 0$, there is no flux through that node and the BC is determined from the neighboring nodes. At the vertical FFBs (similar to the inlet and outlet of the confined flow), the perturbations propagate from the computational domain towards the boundary along outgoing characteristic fronts, in which the local flow information is obtained by using equation (5.25). On the other hand for horizontal FFB, the perturbations propagate nearly along the normal to streamlines. Then, at vertical FFBs, one gets from equations (5.16) for $\theta_g = \frac{\pi}{2}$ as

$$R_{\perp b} = R_u, \quad Q_{\perp b} = -Q_u, \quad (6.10)$$

and for horizontal FFB ($\theta_g = 0$)

$$R_{\perp b} = -Q_v, \quad Q_{\perp b} = R_v. \quad (6.11)$$

In Figure 6.3 the propagations of the Riemann variables at inflow and outflow FFBs are shown. In each case the outgoing waves directions were calculated from the relation (2.71).

6.4 Inflow FFBC formulation

At the vertical FFBs, the perturbation equations (6.3) and (6.5) are solved by an explicit time discretization similar to the confined flow problem. The implicit methods could be used for this purpose which demand solving tridiagonal systems, increasing the computational effort. At the horizontal inflow FFB, equations (6.7) and (6.9) are integrated during the transient time. The information from the numerical solution of

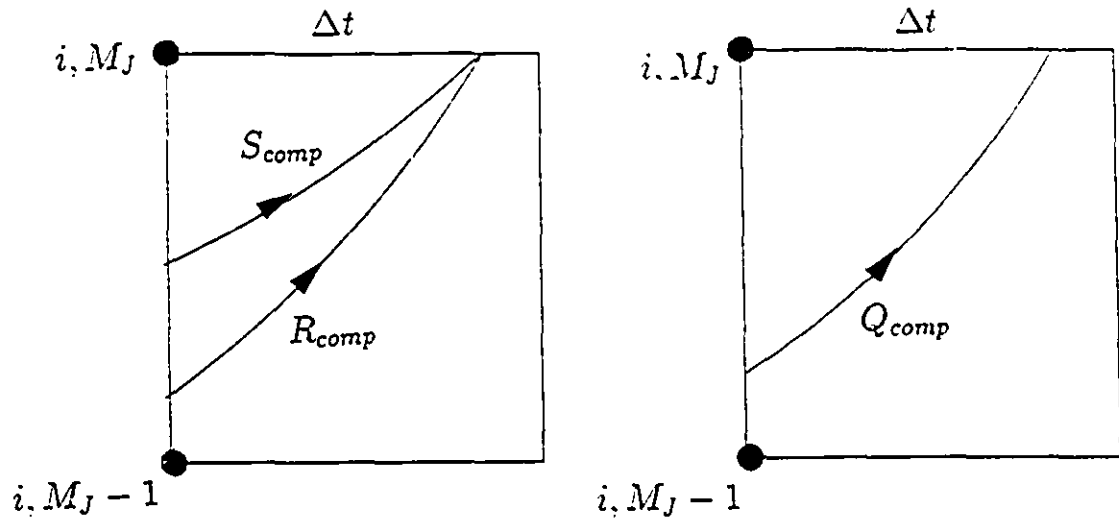


Figure 6.3: Propagations of the outgoing waves at horizontal outflow and inflow FFBs.

computational domain is locally obtained by using the characteristics similar to that discussed in Chapter 5. At supersonic inflow FFBs, all the free-stream flow variables are specified consistently with the characteristic directions of propagation.

6.5 Outflow FFBC formulation

Outflow boundaries in the Cartesian FFB involve the vertical and horizontal parts. Equations (6.4) and (6.8) are integrated at the vertical and horizontal outflow FFBs respectively. For calculating the information from the numerical solution there are two possibilities: algebraic extrapolation and interpolation along characteristic lines (see appendix F). In practice, interpolation along the right-propagating characteristic generated accurate solutions. At a supersonic outflow FFB, based on the characteristic theory, every flow variable is calculated from the computational domain.

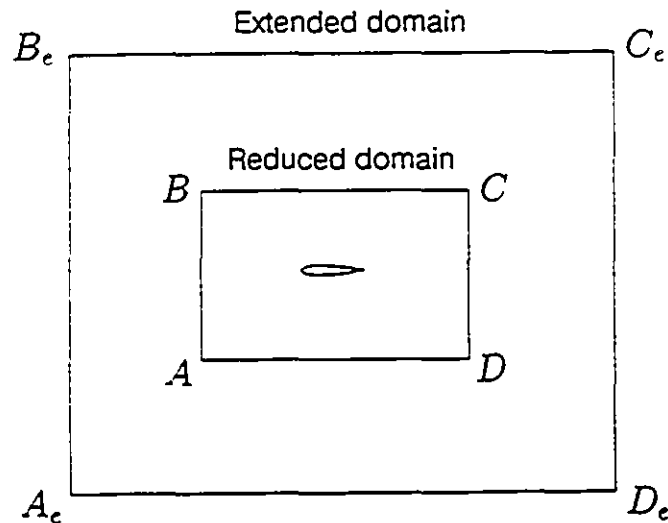


Figure 6.4: Extended and reduced domain configurations for solving the external flow problem.

6.6 Discretization of the far field equations

Perturbation equations which were resulted for the FFBs are discretized similar to the ones in confined flows. Time derivatives are approximated by forward differencing, while spatial derivatives are approximated by central differencing. The vertical FFBs are naturally separated into inflow and outflow parts (namely AB and CD in Figure 6.4). For horizontal parts (AD and BC), one needs to separate the inflow and outflow portions. This is done by considering the fact that, at inflow parts the v -component of the flow velocity is directed inward the computational domain, while at outflow it is reverse. Note that v -component of the velocity is perpendicular to the horizontal FFB. For an O -type outer boundary the velocity vector should be projected along the normal to the outer boundary (see section 5.4).

The outgoing information is interpolated along the outgoing bicharacteristics as confined flow case (see equation (5.25)). Explicit time differencing was used for solving the first-order perturbation equations (6.3)- (6.5) and (6.7)- (6.9).

6.7 Non-isentropic outflow FFBC

For non-isentropic flow crossing the outflow FFBC, the equations are based on the expansions of the modified Riemann variables (was derived in Chapter 5); it takes into account the entropy variations after shock wave and along the normal to the streamline direction. For non-isentropic external flows, the inflow FFBCs are still valid (section 4.5 Chapter 4). For treating the outflow FFBC of a non-isentropic flow over the airfoil, the first-order perturbation equation (5.41) is used

$$\frac{\partial Q_1}{\partial t} + (\beta R_\infty + \alpha Q_\infty) \left[\omega Q_1 \cos \theta + \frac{\partial Q_1}{\partial y} \sin \theta \right] = \frac{\gamma - 1}{8} (\kappa_\infty T_1 + T_2),$$

where T_1 and T_2 are defined in section 5.6. For the airfoil problem with zero incidence, the non-isentropic flow crosses the outflow FFBC at right vertical side (CD in Figure 6.4). Therefore, the above equation is solved numerically along the outflow FFBC.

6.8 Model validation and discussion

In order to compare the effect of conventional FFBC methods and the proposed FFBC model for external flows, the NACA 0012 airfoil (with zero angle of attack) was used. A Cartesian grid was generated considering the flow symmetry. Therefore, the calculations were performed for half domain. The grids were generated starting at the airfoil surface, which is located at the middle of the symmetry line. Equally-spaced grids were used along the chord direction (or symmetry line), while they were stretched along y -direction, starting from the airfoil surface. In the numerical tests, two kinds of domains were used, namely extended and reduced (Figure 6.4). The extended domain consisted of 175×50 grids, accommodated within 7 chords \times 6 chords along the x and y directions respectively. The reduced domain had the dimension of 63×17 grids, placed within 2.5 chords \times 1 chord.

The numerical solutions which were for the reduced computational domain, generated by the proposed FFBC model are compared with the solutions of Schmidt and

Jameson [134] for flows over a NACA 0012 airfoil with zero incidence. As in previous chapters, the subsonic and transonic cases with Mach numbers $M_\infty = 0.6$ and $M_\infty = 0.8$ are considered. Applying the proposed FFBC model allows a substantial reduction of grid points in both x and y directions. Numerical experiments showed that domain reduction along the x -direction affects the solutions more than domain reduction along the y -direction. The Mach number and pressure coefficients of subsonic and transonic flows have been chosen in order to demonstrate the ability of the proposed FFBC models in comparison to the conventional methods of boundary treatment. When the proposed FFBC model for calculating the flow around NACA 0012 airfoil was used, the sizes of block tridiagonal matrices were reduced by a factor of $\frac{1}{N_\xi \times chord}$ along ξ -sweep and $\frac{1}{N_\eta \times chord}$ along η -sweep. Where N_ξ and N_η are integer numbers showing the computational domain extensions along the ξ and η directions respectively.

Figure 6.5 shows the Mach number distributions for subsonic flow over the airfoil with zero incidence. When the conventional FFBC methods were applied at the inflow and outflow FFBCs of a reduced computational domain it generated inaccurate solution in comparison to the solution obtained from the extended computational domain, as shown in Figure 6.5. This is because the conventional FFBC methods (either algebraic extrapolation or one-dimensional characteristic approach) give rise to the reflections from the FFBCs. Also the effect of flow inclination crossing the inflow boundary has been neglected in the conventional FFBC methods. Therefore, conventional FFBC methods are not capable of handling the flow inclination near the boundary.

Pressure distributions on the airfoil for the case of Figure 6.5 are shown in Figure 6.6. The difference in the pressure coefficient, $C_p = (\frac{p}{p_\infty} - 1)/(\frac{\gamma}{2}M_\infty^2)$ follows somehow a different pattern than the Mach number and the discrepancies are larger.

In Figure 6.7 the comparisons were made between the Mach number distributions obtained with the proposed FFBC model for the reduced computational domain and with conventional FFBC method for the extended computational domain. There is good agreement between these solutions. Note that the number of grid points has

been decreased by $\frac{175 \times 50}{63 \times 17} \approx 8$ times for the reduced computational domain.

Figure 6.8 demonstrates the pressure coefficients on the airfoil obtained by Jameson *et al* [71] and by implementing the proposed FFBC model. A fair agreement is observed except at the leading and trailing edges. This is because in the present flow-field solver the grid points are equally distributed along the chord direction.

The convergence histories are shown in Figures 6.9 and 6.10 for the extended computational domain with the conventional FFBC treatment and for the reduced computational domain with the proposed FFBC model.

Figure 6.11 depicts the Mach number distributions for the transonic flow case obtained with the conventional FFBC method. It is noted that the reduction in domain size is performed without altering the grid spacing.

Comparison was made with the solution of Jameson *et al* in Figure 6.12 in order to validate the solutions obtained by the present flow field solver. The differences are due to the grid type and numerical scheme.

The Mach number distribution resulted from a reduced computational domain (with proposed FFBC model) is compared against the extended domain solution within Figure 6.13. A small amount of pre-shock overshooting is observed. It is because in the reduced domain the disturbance reflections emanating from the shock have not been dissipated completely.

Pressure distributions are shown in Figures 6.14 and 6.15 for the conventional and proposed FFBC models respectively. The pressure coefficients have been compared in Figure 6.16. The behavior of the pressure field is somewhat different than the Mach field. In the reduced computational domain Mach numbers are larger (Figure 6.14) in comparison to the base solution (within extended domain). In this case the pressure is shifted along the chord because of the highly nonlinear wave interactions in the reduced domain.

The convergence histories for the transonic case for both extended and reduced computational domains are shown in Figures 6.17 and 6.18. Although, implementing the proposed FFBC model for subsonic flows was accompanied by an iteration reduc-

tion. However, applying the FFBC model to the external flow problem did not show a faster convergence in the transonic regimes. This was the case for the confined flow. It can be one of the limitations of the proposed FFBC model.

Finally, the iso-Mach lines are shown through Figures 6.19 and 6.20.

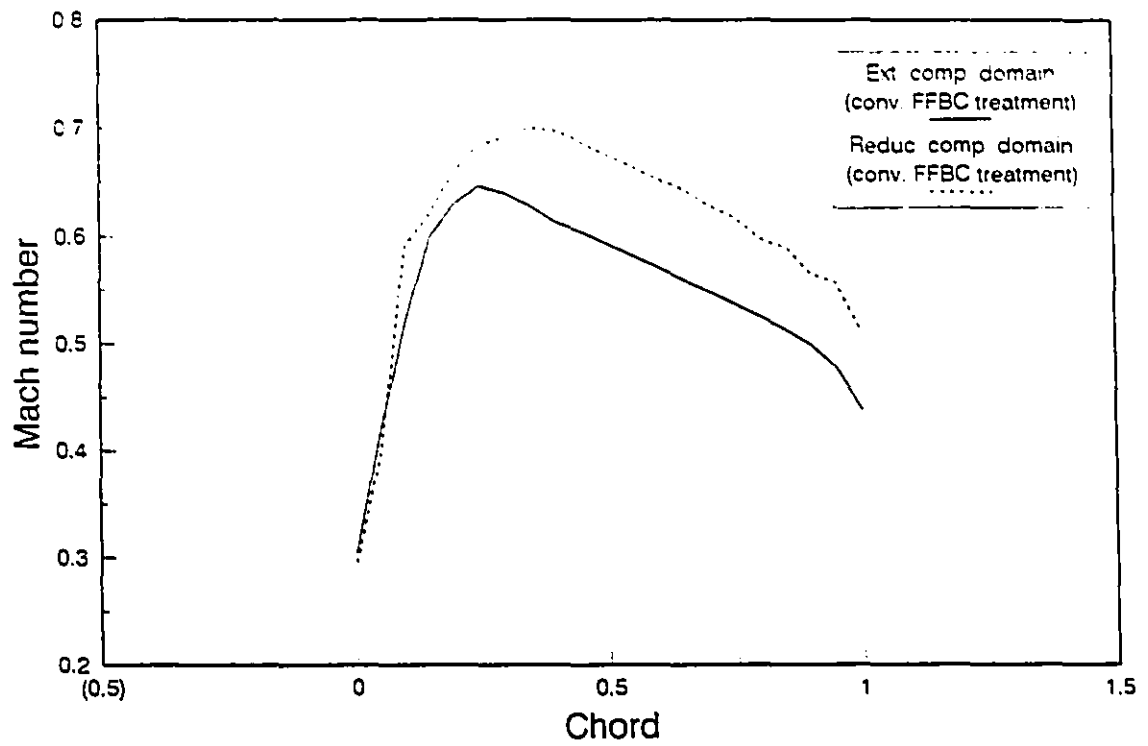


Figure 6.5: Mach number distributions for extended and reduced computational domains obtained by conventional FFBC method, NACA 0012 airfoil. $M_\infty = 0.6$, CFL=2.2.

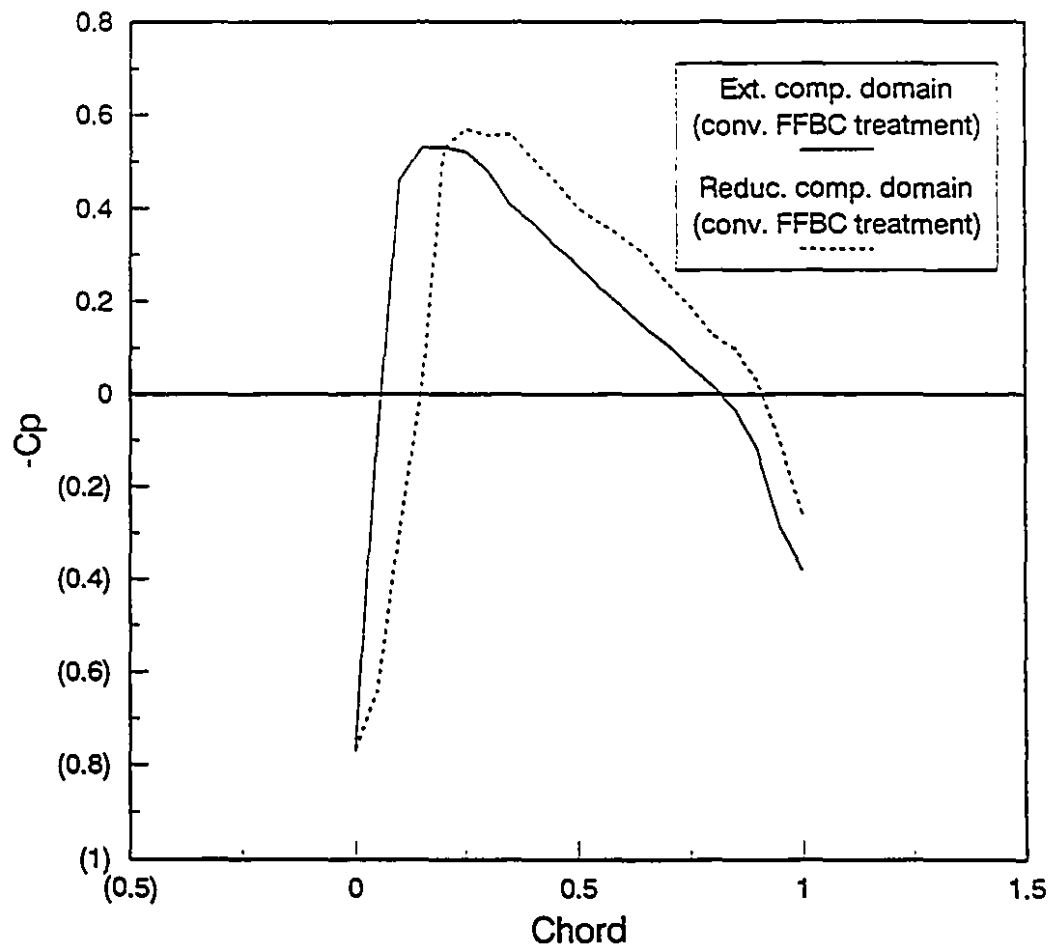


Figure 6.6: Pressure coefficient comparisons for extended and reduced computational domains with conventional FFBC treatments, NACA 0012 airfoil. $M_\infty = 0.6$, CFL=2.2.

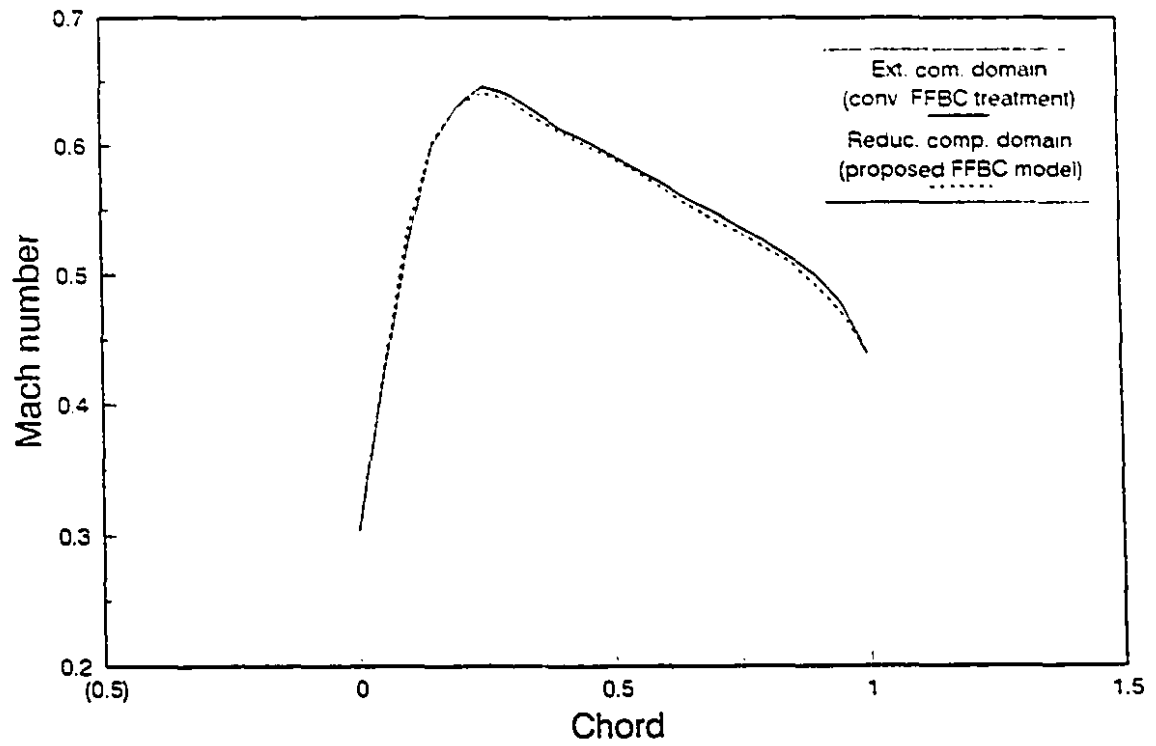
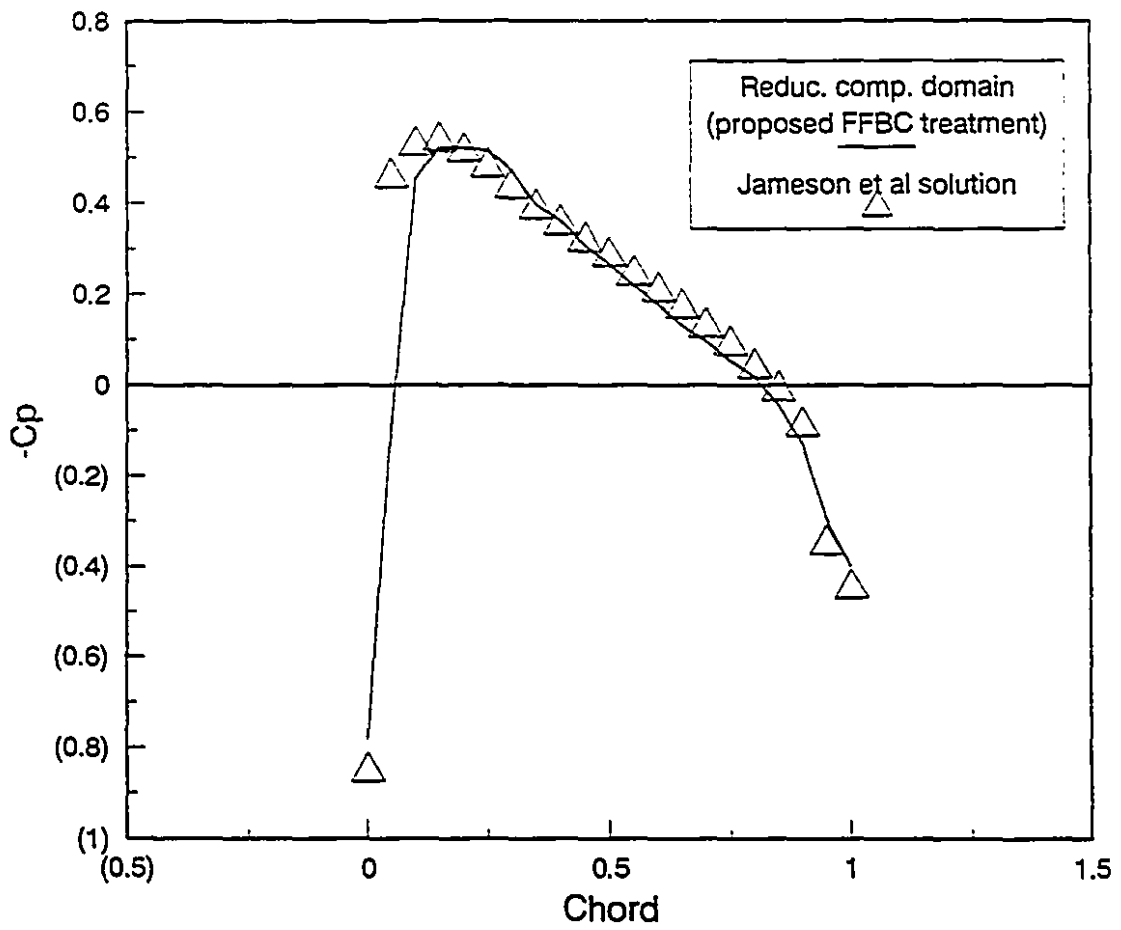


Figure 6.7: Mach numbers obtained from extended computational domain (conventional FFBC method) and reduced computational domain (proposed FFBC model), NACA 0012 airfoil. $M_{\infty} = 0.6$, CFL=2.2.



2000
 1000
 1000
 1000
 REF
 P. 137

Figure 6.8: Pressure coefficient comparisons of the reduced computational domain with the solution of Jameson [71]. $M_\infty = 0.6$.

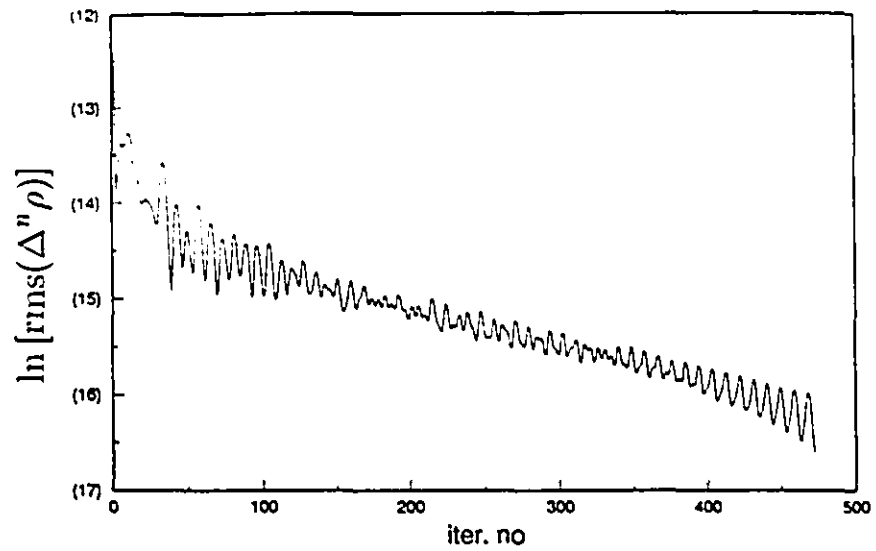


Figure 6.9: Convergence history for NACA 0012 airfoil, extended computational domain. $M_\infty = 0.6$, CFL=2.2.

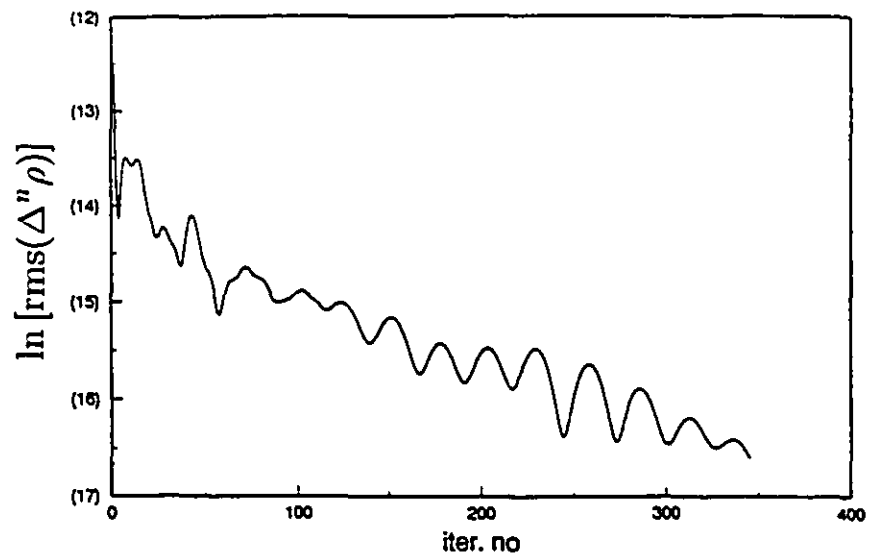


Figure 6.10: Convergence history for NACA 0012 airfoil, reduced computational domain. $M_\infty = 0.6$, CFL=2.2.

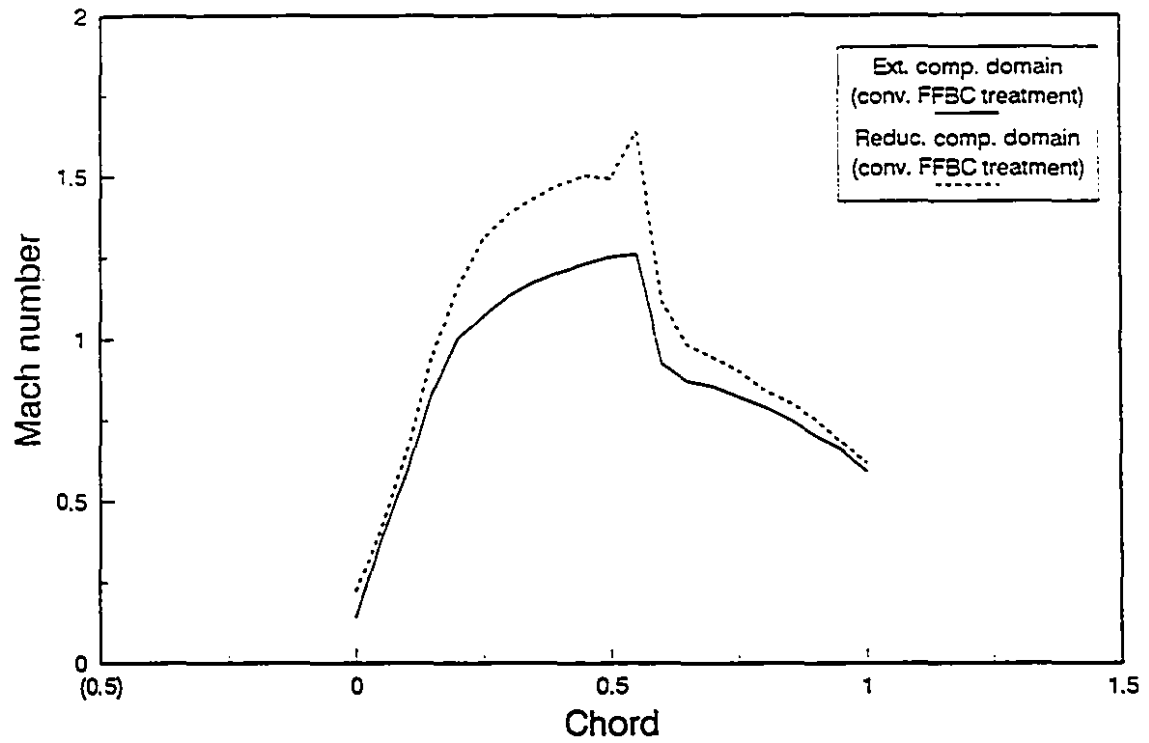


Figure 6.11: Transonic flow: Mach number comparisons of extended and reduced computational domains using conventional FFBCs. NACA 0012 airfoil. $M_\infty = 0.8$, CFL=0.4.

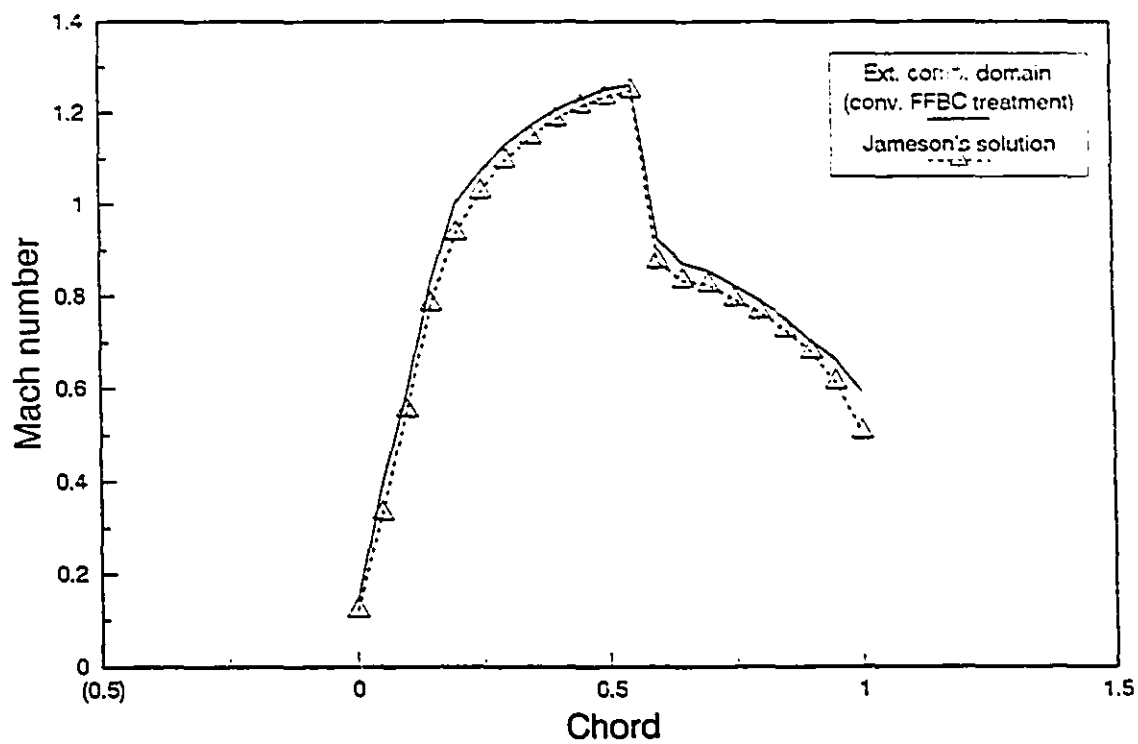


Figure 6.12: Transonic flow: Mach number comparisons of extended computational domain, NACA 0012 airfoil, CFL=0.4, Jameson *et al* solution [68]. $M_\infty = 0.8$, zero incidence.

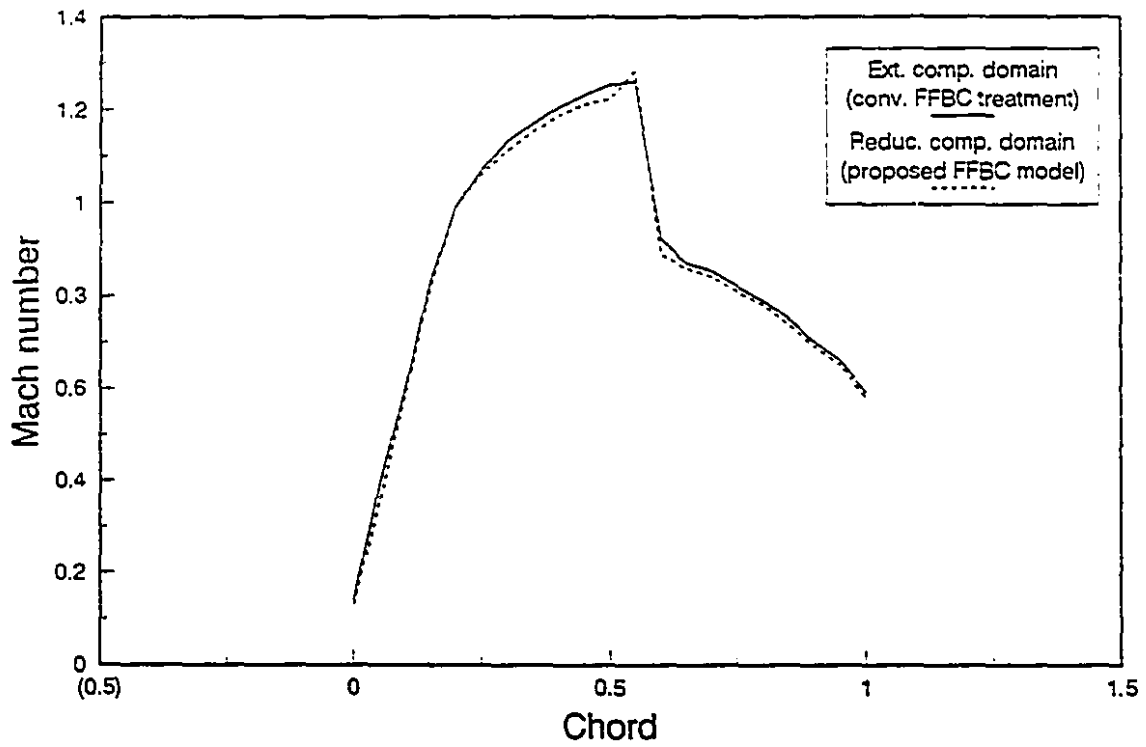


Figure 6.13: Transonic flow: Mach number comparisons of extended computational domain (with conventional FFBC treatments) and reduced computational domain with the proposed FFBC model. $M_\infty = 0.8$, $CFL=0.4$, zero incidence.

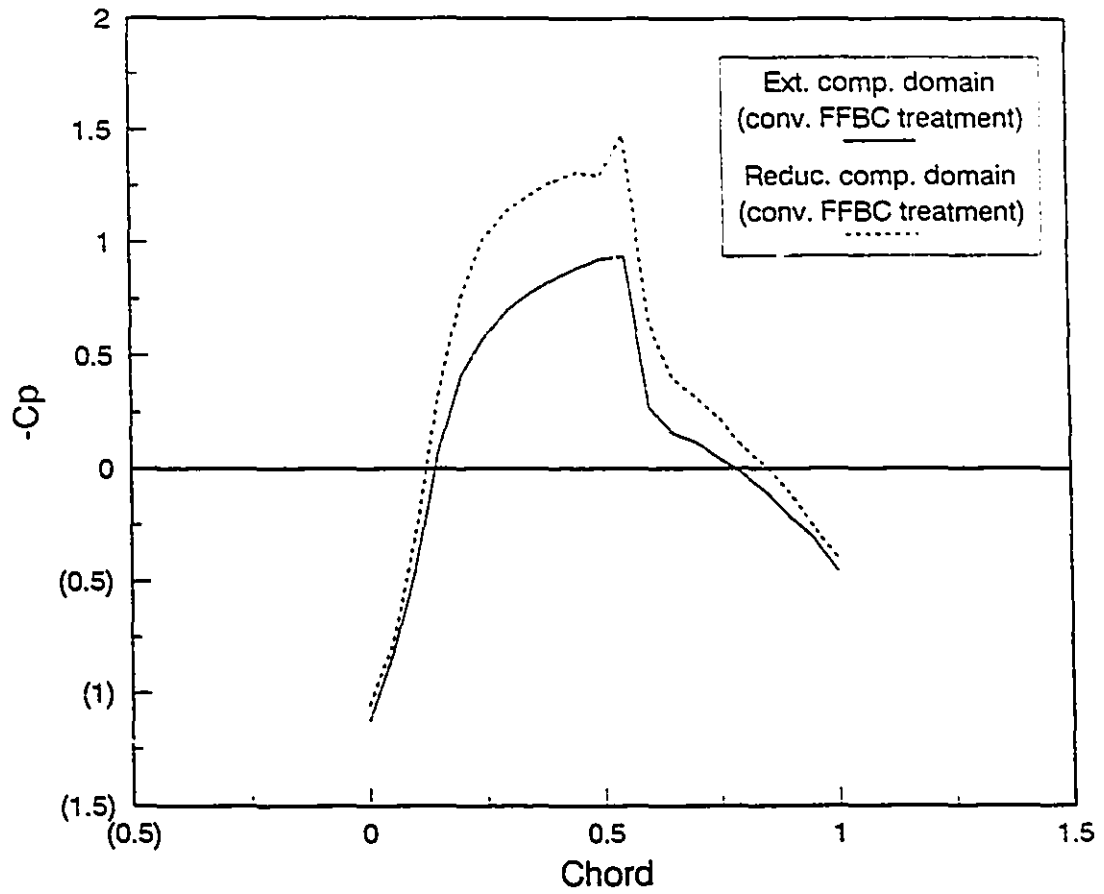


Figure 6.14: Transonic flow: Pressure coefficient comparisons of extended computational domain (conventional FFBC treatments) and reduced computational domain (conventional FFBC treatments). $M_\infty = 0.8$. CFL=0.4, zero incidence.

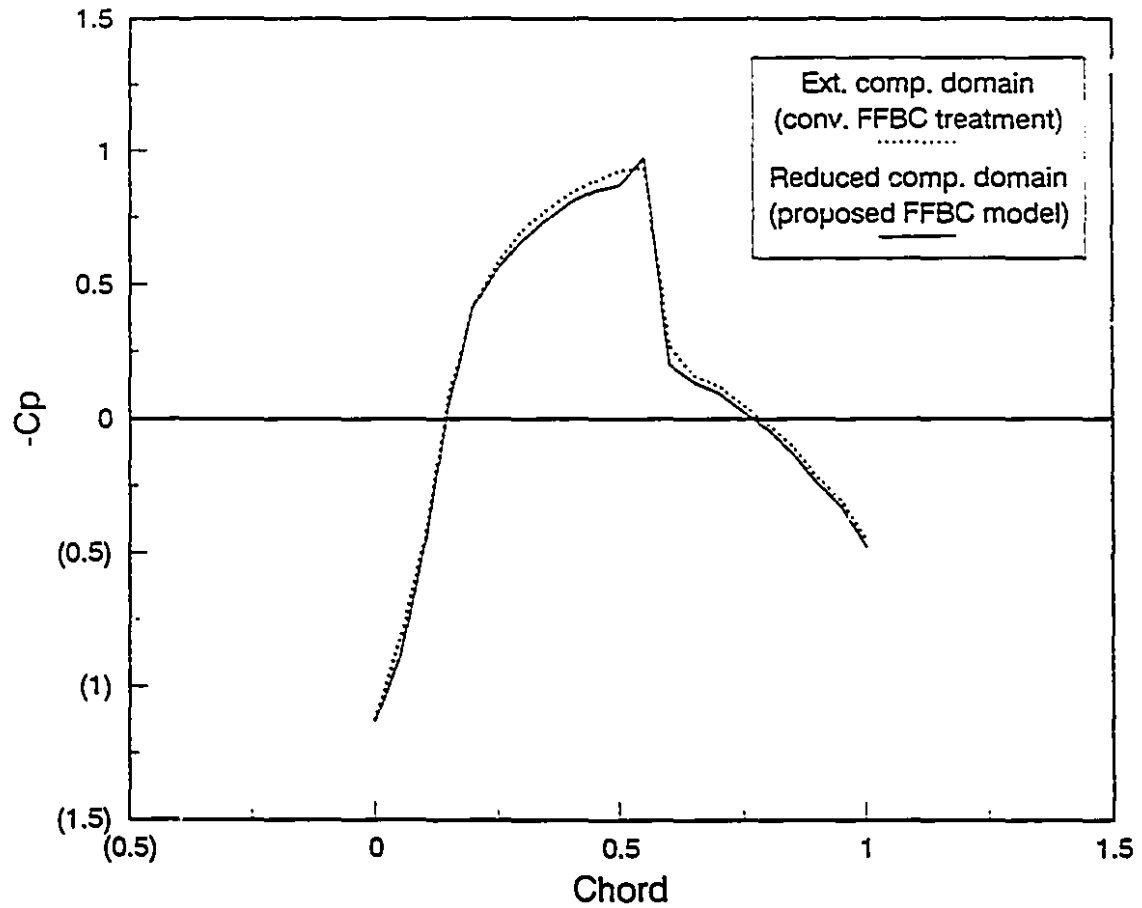


Figure 6.15: Transonic flow: Pressure coefficient comparisons of extended computational domain (conventional FFBC treatment) and reduced computational domain with the proposed FFBC model. $M_\infty = 0.8$, $CFL=0.4$, zero incidence.

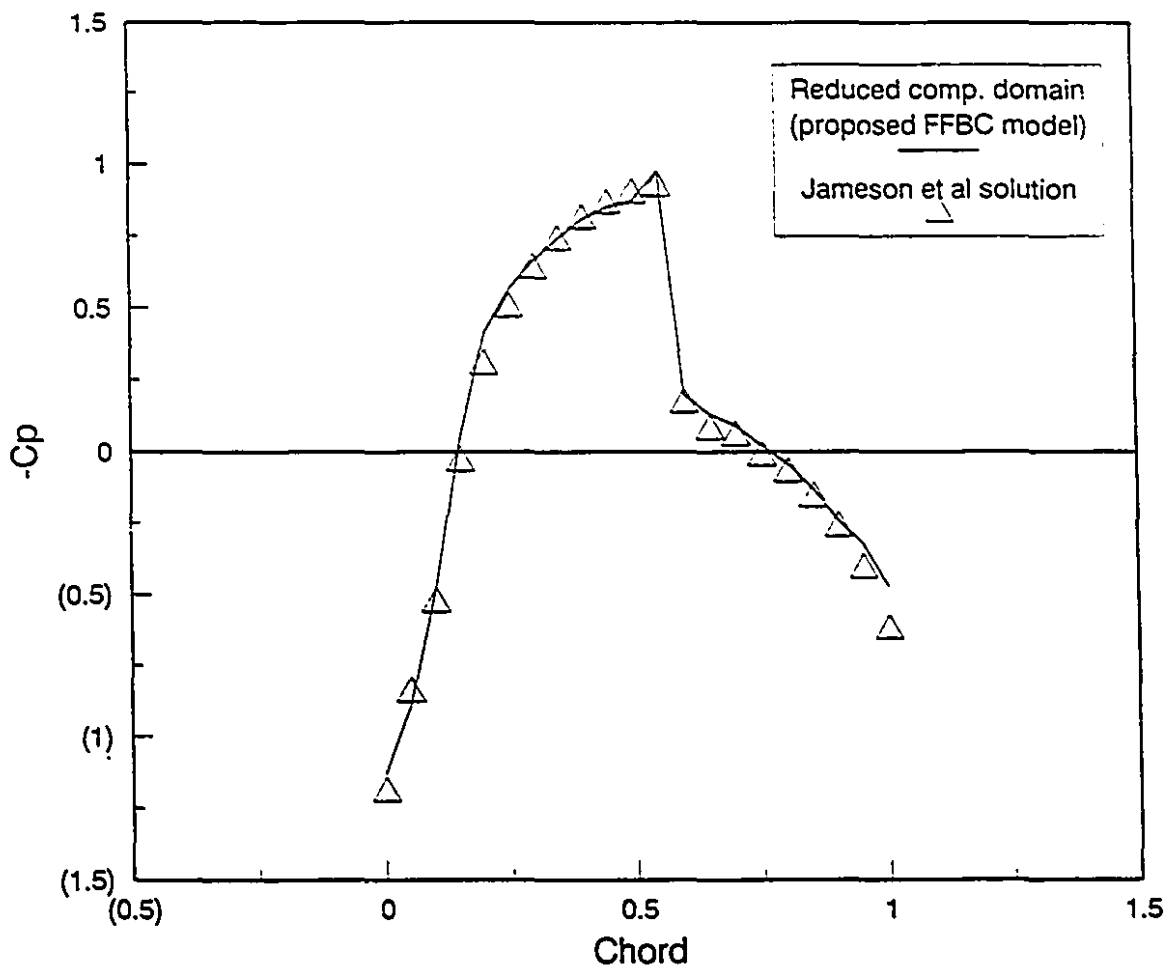


Figure 6.16: Transonic flow: Pressure coefficient comparisons of reduced computational domain (proposed FFBC model) with Jameson *et al* [68] solution. $M_\infty = 0.8$, zero incidence.

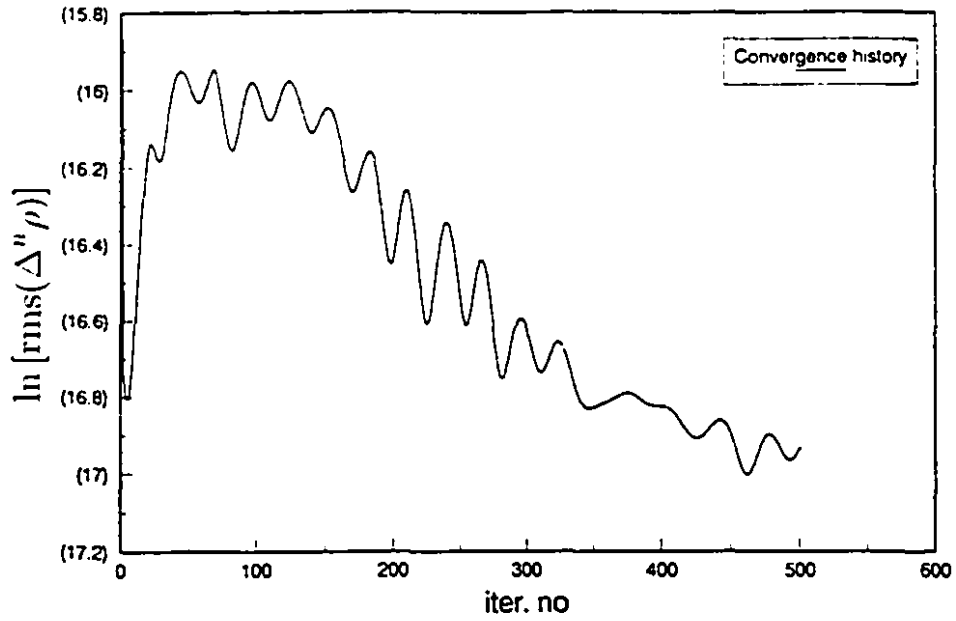


Figure 6.17: Convergence history for NACA 0012 airfoil, extended computational domain. $M_\infty = 0.8$, CFL=0.4.

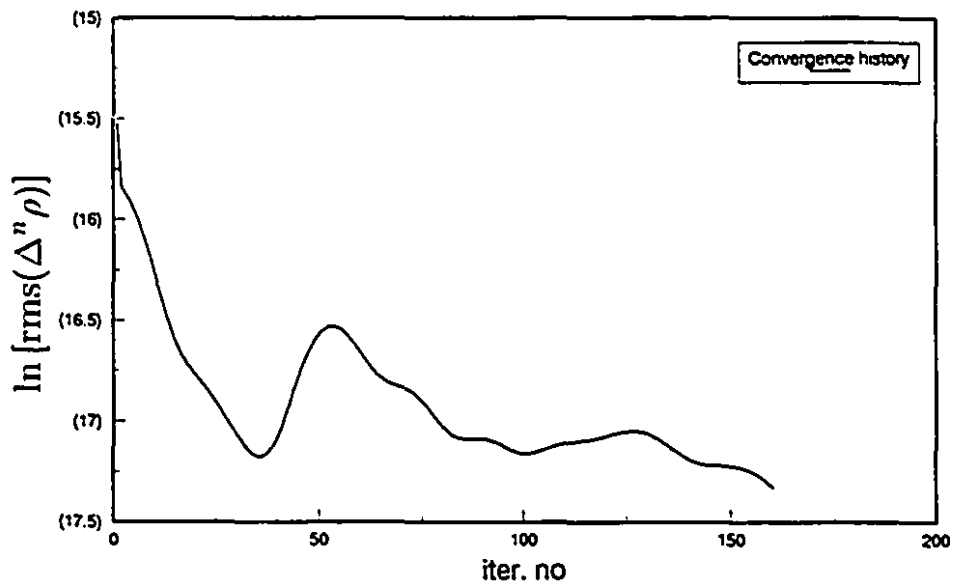


Figure 6.18: Convergence history for NACA 0012 airfoil, reduced computational domain. $M_\infty = 0.8$, CFL=0.4.

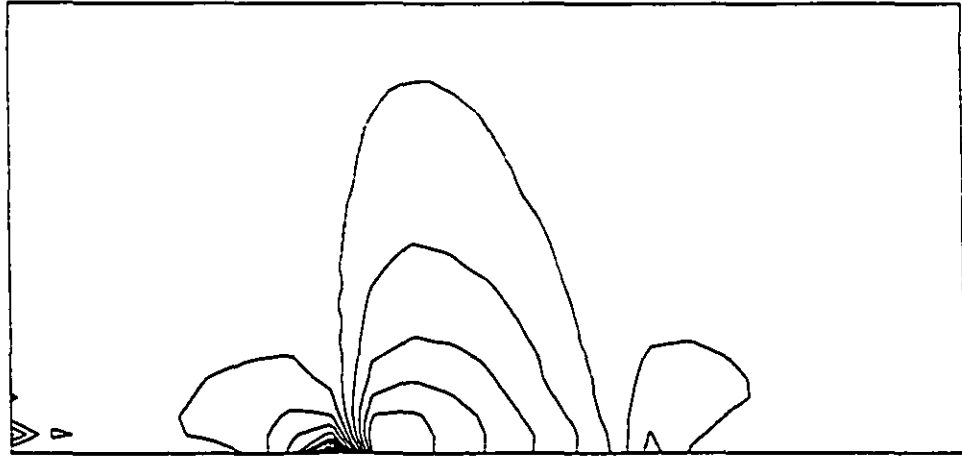


Figure 6.19: Iso-Mach lines for subsonic flow over NACA 0012 airfoil, zero incidence, $M_\infty = 0.6$.

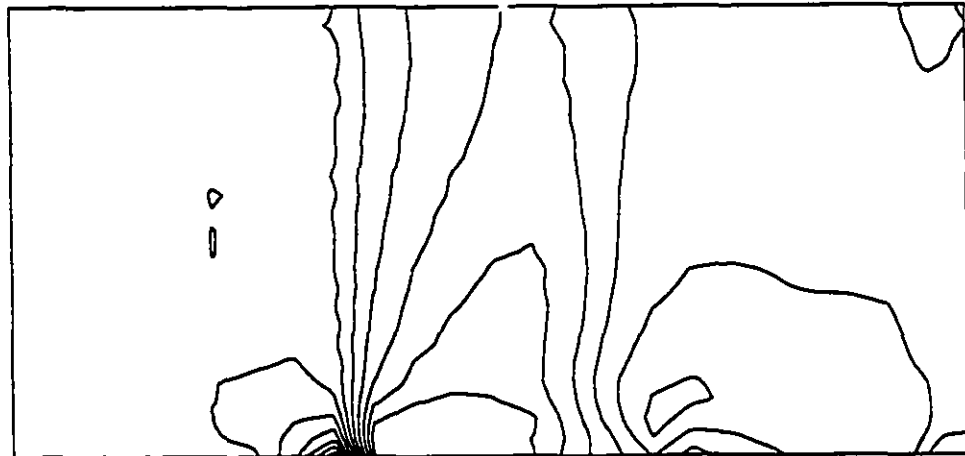


Figure 6.20: Iso-Mach lines for transonic flow over NACA 0012 airfoil, zero incidence, $M_\infty = 0.8$.

Chapter 7

Conclusions

The formulation and implementation of a far field boundary condition (FFBC) model has been reported in this Thesis for compressible subsonic and transonic flows. The developed FFBC model permits a substantial reduction of the computational domain, for both quasi-one- and two-dimensional flows, which leads to a corresponding reduction in computational effort. This has considerable impact on the solution accuracy and the overall computational efficiency. In developing the FFBC model, two kinds of information are required and have been taken into account:

- Information from the far-field regions, by solving the perturbation equations, based on Riemann variables expansions.
- Information from the numerical solution within the computational domain at each time-iteration step.

These are taken into account by using natural coordinates and Riemann variables. The far-field behavior is simulated with an expanded Riemann variables approach and the corresponding perturbation equations. To determine the behavior of the information from the computational domain (which propagates towards the FFBCs), the directions of outgoing waves are found by using the compatibility relations developed in Chapter 2; these directions, rarely considered in previous FFBC methods, are significant for the FFBC formulation of two-dimensional flows.

The time dependent far-field perturbation equations are discretized forward in time and by central differencing in space. Then, these discretized equations are integrated in time and matched with the solution within the computational domain at each iteration step. Thus, at an inflow boundary, the right-propagating Riemann variables are calculated from the discretized far-field equations, whilst the left-propagating ones are determined numerically in the computational domain along the dominant wave directions. The flow angle at the inflow boundary is also calculated numerically by solving its corresponding equation. A similar approach is used at the outflow boundaries.

This FFBC model has been first developed for isentropic quasi-one-dimensional flows and subsequently was extended for two-dimensional internal and external flows. Then, for the FFBC treatment of the transonic flows, for which the outflow boundaries are crossed by nonuniform-entropy flows, the Riemann variables were modified by considering the entropy variations. In this case the perturbation equation is also modified to include the entropy variations.

An implicit ADI scheme has been used for solving the flow-field within the computational domain. However, this FFBC model can be coupled with other numerical Euler solvers as well.

For accurate calculation of the pressure at the solid boundaries, the normal momentum equation was used in conjunction with the characteristic relations, resulting in an improved solution accuracy. Consistent solid boundary treatment reduces reflections in the flow domain thereby decreasing the number of convergence steps required.

Solving quasi-one-dimensional problems using the FFBC model resulted in solutions that are in a very good agreement with the analytic solutions (in terms of accuracy and shock position). For 2D flows, by incorporating the reduced computational domain with the FFBC model, good results were generated in comparison with the solutions obtained with an extended computational domain. Small differences are observed in comparison to the solutions of Ni (for confined flows) and Jameson

(for external flows), which are due to the utilization of a rather coarse grid near the leading and trailing edges of the arc or airfoil.

Applying the proposed FFBC model to the channel flows, the matrix dimension is decreased in the x -direction, while for the external flow problem, the matrix dimension is reduced in both x and y directions. This leads to a considerable memory reduction and a corresponding reduction in the computational effort. Numerical experiments with the proposed FFBC model also showed a reduced number of iterations for the case of subsonic flow, while this reduction was much smaller in the transonic flow. This is due to strong reflections appearing in the presence of a shock wave in the transonic flow regime. The numerical solutions show the capability of the proposed FFBC model in reducing the domain size, while maintaining the solution accuracy.

For the case of external flow (symmetric airfoil with zero angle of attack), applying the proposed FFBC method was found to be effective, especially for vertical FFB, while applying the same FFBC model to the horizontal FFB improved the solution accuracy by only a small amount. This is because along the horizontal FFB, the perturbation variation is very small, compared to the vertical FFBs.

The proposed FFBC model has been validated by comparing the solutions obtained for a reduced computational domain with the exact solutions available for quasi 1D flows and with the quasi 1D and 2D solutions obtained for an extended computational domain by using a conventional FFBC treatment. The number of grid points of the reduced computational domain was in average 8 times smaller in the case of 2D external flows, and about 3 times smaller for quasi 1D and 2D confined flows.

From the above comparisons, it was found that the proposed FFBC model generated very accurate solutions with improved computational efficiency and memory requirements.

7.1 Main Contributions of this Thesis

The main contributions of this Thesis can be summarized as follows:

- A far field boundary condition (FFBC) model has been developed for the compressible subsonic and transonic rotational flows. This model is based on far-field expansions of Riemann variables, which are used in conjunction with the propagation of the characteristics from the computational domain. This takes into account the estimated directions of wave propagation.
- This FFBC model has first been developed for quasi 1D isentropic flows and then has been extended for two-dimensional confined flows in nozzles and for 2D external flows past airfoils. This model has also been extended for non-isentropic flows crossing the outflow boundaries, which is important for the transonic flows involving shock waves inside the computational domain.
- The proposed FFBC model has led to a substantial reduction of the computational domain for a very good accuracy, comparable to that obtained for a much larger domain. This corresponds to a considerable reduction in the number of grid points, which led to substantially improved memory requirements and computational efficiency.
- This FFBC model has been developed in a sufficiently general manner, in order to be used in conjunction with various flow-field solvers. The flow-field solver used in this Thesis for numerical computations was based on an alternating direction implicit scheme.

7.2 Future Extensions

The utilization of the present FFBC model in conjunction with other flow solvers (e.g. finite-volume solvers) is also of interest to be investigated.

Since the far-field behavior and the corresponding boundary conditions have not been investigated in the case of unsteady flows, it is of interest to extend the proposed FFBC model to such problems. Also, extensions of the proposed model to the nonsymmetric external flows have to be considered.

The developed FFBC model could also be used with other first-order hyperbolic systems (such as shallow water flow equations) with some minor modifications.

References

- [1] Abarbanel S. S., Murman E.M., "Stability of Two-Dimensional Hyperbolic Initial Boundary Value Problems for Explicit and Implicit Schemes," *J. Comp. Phys.*, vol.48, pp.160-167, 1982.
- [2] Agrawal S., Vemerland R.E., Verhoff A., Lowrie R.B., "Euler Transonic Solutions Over Finite Wings," *AIAA paper 88-0009*, 1988.
- [3] Anderson W. K., Thomas J. L., Van Leer B., "Comparison of Finite Volume Flux Vector Splittings for the Euler Equations," *AIAA J.*, vol.24, pp.1453-1460, 1986.
- [4] Anderson D. A., Tannehill J. C. and Pletcher R. H., *Computational Fluid Mechanics and Heat Transfer*, Hemisphere, Washington D. C., 1984.
- [5] Atkins H., Casper J., "Nonreflecting Boundary Conditions for Higher-Order Methods," *AIAA J.*, vol.32, no.3, 1994
- [6] Bach G., *Lecture Notes*, McGill University, Canada.
- [7] Bayliss A., Turkel E., "Far Field Boundary Conditions For Compressible Flows," *Numerical Boundary Condition Procedures*, NASA Conference Publication 2201, pp.1-18, 1981, also *J Comp. Phys.*, vol.48, pp.182-199, 1982.
- [8] Bayliss A., Turkel E., "Outflow Boundary Conditions for Fluid Dynamics," *SIAM J Sci. Stat. Comput.*, vol.3, pp.250-259, 1982.
- [9] Bayliss A., Gunzburger M., Turkel E., "Boundary Conditions for the Numerical Solution of Elliptic Equations in Exterior Regions," *SIAM J Appl. Math.*, vol.42, pp.430-451, 1982.
- [10] Bayliss A., Turkel E., "Radiation Boundary Conditions for Wave-Like Equations," *Communications on Pure and Applied Math.*, vol.23, pp.707-725, 1980.
- [11] Beam R. M., Warming R. F., "An Implicit Finite-Difference Algorithm for Hyperbolic Systems in Conservation-Law Form," *J. Comp.Phys.*, vol.22, pp.87-110, 1976.
- [12] Beam R. M., Warming R. F., Yee H. C., "Stability Analysis of Numerical Boundary Conditions and Implicit Difference Approximations for Hyperbolic Equations," *Numerical Boundary Condition Procedures*, NASA Conf. Pub. 2201, 1982.
- [13] Beam R. M., Warming R. F., "An Implicit Factored Scheme for the Compressible Navier-Stokes Equations," *AIAA J.*, vol.16, pp.393-402, 1978.

- [14] Blottner F. G., "Influence of Boundary Approximations and Conditions on Finite-Difference Solutions." *J. Comp. Phys.*, vol.48, pp.246-269, 1982.
- [15] Briley W. R., McDonald H., "On the Structure and Use of Linearized Block Implicit Schemes." *J. Comp. Phys.*, vol.34, pp.54-73, 1980.
- [16] Briley W. and McDonald H., "Solution of Three-Dimensional Compressible Navier-Stokes Equations by an Implicit Technique." *Lecture Notes in Physics*, vol. 35, Springer-Verlag, Berlin, 1975.
- [17] Buning P. G., "Solution of the Two-Dimensional Euler Equations with Generalized Coordinate Transformation Using Flux Vector Splitting." *AIAA paper 82-0971*, AIAA/ASME 3rd Joint Thermophysics, Fluids, Plasma and Heat Transfer Conf. 1982.
- [18] Buratynski E. K., Caughey D. A., "An Implicit Scheme for the Euler Equations Applied to Arbitrary Cascades." *AIAA J.*, vol.24, pp.39-46, 1986.
- [19] Chakravarthy S. R., "Euler Equations-Implicit Schemes and Boundary Conditions." *AIAA J.*, vol.21, pp.699-706, 1983.
- [20] Chen J. H., "Numerical Boundary Conditions and Computational Modes." *J. Comp. Phys.*, vol.13, pp.522-535, 1973.
- [21] Cline M. C., "Stability Aspects of Diverging Subsonic Flow." *AIAA J.*, vol.18, pp.534, 1980.
- [22] Clayton R., Engquist B., "Absorbing Boundary Conditions for Acoustic and Elastic Wave Equations." *Bulletin of the Seismological Soc. of America*, vol.67, pp.1529-1540, 1977.
- [23] Clayton R. W., Engquist B., "Absorbing Boundary Conditions for Wave- Equation Migration." *Geophysics*, vol.45, pp.895-904, 1980.
- [24] Chu C.K. and Sereny A., "Boundary Conditions in Finite Difference Fluid Dynamic Codes." *J. Comp. Phys.*, vol.15, pp.476-491, 1974.
- [25] Daru V., Lerat A., "An Implicit Centered Scheme wich Gives Non- Oscillatory Steady Shocks." *Lecture Notes in Mathematics*, 1270, Nonlinear Hyperbolic Problems, Ed. Carasso C, Raviart P.A., Serre D., 1986.
- [26] Davis J. L., *Wave Propagation in Electromagnetic Media*, Springer-Verlag, 1990.
- [27] De Neef T., Moretti G., "Shock Fitting for Everybody." *Comput. & Fluids*, vol.8, pp. - , 1980
- [28] de Pillis L. G., "Far Field Behavior of Slightly Compressible Flows." Ph.D. Thesis. Dept. of Mathematics, University of California, 1993.
- [29] Eidelman S., Colella P., Shreeve R.P., "Application of the Godunov Method and Its Second-Order Extension to Cascade Flow Modeling." *AIAA J.*, vol.22, pp.1609-1615, 1984.
- [30] Engquist B., Majda A., "Absorbing Boundary Conditions for the Numerical Simulation of Waves." *Mathematics of Computation*, vol.31, pp.629-651, 1977.
- [31] Engquist B. and Majda A., "Numerical Radiation Boundary Conditions for Unsteady Transonic Flow." *J. Comp. Phys.*, vol.40, pp.91-103, 1981.

- [32] Engquist B., Majda A., "Radiation Boundary Conditions for Acoustic and Elastic Wave Calculations." *Communications on Pure and Applied Math.*, vol.32, pp.313-357, 1979.
- [33] Ferm L., Gustafsson B., "A Down-Stream Boundary Procedure for the Euler Equations." *Computers & Fluids*, vol.10, pp.261-276, 1982.
- [34] Fox L., *Numerical Solution of Ordinary and Partial Differential Equations*, Pergamon press, 1962.
- [35] Fung K. Y., "Far Field Boundary Conditions for Unsteady Transonic Flows." *AIAA J.*, vol.19, pp.180-183, 1981.
- [36] Geller R.G., Noack R.M., and Fetter A.L., "Normal Mode Solutions for Absorbing Boundary Conditions." *Geophysical Research Letters*, vol.12, pp.145-148, 1985.
- [37] Giles M., "Non-Reflecting Boundary Conditions for Unsteady Airfoil Calculations." *CFDL-TR Report*, MIT, 1990.
- [38] Giles M., "Nonreflecting Boundary Conditions for Euler Equation Calculations." *AIAA J.*, vol.28, pp.2050-2057, 1990.
- [39] Giles M., "Non-Reflecting Boundary Conditions for the Euler Equations." *CFDL-TR-88-1 report*, MIT, Cambridge, 1988.
- [40] Givoli D., "Review Article: Non-reflecting Boundary Conditions." *J. Comp. Phys.*, vol.94, pp.1-29, 1991.
- [41] Gottlieb D., Gunzburger M., Turkel E., "On Numerical Boundary Treatment for Hyperbolic Systems." *SIAM J Numer. Anal.*, vol.19, pp.671-679, 1982.
- [42] Gottlieb D., Turkel E., "Boundary Conditions for Multistep Finite Difference Methods for Time-Dependent Equations." *J. of Comp. Phys.*, vol.26, pp.181-196, 1978.
- [43] Griffin M. D., Anderson, J. D., "On the Application of Boundary Conditions to Time Dependent Computations for Quasi One-Dimensional Fluid Flows." *Computers & Fluids*, vol.5, pp.127-137, 1977.
- [44] Grosch C. E. and Orszag S. A., "Numerical Solution of Problems in Unbounded Regions: Coordinate Transformation," *J. of Comp. Phys.*, vol.25, pp.273-. 1977.
- [45] Gustafsson B., Ferm L., "Far Field Boundary Conditions for Steady State Solutions to Hyperbolic Systems," *Lecture Notes in Mathematics*, Ed. Carasso C., Raviart P.A., Serre D., Nonlinear Hyperbolic Problems, Proc., St. Etienne, pp.238-252, 1986.
- [46] Gustafsson B., "Far-Field Boundary Conditions for Time-Dependent Hyperbolic Systems," *SIAM J Sci. Stat. Comput.*, vol.9, pp.812-828, 1988.
- [47] Gustafsson B., Kreiss H. O., "Boundary Conditions for Time Dependent Problems with an Artificial Boundary," *J. Comp. Phys.*, vol.30, pp.333-351, 1979.
- [48] Gustafsson B., "The Choise of Numerical Boundary Conditions for Hyperbolic Systems," *J. Comp. Phys.*, vol.48, pp.270-283, 1982.
- [49] Gustafsson B., Kreiss H. O., Sundstrom A., "Stability Theory of Difference Approximations for Mixed Initial Boundary Value Problems," *Mathematics of Computation*, vol.26, pp.649-686, 1972.

- [50] Gustafsson B., "Inhomogeneous Conditions At Open Boundaries for Wave Propagation Problems." *Applied Numerical Mathematics*, North-Holland, vol.4, pp.3-19, 1988.
- [51] Hall K. C., Crawley E. F., "Calculation of Unsteady Flows in Turbomachinery Using the Linearized Euler Equations." *AIAA J.*, vol.27, pp.777-787, 1989.
- [52] Halpern L., "Absorbing Boundary Conditions for the Discretization Schemes of the One-Dimensional Wave Equation." *Mathematics of Computation*, vol.38, pp.415-429, 1982.
- [53] Hedstrom G.W., "Nonreflecting Boundary Conditions for Nonlinear Hyperbolic Systems." *J. Comp.Phys.*, vol.30, pp.222-237, 1979.
- [54] Higdon R. L., "Numerical Absorbing Boundary Conditions for the Wave Equation." *Mathematics of Computation*, vol.49, pp.65-90, 1987.
- [55] Higdon R. L., "Absorbing Boundary Conditions for Difference Approximations to the Multi-Dimensional Wave Equation." *Mathematics of Computation*, vol.47, pp.437-459, 1986.
- [56] Higdon R. L., "Initial-Boundary Value Problems for Linear Hyperbolic Systems." *SIAM Review*, vol.28, pp.177-217, 1986.
- [57] Hagstrom T., Hariharan S.I., "Accurate Boundary Conditions for Exterior Problems in Gas Dynamics." *Mathematics of Computation*, vol.51, pp.581-597, 1988.
- [58] Hariharan S.I., Bayliss A., "Radiation of Sound from Unflanged Cylindrical Ducts." *SIAM J Sci. Stat.Comp.*, vol.6, pp.285-296, 1985.
- [59] Henshaw W. D., Kreiss H. O., Reyna L. G., "Smallest Scale Estimates for the Navier-Stokes Equations for Incompressible Fluids." *Archive for Rational Mechanics and Analysis*, vol.112, pp.21-44, 1990.
- [60] Hindman R. G., "Geometrically Induced Errors and Their Relationship to the Form of the Governing Equations and the Treatment of Generalized Mappings." *AIAA paper 81-1008*, 1981.
- [61] Hirsch C., Verhoff A., "Far Field Numerical Boundary Conditions for Internal and Cascade Flow Computations." *AIAA 89-1943-CP*, 1989.
- [62] Holst T. L., Flonas J., Kaynak U., Chaderjian N. M., "Navier-Stokes Computations About Complex Configurations Including a Complete F-16 Aircraft." *Applied Computational Aerodynamics*, Ed. Henne P. A., vol.125, Progress in Astronautics and Aeronautics series, 1990.
- [63] Holt M., *Numerical Methods in Fluid Dynamics*, Springer-Verlag, 1977.
- [64] Hoffmann C. A., *Computational Fluid Dynamics for Engineers*, vol.2, Engineering Education System, 1993.
- [65] Howell L. H., Trefethen L.N., "Ill-Posedness of Absorbing Conditions for Migration." *Geophysics*, vol.53, pp.593-603, 1988.
- [66] Imanari K., Kodama H., "Nonreflecting Boundary Conditions of Three-Dimensional Euler Equation Calculations for Strut Cascades." *J. of Propulsion and Power*, vol.9, pp.443-448, 1993.

- [67] Israeli M. and Orszag S.A., "Approximation of Radiation Boundary Conditions." *J. Comp. Phys.*, vol.41, pp.115-135, 1981.
- [68] Jameson A., Schmidt W., Turkel E., "Numerical Solution of the Euler Equations by Finite Volume Methods Using Runge Kutta Time Stepping Schemes," *AIAA paper 81-1259*, AIAA 14th Fluid and Plasma Dynamics Conference, 1981.
- [69] Jameson A., "Transonic Aerofoil Calculations Using the Euler Equations," *Numerical Methods in Aeronautical Fluid Dynamics*, Ed. Roe P. L., 1981
- [70] Jameson A., "A Nonoscillatory Shock Capturing Scheme Using Flux Limited Dissipation," *Lectures in Applied Mathematics*, vol.22, pp.345-370, 1985.
- [71] Jameson A., "Steady State Solution of Euler Equations for Transonic Flow," *Transonic Shock and Multidimensional Flows*, Advances in Scientific Computing, Ed. Meyer R. E., pp37-70, 1982.
- [72] Johnston R. L., Pal S. K., "The Numerical Solution of Hyperbolic Systems Using Bicharacteristics," *Mathematics of Computation*, vol.26, pp.377-392, 1972.
- [73] Karni S., "Accelerated Convergence to Steady State by Gradual Far-Field Damping," *AIAA J.*, vol.30, pp.1220-1226, 1992.
- [74] Karni S., "To the Boundary and Back-A Numerical Study," *Int. J for Numerical Methods in Fluids*, vol.13, pp.201-216, 1991.
- [75] Karni S., "Far-Field Filtering Operators for Suppression of Reflections from Artificial Boundaries," Submitted to *SIAM J. on Numerical Analysis*, 1994
- [76] Keller J. B., "Exact Non-reflecting Boundary Conditions." " *J. Comp. Phys.*, vol.82, pp.172-192, 1989.
- [77] Kotschin N. J., Kibel I. A., Rose N. W., *Theoretische Hydromechanik*, vol.2, Akademie-Verlag, Berlin, 1955.
- [78] Kreiss H. O., "Initial Boundary Value Problems for Hyperbolic Systems," *Communications on Pure and Applied Math.*, vol.23, pp.277-298, 1970.
- [79] Kroner D., "Absorbing Boundary Conditions for the Linearized Euler Equations in 2-D," *Mathematics of Computation*, vol.57, pp.153-167, 1991.
- [80] Kwak D., "A Comparative Study of Nonreflective Far-Field Boundary Condition Procedures for Unsteady Transonic Flow Computation," *Numerical Boundary Condition Procedures*, NASA Conference Publication 2201, pp.21-44, 1981.
- [81] Kosloff R., Kosloff D., "Absorbing Boundaries for Wave Propagation Problems," *J. Comp.Phys.*, vol.63, pp.363-376, 1986.
- [82] Lacor C., Hirsch C., "Genuinely Upwind Algorithms for the Multidimensional Euler Equations," *AIAA J.*, vol.30, pp.56-63, 1992.
- [83] Lerat A., "Implicit Methods of Second-Order Accuracy for the Euler Equations," *AIAA J.*, vol.23, pp.33-40, 1985.
- [84] Lerat A., Peyret R., "The Problem of Spurious Oscillations in the Numerical Solution of the Equations of Gas Dynamics," *Lecture Notes in Physics*, Proc. of the 4th Int. Conf. on Numerical Methods in Fluid Dynamics, vol.35, 1975.

- [85] Lerat A., Sides J., Daru V., "Efficient Computation of Steady and Unsteady Transonic Flows by an Implicit Solver," *Advances in Computational Transonics*, Ed. Habashi W.G., 1985.
- [86] Lerat A., Sides J., "A New Finite -Volume Method for the Euler Equations with Applications to Transonic Flows," *Numerical Methods in Aeronautical Fluid Dynamics*, pp.245-288, Ed. Roe P. L., 1982.
- [87] Lindman E. L., "Free Space Boundary Conditions for the Time-Dependent Wave Equation," *J. Comp. Phys.*, vol.18, pp.66-, 1975.
- [88] Marcum D. L. and Hoffman J. D., "Numerical Boundary Condition Procedures for Euler Solvers," *AIAA J.*, vol.25, pp.1054-1062, 1987.
- [89] Mateescu D., Lauzon M., "An Explicit Euler Method for Internal Flow Computation," *Computers and Experiments in Fluid Flow*, Ed. Carlomagno G. M., Brebbia C. A., pp.41-50, Springer-Verlag, 1989.
- [90] Mateescu D., Păidoussis M. P. & Belanger F., "A Time-Integration Method Using Artificial Compressibility for Unsteady Viscous Flows," *J of Sound and Vibration*, vol. 177, pp.197-205, 1994.
- [91] Mateescu D., Păidoussis M. P. & Sim W., "A Spectral Colocation Method for Confined Unsteady Flows with Oscillating Boundaries," *J of Fluids and Structures*, vol. 8, pp.157-181, 1994.
- [92] Mateescu D., Razavi S. E., "Computational Far Field Boundary Conditions For Internal Aerodynamic Problems," *Eleventh Canadian Symposium on Fluid Dynamics*, Alberta, June 1994.
- [93] Mateescu D., Pottier T., Perotin L. & Granger S., "Three-Dimensional Unsteady Viscous Flows Between Oscillating Eccentric Cylinders by an Enhanced Hybrid Spectral Method," *J of Fluids and Structures*, 1995 (in press).
- [94] Mateescu D., Stanescu D., "A Biased Flux Method for Solving the Euler Equations in Subsonic, Transonic and Supersonic Flows," *Seventh Int. Conf. on Computational Methods and Experimental Measurements*, Italy, 1995.
- [95] Mateescu D., Nasrallah P., "Computational Solutions Based on Lagrangian Formulation for Aerodynamic Problems of Unspecified Geometry," *Seventh Int. Conf. on Computational Methods and Experimental Measurements*, Italy, 1995.
- [96] Mateescu D., *Private communications*, 1993.
- [97] Mateescu D., "Unsteady Aerodynamics," *Lecture notes*, McGill University, 1991.
- [98] Mateescu D., "High-Speed Aerodynamics," *Lecture notes*, McGill University, 1993.
- [99] Mateescu D., "Computational Aerodynamics," *Lecture notes*, McGill University, 1992.
- [100] Mateescu D., "Advanced Computational Aerodynamics," *Lecture notes*, McGill University, 1994.
- [101] Mazaheri K., Roe P. L., "New Light on Numerical Boundary Conditions," *AIAA 10th Computational Fluid Dynamics Conference*, Honolulu, HI, 1991.

- [102] Moretti G., "A Physical Approach to the Numerical Treatment of Boundaries in Gas Dynamics," *Numerical Boundary Condition Procedures*, NASA Conference Publication 2201, pp.73-95, 1981.
- [103] Moretti G., "The λ -Scheme," *Computers & Fluids*, vol.7, pp.191-205, 1979.
- [104] Moretti G., "Importance of Boundary Conditions in the Numerical Treatment of Hyperbolic Equations," *High-Speed Computing in Fluid Dynamics*, The Physics of Fluids Supplement II, pp.13-20, 1969.
- [105] Moretti G., "Experiments on Initial and Boundary Conditions," *Numerical and Physical Aspects of Aerodynamical Flows*, Ed. Cebeci T., vol.1, pp.15-34, Springer-Verlag, 1982.
- [106] Murman E. M., Cole J. D., "Calculation of Plane Steady transonic Flows," *AIAA J.*, vol. 9, pp.114-121, 1971.
- [107] Ni R. H., "A Multiple-Grid Scheme for Solving the Euler Equations," *AIAA J.*, vol.20, pp.1565-1571, 1982.
- [108] Olinger J., Sundstrom A., "Theoretical and Practical Aspects of some Initial Boundary Value Problems in Fluid Dynamics," *SIAM J. Appl. Math.*, vol.35, pp.419-, 1978.
- [109] Orlanski L., "A Simple Boundary Condition for Unbounded Hyperbolic Flows," *J. Comp.Phys.*, vol.21, pp.251-269, 1976.
- [110] Owczarek J. A., *Fundamentals of Gas Dynamics*, International Textbook Company, 1964.
- [111] Poinot T. J., Lele S. K., "Boundary Conditions for Direct Simulations of Compressible Viscous Flows," *J. Comp. Phys.*, vol.101, pp.104-129, 1992.
- [112] Pordal H. S., Khosla P. K., Rubin S. G., "Inviscid Steady-Unsteady Flow Calculations," *Computers & Fluids*, vol.19, pp.93-118, 1991.
- [113] Porter R. W., Coakley J. F., "Use of Characteristics for Boundaries in Time Dependent Finite Difference Analysis of Multidimensional Gas Dynamics," *Int. J. for Numer. Methods in Engineering*, vol.5, pp.91-101, 1972.
- [114] Pulliam T. H., "Artificial Dissipation Models for the Euler Equations," *AIAA J.*, vol.24, pp.1931-1940, 1986.
- [115] Pulliam T. H., "Implicit Finite-Difference Methods for the Euler Equations," *Advances in Computational Transonics*, Ed. Habashi W. G., 1985
- [116] Pulliam T. H., "Implicit Solution Methods in Computational Fluid Dynamics," *Appl. Numerical Math.*, vol.2, pp.441-474, 1986.
- [117] Renaut R. A., "Absorbing Boundary Conditions, Difference Operators, and Stability," *J. Comp. Phys.*, vol.102, pp.236-251, 1992.
- [118] Reynolds A. C., "Boundary Conditions for the Numerical Solution of Wave Propagation problems," *Geophysics*, vol.43, pp.1099-1110, 1978.
- [119] Roe P. L., "Remote Boundary Conditions for Unsteady Multidimensional Aerodynamic Computations," *Computers & Fluids*, vol.17, pp.221-231, 1989.

- [120] Roe P. L., "Discrete Models for the Numerical Analysis of Time-Dependent Multidimensional Gas Dynamics." *J. Comp. Phys.*, vol.63, pp.458-476, 1986.
- [121] Roe P. L., "Fluctuations and Signals-A Framework for Numerical Evolution Problems." *Numerical Methods for Fluid Dynamics*, pp.219-257. Ed. Morton K. W., Baines M. J., 1982.
- [122] Roe P. L., "Upwind Differencing Schemes for Hyperbolic Conservation Laws with Source Terms." *Lecture Notes in Mathematics*, 1270, pp.41-51. Eds. Carasso C., Raviart P.A., Serre D., *Nonlinear Hyperbolic Problems*, Springer-Verlag.
- [123] Richtmyer R. D., Morton K. W., *Difference Methods for Initial-Value Problems*, Interscience Pub., John Wiley, 1967.
- [124] Rizzi A., "Numerical Implementation of Solid-Body Boundary Conditions for the Euler Equations." *Zeitschrift Fur Angewm Mathematik und Mechanik (ZAMM)* vol.58, pp.301-304, 1978.
- [125] Rizzi A. W., Inouye M., "Time-Split Finite-Volume Method for Three- Dimensional Blunt-Body Flow," *AIAA J.*, vol.11, pp.1478-1485, 1973.
- [126] Rudy D. H. and Strikwerda J. C., "Boundary Conditions for Subsonic Compressible Navier-Stokes Calculations," *Computers & Fluids*, vol.9, pp.327-338, 1981.
- [127] Rudy D. H. and Strikwerda J. C., "A Nonreflecting Outflow Boundary Condition for Subsonic Navier-Stokes Calculations," *J. Comp. Phys.*, vol.36, pp.55-70, 1980.
- [128] Rudman S., "One-Dimensional Euler Equation Algorithm with a Very High Asymptotic Convergence Rate," *Computers & Fluids*, vol.17, pp.233-245, 1989.
- [129] Zhokin Y. I., Kompaniets L. A., "A Catalogue of the Extra Boundary Conditions for the Difference Schemes Approximating the Hyperbolic Equations," *Computers & Fluids*, vol.15, pp.119-136, 1987.
- [130] Smith W. D., "A Nonreflecting Plane Boundary for Wave Propagation Problems." *J. Comp. Phys.*, vol.15, pp.492-503, 1974.
- [131] Steger J. L., "Implicit Finite-Difference Simulation of Flow about Arbitrary Two-Dimensional Geometries," *AIAA J.*, vol.16, pp.679-686, 1978.
- [132] Steger J. L., Warming R. F., "Flux Vector Splitting of the Inviscid Gasdynamic Equations with Application to Finite-Difference Methods," *J. Comp. Phys.*, vol.40, pp.263-293, 1981.
- [133] Saxer A. P., Giles M. B., "Quasi-Three-Dimensional Nonreflecting Boundary Conditions for Euler Equations Calculations," *J. of Propulsion and Power*, vol.9, pp.263-271, 1993.
- [134] Schmidt W., Jameson A., "Euler Solvers as an Analysis Tool for Aircraft Aerodynamics," *Advances in Computational Transonics*, Ed. Habashi W. G., 1985
- [135] Stanyukowich K. P., *Unsteady Motion of Continuous Media*, Pergamon Press, 1960.
- [136] Thomas J.L., Salas M.D., "Far-Field Boundary Conditions for Transonic Lifting Solutions to the Euler Equations," *AIAA J.*, vol.24, pp.1074-1080, 1986.

- [137] Tompkins W. T., Bush R. H., "Boundary Treatments for Implicit Solutions to Euler and Navier-Stokes Equations." *Numerical Boundary Condition Procedures*, NASA CP 2201, 1981.
- [138] Turkel E., "Progress in Computational Physics." *Computers & Fluids*, vol.11, pp.121-144, 1983.
- [139] Trefethen L. N., "Instability of Difference Models for Hyperbolic Initial Boundary Value Problems." *Communications on Pure and Applied Math.*, vol. XXXVII, pp.329-367, 1984.
- [140] Trefethen L. N., "Group Velocity in Finite Difference Schemes." *SIAM Review*, vol.24, pp.113-136, 1982.
- [141] Trefethen L. N., "Stability of Finite-Difference Models Containing Two Boundaries or Interfaces." *Mathematics of Computation*, vol.45, pp.279-300, 1985.
- [142] Thompson K. W., "Time Dependent Boundary Conditions for Hyperbolic Systems," *J. Comp. Phys.*, vol.68, pp.1-24, 1987.
- [143] Thompson K. W., "Time Dependent Boundary Conditions for Hyperbolic Systems, II," *J. Copm. Phys.*, vol.89, pp.439-461, 1990.
- [144] Usab, Jr W. J., Murman E. M., "Embedded Mesh Solutions of the Euler Equation Using a Multiple-Grid Method." *Numerical Methods in Aeronautical Fluid Dynamics*, Ed. Roe. P. L., 1981.
- [145] Van Dyke M., *Perturbation Methods in Fluid Mechanics*, Academic press, NY, 1964.
- [146] Van Leer B., Thomas J. L., Roe. P. L., "A Comparison of Numerical Flux Formulas for the Euler and Navier-Stokes Equations," *AIAA paper 87-1104*, 1987.
- [147] Verdon J. M., Caspar J. R., "Subsonic Flow Past an Oscillating Cascade with Finite Mean Flow Deflection," *AIAA J.*, vol.18, pp.540-548, 1980.
- [148] Verhoff A., "Far Field Computational Boundary Conditions for Internal Flow Problems," *NPS67-88-001CR report*, Naval Postgraduate School, 1988.
- [149] Verhoff A., Stookesberry D., Agrawal S., "Far-Field Computational Boundary Conditions for Two-Dimensional External Flow Problems," *AIAA J.*, vol.30, pp.2585-2594, 1992
- [150] Verhoff A., Stookesberry D., Agrawal S., "Second-Order Far-Field Computational Boundary Conditions for Inviscid Flow Problems," *AIAA J.*, vol.30, pp.1268-1276, 1992
- [151] Verhoff A., O'Neil P.J., "A Natural Formulation for Numerical Solution of the Euler Equations," *AIAA paper 84-0163*, 1984.
- [152] Verhoff A., Stookesberry D., Hopping B., Michal T., "Supersonic/Hypersonic Euler Flowfield Prediction Method for Aircraft Configurations," *Applied Computational Aerodynamics*, Ed. Henne P. A., vol.125, Progress in Astronautics and Aeronautics, 1990.
- [153] Vichnevetsky R., "Wave Propagation Analysis of Difference Schemes for Hyperbolic Equations:A review," *Int. J. for Numerical Methods in Fluids*, vol.7, pp.409-452, 1987.

- [154] Vinokur M., "An Analysis of Finite-Difference and Finite-Volume Formulations of Conservation Laws." *J. Comp. Phys.*, vol.81, pp.1-52, 1989.
- [155] Vinokur M., "Conservation Equations of Gas-Dynamics in Curvilinear Coordinate Systems." *J. Comp. Phys.*, vol.14, pp.105-125, 1974.
- [156] Warming R. F., Beam R. M., "On the Construction and Application of Implicit Factored Schemes for Conservation Laws," *SIAM-AMS Proc.*, vol.11, pp.85-129, 1978.
- [157] Whitham G. B., "*Linear and nonlinear waves*", Wiley-Interscience pub., 1974
- [158] Wornom S. F., "Application of Two-Point Implicit Central-Difference Methods to Hyperbolic Systems." *Computers & Fluids*, vol.20, pp.321-331, 1991.
- [159] Wornom S. F., Hafez M. M., "Implicit Conservative Schemes for the Euler Equations." *AIAA J.*, vol.24, pp.215-223, 1986.
- [160] Wornom S. F., Hafez M. M., "A Rule for Selecting Analytical Boundary Conditions for the Conservative Quasi-One-Dimensional Nozzle Flow Calculations." *AIAA paper 84-0431*, AIAA 22nd Aerospace Science Meeting, Reno, Nevada, 1984.
- [161] Wubs F. W., Boerstoeel J. W. and Van Der Wees A. J., "Grid-Size Reduction in flow calculations on infinite domains by higher-order far-field asymptotics in numerical boundary conditions." *J. of Engineering Mathematics*, vol.18, pp.157-177, 1984.
- [162] Yee H. C., "Numerical Approximation of Boundary Conditions with Applications to Inviscid Equations of Gas Dynamics," *NASA Technical Memorandum 81265*, 1981.
- [163] Yee H. C., Beam R. M., Warming R. F., "Stable Boundary Approximations for a Class of Implicit Schemes for the One-Dimensional Inviscid Equations of Gas Dynamics." *AIAA paper 81-1009*, 1981.
- [164] Zucrow M. J., Hoffman J. D., *Gas Dynamics*, vol. II, John Wiley, 1976.

Appendix A

Compatibility Equations for the 2D Euler Equations

The equivalent characteristic form of the time-dependent Euler equations in two spatial dimensions is derived here. First the procedure for the x -momentum equation is discussed and for the y -momentum it can be repeated as well. The x -momentum equation is expressed as

$$\frac{Du}{Dt} + \frac{1}{\rho} \frac{\partial p}{\partial x} = 0, \quad (\text{A.1})$$

Taking the derivative of the isentropic relation yields

$$\begin{aligned} \frac{\partial}{\partial x} \left(\frac{p}{\rho^\gamma} \right) = 0 &\implies \frac{\partial p}{\partial x} = a^2 \frac{\partial \rho}{\partial x}, \\ \frac{\partial p}{\partial x} &= \frac{Dp}{D\rho} \frac{\partial \rho}{\partial x}. \end{aligned} \quad (\text{A.2})$$

Introducing relation (A.2) into the equation (A.1) results in

$$\frac{Du}{Df} \frac{Df}{Dt} + \frac{1}{\rho} \frac{Dp}{D\rho} \frac{\partial \rho}{\partial x} = 0. \quad (\text{A.3})$$

Substituting $\phi = \frac{Df}{Dt}$ in the equation (A.3) gives

$$\frac{Du}{Df} \phi + \frac{1}{\rho} \frac{Dp}{D\rho} \frac{\partial \rho}{\partial x} = 0. \quad (\text{A.4})$$

Taking the partial derivatives on both sides of the characteristic front $f(x, y, t) = 0$ leads to a general relationship called the kinematic condition [135]. This relation for

ρ is

$$\frac{\frac{\partial \rho}{\partial t}}{\frac{\partial f}{\partial t}} = \frac{\frac{\partial \rho}{\partial x}}{\frac{\partial f}{\partial x}} = \frac{\frac{\partial \rho}{\partial y}}{\frac{\partial f}{\partial y}} = \frac{D\rho}{Df}. \quad (\text{A.5})$$

From the kinematic condition (A.5), one gets

$$\frac{\partial \rho}{\partial x} = \frac{D\rho}{Df} \frac{\partial f}{\partial x}. \quad (\text{A.6})$$

Introducing the relation (A.6) into the x -momentum equation (A.4) yields

$$\frac{Du}{Df} \phi + \frac{1}{\rho} \frac{Dp}{D\rho} \frac{D\rho}{Df} \frac{\partial f}{\partial x} = 0. \quad (\text{A.7})$$

or after simplification

$$\phi Du + \frac{1}{\rho} \frac{\partial f}{\partial x} Dp = 0. \quad (\text{A.8})$$

In a similar fashion the following relation for the y -momentum equation can be resulted

$$\phi Dv + \frac{1}{\rho} \frac{\partial f}{\partial y} Dp = 0. \quad (\text{A.9})$$

Now consider the continuity equation expressed as

$$\frac{D\rho}{Dt} + \rho \left(\frac{\partial u}{\partial x} + \frac{\partial v}{\partial y} \right) = 0. \quad (\text{A.10})$$

From kinematic conditions (A.5) for u , v and ρ , one could write

$$\frac{\partial u}{\partial x} = \frac{Du}{Df} \frac{\partial f}{\partial x}, \quad \frac{\partial v}{\partial y} = \frac{Dv}{Df} \frac{\partial f}{\partial y}, \quad \frac{D\rho}{Dt} = \frac{D\rho}{Df} \frac{Df}{Dt}. \quad (\text{A.11})$$

Considering the relations (A.11), the continuity equation (A.10) can be expressed as

$$\frac{D\rho}{Df} \phi + \rho \left(\frac{Du}{Df} \frac{\partial f}{\partial x} + \frac{Dv}{Df} \frac{\partial f}{\partial y} \right) = 0, \quad (\text{A.12})$$

simplifying the Df yields

$$\rho \frac{\partial f}{\partial x} Du + \rho \frac{\partial f}{\partial y} Dv + \phi D\rho = 0. \quad (\text{A.13})$$

Differentiating the isentropic relation yields

$$\frac{D}{Dt} \left(\frac{p}{\rho^\gamma} \right) = 0 \implies \frac{Dp}{Dt} - a^2 \frac{D\rho}{Dt} = 0. \quad (\text{A.14})$$

Expressing the equation (A.14) with respect to ϕ , one gets

$$\frac{Dp}{Df} \frac{Df}{Dt} - a^2 \frac{D\rho}{Df} \frac{Df}{Dt} = 0. \quad (\text{A.15})$$

or

$$\frac{Dp}{Df} \phi - a^2 \frac{D\rho}{Df} \phi = 0. \quad (\text{A.16})$$

Finally the continuity equation (A.13), becomes

$$\phi Dp - a^2 \phi D\rho = 0.$$

Thence system of time-dependent Euler equations is equivalent to

$$\begin{cases} \phi Du + 0Dv + \frac{1}{\rho} \frac{\partial f}{\partial x} Dp + 0D\rho = 0 \\ 0Du + \phi Dv + \frac{1}{\rho} \frac{\partial f}{\partial y} Dp + 0D\rho = 0 \\ \rho \frac{\partial f}{\partial x} Du + \rho \frac{\partial f}{\partial y} Dv + 0Dp + \phi D\rho = 0 \\ 0Du + 0Dv + \phi Dp - a^2 \phi D\rho = 0 \end{cases} \quad (\text{A.17})$$

In matrix form the system (A.17) reads

$$\begin{bmatrix} \phi & 0 & \frac{1}{\rho} \frac{\partial f}{\partial x} & 0 \\ 0 & \phi & \frac{1}{\rho} \frac{\partial f}{\partial y} & 0 \\ \rho \frac{\partial f}{\partial x} & \rho \frac{\partial f}{\partial y} & 0 & \phi \\ 0 & 0 & \phi & -a^2 \phi \end{bmatrix} \begin{bmatrix} Du \\ Dv \\ Dp \\ D\rho \end{bmatrix} = 0. \quad (\text{A.18})$$

In order to have non-zero solution, the determinant of the coefficient matrix should be zero. Thereby solving the equation for the determinant it follows that

$$\phi^2 \{ \phi^2 - a^2 [(\frac{\partial f}{\partial x})^2 + (\frac{\partial f}{\partial y})^2] \} = 0, \quad (\text{A.19})$$

which has the trivial solution

$$\phi = 0, \quad (\text{A.20})$$

and other roots as

$$\phi = \pm a \sqrt{(\frac{\partial f}{\partial x})^2 + (\frac{\partial f}{\partial y})^2}. \quad (\text{A.21})$$

Appendix B

Natural Coordinate Formulation of the Euler Equations

In order to derive the Euler equations in natural coordinate system (or streamline coordinates) one can start from the Figure B.1, in which the upcoming relations hold between the Cartesian and streamline coordinates:

$$\begin{bmatrix} dx \\ dy \end{bmatrix} = \begin{bmatrix} \cos \theta & -\sin \theta \\ \sin \theta & \cos \theta \end{bmatrix} \begin{bmatrix} ds \\ dn \end{bmatrix}, \quad (\text{B.1})$$

or reversely

$$\begin{bmatrix} ds \\ dn \end{bmatrix} = \begin{bmatrix} \cos \theta & \sin \theta \\ -\sin \theta & \cos \theta \end{bmatrix} \begin{bmatrix} dx \\ dy \end{bmatrix}. \quad (\text{B.2})$$

The differential operators can be written as

$$\begin{bmatrix} \partial/\partial s \\ \partial/\partial n \end{bmatrix} = \begin{bmatrix} \cos \theta & \sin \theta \\ -\sin \theta & \cos \theta \end{bmatrix} \begin{bmatrix} \partial/\partial x \\ \partial/\partial y \end{bmatrix}, \quad (\text{B.3})$$

and

$$\begin{bmatrix} \partial/\partial x \\ \partial/\partial y \end{bmatrix} = \begin{bmatrix} \cos \theta & -\sin \theta \\ \sin \theta & \cos \theta \end{bmatrix} \begin{bmatrix} \partial/\partial s \\ \partial/\partial n \end{bmatrix}. \quad (\text{B.4})$$

The following relations stand for the orthonormal unit vectors, which are depicted in Figure B.1

$$\begin{bmatrix} \mathbf{i}_s \\ \mathbf{i}_n \end{bmatrix} = \begin{bmatrix} \cos \theta & \sin \theta \\ -\sin \theta & \cos \theta \end{bmatrix} \begin{bmatrix} \mathbf{i} \\ \mathbf{j} \end{bmatrix} \quad (\text{B.5})$$

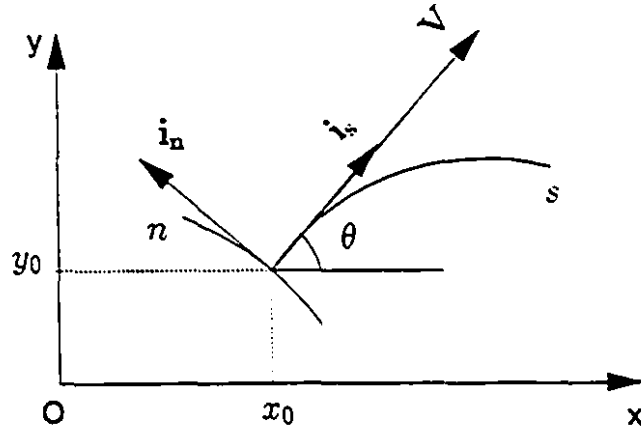


Figure B.1: Cartesian and Natural coordinates.

or reversely

$$\begin{bmatrix} \mathbf{i} \\ \mathbf{j} \end{bmatrix} = \begin{bmatrix} \cos \theta & -\sin \theta \\ \sin \theta & \cos \theta \end{bmatrix} \begin{bmatrix} \mathbf{i}_s \\ \mathbf{i}_n \end{bmatrix} \quad (\text{B.6})$$

By the aid of aforementioned relations, the derivatives of the unit vectors appearing in the calculations are:

$$\begin{aligned} \frac{\partial \mathbf{i}_s}{\partial t} &= \mathbf{i}_n \frac{\partial \theta}{\partial t}, & \frac{\partial \mathbf{i}_s}{\partial s} &= \mathbf{i}_n \frac{\partial \theta}{\partial s}, \\ \frac{\partial \mathbf{i}_n}{\partial n} &= \mathbf{i}_n \frac{\partial \theta}{\partial s}, & \frac{1}{R_c} &= \frac{\partial \theta}{\partial s}, \end{aligned} \quad (\text{B.7})$$

where R_c shows the radius of curvature of the streamline. The velocity vector is always tangent to the streamline in which

$$\mathbf{V} = q \mathbf{i}_s. \quad (\text{B.8})$$

In natural coordinate system the material derivative and gradient operators take the form

$$\begin{aligned} \frac{D}{Dt} &= \frac{\partial}{\partial t} + q \frac{\partial}{\partial s}, \\ \nabla &= \frac{\partial}{\partial s} \mathbf{i}_s + \frac{\partial}{\partial n} \mathbf{i}_n. \end{aligned} \quad (\text{B.9})$$

In coordinate-free form, the continuity and momentum equations can be expressed as

$$\frac{D\rho}{Dt} + \rho \nabla \cdot \mathbf{V} = 0, \quad (\text{B.10})$$

$$\frac{DV}{Dt} + \frac{1}{\rho} \nabla p = 0. \quad (\text{B.11})$$

Considering the well-known gas dynamic relations for isentropic flow of an ideal gas [110]

$$\frac{D\rho}{\rho} = \frac{2}{\gamma - 1} \frac{Da}{a}. \quad (\text{B.12})$$

$$\frac{Dp}{p} = \frac{2\gamma}{\gamma - 1} \frac{Da}{a}. \quad (\text{B.13})$$

After substituting from equation (B.12) into the continuity equation (B.10)

$$\frac{Da}{Dt} + \frac{\gamma - 1}{2} a \nabla \cdot \mathbf{V} = 0 \quad (\text{B.14})$$

The divergence of the velocity field, which will be used later in the continuity equation is calculated by using the rules from tensor analysis

$$\begin{aligned} \nabla \cdot \mathbf{V} &= \mathbf{i}_s \cdot \frac{\partial}{\partial s} (q \mathbf{i}_s) + \mathbf{i}_n \cdot \frac{\partial}{\partial n} (q \mathbf{i}_s) \\ &= \mathbf{i}_s \cdot \left[\mathbf{i}_s \frac{\partial q}{\partial s} + q \frac{\partial \mathbf{i}_s}{\partial s} \right] + \mathbf{i}_n \cdot \left[\mathbf{i}_s \frac{\partial q}{\partial n} + q \frac{\partial \mathbf{i}_s}{\partial n} \right]. \end{aligned} \quad (\text{B.15})$$

By doing the expansions of the vector derivatives and considering the corresponding relations one has

$$\nabla \cdot \mathbf{V} = \frac{\partial q}{\partial s} + q \mathbf{i}_s \cdot \frac{\mathbf{i}_n}{R_c} + \mathbf{i}_n \cdot \mathbf{i}_s \frac{\partial q}{\partial n} + \mathbf{i}_n \cdot q \frac{\partial \theta}{\partial n} \mathbf{i}_n. \quad (\text{B.16})$$

considering that

$$\frac{\partial \mathbf{i}_s}{\partial s} = \frac{\mathbf{i}_n}{R_c}, \quad \mathbf{i}_s \cdot \mathbf{i}_n = 0. \quad (\text{B.17})$$

Finally the velocity divergence reduces to

$$\nabla \cdot \mathbf{V} = \frac{\partial q}{\partial s} + q \frac{\partial \theta}{\partial n}. \quad (\text{B.18})$$

Introducing the velocity divergence (B.18) into the continuity equation (B.10) yields

$$\frac{\partial a}{\partial t} + q \frac{\partial a}{\partial s} + \frac{\gamma - 1}{2} a \left(\frac{\partial q}{\partial s} + q \frac{\partial \theta}{\partial n} \right) = 0. \quad (\text{B.19})$$

The material derivative in the momentum equation (B.11) reads

$$\frac{DV}{Dt} = \frac{D}{Dt}(q\mathbf{i}_s) = \frac{\partial}{\partial t}(q\mathbf{i}_s) + q\frac{\partial}{\partial s}(q\mathbf{i}_s).$$

By expanding the derivatives of the velocity vector, one gets

$$\frac{DV}{Dt} = \left(\frac{\partial q}{\partial t}\mathbf{i}_s + q\frac{\partial \mathbf{i}_s}{\partial t}\right) + \left(q\frac{\partial q}{\partial s}\mathbf{i}_s + q^2\frac{\partial \mathbf{i}_s}{\partial s}\right).$$

Considering the vector derivatives

$$\frac{\partial \mathbf{i}_s}{\partial t} = \mathbf{i}_n \frac{\partial \theta}{\partial t}, \quad \frac{\partial \mathbf{i}_s}{\partial s} = \mathbf{i}_n \frac{\partial \theta}{\partial s},$$

one could write

$$\frac{DV}{Dt} = \left(\frac{\partial q}{\partial t} + q\frac{\partial q}{\partial s}\right)\mathbf{i}_s + \left(q\frac{\partial \theta}{\partial t} + q^2\frac{\partial \theta}{\partial s}\right)\mathbf{i}_n. \quad (\text{B.20})$$

Pressure gradient is expressed as

$$\nabla p = \frac{\partial p}{\partial s}\mathbf{i}_s + \frac{\partial p}{\partial n}\mathbf{i}_n. \quad (\text{B.21})$$

Introducing the equations (B.20) and (B.21) into the coordinate-free momentum equation, results in the s - and n -momentum equations respectively

$$\frac{\partial q}{\partial t} + q\frac{\partial q}{\partial s} + \frac{1}{\rho}\frac{\partial p}{\partial s} = 0, \quad (\text{B.22})$$

$$q\frac{\partial \theta}{\partial t} + q^2\frac{\partial \theta}{\partial s} + \frac{1}{\rho}\frac{\partial p}{\partial n} = 0. \quad (\text{B.23})$$

When the Riemann variables $R = q + \frac{2}{\gamma-1}a$ and $Q = q - \frac{2}{\gamma-1}a$ (derived in the Chapter 2) are introduced into the continuity equation (B.19) and s -momentum equation (B.22), also the pressure gradients are replaced according to $\frac{1}{\rho}\frac{\partial p}{\partial s} = \frac{2}{\gamma-1}a\frac{\partial a}{\partial s}$ and $\frac{1}{\rho}\frac{\partial p}{\partial n} = \frac{2}{\gamma-1}a\frac{\partial a}{\partial n}$, in the same equations it follows that

$$\begin{aligned} \frac{\partial(R-Q)}{\partial t} + \frac{R+Q}{2}\frac{\partial(R-Q)}{\partial s} + \frac{\gamma-1}{4}(R-Q)\frac{\partial(R+Q)}{\partial s} &= -\frac{\gamma-1}{4}(R^2-Q^2)\frac{\partial \theta}{\partial n}, \\ \frac{\partial(R+Q)}{\partial t} + \frac{R+Q}{2}\frac{\partial(R+Q)}{\partial s} + \frac{\gamma-1}{4}(R-Q)\frac{\partial(R-Q)}{\partial s} &= 0. \end{aligned} \quad (\text{B.24})$$

Then, above equations in terms of R and Q are added and subtracted as

$$\begin{aligned} \frac{\partial R}{\partial t} + (\alpha R + \beta Q)\frac{\partial R}{\partial s} &= -\frac{\gamma-1}{8}(R^2-Q^2)\frac{\partial \theta}{\partial n}, \\ \frac{\partial Q}{\partial t} + (\beta R + \alpha Q)\frac{\partial Q}{\partial s} &= +\frac{\gamma-1}{8}(R^2-Q^2)\frac{\partial \theta}{\partial n}, \end{aligned} \quad (\text{B.25})$$

The n -momentum equation (B.23), first divided by q then the equivalents $q = \frac{1}{2}(R+Q)$ and $\frac{1}{q} \frac{\partial q}{\partial t} = \frac{2}{\gamma-1} a \frac{\partial a}{\partial t}$ are introduced, it leads to

$$\frac{\partial \theta}{\partial t} + \frac{R+Q}{2} \frac{\partial \theta}{\partial s} = -\frac{\gamma-1}{4} \frac{R-Q}{R+Q} \frac{\partial(R-Q)}{\partial n}. \quad (\text{B.26})$$

Appendix C

Entropy Based formulation of the Euler Equations

Considering the thermodynamic relation for pressure, one can start with

$$p = p(\rho, S), \quad (\text{C.1})$$

the partial derivative of the pressure as a function of density and entropy, with respect to the streamline coordinate, s , can be expressed as

$$\frac{\partial p}{\partial s} = \left(\frac{\partial p}{\partial \rho}\right)_s \frac{\partial \rho}{\partial s} + \left(\frac{\partial p}{\partial S}\right)_\rho \frac{\partial S}{\partial s}, \quad (\text{C.2})$$

or

$$\frac{\partial p}{\partial s} = a^2 \frac{\partial \rho}{\partial s} + \left(\frac{\partial p}{\partial S}\right)_\rho \frac{\partial S}{\partial s}. \quad (\text{C.3})$$

Note that for isentropic flows only the first term in the equation (C.2) would exist. The s -momentum equation in the streamline coordinate system reads

$$\frac{\partial q}{\partial t} + q \frac{\partial q}{\partial s} + \frac{1}{\rho} \frac{\partial p}{\partial s} = 0. \quad (\text{C.4})$$

Now one could introduce the equivalent for the pressure derivative in equation (C.4), from the equation (C.3) as

$$\frac{\partial q}{\partial t} + q \frac{\partial q}{\partial s} + \frac{a^2}{\rho} \frac{\partial \rho}{\partial s} + \frac{1}{\rho} \left(\frac{\partial p}{\partial S}\right)_\rho \frac{\partial S}{\partial s} = 0. \quad (\text{C.5})$$

In order to find the equivalents of the third and fourth terms in the equation (C.5), we start from the first law of thermodynamics, which reads

$$TdS = c_p \frac{dT}{T} - \frac{dp}{\rho}, \quad dh = c_p dT. \quad (C.6)$$

From the equation of state of an ideal gas, one could come up with

$$dS = c_p \frac{dT}{T} - \frac{dp}{\rho T}. \quad (C.7)$$

$$\frac{dT}{T} = \frac{dp}{p} - \frac{d\rho}{\rho}. \quad (C.8)$$

Having the relation $c_p = \frac{\gamma}{\gamma-1}R$ for specific heat at constant pressure and R being the universal gas constant, also considering the equation of state of an ideal gas, one gets

$$dS = \frac{R}{\gamma-1} \left[\frac{dp}{p} - \gamma \frac{d\rho}{\rho} \right] \quad (C.9)$$

From equation (C.1), the total derivative of pressure can be written as

$$dp = \left(\frac{\partial p}{\partial S} \right)_\rho dS + \left(\frac{\partial p}{\partial \rho} \right)_S d\rho. \quad (C.10)$$

Using the equation (C.9), the total derivative of the pressure is calculated as

$$dp = \frac{\gamma-1}{R} p dS + \gamma \frac{p}{\rho} d\rho. \quad (C.11)$$

Comparing the equations (C.10) and (C.11) yields the following relations

$$\begin{aligned} \left(\frac{\partial p}{\partial S} \right)_\rho &= \frac{\gamma-1}{R} p \\ \left(\frac{\partial p}{\partial \rho} \right)_S &= \gamma \frac{p}{\rho} = a^2. \end{aligned} \quad (C.12)$$

Using equations (C.12) and definition of c_p , it follows that

$$\frac{1}{\rho} \left(\frac{\partial p}{\partial S} \right)_\rho = \frac{a^2}{c_p}. \quad (C.13)$$

Now, we are to find an equivalent expression for the term, $\frac{a^2}{\rho} \frac{\partial \rho}{\partial s}$. Considering the relation for the speed of sound and the isentropic relation as

$$a^2 = \gamma \frac{p}{\rho}, \quad \frac{p}{\rho^\gamma} = \text{const}, \quad (C.14)$$

thereby eliminating the pressure between the above relations and taking the derivative with respect to s and simplifying, yields

$$\frac{a^2}{\rho} \frac{\partial \rho}{\partial s} = \frac{2}{\gamma - 1} a \frac{\partial a}{\partial s}. \quad (\text{C.15})$$

Therefore, the s -momentum equation will have the following form, in which the entropy is present

$$\frac{\partial q}{\partial t} + q \frac{\partial q}{\partial s} + \frac{2}{\gamma - 1} a \frac{\partial a}{\partial s} + \frac{a^2}{c_p} \frac{\partial S}{\partial s} = 0. \quad (\text{C.16})$$

This formulation together with continuity equation forms the basis for the Euler equations in terms of the extended Riemann variables in natural coordinate system.

The derivation of the extended Riemann variables is given below for 1-D flows. For the streamline coordinate system the procedure is similar. From [110], one has

$$\pm du + \frac{2}{\gamma - 1} da = \frac{1}{\gamma} ad\left(\frac{S'}{R}\right), \quad (\text{C.17})$$

where S' and R represent the entropy and gas constant respectively. Integrating the equations (C.17) and arranging, yields

$$\pm u + \left[\frac{2}{\gamma - 1} - \frac{S'}{\gamma R} \right] a = \text{const}_{1,2}, \quad (\text{C.18})$$

where we define the modified entropy as

$$S = \frac{2}{\gamma - 1} - \frac{S'}{\gamma R}, \quad (\text{C.19})$$

where the entropy S' has the expression similar to equation (C.9), hence, using the equation (C.9) in the equation (C.19), after differentiation and integration leads to

$$S = \frac{2}{\gamma - 1} - \frac{1}{\gamma(\gamma - 1)} d \ln \frac{p}{\rho^\gamma}. \quad (\text{C.20})$$

Also, one can extract the extended Riemann variables from equations (C.18) as

$$R = u + Sa, \quad Q = u - Sa. \quad (\text{C.21})$$

Appendix D

Riemann Variable Formulation of the Euler Equations

In order to deal with the true information propagations, the unsteady Euler equations of motion in natural coordinate system are employed. Formulation begins with the continuity and s-momentum equations. One can start with the continuity equation which reads

$$\frac{\partial a}{\partial t} + q \frac{\partial a}{\partial s} = -\frac{\gamma-1}{2} a \frac{\partial q}{\partial s} - \frac{\gamma-1}{2} a q \frac{\partial \theta}{\partial n}, \quad (\text{D.1})$$

multiplying both sides by S and then adding the zero term $a \frac{DS}{Dt} = a \left[\frac{\partial S}{\partial t} + q \frac{\partial S}{\partial s} \right] = 0$ to the left hand side results in

$$S \left(\frac{\partial a}{\partial t} + q \frac{\partial a}{\partial s} \right) + a \frac{DS}{Dt} = -\frac{\gamma-1}{2} a S \frac{\partial q}{\partial s} - \frac{\gamma-1}{2} a q S \frac{\partial \theta}{\partial n}, \quad (\text{D.2})$$

rearranging the terms in the left hand side and adding the term $a \frac{\partial q}{\partial s}$ to both sides of equation (D.2), yields

$$\frac{\partial(Sa)}{\partial t} + q \frac{\partial(Sa)}{\partial s} + a \frac{\partial q}{\partial s} = a \frac{\partial q}{\partial s} - \frac{\gamma-1}{2} a S \frac{\partial q}{\partial s} - \frac{\gamma-1}{2} a q S \frac{\partial \theta}{\partial n}. \quad (\text{D.3})$$

One could introduce for the quantities Sa and q the following relations (see Appendix C)

$$R - Q = 2aS, \quad R + Q = 2q, \quad (\text{D.4})$$

where the Riemann variables have been modified to include the entropy effect. For their derivation one may start with the formulations given in [110]. Hence, the equation (D.3) becomes

$$\frac{\partial(R-Q)}{\partial t} + q \frac{\partial(R-Q)}{\partial s} + a \frac{\partial(R+Q)}{\partial s} = -\frac{\gamma-1}{2} a \left(S - \frac{2}{\gamma-1}\right) (2) \frac{\partial q}{\partial s} - (2) \frac{\gamma-1}{2} a q S \frac{\partial \theta}{\partial n}. \quad (D.5)$$

The equation (D.5) is the continuity equation which was expressed in terms of the left- and right-propagating Riemann variables, defined in natural coordinate system. Now we are going to convert the s -momentum equation in terms of the Riemann variables. The s -momentum equation in natural coordinate system reads

$$\frac{\partial q}{\partial t} + q \frac{\partial q}{\partial s} + \frac{2}{\gamma-1} a \frac{\partial a}{\partial s} + a^2 \frac{\partial(S'/c_p)}{\partial s} = 0, \quad (D.6)$$

The entropy can be set as following (see Appendix C)

$$S = \frac{S'}{c_p} = \frac{2}{\gamma-1} - \frac{1}{\gamma(\gamma-1)} \ln \frac{p}{\rho^\gamma}, \quad (D.7)$$

The entropy S on the far field boundary is measured with respect to the free-stream entropy, denoted by S_∞ . So, using the relation (D.7), one gets

$$\frac{\partial q}{\partial t} + q \frac{\partial q}{\partial s} + a^2 \frac{\partial S}{\partial s} = -\frac{2}{\gamma-1} a \frac{\partial a}{\partial s}, \quad (D.8)$$

adding the term $aS \frac{\partial S}{\partial s}$ to both sides of the equation (D.8) and rearranging, results

$$\frac{\partial q}{\partial t} + q \frac{\partial q}{\partial s} + a \left[a \frac{\partial S}{\partial s} + S \frac{\partial a}{\partial s} \right] = a \left(S - \frac{2}{\gamma-1} \right) \frac{\partial a}{\partial s}, \quad (D.9)$$

Introducing from relations (D.4), for the velocity q and rearranging the terms, one has

$$\frac{\partial(R+Q)}{\partial t} + q \frac{\partial(R+Q)}{\partial s} + a \frac{\partial(R-Q)}{\partial s} = \frac{\gamma-1}{2} a \left(S - \frac{2}{\gamma-1} \right) (2) \frac{2}{\gamma-1} \frac{\partial a}{\partial s}. \quad (D.10)$$

Equation (D.10) expresses the s -momentum equation in terms of the Riemann variables. Now, when the equations (D.5) and (D.10) are added and subtracted in order

to give the following equations, partly decoupled in terms of the left- and right-propagating Riemann variables

$$\frac{\partial R}{\partial t} \div (q \div a) \frac{\partial R}{\partial s} = -\frac{\gamma-1}{2} a \left(S - \frac{2}{\gamma-1} \right) \left(\frac{\partial q}{\partial s} - \frac{2}{\gamma-1} \frac{\partial a}{\partial s} \right) - \frac{\gamma-1}{2} a q S \frac{\partial \theta}{\partial n}, \quad (\text{D.11})$$

$$\frac{\partial Q}{\partial t} \div (q - a) \frac{\partial Q}{\partial s} = \frac{\gamma-1}{2} a \left(S - \frac{2}{\gamma-1} \right) \left(\frac{\partial q}{\partial s} + \frac{2}{\gamma-1} \frac{\partial a}{\partial s} \right) + \frac{\gamma-1}{2} a q S \frac{\partial \theta}{\partial n}. \quad (\text{D.12})$$

Appendix E

Kinematic Conditions for the Compressible Flows

In the case of weak discontinuities, when the derivatives become discontinuous in various aspects, displacing and deforming, lying on one single plane, that condition requires the satisfaction of certain relations between the jumps of the specified derivatives. These are a consequence of geometric (or kinematics image of the movement) and appear independently of the gasdynamic relations. These conditions are called conditions of kinematic compatibility. To satisfy this condition, we assume that the function $\Psi(x, y, t)$ is continuous in the whole space occupied by the fluid, but its first derivatives on a plane represented by

$$f(x, y, t) = 0, \quad (\text{E.1})$$

are discontinuous. Then we define a continuous function Ψ , with continuous derivatives on the surface (E.1)

$$\Psi(x, y, t) = \text{const.} \quad (\text{E.2})$$

Taking the derivative of the surface (E.1), one gets

$$d\Psi = \frac{\partial\Psi}{\partial x}dx + \frac{\partial\Psi}{\partial y}dy + \frac{\partial\Psi}{\partial t}dt = 0, \quad (\text{E.3})$$

which represent the only condition that our coordinates have to satisfy along the surface. Considering the relations (E.3) and (E.1), one can write

$$\nabla \Psi \cdot dr = 0, \quad \nabla f \cdot dr = 0. \quad (\text{E.4})$$

Comparing relations (E.3) and (E.5) it follows that, at all the points of the discontinuity plane and at any time the upcoming relation holds

$$\frac{\frac{\partial \Psi}{\partial x}}{\frac{\partial f}{\partial x}} = \frac{\frac{\partial \Psi}{\partial y}}{\frac{\partial f}{\partial y}} = \frac{\frac{\partial \Psi}{\partial t}}{\frac{\partial f}{\partial t}} = \mu_{\Psi}, \quad (\text{E.5})$$

where $\mu_{\Psi} = \frac{d\Psi}{df}$ is a function of coordinates and time.

We now consider the function $\Psi(x, y, t)$, which is continuous in the whole (x, y, t) space and has continuous derivatives in space and time. The relation (E.5) is called the kinematic condition. For the case of Euler equations, in the relation (E.5), Ψ can be any of the flow parameters like ρ , u etc. Interested reader is referred to [77, 135].

Appendix F

Roe's Estimation of the Outgoing Wave Direction

In the far field region away from the solid boundaries the flow variables can be expanded as

$$\begin{aligned}\rho &= \rho_\infty + \epsilon\rho_1 + \dots, \\ u &= u_\infty + \epsilon u_1 + \dots, \\ v &= v_\infty + \epsilon v_1 + \dots, \\ p &= p_\infty + \epsilon p_1 + \dots,\end{aligned}\tag{F.1}$$

where v_∞ is usually zero. Insertion of expansions (F.1) into the system of equations (5.2) gives

$$\begin{aligned}\frac{\partial p_1}{\partial t} + u_\infty \frac{\partial p_1}{\partial x} + \rho_\infty \left(\frac{\partial u_1}{\partial x} + \frac{\partial v_1}{\partial y} \right) &= 0, \\ \frac{\partial u_1}{\partial t} + u_\infty \frac{\partial u_1}{\partial x} + \frac{1}{\rho_\infty} \frac{\partial p_1}{\partial x} &= 0, \\ \frac{\partial v_1}{\partial t} + u_\infty \frac{\partial v_1}{\partial x} + \frac{1}{\rho_\infty} \frac{\partial p_1}{\partial y} &= 0, \\ \frac{\partial p_1}{\partial t} + u_\infty \frac{\partial p_1}{\partial x} + \rho_\infty a_\infty^2 \left(\frac{\partial u_1}{\partial x} + \frac{\partial v_1}{\partial y} \right) &= 0.\end{aligned}\tag{F.2}$$

Equations (F.2) are partly uncoupled, in that p_1 does not appear in the last three but could be found after these have been solved. From now on the first equation is

excluded. An equation holding in a characteristic plane can be obtained by multiplying the second and third equations by $\rho_\infty a_\infty \cos \varphi$, and $\rho_\infty a_\infty \sin \varphi$ respectively and adding them to fourth equation, the result is

$$\begin{aligned} & \left[\frac{\partial p_1}{\partial t} + (u_\infty + a_\infty \cos \varphi) \frac{\partial p_1}{\partial x} + a_\infty \sin \varphi \frac{\partial p_1}{\partial y} \right] + \\ & \rho_\infty a_\infty \cos \varphi \left[\frac{\partial u_1}{\partial t} + (u_\infty + \frac{a_\infty}{\cos \varphi}) \frac{\partial u_1}{\partial x} \right] + \\ & \rho_\infty a_\infty \sin \varphi \left[\frac{\partial v_1}{\partial t} + u_\infty \frac{\partial v_1}{\partial x} + \frac{a_\infty}{\sin \varphi} \frac{\partial v_1}{\partial y} \right] = 0. \end{aligned} \quad (\text{F.3})$$

The equation (F.3) can be arranged as

$$\begin{aligned} & \left[\frac{\partial}{\partial t} + (u_\infty + a_\infty \cos \varphi) \frac{\partial}{\partial x} + a_\infty \sin \varphi \frac{\partial}{\partial y} \right] [p_1 + \rho_\infty a_\infty (u_1 \cos \varphi + v_1 \sin \varphi)] + \\ & \rho_\infty a_\infty^2 \left[\sin \varphi \frac{\partial}{\partial x} - \cos \varphi \frac{\partial}{\partial y} \right] (u_1 \sin \varphi - v_1 \cos \varphi) = 0. \end{aligned} \quad (\text{F.4})$$

The first operator in equation (F.4) acts along a particular bicharacteristics (TP in Figure F.1) on the sum of pressure plus $\rho_\infty a_\infty$ times the component of velocity in the direction φ . The second operator in equation (F.4) acts only in space, perpendicularly to the direction φ , on the velocity component in its own direction (PQ). Bayliss and Turkel [7] combined the equations (F.2), and got the following wave equation

$$\frac{\partial^2 p_1}{\partial t^2} + 2u_\infty \frac{\partial^2 p_1}{\partial x \partial t} - (a_\infty^2 - u_\infty^2) \frac{\partial^2 p_1}{\partial x^2} - a_\infty^2 \frac{\partial^2 p_1}{\partial y^2} = 0. \quad (\text{F.5})$$

Equation (F.5) is transformed which implies that p_1 obeys a regular wave equation

$$\frac{\partial^2 p_1}{\partial \tau^2} - \frac{\partial^2 p_1}{\partial \zeta^2} - \frac{\partial^2 p_1}{\partial y^2} = 0, \quad (\text{F.6})$$

where

$$\begin{aligned} \zeta = \frac{x}{B}, \quad y = y, \quad \tau = Ba_\infty t + M_\infty \frac{x}{B}, \\ M_\infty = \frac{u_\infty}{a_\infty}, \quad B = \sqrt{1 - M_\infty^2}. \end{aligned} \quad (\text{F.7})$$

By changing the variables, equation (F.6) can be written as

$$\frac{\partial^2 p_1}{\partial \tau^2} - \frac{\partial^2 p_1}{\partial r^2} - \frac{1}{r} \frac{\partial p_1}{\partial r} - \frac{1}{r^2} \frac{\partial^2 p_1}{\partial \nu^2} = 0. \quad (\text{F.8})$$

which presents a decaying outgoing solution. Also, equation (F.12) satisfies exactly

$$\frac{\partial p_1}{\partial \tau} + \frac{\partial p_1}{\partial r} + \frac{p_1}{2r} = 0. \quad (\text{F.13})$$

Equation (F.13) holds along an outgoing bicharacteristic of equation (F.11). Under the transformation inverse to equation (F.7), the bicharacteristics of equation (F.11) should become the bicharacteristics of the system (F.2). In Cartesian coordinates the equation (F.13) is written as

$$\frac{1}{a_\infty B} \left(1 - \frac{M_\infty x}{Br}\right) \frac{\partial p_1}{\partial t} + \frac{1}{r} \left(x \frac{\partial p_1}{\partial x} + y \frac{\partial p_1}{\partial y} + \frac{p_1}{2}\right) = 0. \quad (\text{F.14})$$

The distinguished bicharacteristic equation (F.14) then becomes

$$\frac{\partial p_1}{\partial t} + \frac{B^2 a_\infty}{Br - M_\infty x} \left[x \frac{\partial p_1}{\partial x} + y \frac{\partial p_1}{\partial y} + \frac{1}{2}(p_1 - p_\infty) \right] = 0 \quad (\text{F.15})$$

The differential operator in equation (F.15) coincides with the bicharacteristic operator in equation (F.3) if one chooses

$$\sin \varphi = \frac{B^2 y}{Br - M_\infty x}, \quad (\text{F.16})$$

where the x and y show the coordinates of the grid points on the far field boundary.

Appendix G

Characteristic Interpolation at Boundaries

The characteristic interpolation which was used in the previous Chapters is a stable than the extrapolation for approximating the unknown values. Numerical experiments proved the stability of the characteristic interpolation method. Here the one-dimensional case is considered, however it can be used for two-dimensional flows in order to interpolate the selected bicharacteristics. Considering the Figure G.1, the slopes of the left-propagating Riemann variables at the grid points i and $i + 1$ are typically known from the previous time step. From characteristic relations their slopes are

$$m_i^- = \frac{1}{u_i - a_i}, \quad m_{i+1}^- = \frac{1}{u_{i+1} - a_{i+1}}, \quad (\text{G.1})$$

where u_i, u_{i+1} and a_i, a_{i+1} show the velocities and sound speeds at grid points i and $i + 1$ respectively.

At a certain time (Δt), the left-propagating Riemann variable, Q , does not usually pass exactly through the grid points i or $i + 1$. It is somewhere between (at point M), and has the slope

$$m_M^- = \frac{1}{u_M - a_M}. \quad (\text{G.2})$$

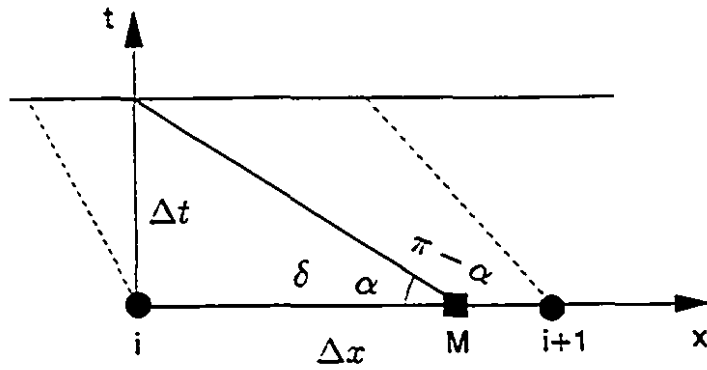


Figure G.1: Grid points near to the boundary in (x, t) space and their correspondent characteristic lines.

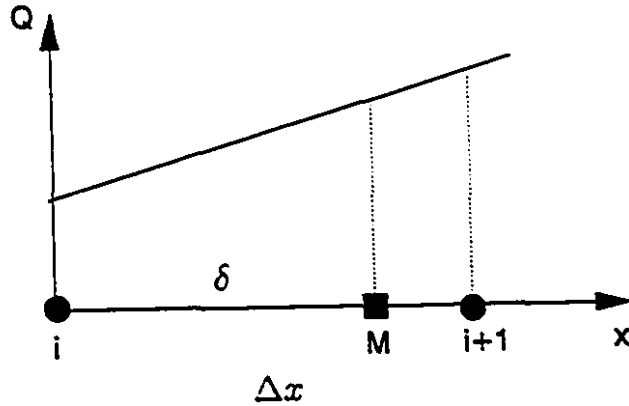


Figure G.2: Interpolating for the left-propagating characteristic slope.

Now consider the Q as linear function of distance, x . The distance between the grid points i and $i + 1$ is taken to be Δx . From Figure G.2 the equation of line satisfying the grid points $i(0, Q_i)$ and $i + 1(\Delta x, Q_{i+1})$ follows

$$Q = \left(1 - \frac{x}{\Delta x}\right)Q_i + \frac{x}{\Delta x}Q_{i+1}. \quad (\text{G.3})$$

The point $M(\delta, Q_M)$ should satisfy the equation (G.3), therefore

$$Q_M = \left(1 - \frac{\delta}{\Delta x}\right)Q_i + \frac{\delta}{\Delta x}Q_{i+1}. \quad (\text{G.4})$$

In a similar manner the slope at M can be written as

$$m_M^- = \left(1 - \frac{\delta}{\Delta x}\right)m_i^- + \frac{\delta}{\Delta x}m_{i+1}^-. \quad (\text{G.5})$$

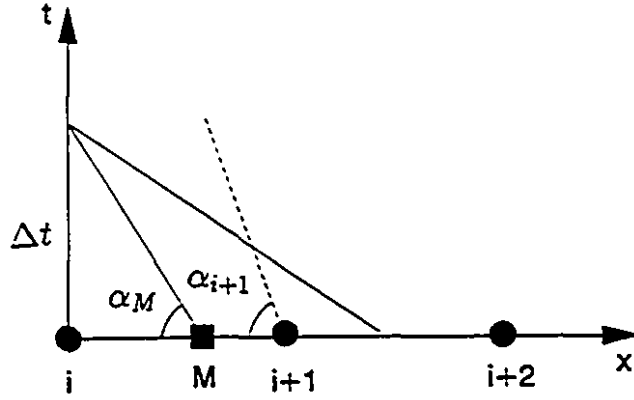


Figure G.3: Comparison of the slopes for left-propagating Riemann variables in order to find the suitable grid points for interpolation.

From Figure G.1, one can determine the slope of Riemann variable at M

$$m_{\bar{M}} = \tan(\pi - \alpha) = -\tan \alpha = -\frac{\Delta t}{\delta}. \quad (\text{G.6})$$

Equating (G.5) and (G.6), one gets the following equation

$$\left(1 - \frac{\delta}{\Delta x}\right)m_{\bar{i}} + \frac{\delta}{\Delta x}m_{\bar{i+1}} = -\frac{\Delta t}{\delta}. \quad (\text{G.7})$$

Everything is known in the equation (G.7) except δ . A test is done in order to clarify that the point M is lying between i and $i+1$ at each iteration step

$$\alpha_M = \tan^{-1} \left| \frac{1}{u_M - a_M} \right|, \quad \alpha_{i+1} = \tan^{-1} \left| \frac{1}{u_{i+1} - a_{i+1}} \right|, \quad (\text{G.8})$$

if $\alpha_M < \alpha_{i+1}$, then the interpolation is performed between the grid points $i+1$ and $i+2$. The quadratic equation (G.7) can be written as

$$(m_{\bar{i+1}} - m_{\bar{i}})\delta^2 + (m_{\bar{i}}\Delta x)\delta + \Delta x\Delta t = 0. \quad (\text{G.9})$$

Hence, the value of δ is calculated from the equation (G.9).

Appendix H

Determination of the Separation Factor

For steady flow the equations (5.4) can be simplified as

$$\begin{aligned} (M^2 - 1) \frac{\partial \Omega}{\partial s} + 2qM \frac{\partial \theta}{\partial n} &= 0, \\ M^2 \frac{\partial \theta}{\partial s} + \frac{2}{\gamma - 1} \frac{1}{\Omega} \frac{\partial \Omega}{\partial n} &= 0. \end{aligned} \quad (\text{H.1})$$

where

$$\Omega = R - Q, \quad M = \frac{q}{a}. \quad (\text{H.2})$$

The first equation is obtained by subtracting the first and second equations in the system (5.4), and defining a new dependent variable Ω . The second equation in (H.1) is obtained by using the equation (B.23) and expressing it in terms of Ω . The functions Ω and θ can be expanded into the asymptotic series as following

$$\begin{aligned} \Omega &= \Omega_\infty + \Omega_1 + \dots, \\ \theta &= \theta_\infty + \theta_1 + \dots, \end{aligned} \quad (\text{H.3})$$

where

$$\begin{aligned} \Omega_\infty &= R_\infty - Q_\infty, \\ \Omega_1 &= R_1 - Q_1. \end{aligned} \quad (\text{H.4})$$

Also for confined flow applications θ_∞ is usually zero. If the operators in equation (5.6) are expanded, one can write up to the first-order terms

$$\begin{aligned}\frac{\partial}{\partial s} &= \frac{\partial}{\partial x} + \theta_1 \frac{\partial}{\partial y}, \\ \frac{\partial}{\partial n} &= -\theta_1 \frac{\partial}{\partial x} + \frac{\partial}{\partial y}.\end{aligned}\tag{H.5}$$

Therefore the equations (H.1) up to the first order become

$$\begin{aligned}B^2 \frac{\partial \Omega_1}{\partial x} - 2q_\infty M_\infty \frac{\partial \theta_1}{\partial y} &= 0, \\ 2q_\infty M_\infty \frac{\partial \theta_1}{\partial x} + \frac{\partial \Omega_1}{\partial y} &= 0,\end{aligned}\tag{H.6}$$

where $B = \sqrt{1 - M_\infty^2}$. Equations (H.6) can be solved by separation of variables assuming

$$\begin{aligned}\Omega_1 &= 2q_\infty M_\infty e^{\omega x} f(y), \\ \theta_1 &= e^{\omega x} g(y),\end{aligned}\tag{H.7}$$

where ω is the unknown separation constant. Equations (H.6) then reduce to the system of ordinary differential equations

$$\begin{aligned}B^2 \omega f - g' &= 0, \\ \omega g + f' &= 0,\end{aligned}\tag{H.8}$$

with boundary conditions on the solid walls

$$g(0) = g(1) = 0\tag{H.9}$$

Eliminating f gives

$$g'' + B^2 \omega^2 g = 0,\tag{H.10}$$

which has the general solution

$$g(y) = k_1 \sin(B\omega y) + k_2 \cos(B\omega y).\tag{H.11}$$

To satisfy the boundary conditions (H.9), the k_2 should be zero and therefore

$$\omega = \pm \frac{n\pi}{B}, \quad (n = 1, 2, \dots) \quad (\text{H.12})$$

For $n = 1$, one gets

$$\omega = \pm \frac{\pi}{\sqrt{1 - M_\infty^2}}. \quad (\text{H.13})$$

Appendix I

Block-tridiagonal System of Equations

The discretization of Euler equations by a three-point implicit method generates a block-tridiagonal system. In a block-tridiagonal coefficient matrix the non-zero sub-matrices are in the diagonal and either side of it. In the present analysis, the resulted matrix is inverted at each step in the transient time. So the solution at each iteration involves solving the two sweeps in both ξ and η directions. The dimension of block-tridiagonal matrix for each sweep is equal to the number of grid points in either direction. In general the system of block-tridiagonal equations reads

$$S\Delta Q = R, \quad (I.1)$$

where ΔQ and R are the vectors for the unknown coefficients and the boundar conditions, respectively. S represents the block-tridiagonal matrix expressed as

$$S = \begin{bmatrix} B_2 & C_2 & 0 & 0 & 0 & 0 \\ A_3 & B_3 & C_3 & 0 & 0 & 0 \\ 0 & \cdot & \cdot & \cdot & 0 & 0 \\ 0 & 0 & \cdot & \cdot & \cdot & 0 \\ 0 & 0 & 0 & A_{m-2} & B_{m-2} & C_{m-2} \\ 0 & 0 & 0 & 0 & A_{m-1} & B_{m-1} \end{bmatrix}, \quad (I.2)$$

where A_i , B_i and C_i are matrices of order (3×3) for quasi-one-dimensional and (4×4) for two-dimensional flows.

To solve the system of equations, the elimination method with factorization is utilized. In the first equation, $B_2\Delta Q_2 + C_2\Delta Q_3 = R_2$, involves only ΔQ_2 and ΔQ_3 . Using this equation and the second one to eliminate ΔQ_3 , the new second equation involves only ΔQ_2 and ΔQ_4 . Continuing this procedure to the last equation where ΔQ_{m-2} has been eliminated, the new last equation only involves ΔQ_{m-1} . Therefore, ΔQ_{m-1} can be determined and the result is applied to the new $(m-2)$ th equation to determine ΔQ_{m-2} . Applying the solution of the i th equation to the $(i-1)$ th equation up to $i = 2$, ΔQ_{i-1} is determined. The algorithm for doing all of this will now be described. Let us consider the following factorization.

$$\begin{aligned}
 S &= LU \\
 &= \begin{bmatrix} \Gamma_2 & 0 & 0 & 0 & 0 & 0 \\ A_3 & \Gamma_3 & 0 & 0 & 0 & 0 \\ 0 & . & . & 0 & 0 & 0 \\ 0 & 0 & . & . & 0 & 0 \\ 0 & 0 & 0 & A_{m-2} & \Gamma_{m-2} & 0 \\ 0 & 0 & 0 & 0 & A_{m-1} & \Gamma_{m-1} \end{bmatrix} \begin{bmatrix} I & \Lambda_2 & 0 & 0 & 0 & 0 \\ 0 & I & \Lambda_3 & 0 & 0 & 0 \\ 0 & 0 & . & . & 0 & 0 \\ 0 & 0 & 0 & . & . & 0 \\ 0 & 0 & 0 & 0 & I & \Lambda_{m-2} \\ 0 & 0 & 0 & 0 & 0 & I \end{bmatrix}, \quad (1.3)
 \end{aligned}$$

where I is the identity matrix of order m . The square matrices Γ_i and Λ_i are determined as follows:

$$\Gamma_2 = B_2 \quad \text{and} \quad \Lambda_2 = B_2^{-1}C_2,$$

$$\Gamma_i = B_i - A_i\Lambda_{i-1} \quad \text{for} \quad i = 3, 4, \dots, m-1$$

and

$$\Lambda_i = B_i^{-1}C_i \quad \text{for} \quad i = 3, 4, \dots, m-2$$

The system of equations given by (I.1) is now equivalent to

$$LZ = R, \quad (1.4)$$

where

$$Z = U\Delta Q. \quad (1.5)$$

Rewriting (1.4), one obtains

$$\begin{bmatrix} \Gamma_2 & 0 & 0 & 0 & 0 & 0 \\ A_3 & \Gamma_3 & 0 & 0 & 0 & 0 \\ 0 & . & . & 0 & 0 & 0 \\ 0 & 0 & . & . & 0 & 0 \\ 0 & 0 & 0 & A_{m-2} & \Gamma_{m-2} & 0 \\ 0 & 0 & 0 & 0 & A_{m-1} & \Gamma_{m-1} \end{bmatrix} \begin{bmatrix} Z_2 \\ Z_3 \\ . \\ . \\ Z_{m-2} \\ Z_{m-1} \end{bmatrix} = \begin{bmatrix} R_2 \\ R_3 \\ . \\ . \\ R_{m-2} \\ R_{m-1} \end{bmatrix}, \quad (1.6)$$

from which

$$Z_2 = \Gamma_2^{-1} R_2,$$

and

$$Z_i = \Gamma_i^{-1} (R_i - A_i Z_{i-1}) \quad \text{for } i = 3, 4, \dots, m-1.$$

Equation (1.5) is then expressed as

$$\begin{bmatrix} I & \Lambda_2 & 0 & 0 & 0 & 0 \\ 0 & I & \Lambda_3 & 0 & 0 & 0 \\ 0 & 0 & . & . & 0 & 0 \\ 0 & 0 & 0 & . & . & 0 \\ 0 & 0 & 0 & 0 & I & \Lambda_{m-2} \\ 0 & 0 & 0 & 0 & 0 & I \end{bmatrix} \begin{bmatrix} \Delta Q_2 \\ \Delta Q_3 \\ . \\ . \\ \Delta Q_{m-2} \\ \Delta Q_{m-1} \end{bmatrix} = \begin{bmatrix} Z_2 \\ Z_3 \\ . \\ . \\ Z_{m-2} \\ Z_{m-1} \end{bmatrix}, \quad (1.7)$$

from which

$$\Delta Q_{m-1} = Z_{m-1},$$

and

$$\Delta Q_i = Z_i - \Lambda_i \Delta Q_{i+1} \quad \text{for } i = m-1, m-2, \dots, 3, 2$$

For sweep in x -direction $m = M_I$, and for y -direction $m = M_J$. In which M_I and M_J are the maximum number of grid points in either direction.

In the present work, the size of the block-tridiagonal matrix S can be reduced considerably when the proposed model of FFBCs is applied. Hence the storage required for solving the system is substantially reduced.